



MAX-PLANCK-GESELLSCHAFT

Max Planck **Graduate Center**  
mit der Johannes Gutenberg-Universität Mainz



JOHANNES GUTENBERG  
UNIVERSITÄT MAINZ

# **Amyloid-like Peptide Nanostructures for Controllable Cell-Material Interactions**

Dissertation

zur Erlangung des akademischen Grades eines  
„Doctor rerum naturalium“ (Dr. rer. nat.) der Fachbereiche:

08 - Physik, Mathematik und Informatik  
09 - Chemie, Pharmazie, Geographie und Geowissenschaften  
10 - Biologie  
Universitätsmedizin

vorgelegt von

**Adriana Maria Ender, geborene Sobota**

Mainz, August 2023

-D77-

Mainzer Dissertation

Dekanin: [REDACTED]

I. Gutachter: [REDACTED]

II. Gutachter: [REDACTED]

Eingereicht am: 10.08.2023

Tag der mündlichen Prüfung: 27.09.2023

Die vorliegende Arbeit wurde in der Zeit vom Oktober 2018 bis August 2023 am Max-Planck-Institut für Polymerforschung in dem Arbeitskreis von [REDACTED] angefertigt. Im Zeitraum von Februar 2021 bis Februar 2022 wurde die Arbeit aufgrund von Mutterschutz und Elternzeit unterbrochen.

Hiermit versichere ich gemäß § 11 Abs.4 der Promotionsordnung vom 26.05.2009

*“I hereby declare that I wrote the dissertation submitted without any unauthorized external assistance and used only sources acknowledged in the work. All textual passages which are appropriated verbatim or paraphrased from published and unpublished texts as well as all information obtained from oral sources are duly indicated and listed in accordance with bibliographical rules. In carrying out this research, I complied with the rules of standard scientific practice as formulated in the statutes of Johannes Gutenberg-University Mainz to insure standard scientific practice.”*

Mainz, August 2023

Adriana Ender





# Acknowledgements

## Abstract

Amyloids are extracellular depositions of fibrils with a certain morphological structure, characteristic X-ray diffraction pattern and an affinity for the histochemical stain Congo red. Since the 20th century, amyloids have been predominantly associated with neurodegenerative disorders like Alzheimer's or Parkinson's disease. However, also functional amyloids and amyloid-like fibrils exist that have gained much interest in medical applications. "Amyloid-like fibrils" are synthetic fibrils that exhibit amyloid characteristics. Due to their rapid assembly into peptide fibrils, amyloid-forming peptides show several advantages over other synthetic scaffold materials, such as prolonged half-life, thixotropic character and a diversity of mechanical, structural and biological properties providing an adhesive character towards a variety of macromolecules, viruses as well as biological membranes. Therefore, amyloids mimic certain structural features of the extracellular matrix (ECM) components and are thus used in applications like tissue engineering, in which functional components are assembled that can repair, preserve or improve damaged tissue. Here, the interaction of amyloids and amyloid-like fibrils with cell membranes was extensively studied during the last years, revealing amyloids' and amyloid-like fibrils' ability to promote cell-attachment, viability and growth without displaying toxicity and immunogenicity. Some studies could even disclose a higher effectivity of amyloidogenic structures compared to native ECM components. To gain a deeper understanding of cell-amyloid interactions, several mechanisms have been postulated providing solid findings about the role of amyloids physico-chemical and topographical characteristics during cell-amyloid interaction. Nowadays, researchers could demonstrate that through rational peptide design, biological activity of amyloidogenic structures could be tailored to a specific application. Such achievements are only possible because of the relationship between peptide sequence, nanostructure and macroscopic properties that exist in amyloids. Advanced synthesis and purification techniques allow systematic variations in the peptide sequence and studying of such relationships in detail.

The creation of bioactive scaffolds for applications like tissue engineering requires precise control over cell-material interactions to generate specific cellular responses. Within this thesis, for the first time, a two-dimensional amyloid-like scaffold has been designed with the aim to precisely control cell behavior such as cell adhesion. Here,

we could show that through controlled chemical reactions, the amyloid-like scaffold was defunctionalized, destroyed or disassembled locally, which allowed the subsequent fabrication of macroscopic cell patterns and gradients on surfaces.

In the first project of my thesis, I could demonstrate that self-assembly of amyloid-like peptides could be controlled by several external stimuli in solution. The amphiphilic peptide sequence KIKISQINM was used as a prototype for rational peptide design. On the one hand, this peptide formed amyloid fibrils with high intrinsic cell-adhesive character. Furthermore, KIKISQINM allowed the introduction of peptide variations in geometry as well as polarity, which affected the (dis)assembly by simple exposure to stimuli found in cells like pH changes or reactive oxygen species. Here, the transformation of this sequence into the so-called “depsi-peptide” prevented fibril formation due to enhanced solubility. Depsi-peptides can reveal a kinked, non-assembling structure that is linearized *via* an *O,N*-acyl switch triggered by hydrolytic removal of the N-terminal carbamate protecting group of the serine. The physiological pH of the solution induced the linearization of the peptide and led to spontaneous self-assembly into nanofibrils. As the sequence additionally contained methionine, its oxidation into the more polar methionine sulfoxide reduced the amphiphilic character of the sequence and the interactions between peptides led to a subsequent disassembly of the superstructure. This project provided the groundwork for the following studies demonstrating the ease of integration of chemical tools for controlled assembly and disassembly of amyloid-like nanostructures. Furthermore, these results corroborated the fact that changes in amphiphilicity and solubility affected peptide self-assembly, which has been an important observation and led to the subsequent project.

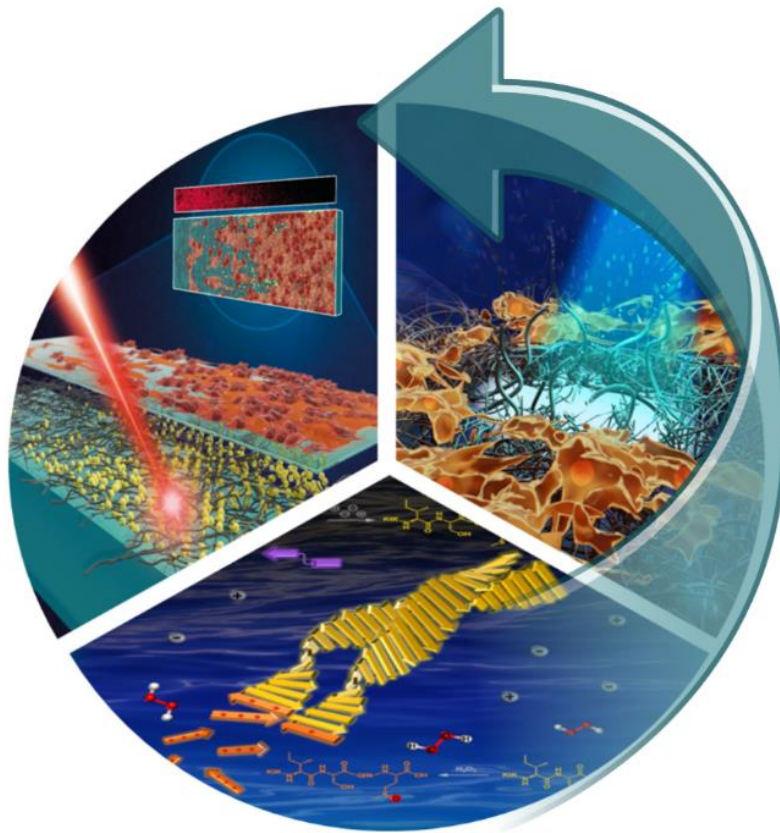
In the first project, dissociation of fibrils has been achieved through an oxidation reaction by applying hydrogen peroxide. In the next project, I was interested in the controlled cell-adhesion on surfaces by external chemical or physical stimuli. Consequently, two approaches were elaborated, in which cell-adhesiveness was directed by either the destruction of topography or by (de)functionalization of the conserved material topography. For the realization of these two goals, light was selected as external stimulus as it offers the possibility of precise patterning and gradient formation in a time as well as a space independent fashion. Henceforth, in the following projects, *o*-nitrobenzyl ester was used as a photocleavable linkage group (PCL), whose cleavage is triggered by UV light. Moreover, CKFKFQF was selected as



cell adhesive scaffold. This sequence assembled into amyloid-like fibrils with high  $\beta$ -sheet content displaying a biocompatible, cell-adhesive, and cell-supporting character. The hypothesis of controlling cell-adhesiveness by the destabilization of the scaffold was based on the postulated connection between amyloids' bioactivity, morphology and high  $\beta$ -sheet content. Hence, the bioactive amyloidogenic peptide CKFK-PCL-FQF was designed. Through UV-induced cleavage into hydrophilic CKFK and lipophilic PCL-FQF peptide fragments of the amyloid-like scaffold, a loss of cell-adhesiveness occurred locally based on the disintegrated  $\beta$ -sheet rich secondary structure. By drop-casting of preformed fibrils on surfaces and using a photolithographic technique, we were able to create defined amyloid patterns of cell-adhesive and non-adhesive regions with different resolutions up to 10  $\mu\text{m}$  precision, exhibiting interactive features *versus* different cell lines. In contrast, the approach of the last project mainly addressed the (de)functionalization of intact scaffolds topography. Here, amyloids were modified with the model epitope RGD *via* a PCL linker resulting in the amyloid-forming peptide sequence RGD-PCL-CKFKFQF. The RGD epitope enhanced threefold the inherent bioactivity of the CKFKFQF fibrils and was therefore a potent tool to disclose the full potential of the light-triggered amyloid-based platform to create bioactive spatial gradients. Consequently, preformed RGD-functionalized fibrils were sprayed on a cell-repellent surface and irradiated gradually through a movable mask creating a 5 cm RGD-gradient. This molecular gradual distribution was characterized covering multiple length scales ranging from micrometers to centimeters demonstrating its bioactivity through a cell density gradient. This project demonstrated the ability of the UV-triggered platform to create infinitesimal, UV-dose dependent changes of exposed biofunctionalization on a cm-length scale.

In summary, we could show that through rational peptide design, we were able to achieve controlled surface patterns and gradients of *per se* bioactive or amyloid-like nanostructures. Simple variations in the primary structure either enhanced or decreased their cell-supportive character based on changes in the scaffolds morphology or presentation of chemical epitopes on a scaffold. Consequently, we concluded our findings as a forerunner in the discovery of deeper understanding of amyloid morphology-cell reaction relationship. The two-dimensional UV-triggered amyloid-based platform reported herein could inspire prospective 3D materials in

medical applications like tissue engineering and drug delivery as amyloid fibrils emerge as adaptive functional scaffold materials.



## Zusammenfassung

Extrazelluläre fibrilläre Ablagerungen mit einer definierten Morphologie, einem charakteristischen Röntgenbeugungsmuster sowie der Affinität zu dem Farbstoff Kongorot werden als Amyloide bezeichnet. Diese sind bereits seit dem 20. Jahrhundert vorrangig dafür bekannt, dass sie mit neurodegenerativen Erkrankungen wie Alzheimer oder Parkinson in Verbindung gebracht werden. Allerdings werden zunehmend so genannte „funktionelle Amyloide“ entdeckt, welche diesem zuvor erwähnten Klischee der Amyloide widersprechen und auch in der Zelle wichtige Funktionen übernehmen können. Aus diesem Grund gewinnen Amyloid-ähnliche Strukturen (Synthetische Fibrillen mit Amyloid-Eigenschaften) immer mehr an Bedeutung in medizinischen Anwendungen. Amyloide aber auch Amyloid-ähnliche Strukturen weisen aufgrund ihrer schnellen Selbstassemblierung zu fibrillären Strukturen diverse Vorteile gegenüber anderen synthetischen Gerüstmaterialien auf, wie z. B. eine längere Halbwertszeit, thixotrope Eigenschaften und eine Vielzahl mechanischer, struktureller und biologischer Eigenschaften, welche eine adhäsive Wirkung gegenüber einer Vielzahl von Makromolekülen, Viren und biologischen Membranen zur Folge haben. Diese Eigenschaften der Amyloide liefern eine starke Ähnlichkeit mit Komponenten der extrazellulären Matrix (EZM), weshalb sie gerne im Bereich des Tissue Engineering Verwendung finden. Beim Tissue Engineering wird aus verschiedenen funktionellen Komponenten ein Ersatzgewebe „gezüchtet“, welches in der Lage ist, geschädigtes Gewebe zu regenerieren und/oder zu ersetzen. Aus diesem Grund wurde in den letzten Jahren insbesondere die Wechselwirkung von Amyloiden mit Zellmembranen umfassend untersucht. Studien zeigten, dass Amyloide in der Lage sind, sowohl die Zelladhäsion als auch die Vitalität und das Wachstum von Zellen zu fördern, ohne Toxizität und Immunogenität zu entwickeln. Diesbezüglich konnte gezeigt werden, dass amyloide Strukturen sogar eine höhere Wirksamkeit im Vergleich zu nativen EZM-Komponenten entwickeln können. Um ein tieferes Verständnis der Zell-Amyloid-Wechselwirkungen zu ermöglichen, wurden mehrere Mechanismen postuliert, die eine Reihe von Erkenntnissen über die Rolle der physikalisch-chemischen und topografischen Eigenschaften von Amyloiden liefern. Infolgedessen kann durch rationales Peptiddesign eine zielgerichtete Steigerung der biologischen Aktivität amyloidogener Strukturen erreicht werden. Dieser Erfolg beruht hauptsächlich auf der Nanostruktur der Amyloide, welche mit ihren einfachen

Synthese-, Modifikations- und Aufreinigungsmöglichkeiten einen großen Forschungsfreiraum bereithält.

Nichtsdestotrotz ist eine präzise Kontrolle der Zell-Material-Interaktionen, die zur Ausbildung spezieller Zellfunktionen führen kann, für die Entwicklung bioaktiver Gerüste z.B. im Bereich des Tissue Engineering von großer Bedeutung. Im Rahmen dieser Arbeit wurde erstmals ein zweidimensionales amyloidähnliches Gerüst entwickelt und untersucht, welches das Ziel verfolgt, die Adhäsion von Zellen mit hoher räumlicher Auflösung präzise zu steuern. Wir konnten zeigen, dass durch regulierte Defunktionalisierung sowie Zerstörung/Desassemblierung des Amyloidgerüsts die Kontrolle über die Bioaktivität erreicht werden kann. Mittels Herstellung makroskopischer Zellmuster und Gradienten auf Oberflächen konnte diese Errungenschaft visualisiert und bewiesen werden.

Im ersten Projekt wird gezeigt, dass die Selbstorganisation amyloidähnlicher Peptide in Lösung durch verschiedene äußere Reize gesteuert werden kann. Hierfür wurde die amphiphile Sequenz KIKISQINM als Prototyp für das anschließende Peptiddesign verwendet. Zum einen ist bekannt, dass diese Peptidsequenz Amyloidfibrillen mit hoher intrinsischer zelladhäsiver Wirkung bildet. Darüber hinaus ermöglicht KIKISQINM die Einführung von chemischen Variationen, welche eine Auswirkung auf die Morphologie und die Polarität der Struktur haben. Die Änderungen in der Morphologie und Polarität werden durch einfache Stimuli wie pH-Änderungen oder lokale Oxidationsreaktionen ausgelöst, welche auch in Zellen vorkommen und die die (Des-)Assemblierung der Strukturen einleiten. Die Einführung des sogenannten Depsi-Peptids verhindert beispielweise die sofortige Umwandlung des Peptids in die fibrilläre Form aufgrund seiner nichtlinearen Form. Die Linearisierung dieses geknickten Peptids kann mittels einer *O,N*-Acyl-Verschiebung stattfinden, welche durch den physiologische pH-Wert der Lösung ausgelöst wird. Die vorangegangene Hydrolyse der N-terminalen Carbamat-Schutzgruppe des Serins initiiert diesen Schritt. Die linearen Peptide wiederum sind somit in der Lage, durch spontane Selbstorganisation der Moleküle Nanofibrillen zu bilden. Ebenso führt das Vorhandensein von Methionin in der Sequenz in oxidativer Umgebung zur Bildung von Methioninsulfoxid. Dies hat eine Zerstörung des amphiphilen Charakters der Sequenz zur Folge, was die Wechselwirkungen zwischen den Peptiden reduziert, wodurch die

Überstruktur auseinanderfällt. Dieses Projekt demonstriert, wie simple chemische Werkzeuge für den kontrollierten Auf- und Abbau amyloidähnlicher Nanostrukturen verantwortlich sein können und bilden somit die Basis für die nachkommenden Arbeiten. Darüber hinaus bestätigen diese Ergebnisse die Tatsache, dass Änderungen in der Amphiphilie den selbstorganisierenden Charakter beeinflussen, der für das nachfolgende Projekt von grundlegender Bedeutung ist.

Das Ziel der folgenden beiden Projekte war es, eine kontrollierte Zelladhäsion auf Oberflächen zu erreichen. Folglich wurden zwei Ansätze ausgearbeitet, bei denen die Zelladhäsion entweder durch die Zerstörung der Topographie oder durch (De)Funktionalisierung der konservierten Materialtopographie kontrolliert wurde. Da als äußerer Reiz Licht die Möglichkeit einer präzisen Musterung und Gradientenbildung in zeit- und raumunabhängiger Weise bietet, wurde dieser als Stimulus zur Verwirklichung der zuvor erwähnten Ziele der nächsten Projekte gewählt. Von nun an wird *o*-Nitrobenzylester in den folgenden Arbeiten als photospaltbare Verknüpfungsgruppe (PCL) benötigt, deren Spaltung durch UV-Licht ausgelöst wird. Im zweiten Projekt wurde CKFKFQF als Gerüst für das Peptiddesign ausgewählt. Diese Sequenz assembliert zu amyloidähnlichen Fibrillen mit hohem  $\beta$ -Faltblattgehalt, die einen biokompatiblen und zelladhäsiven Charakter aufweisen. Die Hypothese des zweiten Projekts basierte auf dem postulierten Zusammenhang zwischen der Bioaktivität, Morphologie und dem hohen  $\beta$ -Faltblattgehalt von Amyloiden. Somit wurde das bioaktive amyloidogene Peptid CKFK-PCL-FQF entwickelt, welches durch UV-induzierte Spaltung in ein hydrophiles CKFK- und ein lipophiles PCL-FQF-Fragment zerfällt. Dies hat den Verlust der Zelladhäsionsfähigkeit aufgrund der Schädigung der  $\beta$ -faltblattreichen Sekundärstruktur zur Folge.

Nachdem die intakten Peptid-Fibrillen auf eine Oberfläche mittels der drop-casting Methode aufgetragen wurden, konnten wir zeigen, dass mithilfe einer photolithografischen Technik definierte Muster zelladhäsiver und nichtadhäsiver Bereiche mit unterschiedlichen Auflösungen bis zu einer Genauigkeit von 10  $\mu\text{m}$  erzeugt werden konnten. Im Gegensatz dazu befasste sich der Ansatz des letzten Projekts lediglich mit der (De-)Funktionalisierung der Topographie eines noch intakten Gerüsts. Hier wurde das amyloidbildende Peptid mit dem Modell-Epitop RGD über den PCL modifiziert, und kreierte das Peptid RGD-PCL-CKFKFQF. Das RGD-Epitop steigerte die inhärente Bioaktivität der CKFKFQF-Fibrillen um das Dreifache und ist

daher ein wirksames Werkzeug, um das volle Potenzial der lichtgesteuerten Amyloid-basierten Plattform zu entfalten. Somit wurden vorgeformte RGD-funktionalisierte Fibrillen auf eine zellabweisende Oberfläche gesprüht und nach und nach durch eine bewegliche Maske bestrahlt, wodurch ein RGD-Gradient von 5 cm entstand. Diese graduelle molekulare Verteilung zeichnete sich dadurch aus, dass sie mehrere Längenskalen abdeckte, die von Mikrometern bis hin zu Zentimetern reichten, und ihre Bioaktivität durch einen Zelldichtegradienten demonstriert. Dieses Projekt zeigt somit das Potenzial der UV-gesteuerten Plattform, infinitesimale, UV-dosisabhängige Änderungen der exponierten Biofunktionalisierung auf einer cm-Längenskala zu erzeugen.

Zusammenfassend konnten wir zeigen, dass durch Modifizierung der Peptidsequenz kontrollierte Veränderungen der Struktur und Bioaktivität amyloidähnlicher Materialien erreicht werden können. Diese einfachen Variationen in der Primärstruktur äußern sich in den Änderungen der Gerüstmorphologie oder der Präsentation chemischer Epitope und können sowohl zu einer Verstärkung als auch zu einer Verringerung des zellunterstützenden Charakters führen. Unsere Ergebnisse können somit als Vorreiter für ein besseres Verständnis der Interaktion von Amyloiden mit Zellen betrachtet werden. Da Amyloidfibrillen auch als adaptive funktionelle Gerüstmaterialien angesehen werden können, bildet unsere amyloidbasierte UV-gesteuerte Plattform die Grundlage für zukünftige dreidimensionalen Erfindungen in medizinischen Forschungsbereichen wie Tissue Engineering und Drug Delivery.

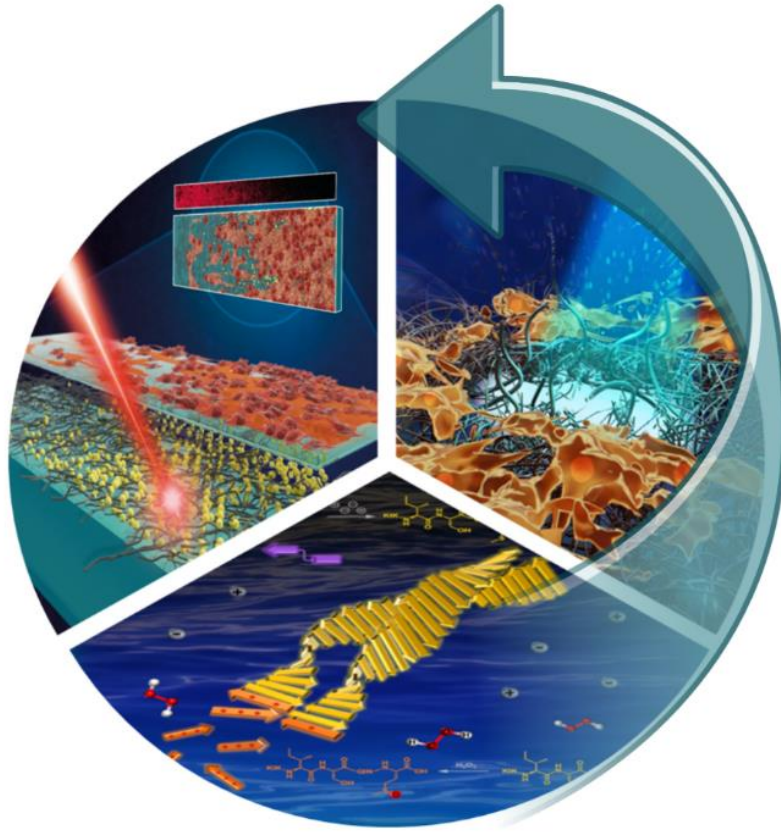


# Table of Contents

Abstract .....	7
Zusammenfassung .....	11
1. Introduction .....	19
1.1. General Introduction to Amyloids .....	19
1.1.1. Terminology of Amyloids and Occurrence in living Organisms .....	19
1.1.2. Supramolecular Structure of Amyloids and Characterization Methods .....	22
1.2. Cell-Material Interactions and Regulation of Cell Behaviour .....	28
1.2.1. General Introduction of Cell-Material Interactions .....	28
1.2.2. Spatio-temporal Representation of Cell-adhesive Parameters .....	33
1.3. Structure-Activity-Relationship of Amyloid-like Fibrils by studying their Cell-Material Interactions .....	35
1.3.1. "Activity" of Amyloids and Amyloid-like Fibrils towards Cells .....	35
1.3.2. Mechanism of Interactions of Amyloid-like Fibrils with Cells .....	38
1.3.3. Rational Sequence Design of Amyloid-like Fibrils for Cell Activity Improvement .....	39
1.4. Strategies for controlled Assembly/Disassembly of Amyloid-like Materials .....	43
1.5. Amyloid-like Materials in Medical Applications .....	49
1.5.1. Amyloid-like Materials in Drug Delivery .....	49
1.5.2. Amyloid-like Materials as Retroviral Enhancers .....	51
1.5.3. Amyloid-like Materials as Scaffolds in Tissue Engineering .....	53
1.6. References .....	59
2. Motivation, Aims and Conceptual Design .....	72
3. Orthogonally Stimulated Assembly/Disassembly of Depsipeptides by Rational Chemical Design .....	76
3.1. Contributions .....	76
3.2. Abstract .....	77
3.3. Results and Discussion .....	77
3.4. Conclusion and Outlook .....	85
3.5. Acknowledgements .....	86
3.6. References .....	87
3.7. Supporting Information .....	89
3.7.1. Materials and instruments .....	89
3.7.2. Synthesis .....	91



3.7.3.	Characterization .....	96
3.7.4.	Literature .....	107
4.	Photoinduced Amyloid Fibril Degradation for Controlled Cell Patterning .....	108
4.1.	Contributions .....	108
4.2.	Abstract .....	109
4.3.	Introduction.....	110
4.4.	Results and Discussion .....	113
4.4.1.	Design, Synthesis, and Characterization of the Photoresponsive Self-Assembling Peptide.....	113
4.4.2.	Secondary Structure and Morphology of Amyloid-like Fibrils is Altered after Irradiation.....	115
4.4.3.	Photopatterning of Fibril-Coated Surfaces.....	118
4.4.4.	Spatially Controlled Cell Pattern.....	119
4.5.	Conclusion.....	120
4.6.	Experimental Section/Methods .....	121
4.6.1.	Materials.....	121
4.6.2.	Methods .....	122
4.7.	Acknowledgements .....	126
4.8.	References .....	128
4.9.	Supporting Informations.....	132
4.9.1.	Methods .....	132
4.9.2.	Additional Characterization CKFK-PCL-FQF 1 .....	134
4.9.3.	Additional Characterization CKFK-NCL-FQF 4 .....	138
4.9.4.	Peptide Coating and Patterning .....	141
4.9.5.	References.....	149
5.	Cell-instructive surface gradients of photo-responsive amyloid-like fibrils .....	153
5.1.	Contributions .....	153
5.2.	Abstract .....	154
5.3.	Introduction.....	154
5.4.	Materials and Methods .....	158
5.4.1.	Materials.....	158
5.4.2.	Methods .....	159
5.5.	Results and Discussion .....	164
5.5.1.	Design and Synthesis of a Photoresponsive Self-assembling Peptide 164	
5.5.2.	Functional Gradients on Surfaces .....	168

5.5.3.	Fabrication of RGD-Gradient on Glass Substrates .....	170
5.5.4.	A549 Cell-Gradient formation.....	171
5.6.	Conclusion.....	172
5.7.	Acknowledgements .....	173
5.8.	References .....	173
5.9.	Supporting Information .....	177
5.9.1.	Materials for Linker Synthesis .....	177
5.9.2.	Instruments .....	177
5.9.3.	Synthesis.....	180
5.9.4.	Additional Characterization RGD-NCL-CKFKQF (16).....	191
5.9.5.	Additional Characterization RGD-PCL-CKFKQF (15) .....	197
5.9.6.	References.....	199
6.	Summary and Outlook.....	200
	Amino Acid Code.....	203
	Appendix .....	204

# 1. Introduction

## 1.1. General Introduction to Amyloids

### 1.1.1. Terminology of Amyloids and Occurrence in living Organisms

The term “amyloid” (*amylum* [latin] = starch) means “starch-like” and was first introduced in medical literature by *Rudolf Virchow* in 1854. He discovered that parts of the brain show positive reaction with iodine and sulfuric acid, which indicates starch or cellulose-related substances. Consequently, he named the stained substance “amyloid”.<sup>[1]</sup> Only five years later *Friedrich* and *Kakulé* found out that these “amyloid” deposits were protein-derived and the term turns out to be a misnomer.<sup>[2–5]</sup> Nowadays, the terminology “amyloid” seems to endure *inter alia* in the field of pathological diagnosis as the *Nomenclature Committee of the International Society of Amyloidosis* has defined amyloids as extracellular depositions of fibrils with definite characteristics in electron microscopy, typical X-ray diffraction pattern and their affinity for Congo red with resulting green birefringence. Likewise, synthetic fibrils with amyloid characteristics were termed as “amyloid-like fibrils”.<sup>[6,7]</sup>

As described above, amyloids were historically shaped for being associated with a large number of neurodegenerative diseases including Parkinson’s disease, diabetes type II, amyotrophic lateral sclerosis and prion diseases.<sup>[8,9]</sup> In 1901, *Dr. Eugene L. Opie* first identified the formation of amyloid deposits in the pancreas of Type II diabetes patients.<sup>[10,11]</sup> Four years later, in 1905 *Aloysius Alzheimer* first described the Alzheimer’s disease (AD) by the discovery of biomaterial depositions in the brain of a demented patient post mortem. Until today, the key amyloid-forming proteins were clearly identified for each disease like the A $\beta$  protein for AD and the islet amyloid polypeptide (IAPP) or amylin in type II diabetes.<sup>[10]</sup>

On the other hand, amyloids do not always have a pathological nature but can be useful for various cellular tasks. They seem to be highly regulated and their amyloid conformation represents a fundamental structural motif with unique biophysical characteristics that is capable of performing multiple functions.<sup>[8,12–15]</sup> These amyloids were named “functional amyloids” and occur in bacteria, fungi as well as in mammalian tissues.<sup>[9,12,14,15]</sup> Referring back to the nomenclature of amyloids, *Jeffery W. Kelly* proposed the term “amyloidin” for functional amyloids. He and his group found that the

so-called Pmel17 (premelanosome protein 17) amyloid serves as a scaffold for the polymerization of tyrosine derivatives into melanin. Moreover, they hypothesized that amyloids protect the cells from toxic effects of reactive melanin intermediates. *Jeffery W. Kelly et al.* were one of the first indicating a non-pathological role of amyloid, and supposed a steady growth of the number and diversity of functional amyloids.<sup>[13,16]</sup> The proposed term “amyloidin” has not prevailed but since the last decade, functional amyloids have emerged in an increasing number displaying various biological functions in the mammalian organism *inter alia* during long-term-potential, sperm assortment and peptide hormone storage.<sup>[8,13,17,18]</sup> In the following Table 1 some examples of functional amyloids and their functions are listed.

*Table 1: List of examples of functional amyloids in mammals. CPEB3 = cytoplasmic polyadenylation element binding protein 3; FXR 1 = fragile-X mental retardation autosomal 1; MBP = major basic protein; PAP = prostatic acidic phosphatase; Pmel 17 = premelanosome protein 17; RIP = receptor interacting protein kinase; RNA = ribonucleic acid; SEM = semenogelin proteins.*

<b>Protein</b>	<b>Function in amyloid form</b>	<b>References</b>
<b>Pmel17 protein</b>	Template for melanin synthesis in melanosome and sequestration of toxic intermediates	[12,13,19–21]
<b>CPEB3</b>	Synaptic plasticity; modulation of long-term memory	[22]
<b>Peptide hormones</b>	Storage of (pro)-hormones	[23]
<b>PAP</b> <b>SEM1 /SEM2</b>	Antimicrobial functions; protection of sperm cells; filter function that select only sperm of high quality for the fertilization; semen derived enhancer of virus infection (SEVI)	[17,24,25]
<b>FXR1</b>	Regulation of RNA stability and translation	[26]
<b>Fibrin peptides</b>	Regulation of blood cloth (activation of factors in hemostasis and platelet formation)	[27–29]
<b>MBP</b>	Inert storage of toxic MSP	[30]
<b>RIP1/RIP3</b>	Signaling and cell death of necroptosis	[31]

There are still raising speculations about additional manifestations of functional amyloids in living organisms. In 2019, *Sopova et al.* were able to identify the FXR1 (fragile-X mental retardation autosomal 1) protein in the brain of young healthy rats,

which is known to regulate memory and emotions. This extracted protein showed the formation of resistant amyloid structures, which affect RNA (ribonucleic acid) stability and were suggested to regulate the RNA translation.<sup>[26]</sup> Recent studies on the function of the FXR1 amyloid led to the hypothesis that the storage of RNA molecules plays a crucial role in cellular stress responses. Moreover, they claimed that the FXR1 amyloid fibrils became an essential component of brain neurons during the vertebrate evolution.<sup>[32]</sup>

There were also certain indications that some amyloid-related pathologies have their origin in the appearance of functional amyloids. For example, it has been postulated that pathogenic A $\beta$  amyloids could also reveal certain positive features. Apart from that, it has been observed that A $\beta$  deposits occur in the brains of persons after several head trauma or brain injury, which leads to a slightly increased chance of getting AD.<sup>[8,9,33,34]</sup> Here, the damage to the nerve axons could cause an accumulation of APP, which results in increased A $\beta$  production. These A $\beta$  depositions are hypothesized to contain the blood loss from damaged brain tissue and thus they could play an important role in maintaining vascular integrity.<sup>[8,9,34]</sup>

Summarizing, there is a huge diversity in amyloid activity towards the living organism. Some amyloids serve as template while others induce a specific cell-toxic response.<sup>[35]</sup> There have been several groups who hypothesized the reasons of amyloids' diverse functionalities in the body. First, according to the rapid self-assembly of functional amyloids in comparison to pathological amyloids, the formation of potentially toxic oligomers could be reduced. Smaller peptide aggregates, so-called amyloid oligomers are known to be the most cytotoxic species in the amyloid forming pathway. Second, the presence of functional amyloids seems to be highly regulated through a number of cells safeguards like chaperones and compartmentalization to prevent toxic effects.<sup>[9,35]</sup> Third, amyloids structural diversity caused for example through changed assembling conditions might be one of the reasons for different activities among amyloids.<sup>[9]</sup>

To elucidate the structure-activity relationship in more detail amyloids structural characteristics, their self-assembly into defined structures and their bioactivity towards cells will be discussed in the subsequent sections.

## 1.1.2. Supramolecular Structure of Amyloids and Characterization Methods

Amyloids and amyloid-like structures can be formed by different peptides and proteins. Proteins, synthetic short amphiphilic peptides, hybrid amphiphilic molecules and even single amino acids can form amyloids or amyloid-like structures under certain conditions.<sup>[36–39]</sup>

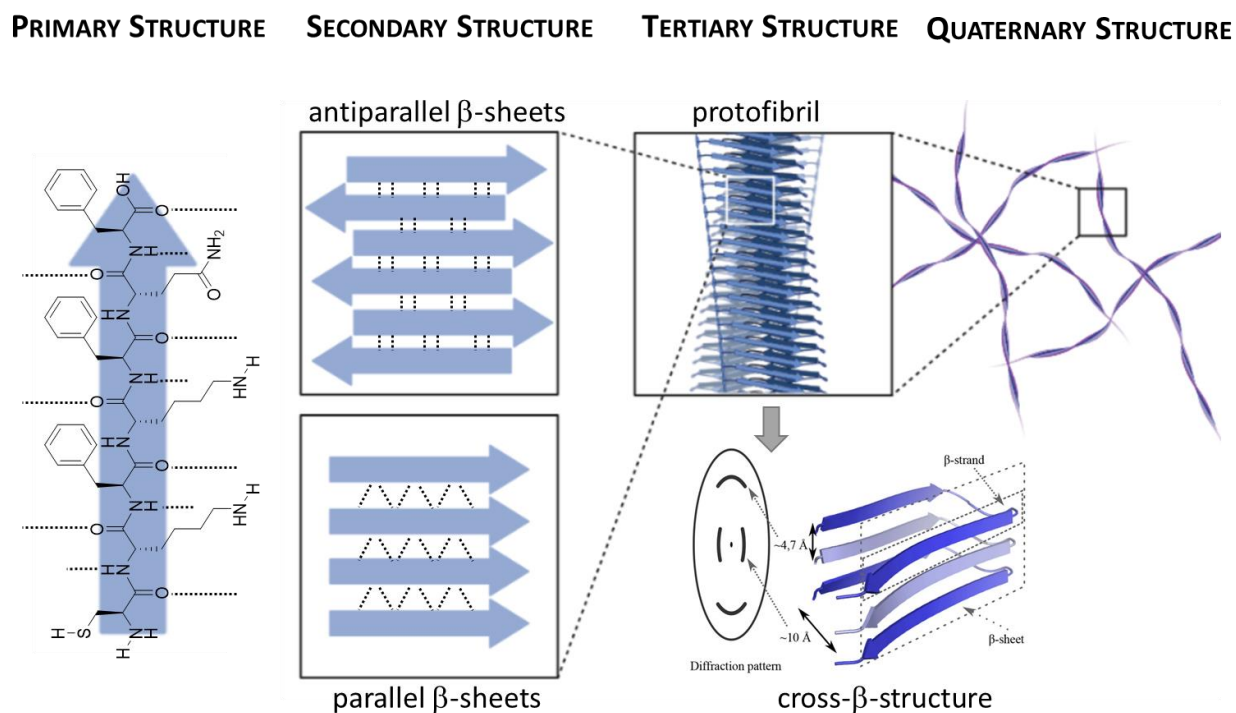


Figure 1: Overview of amyloidogenic peptide self-assembly from primary structure into quaternary structures. Figure was created with BioRender and adapted from Ref. <sup>[40]</sup> with permission from Springer Nature.

These “monomers” self-assemble *via* non-covalent interactions into a secondary structure that consists of an arrangement of  $\beta$ -strands into antiparallel or parallel  $\beta$ -sheets. The distance between  $\beta$ -strands in the sheet is typically  $4.7 - 4.8 \text{ \AA}$ .<sup>[9,11,40–42]</sup> The tertiary structure of amyloids is caused by the so-called cross- $\beta$ -arrangement, which classifies the aggregates as amyloid or amyloid-like structure and shows a specific pattern in the X-ray fiber diffraction (XRD). It was shown that the cross- $\beta$ -arrangement is stabilized by dry steric interfaces (steric zipper) and form the protofibril.<sup>[9,40,42–44]</sup> Here, the  $\beta$ -sheets are oriented perpendicular to the protofibrils’ axis and are located at a specific distance of about  $10 \text{ \AA}$  from each other.<sup>[9,40,43]</sup> Further, through interactions between two or even more protofibrils, in which the

protofibrils are twisted around each other, an individual fibril showcases a highly organized hierarchical quaternary structure.<sup>[9,11,40,43]</sup>

The complex amyloid fibrillation mechanism contains an aggregation network, which can be roughly categorized into three macroscopic phases.<sup>[9]</sup> The lag phase is the earliest phase, in which the soluble monomers start to interact with each other to a variety of different soluble species called oligomers. This so-called primary nucleation process is followed by the elongation phase with rapid fibril growth. Typically, elongation means the incorporation of monomeric units at the end of an existing fibril. But in some cases, fibril growth can also occur through fibril-fibril aggregation. At the end of the elongation phase saturation occurs, in which mature fibrils are formed. The typical kinetic growth of a fibril with its three macroscopic phases is depicted in the following figure.<sup>[9,11,45]</sup>

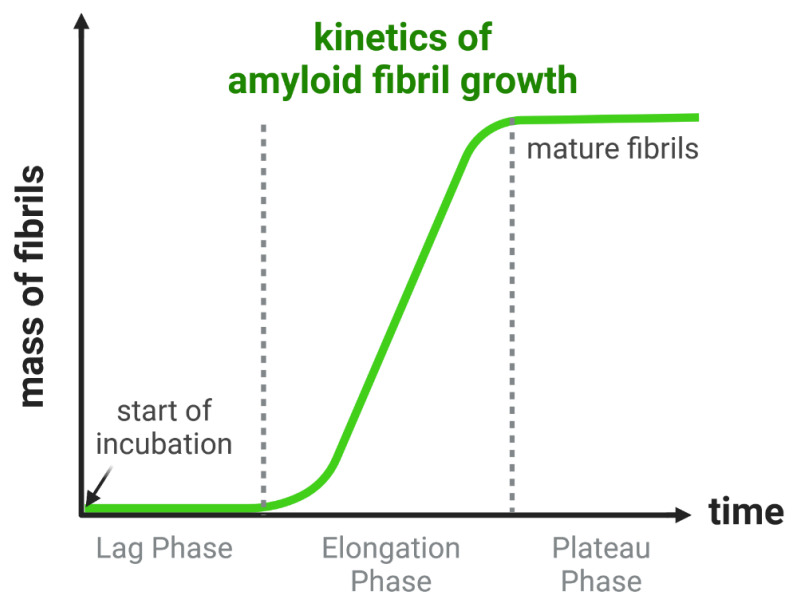


Figure 2: Kinetics of amyloid formation. Graphic was created with BioRender and is based on an illustration from Ow et al.<sup>[9]</sup>

Consequently, the self-assembling process is of high complexity as each macroscopic phase has many microscopic events that can influence each other resulting in many possible ways how these structures are formed.<sup>[45–47]</sup> It is of high importance to elucidate the structures appearing during fibrillation as there are several indications that polymorphic structures reveal different mechanical properties as well as cytotoxic activities.<sup>[11,48–51]</sup>

A variety of characterization techniques exist that allow the identification of amyloids as well as the elucidation of their structures and formation mechanism. Some of them are listed in the subsequent Table 2.<sup>[9,43,45,52–55]</sup>



Table 2: Examples of characterization methods for elucidating the structures of amyloids and their self-assembling mechanism. AFM = Atomic force microscopy; ATR = Attenuated total reflectance; CD = Circular Dichroism; FTIR = Fourier transform infrared; NMR = Nuclear magnetic resonance; TEM = Transmission electron microscopy; XRD = X-ray diffraction.

Method	Characterization	Reference
<b>XRD</b>	Secondary and tertiary structure	[43,52]
<b>Fluorescent dyes</b>	Identification of $\beta$ -sheet rich structures, oligomer identification, kinetics	[43,55–58]
<b>CD spectroscopy</b>	Secondary structure, comparison of structural changes during fibril growth	[43,52]
<b>(ATR)-FTIR</b>	Secondary structure (clarification of parallel (fibrils)/antiparallel (oligomers) $\beta$ -sheets, detect growth of $\beta$ -sheet structures)	[43,46,52,54,59]
<b>TEM</b>	Morphology, length, width	[43,52]
<b>AFM</b>	Morphology, mechanical properties, study of fibrils on a surface: length, distribution, height and width, <i>in situ</i> monitoring of fibril growth on surface	[43,52]
<b>Solid-state NMR</b>	Secondary and tertiary structure	[44,46,52,53]

Specific fluorescent dyes were found that could allow fast identification of amyloids as well as their formation mechanism in some cases.<sup>38</sup> These dyes could be considered as molecular rotors and when binding selectively to amyloids, they reveal characteristic emission properties. They undergo an intramolecular twisting motion upon photo-excitation with a subsequent return to the ground state of the molecule resulting in a specific emission.<sup>[57,58,60–62]</sup> Two examples, Congo red (CR) and Thioflavin T (ThT) have a long history of practice in classifying amyloid fibrils.<sup>[43]</sup> The specificity of these dyes affinity towards fibrils is based on their intercalation between molecules of structures with a high  $\beta$ -sheet content. After binding to the amyloid structure, CR gives a characteristic green birefringence and a shift in the absorbance maximum from 490 nm to 540 nm. It is applied in diagnoses of amyloids in *ex vivo* settings only as there is some evidence that its intercalation affects the oligomerization process and that it also interacts with other proteins. In contrast to CR, ThT has

become one of the “gold standards” for selective identification and clarification of amyloids kinetics.<sup>[55,56,60,63]</sup> ThT exhibits an enhanced fluorescence when binding to amyloid with a characteristic blue shift in the emission spectrum from 510 nm to 480 nm.<sup>[55]</sup> Furthermore, this dye shows differences in its emission properties for different amyloids and different assembling-stages of the same amyloid. For example, by comparing fibrils with oligomeric structures, the fluorescence intensity of ThT is much higher after binding to the mature fibrils.<sup>[55,58]</sup>

As it is claimed that the secondary structure is one of the major differences between oligomers (antiparallel  $\beta$ -sheets) and fibrils (parallel  $\beta$ -sheets), FTIR (Fourier-transform infrared) spectroscopy offers a useful technique as it is able to distinguish antiparallel from parallel  $\beta$ -sheets by analyzing the amide I ( $\sim 1700$ - $1600\text{ cm}^{-1}$ ) and amide II ( $\sim 1600$ - $1500\text{ cm}^{-1}$ ) regions. It should be noticed, that the amide II region is less informative than amide I.<sup>[54,59,64]</sup> By analyzing the ratio of absorbance at  $1695/1630\text{ cm}^{-1}$ , the growth of the  $\beta$ -sheet structure can be detected. The disappearance of intensity at  $1650\text{ cm}^{-1}$  is an additional indication for the transformation from oligomers into fibrils.<sup>[45,54]</sup> By circular dichroism measurements (CD) it is additionally possible to compare the changes in the secondary structure during the aggregation process.<sup>38</sup> In order to reveal the tertiary structure, XRD measurements and solid state NMR become useful techniques to custom.<sup>[45,48]</sup>

The morphology of amyloids can be *inter alia* measured by static and dynamic light scattering (SLS/DLS) techniques. Here, the size increase of the aggregates during the fibrillation process can be monitored. Microscopy techniques like transmission electron microscopy (TEM) as well as atomic force microscopy (AFM) allow to analyze the morphological changes and the dimension of the nanostructure. AFM can also be used for *in situ* monitoring of fibril formation on surfaces.<sup>[45,49]</sup> The combination of ThT fluorescence measurements and total reflection microscopy (TIRF) is also commonly used to follow the elongation of fibrils in real-time. In comparison to this method, it could be shown that the high detection efficiency of single-molecule techniques (like smFRET = single-molecule Förster resonance energy transfer) allows an improvement in fluorescence through binding to fibrils as well as to oligomers. With this method it is possible to track fibril growth and observe aggregates smaller than  $\sim 250\text{ nm}$ .<sup>[43,50,65]</sup> By combining single-molecule fluorescence lifetime imaging

(smFLIM) with an image analysis such as deep neural network (FNet), the observation of separate individual fibrils' elongation over time is possible.<sup>[47]</sup>

Summarizing, all these techniques help get deeper insights of the self-assembly process concerning its complexity and identifying the resulting structural variants. Hence, this previously mentioned complexity can be explained by the huge variety of inter-monomer and inter-fibril interactions that are determined by the amyloids primary structure.<sup>[40,43,66]</sup> The most important interactions in amyloid assembly are hydrogen bonds as they are responsible for intermolecular backbone stability and  $\beta$ -sheet formation. Moreover, hydrophobic interactions (like  $\pi$ - $\pi$  - interactions that occur in aromatic side chains), as well as salt bridges are known to play an important role by supporting monomer binding.<sup>[9,37,67]</sup> Even though the amyloid self-assembling process is declared as a supramolecular rearrangement as its nanostructure is only held by non-covalent interactions, changes in primary structure can lead to additional interactions that may change the suprastructure.<sup>[68]</sup> For example, the insertion of disulfides in cysteine-containing sequences cause the formation of covalent bonds between different monomers. These sequences are supposed to create longer fibrils with higher stability, which contribute to different amyloid bioactivities<sup>[40,43,69]</sup> Due to the fact that the usage of simple, chemical elements like amino acids with different side chains can create a diversity of function, amyloids can be compared in many ways to linguistics. Letters (amino acids) that form words (peptide sequences) can assemble into sentences ( $\beta$ -strands), which are gathered into paragraphs (protofilaments), chapters (fibrils) and lastly to an entire book (2D or 3D scaffold). Hence, it might be helpful to recognize the “syntactic pattern” of “the amyloid language” such as similarities in sequence and/or structure to gain more control about the structure-activity relationship of amyloids and amyloid-like materials. This knowledge might offer a powerful design strategy for the development of new nanomaterials.<sup>[70,71]</sup>

Beginning with a general introduction of cell-material interactions (chapter 1.2), the next chapters will offer deeper insights into the sequential design of functional amyloid-like materials and their resulting functional activity in promoting cell-material interactions (chapter 1.3).

## 1.2. Cell-Material Interactions and Regulation of Cell Behaviour

### 1.2.1. General Introduction of Cell-Material Interactions

Cell-material interactions play a crucial role on cell function and tissue development. In nature, the extracellular matrix (ECM), which refers to the soft, heterogeneous network around cells, enables them to perform its diverse functions such as differentiation, migration, communication and apoptosis as well as tissue organization.<sup>[72,73]</sup> There is a great interest to design a soft ECM-like synthetic matrix that allows to maintain cells viable and stimulates cellular processes to control cellular function. Thus, understanding the complex processes of cell-material interactions is fundamental for the creation of functional biomaterials and is related to understanding the system of physico-chemical reactions between cells and the material.<sup>[74,75]</sup>

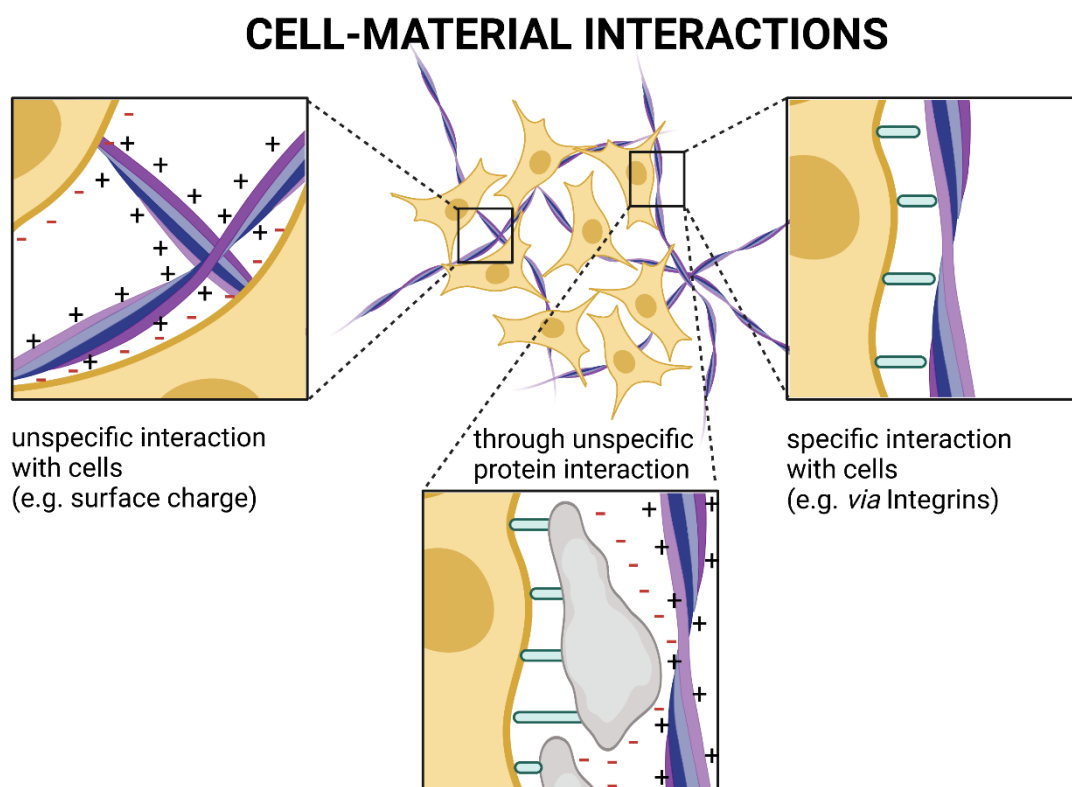


Figure 3: Illustration of specific and unspecific cell-material interaction. Graphic was created with BioRender and is based on data from Masters et al.<sup>[73]</sup>

Depending on the distance between cell and material, the interactions proceed in different ways. Surface recognition starts at a distance of  $\sim 1\mu\text{m}$  through unspecific

interactions between the pericellular envelope and the surface (Figure 3, left).<sup>[73]</sup> Through weak and cooperative interactions, stronger cell-material contacts at nanometer-scale distances occur and initiate the recognition of certain molecular motifs, which play a crucial role in the specific interactions of materials with the cell-surface (Figure 3, right).<sup>[75]</sup> Here, material-bound ligands such as RGD sequences can interact specifically with cell-surface receptors such as integrins.<sup>[75]</sup> Furthermore, non-specific material-protein interactions mediated by cell-material binding mostly determine cellular responses to the material as protein adsorption occurs within seconds, long before the first cells reach the surface. The adhesion of cells to the protein layer is as well provided by cell adhesion receptors. (Figure 3, middle).<sup>[73,75,76]</sup>

There are several classes of cell-surface receptors on mammalian cells existing like integrins, selectins and immunoglobulins.<sup>[72,73,76]</sup> Integrins are one of the most common targeted receptors as they bind the majority of extracellular matrix proteins such as collagen, laminin and fibronectin. Most integrin ligands are found as short peptide sequences within extracellular matrix proteins like the well-known peptide motif RGD (Arginine-Glycine-Aspartic acid), which exists in a variety of ECM proteins. Integrin recognition of this ligand occurs in almost all cell types and acts to promote their adhesion.<sup>[72,73,76,77]</sup> Even though ligand binding of integrin proceeds with a relatively low affinity, their high surface presentation enables the cell to explore its environment without losing attachment. The success of strong cell-material interactions relating to the integrin-mediated mechanism depends on the affinity and avidity of integrin receptors, which affects the effectivity of the so-called “outside-in” signalling cascade through integrin activation. Conformational changes of the receptor as well as receptor clustering are responsible for variations in affinity and avidity. They can be triggered by a variety of signals inducing the “inside-out” signalling pathway like the activation of other surface receptors or the recognition of cytoskeletal structures. The before mentioned “outside-in” signalling allows cells to gain information about their extracellular environment through integrin-ligand binding and then transmit the information to the cytoplasm. As integrins are directly connected with bundles of actin filaments, they can initialize the formation of focal adhesions. These are integrin-based structures that mediate strong cell-substrate adhesion, cell spreading and enable signal transduction between ECM and cell cytoplasm.<sup>[72,73,75]</sup>

Proteins such as fibronectin or fibrinogen, which were secreted by cells, occur in body fluids or they are used in culture medium. By protein adsorption to the material, cell-material interactions can be initialized. Here, the type and density of the protein that is presented on the surface of the material is a main factor regulating the cell function.<sup>[73,74,76,78]</sup> For instance, hyaluronan has an exclusive role in the initial and long-term cell-material interaction processes. It acts as a modulator of cell adhesion as it can serve either as a mediator or an inhibitor.<sup>[78,79]</sup> Protein adsorption can be mediated by both thermodynamic and electrostatic reasons.<sup>[73]</sup> The key thermodynamic regulator in protein-material interactions is the “hydrophobic effect”. This effect describes the interaction of water with a hydrophobic surface, in which water molecules poorly bind to the surface. As soon as water molecules are released from the hydrophobic material into the bulk solvent, the resulting entropic gain leads to a favourable adsorption of lipophilic patches of the protein to the surface. Hydrophobic sequences are originally folded in a way that water interactions are minimized to prevent irreversible protein adsorption accompanied by protein denaturation, which are caused by extremely hydrophobic materials. By undergoing an interaction with the hydrophobic surface the proteins have to change their conformations, which normally affects the cellular recognition and binding affinity to the cell.<sup>[73]</sup> A study of *Keselowsky et al.* shows that the central binding domain of the serum protein fibronectin (FN), that leads to an improved cell adhesion, was preserved after binding to hydrophilic surfaces.<sup>[80]</sup> Additionally, several studies have shown that optimal cell adhesion, proliferation, cell growth and the organization of focal adhesion complex occurs on materials of moderate hydrophilicity with a water contact angle (WCA) of about 40°-65° whereas extreme surface hydrophilicity inhibits protein adsorption as the adhesion-mediating proteins are bound too loosely.<sup>[73,74,76]</sup>

However, several groups could indicate that the surface charges play a more significant role for cell attachment and spreading than the wettability.<sup>[81,82]</sup> For example, human MG-63 osteoblasts that were cultured on negatively charged poly(styrene sulfonate) (PSS) ( $\zeta$ -potential = -82 mV) in comparison to positively charged plasma polymerized allylamine (PPAAm) ( $\zeta$ -potential = +8 mV) with similar WCA of 68°, showed a higher initial cell area spreading course on PPAAm surfaces.<sup>[81]</sup> Nevertheless, a very high  $\zeta$ -potential of about +50 mV reduces the cell area spreading course indicating that cells seem to favor only a small spectrum of  $\zeta$ -potentials, being

neither negative nor highly positive.<sup>[81]</sup> The reason for the higher tendency of protein binding to cationic surfaces is the electrostatic interaction between the positively charged surface and the proteins, which usually possess a negative net charge. In protein-free environments, positively charged functional groups have even an enhanced role in promoting cell adhesion, probably due to the fact that cells exhibit a negatively charged chondroitin surface within the glycocalyx, which facilitates cell-material binding.<sup>[73]</sup> Beside the regulation of specific cell-material interactions *via* integrins, precise alternations in surface chemistry offer an easy method to guide a desired cellular response by substrate-directed control of protein activity and affinity.<sup>[73,79]</sup>

Furthermore, mechanical properties of biomaterial scaffolds like their rigidity or strength are also important as they can influence a broad variety of fundamental functions such as cell attachment, migration, proliferation, differentiation including gene expression, metabolism, cytokine secretion and cell cycle progression.<sup>[83]</sup> For example, hydrogels with stiffness values around 840 kPa can stimulate both pro- and anti-inflammatory cytokines compared to hydrogels with lower stiffness (~130 kPa). Thus indicating that softer hydrogels result in suppression of inflammatory responses.<sup>[83]</sup> Moreover, mechanical properties of the material are regulating local tension at adhesion sites resulting in activation of signalling cascades such as phosphorylation of local tyrosine, thus inducing cell attachment. In the case of a very soft polyacrylamide gel surface, the surface is not able to withstand traction forces exerted by cells. This results in rounded cells that are not able to spread and consequently undergo apoptosis.<sup>[71,73,76]</sup> Some cell types are able to distinguish between different stiffness ranges of the scaffold such as T cells, which possess T cell receptors acting as mechanosensors. T cells also become more active on stiff surfaces (~100 kPa) in comparison to softer surfaces. Interestingly, stem cells differentiate better when cultured on surfaces with dissimilar stiffness.<sup>[83]</sup> When cultured on a soft 2D-matrix (0.1-1 kPa), neurogenic differentiation was prompted, matrices with a medium stiffness (8-17 kPa) stimulated myogenic differentiation and matrices with high stiffness (25-40 kPa) promoted osteogenic differentiation.<sup>[83]</sup>

In nature, the ECM consists of a complex topography involving fibrillar tangled structures with various nanoscale dimensions forming a multifaceted network that can specifically interact with cells. Hence, topographical features influence the protein- and

cell-material interaction next to surface chemistry. Interestingly, many studies have shown that the local nanoenvironment plays even a more important role than surface chemistry possibly due to the fact that nanometer-size topographical features are more closely to mimic the natural ECM than larger ones. Consequently, several topographies were studied revealing that different landscapes elicit not only cell adhesion but altered cell functions dependent on the cell type. Some of the results were summarized in the following table.<sup>[73,75,76,79]</sup>

Table 3: Cell function caused by different topological features based on data of Masters et al. <sup>[73]</sup>

<b>Topographical features</b>	<b>Cell type</b>	<b>Cell functions examined</b>
Fibers	Chondrocytes	Cytoskeletal organization
General roughness	Dermal fibroblasts	Differentiation
Pores	Gingival fibroblasts	Migration
Grooves	Dermal keratinocytes	ECM orientation
Spikes	Leukocytes	Proliferation
Pits	Epithelial cells	Focal adhesion formation
Spheres	Heart fibroblasts	Orientation

For example, microporous scaffolds facilitate cell migration, cell infiltration and blood vessel formation. They also influence cellular adhesion and lineage-specific differentiation such as for human MSC, microporosity aids adhesion and osteogenic differentiation.<sup>[83]</sup>



## 1.2.2. Spatio-temporal Representation of Cell-adhesive Parameters

In general, cell-material interaction turns out to be a complicated process that is affected by the type of applied cells and a bunch of mechanical and physico-chemical parameters of the surface like hydration, electrostatic interactions, free energy, steric repulsion and topography influence. Through cell-material interactions cells receive, process and respond to information accessible in the close environment. The fine control over the information flow results in the control over cell behaviour.<sup>[74–76,84]</sup> Thus, spatio-temporal presentation of physico-chemical parameters or biologically active ligands to the cell surface play a crucial role in inducing cellular responses. For example, physico-chemical gradients existing in nature are fundamental for numerous biological processes *inter alia* for angiogenesis and inflammation. Here, gradual distribution of the vascular endothelial growth factor A stimulates blood vessel formation and a chemokine concentration gradient triggers neutrophil migration during wound repair.<sup>[85,86]</sup> Directed cell migration can be the result of cells ability to respond to various types of environmental signals such as diffusible chemical cues (chemotaxis), immobilized chemical cues (haptotaxis), mechanical cues (durotaxis), substrates geometric features (topotaxis / contact guidance) and electric fields (galvanotaxis).<sup>[87]</sup>

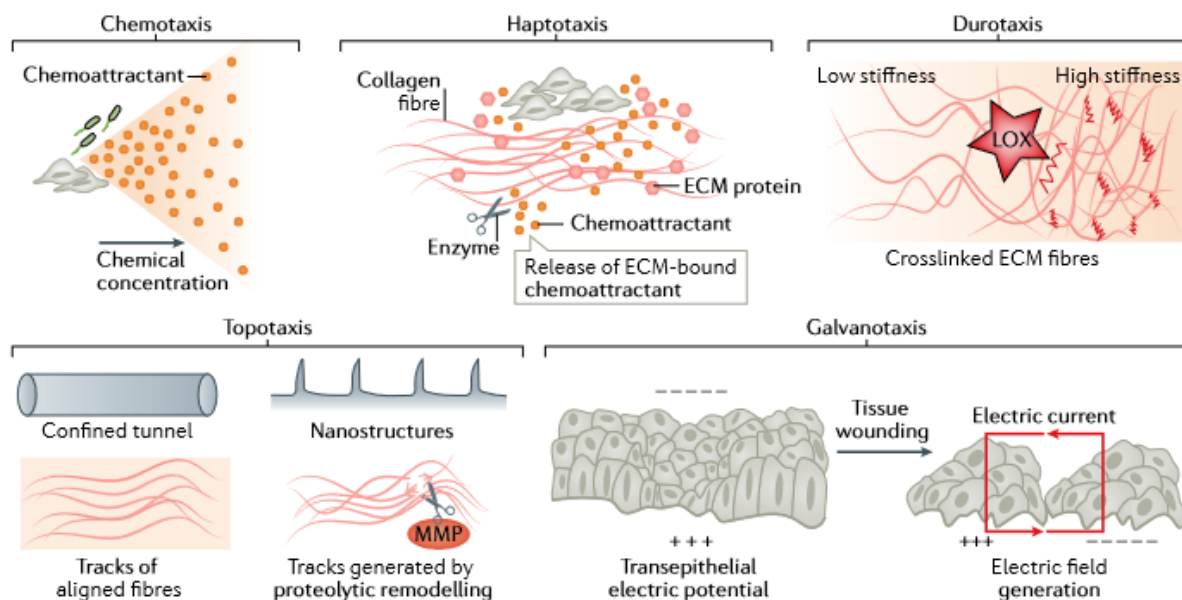


Figure 4: Different ways of cue generation for directed cell migration. During chemotaxis, bacteria or cells release soluble chemoattractants to form chemical gradients. During haptotaxis, cells release ECM proteins and chemokines that are immobilized on ECM. In certain cases, immobilized chemokines are released from the ECM and provide soluble cues for chemotaxis. During durotaxis, lysyl oxidase (LOX) can generate stiffness gradients within the ECM. During topotaxis, metalloproteinases (MMPs) or deformation generate directional signals in tissue

structures. During galvanotaxis, at wounding sides an electric field is generated caused by the loss of transepithelial potential. This potential provides guidance cues for cells which are involved in tissue repair. Reprinted from Ref.<sup>[87]</sup> with permission from Springer Nature.

Material systems that enable precise control over cell-material interactions are desirable in the creation of materials for biological applications like for tissue engineering. Here, spatial variations of minimum one characteristic feature, either a physical (e.g. stiffness), morphological (e.g. porosity) or chemical (e.g. hydrophilicity) have been included in the fabrication of synthetic ECMs.<sup>[88,89]</sup> Some examples of the resulting spatial cell patterning techniques include either presentation or removal of bioactive molecules on the scaffold surface or changes in physical scaffold characteristics by crosslinking or bond scission.<sup>[90,91,100–104,92–99]</sup> The dynamic control over the cell-material interactions can be achieved through stimuli responsiveness (e.g. temperature, pH, electric field biochemical signals or light).<sup>[104–108]</sup> The latter one has been of particular interest as photoresponsive materials offer an external regulation with the maximum precision in space and time. Furthermore, light is not invasive and patterning as well as gradient formations in the 2D or 3D environment can be realized.<sup>[86,104]</sup> As mentioned above, natural gradients direct cell migration that plays a crucial role in embryonic development, wound healing and immune responses. Therefore, gradient formation techniques are of particular interest in the field of tissue engineering.<sup>[109]</sup> Especially, chemical, mechanical and physical gradients are most widely studied. There are several techniques to fabricate gradients including techniques such as surface grafting of gradient-building blocks on a substrate by adsorption or covalent binding.<sup>[109–111]</sup> For example, *S. Yu et al.* immobilized a cell resisting PEG layer on a glass substrate with a density gradient of azide groups by rinsing the glass substrate vertically in a gradient solution of two PEG molecules (NH<sub>2</sub>-PEG-N<sub>3</sub> and mPEG-NH<sub>2</sub>).<sup>[112]</sup> Here, the concentration of NH<sub>2</sub>-PEG-N<sub>3</sub> increased from the top to the bottom within a range of 10 mm creating a vertical gradient. Subsequently, a density gradient of VAPG peptides was created by clicking the peptides on NH<sub>2</sub>-PEG-N<sub>3</sub> functionalized substrate.<sup>[112]</sup> Physical gradients, for instance, can be formed by modulations of rigidity, surface roughness or porosity, which varies across the substrate by methods like chemical etching, functionalization with nanoparticles and diverse printing techniques.<sup>[109,111,113–116]</sup> Especially, multicomponent gradients that include combined chemical and physical gradients are of particular interest as they can better mimic the complex natural environment.<sup>[117]</sup>

## 1.3. Structure-Activity-Relationship of Amyloid-like Fibrils by studying their Cell-Material Interactions

### 1.3.1. “Activity” of Amyloids and Amyloid-like Fibrils towards Cells

As amyloids possess a highly repetitive organisation of charged and hydrophobic moieties on its fibrillar surface, they tend to display a strong adhesiveness towards a variety of small molecules, macromolecules and (bio)polymers like proteins, DNA/RNA, viruses and biological membranes.<sup>[72,118–121]</sup> Coatings of amyloid-like nanomaterials from nature-derived amyloidogenic structures such as hydrophobin, transthyretin and laminin revealed a strong cell adhesive and cell supportive character towards different cell types lacking cell toxicity.<sup>[121–128]</sup>

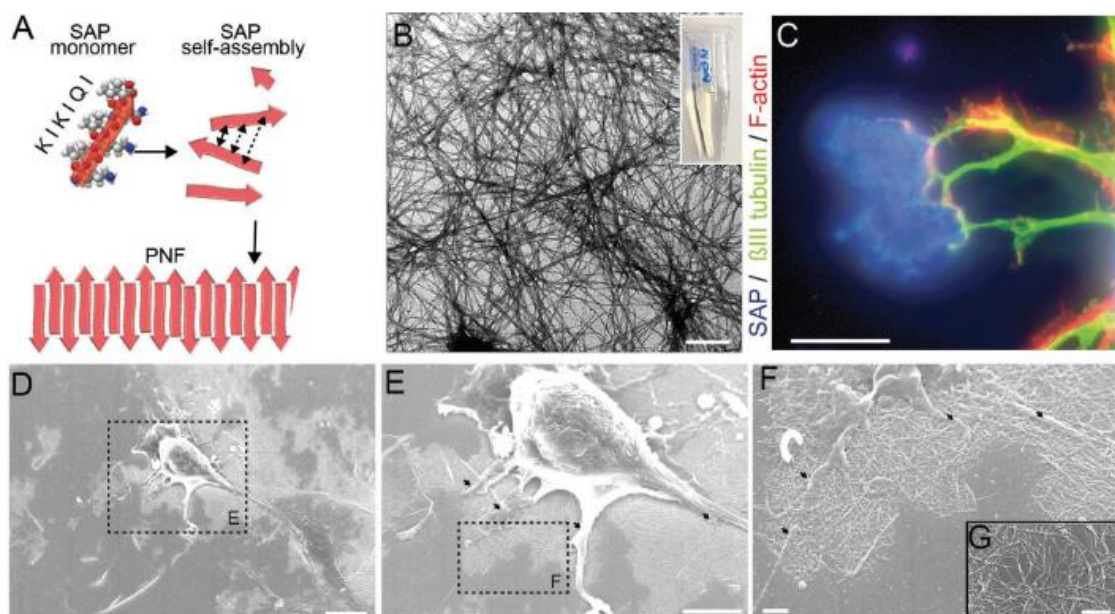


Figure 5: Amyloid-like scaffolds for neuronal cell adhesion. A) Scheme of self-assembly of sequence KIKIQI (self-assembling peptide = SAP) into amyloid-like fibrils, here PNF = peptide nano fibrils. B) TEM pictures of nano fibril solution. C) Coated glass surfaces with fibrils form plaques (blue) and serve as adhesion points for nerve fibers (green). D-G) SEM pictures of primary neurons plated on amyloid-like fibrils with formed cellular protrusions (black arrows). Scale bars: (B) 600 nm; (C) 20  $\mu\text{m}$ ; (D) 100  $\mu\text{m}$ ; (E) 50  $\mu\text{m}$ ; (F) 10  $\mu\text{m}$ ; (G) 5  $\mu\text{m}$ . Reprinted from Ref. <sup>[126]</sup> with permission from John Wiley and Sons.

Gras *et al.* performed the first cell adhesion study on peptide fibrils derived from the amyloidogenic protein transthyretin<sub>105-115</sub>, named TTR.<sup>[127]</sup> They tested TTR amyloid-like fibrils as well as the C-terminal modifications TTR-RGD as activity enhancer and TTR-RAD as a control sequence towards attachment of mouse fibroblast cells (3T3). The study indicated that TTR fibrils show a fibronectin (FN) comparable bioactivity that can be further enriched by the incorporation of the RGD moiety. The supportive cell attachment character of unmodified TTR was suggested to proceed *via* an unspecific

cell-material interaction mechanism, which was not further investigated in this study. TTR-RAD fibrils, however showed a reduced cell attachment in comparison to TTR. Furthermore, for the RGD modified TTR sequence the authors ascribed the RGD moiety as the dominant signal towards cell attachment so that the RGD-fibrils interact specifically *via* the RGD motif with cells.<sup>[72,127]</sup> Consequently, the intrinsic bioactivity of amyloids can be further modified through simple functionalization.<sup>[72,127,129]</sup>

Hence, several studies were performed to indicate the physico-chemical reasons for the inherent cell supportive characteristics of amyloids and amyloid-like structures by investigating its wettability, charge, rigidity, concentration dependency and topographical impact concerning their effect on cell activity.<sup>[123,126,130–133]</sup>

As already discussed in the previous chapter, changes in wettability of surfaces can vary the biocompatibility and alter cell attachment properties. The ability of amyloids to adjust this property has been extensively examined with fungi-derived amyloidogenic proteins named hydrophobins. These amphiphilic structures can form chemically robust layers that can adhere either to hydrophobic or hydrophilic surfaces significantly changing their wettability.<sup>[122,134–138]</sup> For example, coating of hydrophobic polycaprolactone (water contact angle (WCA) =  $106.8^\circ \pm 3.9^\circ$ ) with hydrophobin changed the surface wettability to a moderate hydrophilicity of  $61.3^\circ \pm 2.5^\circ$ . On the other hand, by coating the hydrophilic Mica substrate (WCA =  $5.1^\circ \pm 1.2^\circ$ ) the WCA risen up to  $15.7^\circ \pm 1.4^\circ$ .<sup>[134,135]</sup> This phenomenon could be explained by the amphiphilic character of hydrophobins as when they are coated for example on PCL fibrils, its hydrophobic parts were attached to the hydrophobic polycaprolactone surfaces and its hydrophilic parts to the outermost surface hence improving the wettability and the mitochondrial activity of fibroblasts.<sup>[135,138,139]</sup> Results of *M.I Janssen et al.* additionally indicated that the growth and activity of fibroblasts were not only determined by the wettability of hydrophobins but as well by the chemical compositions of the exposed parts of the amyloid layer.<sup>[123]</sup>

In addition to these findings, Schilling *et al.* could show a detailed study of amyloid-like structures investigating their chemical and physical features towards cell activity. They screened 27 different amyloid-like structure forming sequences for their ability to enhance cell adhesion and neurite growth. All sequences were based on the peptide sequence QCKIKQIINMWQ from the envelope glycoprotein GP120<sub>417–428</sub> of human

immunodeficiency virus (HIV). Their results indicated a trend in the charge according to cell adhesion in which positively net charged sequences showed enhanced cell adhesion and growth to varying degrees due to diversities in the sequence. Negatively charged sequences failed in cell adhesion properties. The most promising peptides of all screened sequences were RGDKIKIQIC (SAP5c), Fmoc-KIKIQI (SAP1e), and CKFKFQF (SAP2e). The authors claimed that besides the positive  $\zeta$ -potential, the materials fibrillar morphology with thicker,  $\beta$ -sheet content rich elements providing higher stiffness and persistence in length show enhanced bioactivity. Considering the morphology, higher conversion rates delivered improved results towards neuronal activity as well. Furthermore, they could show that the neuronal activity of the fibrillar coating was concentration dependent as the minimum concentration of about  $10 \mu\text{g mL}^{-1}$  was required to display a cell adhesive character.<sup>[126]</sup>

The research of *Reynolds et al.* supported the results of concentration dependency towards cell binding activity. Here, they could demonstrate that the increased coverage of the amyloid network promotes spreading and the generation of focal adhesions of cultured fibroblast and epithelial cells. Additionally, they suggested that the surface coverage influences cell adhesion more efficiently than the thickness of the individual fibril.<sup>[125]</sup> An additional study of *Reynolds* and co-workers discovered the topographical and chemical impacts of amyloid fibrils on cells by deposition of a plasma polymer on the fibrous network.<sup>[133]</sup> This polymer deposition covered all chemical effects by preserving the topographical features of the amyloid fibrils, which allows the decoupling of these two effects. Their results indicated that topography of fibrillar coating has a main impact on cells viability whereas cell attachment is mainly influenced by chemical signals. Furthermore, the spreading course of epithelial cells was revealed to be controlled by both topographical and chemical effects.<sup>[133]</sup>

### 1.3.2. Mechanism of Interactions of Amyloid-like Fibrils with Cells

In order to reveal the amyloid-cell interaction mechanism, numerous studies *inter alia* by *Katagiri et al.* could show that supported by fibrils positive charge, amyloid-cell attachment can be mediated by syndecan or laminin interaction mechanism depending on fibrils sequential construction. Here, they implemented studies with amyloidogenic sequences derived from specific mouse laminin peptides by examining the impact of individual amino acids towards fibril formation and cell activity.<sup>[132,140,141]</sup> Furthermore, *Schütz et al.* performed scanning electron and time-lapse confocal microscopy to gain a better understanding of the exact mechanism of how amyloids interact with the cell surface.<sup>[142]</sup> They found that cellular protrusions engage amyloid fibrils and pull them towards the cell body, which concludes that the fibrillar superstructure itself contributes to their activity.<sup>[142]</sup> Consequently, the amyloid-like fibril morphology is essential to induce cell contacts.<sup>[132,140–142]</sup> This assumption was explicitly studied by *Maji* and co-workers, as they claimed that amyloids possess a generic bioactive character. They explored more than 20 different non-toxic amyloidogenic sequences with various lengths on their cell adhesion and spreading properties revealing a hypothetical cell adhesion mechanism. They claimed that regardless of the peptides sequence and charge, amyloids support cell adhesion through stimulation of integrin expression and formation leading to creation of focal adhesions.<sup>[72,121]</sup> As several studies showed that amyloids and amyloid-like materials can initiate cell attachment by entrapping serum proteins on their surface, *Maji et al.* could in fact observe a decrease in cell attachment by performing experiments in serum-free medium. Nonetheless, these amyloids and amyloid-like materials still exhibited cell attachment properties. Furthermore, they could detect cell adhesion to amyloids by using red blood cells, which lack the integrin machinery. Based on these and other supportive results, they suggested lipid-amyloid interactions as the first step for cell adhesion. They could additionally observe that amyloids show a similar cell binding behaviour compared to collagen, which is one of the prominent fibrillar ECM structures. So they proposed that amyloids, similar to fibrillar ECM components, are recognized by the cell, which then mediates special down streaming pathways resulting for example in integrin expression and clustering.<sup>[72,121]</sup>

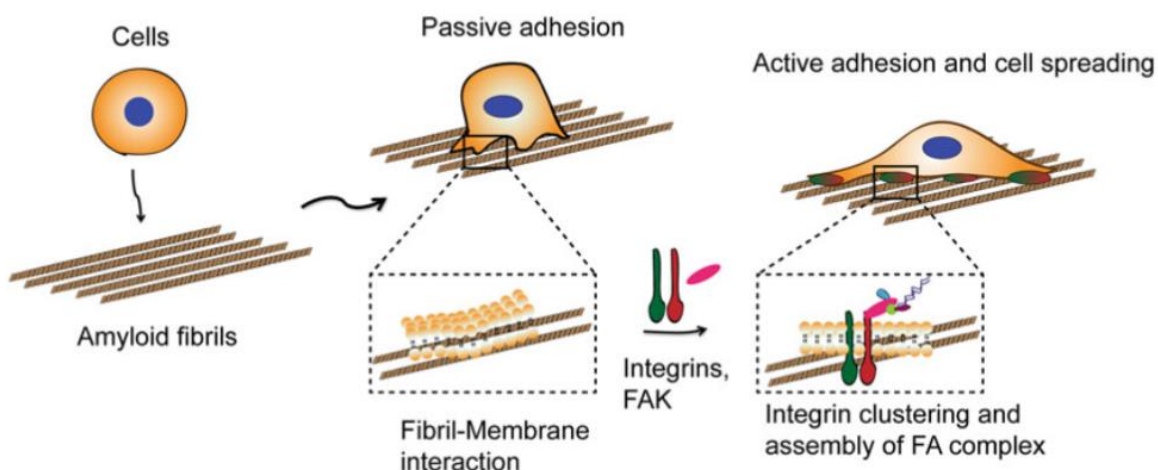


Figure 6: Schematic illustration of mechanism of mammalian cell adhesion on amyloid fibrils initiated by lipid-fibril interaction and followed by integrin clustering, focal adhesion formation and cell spreading. Reprinted from Ref. [143] with permission from Springer Nature.

Finally, these studies elucidated that both specific and unspecific material recognition pathways are involved in cell-amyloid interactions, which should be definitely taken into account in the process of amyloid-like scaffold investigation.<sup>[125–127,129,133,144]</sup>

### 1.3.3. Rational Sequence Design of Amyloid-like Fibrils for Cell Activity Improvement

As already discussed in the previous section, the achievement of a functional amyloid-like material with high cell-attachment properties lacking toxicity is guaranteed when the fibrils net charge is in a positive range, their hydrophilicity is moderate, the conversion rate into mature fibrils is high, and a fibrillar topology is given with a high  $\beta$ -sheet amount. The discovery of an amyloid forming sequence with all these characteristics could be regulated through rational sequence design. However, the optimization of self-assembling nanostructures could reveal challenging as the rational design approaches have to face multiparameter and multiscale challenges.<sup>[118]</sup> Moreover, it should be considered that the predominant fibril morphology can be controlled by subtle variations in growth conditions which can affect the bioactivity.<sup>[71,145]</sup> This observation requires consistent fibril growth conditions during the sequence optimization process.

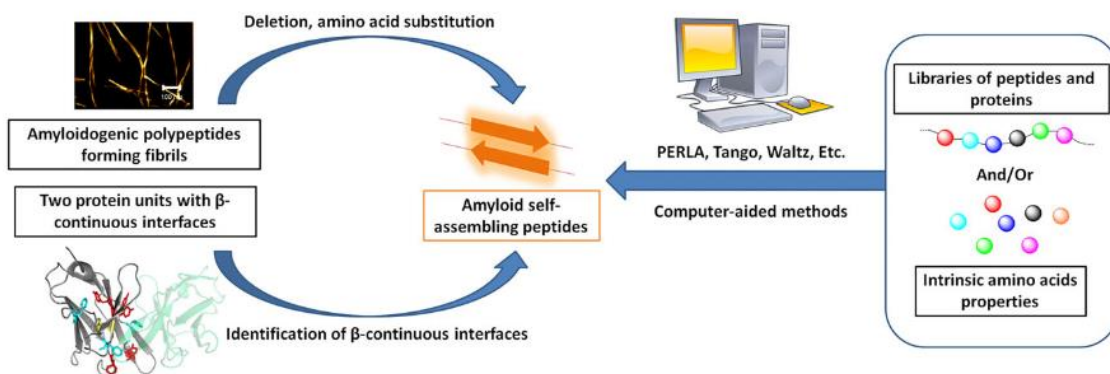


Figure 7: Illustration of strategies and workflow for the design and identification of amyloid self-assembling peptides. Reprinted from Ref. [66] with permission from John Wiley and Sons.

There are several strategies for the rational design of amyloid self-assembling peptides including top-down approaches like starting from amyloidogenic biological proteins (e.g.,  $\alpha$ -synuclein, Tau, lysozyme or A $\beta$ ) or identification of  $\beta$ -continuous interfaces between two protein units. Here, two protein units interact in an antiparallel fashion with each other. Third, *de novo* syntheses by using computer-aided methods such as protein engineering rotamer library algorithm (PERLA), Tango or Waltz were used as well.<sup>[66]</sup> For example, *M. López de la Paz et al.* used a bottom-up approach based on a computer calculated algorithm for a *de novo* design of amyloid-like sequences. This method greatly facilitated the identification and rationalization of elements in the sequence that favor the self-assembly process into amyloid fibrils. Moreover, single-point mutations or deletions allow the identification of specific interactions such as hydrophobic interactions.<sup>[67,146]</sup> For example, *Katagiri et al.* performed an alanine substitution analysis of sequences derived from specific mouse laminin peptides to elucidate the essential amino acids for  $\beta$ -sheet formation and bioactivity. By alternating specific amino acids at certain positions they could vary the amount of activity towards cells and the fibril formation tendency.<sup>[140,147,148]</sup> Therewith, sequential peptide modification allowed the identification of mechanical and morphological differences by varying the  $\beta$ -sheet amount of amyloids. Especially short peptides were sensitive to changes in their amino acid sequence as minor changes can lead to major activity variations.<sup>[118]</sup> For instance, *Schilling et al.* could show that the attachment of an additional Cysteine at the N-terminus of the KFKFQF sequence resulted in an enhanced activity towards neuronal outgrowth.<sup>[126]</sup> The cysteine-containing fibrils (CKFKFQF) showed thicker, more stable morphologies with higher  $\beta$ -sheet contents.<sup>[118,126]</sup> The correlation of  $\beta$ -sheet quantity and mechanical properties



was already discussed by several groups indicating that increased  $\beta$ -sheet amount is correlated to enlarged persistence length and stiffness.<sup>[71,126,149]</sup> In general, amyloids exhibit remarkably high stiffness with Young's Modulus ( $E$ ) values similar to the most rigid proteinaceous materials like intermediate filaments, collagen and tendons.<sup>[71]</sup> Here, highest  $E$  values were observed for short peptides, whereas longer amyloidogenic peptides tend to exhibit lower  $E$  values due to increased structural disorder.<sup>[71,150]</sup> *In silico* studies elucidated the same trend even on larger scales as highly organized assemblies of short amyloid fibrils have larger moduli than less organized superstructures of longer amyloid fibrils.<sup>[71]</sup> Consequently, the  $E$  values originated largely from the backbone hydrogen-bonding network and correlated as already mentioned with the  $\beta$ -sheet content of the fibril. Modulations of mechanical properties could further be regulated through side chain interactions such as  $\pi$ - $\pi$ -interactions.<sup>[71]</sup> By incorporation of aromatic amino acids in the peptides sequence not only an acceleration of the self-assembly process could be achieved but stabilization of the nanostructure as well.<sup>[126,151–153]</sup> The huge impact of  $\pi$ - $\pi$ -interactions on the fibrils assembly propensity could exemplarily be shown by *Sieste et al.*. The comparison of conversion rates of CKIKIQI (CR = 54%) and CKFKFQF (CR = 95%) determined a greater assembly tendency of sequences that can undergo  $\pi$ - $\pi$ -interactions.<sup>[118]</sup> While their influence on fibrils nanomechanics could be demonstrated by the dipeptide FF, which was found at the core of the Amyloid- $\beta$  sequence. This simple chemical structure exhibited a vast number of morphologies with  $E$  values in the range of 19 GPa. Interestingly, materials with  $E$  values above 20 GPa contained covalent or metallic interactions. Accordingly, FF nanomaterials belong to the stiffest presently known amyloid-derived biological materials.<sup>[71,150,154,155]</sup>

The enhancement of peptides  $\beta$ -sheet content could also be achieved *via* optimization of peptides amphiphilic pattern as their resulting morphology is determined by construction of a bilayer structure in polar solvents. Here, hydrophobic domains created the fibril core and hydrophilic side chains are arranged at the fibril surface. By simplifying the self-assembling sequence into four basic features according to their hydrophobicity (hydrophilic and lipophilic amino acids) and charge (negative and positive), *Sieste et al.* could achieve the best results by designing peptides with alternating hydrophobic and positively charged amino acids. For example, the intrinsic switch of (Q) and (I) of the CKIKQII sequence into CKIKIQI led to a higher content of

intermolecular  $\beta$ -sheets. Similar to single amino acid additions or deletions, the effect remained higher for shorter sequences than for longer molecules.<sup>[118,156]</sup>

Furthermore, as already expected from the previously discussed section the incorporation of positively charged amino acids such as lysines (K) showed good cell attachment properties and promoted neurite outgrowth.<sup>[118,148]</sup> Likewise, sequence modifications with bioactive molecules like RGD also enhanced cell attachment properties considering the specific cell attachment mechanism.<sup>[72,127,129]</sup> Interestingly, *Gras et al.* could elucidate that the insertion of C-terminal **GGRGDS** functionalization on the transthyretin<sub>105-115</sub> peptide (TTR1) did not only affect cell-material interaction on 3T3 cells but also varied the fibril morphology in terms of creating fibrils with broader widths.<sup>[127]</sup> In contrast, *Schilling et al.* could reveal that only N-terminal RGD functionalization could enhance neuronal activity of created fibrils and led to higher cross-sectional height. In this study, the functionalization was performed on a sequence derived from the HIV envelope glycoprotein GP120<sub>417-428</sub>.<sup>[126]</sup> These results showcased the challenge of sequential optimization of amyloid-like materials concerning different biological effects of similar modifications. Consequently, the optimization process of each  $\beta$ -sheet forming sequence must be tailored to its application and its initial sequence. Furthermore, modifications of amyloids with additional bioactive molecules allows an extension of the inherent bioactivity of amyloids and can be tuned specifically depending on the desired cellular reaction.

## 1.4. Strategies for controlled Assembly/Disassembly of Amyloid-like Materials

In nature, functional amyloids are highly regulated by cells compared to pathological amyloids. This control is *inter alia* concerning their assembling and disassembling behaviour.<sup>[13,14]</sup> In order to design amyloid-based functional materials with controllable cellular activity, the control over its (dis)assembly is a prerequisite as it predicts the (de)activation of amyloids inherent bioactivity by adjusting the amount and composition of adsorbed protein layers. Moreover, a regulated degradation of this scaffold material is an essential criterion in tissue engineering as it allows a controlled exchange of the scaffold with the regenerated tissue.<sup>[157]</sup>

Even though amyloid structures are known to be thermodynamically highly stable and their disassembly requires of strong denaturants *in vitro*, their destabilization as well as formation could be affected by changes in solvent conditions like pH, peptide concentration, ionic strength and temperature by influencing the equilibrium of fibril formation.<sup>[11,158–162]</sup> Furthermore, a wide range of different additives has been reported that interfered with fibril stability, which could be further divided in passive and active additives.<sup>[159]</sup> Passive additives exerted their effects through binding interactions<sup>[159]</sup> for example in case of PEG-chains,<sup>[163]</sup> carbon nanotubes,<sup>[164]</sup> ruthenium-complexes,<sup>[165]</sup> fullerenes,<sup>[166]</sup> amphiphilic polyphenylene dendrimers,<sup>[167]</sup> gold nanoparticles with additional polydopamine coating<sup>[168]</sup> and magnetoferritin and reconstructed ferritin<sup>[169]</sup>. On the other hand, active additives operate through energy expenditure such as molecular chaperones in biological amyloid disaggregation processes.<sup>[17,159,170–174]</sup> For instance, *T.P.J. Knowls* and his group could show that chaperones of the Hsp 70 family could disaggregate even “irreversible”  $\alpha$ -synuclein amyloid fibrils species that are related to the Parkinson’s disease. They suggested a six steps reaction for the disaggregation process.<sup>[172]</sup>

The incorporation of stimulus-sensitive groups in the peptide sequence represents an approach with superior control over disassembly of amyloid-like functional materials to gain controllable activity. Several stimulus-sensitive groups exist that can control the assembly and disassembly of amyloids and amyloid-like fibrils.<sup>[175]</sup> In the following modifications sensitive to pH, oxidative agents and UV light are going to be presented. Starting with the usage of simple amino acids that are sensitive to external signals like

oxidative agents and pH changes by inducing a transformation in the hydrophobic/hydrophilic balance of the self-assembly. For example, the usage of thioether functional groups has been a promising approach to control the assembly of supramolecular building blocks *inter alia* for  $\beta$ -sheet-rich nanostructures. Here, the oxidation of the thioether to the sulfoxide species generated a huge increase of hydrophilicity, which led to molecular disassembly.<sup>[176–178]</sup> The work of *Besenius* and his group demonstrated how the usage of thioether containing methionine in a C<sub>3</sub>-symmetric amphiphilic peptide with the sequence GFEMEM led to disassembly of preformed  $\beta$ -sheet-rich nanostructures upon oxidation whereas methionine in the unoxidized state supported the  $\beta$ -sheet formation as it is a hydrophobic amino acid (Figure 8).<sup>[178]</sup>

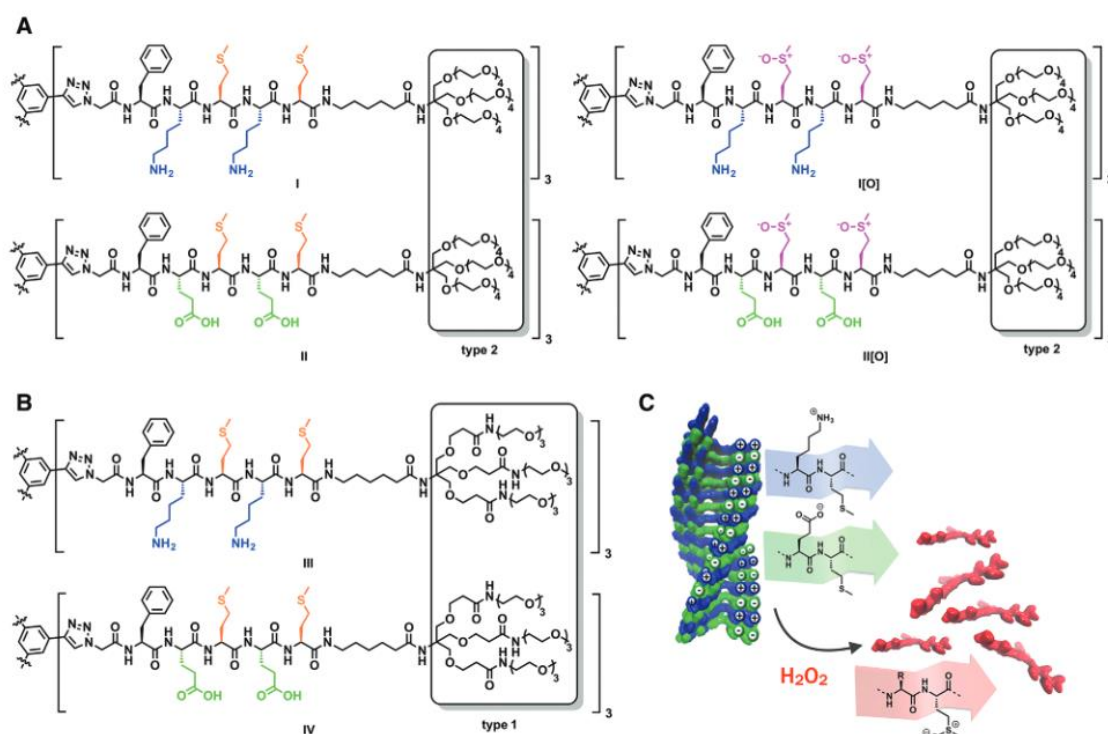


Figure 8: A) Illustration of FKMKM and FEMEM containing monomers I and II with the oxidized monomers I(O) and II(O) with dendron type 2, B) scheme of FKMKM and FEMEM containing monomers with dendron type 1 (III, IV) C) as well as a schematic illustration of amyloid disassembly caused by methionine oxidation and subsequent repulsive interactions. Reprinted from Ref.<sup>[178]</sup> with permission from John Wiley and Sons. This work is licensed under a Creative Commons Attribution 4.0 International License.

Furthermore, through careful placement of pH-responsive amino acids in the peptide sequence, the same group could demonstrate reversible assembly and disassembly in response to pH variation.<sup>[177]</sup> As the hydrophilicity increased upon protonation either of the N-/C-terminus or certain amino acid side chains such as lysine (K), histidine (H) or aspartic (D) and glutamic acid (E), they could show that the FEMEM containing

molecule was highly pH dependent. Under acidic conditions the glutamic acid (E) residues were protonated favoring a  $\beta$ -sheet forming assembly, whereas their deprotonated state under basic conditions led to electrostatic repulsion and disassembly.<sup>[177,179]</sup>

Moreover, the usage of the so-called “O-acyl isopeptides”, also named “depsipeptides”, is an additional strategy to gain control over amyloids self-assembly *via* pH switch. Here, peptide synthesis proceeds on the oxygen residue of the side chain of serine (S) or threonine (T) instead of on the N-terminus and creates a kink in the peptide backbone as well as an additional free amino residue, which increases the hydrophilicity of the peptide. The kinked peptide is stable in acidic conditions and starts to linearize above the pH of 2 (Figure 9).<sup>[36,180]</sup>

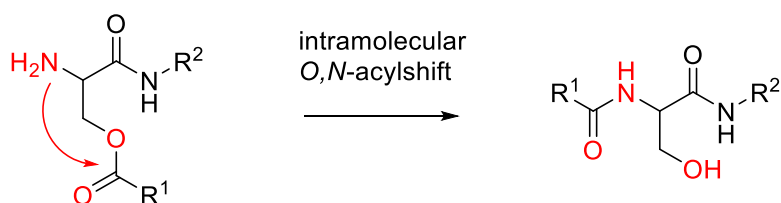


Figure 9: Mechanism of intramolecular O,N-acylshift of the kinked depsipeptide.<sup>[36]</sup>

Originally, this strategy was used to overcome solubility issues in the synthesis of certain peptides and to facilitate their purification. Likewise, it was used for the design of prodrugs as their solubility was higher in the depsipeptide form. The migration to the N-acyl drug proceeded under physiological conditions in a short time without any side reactions.<sup>[181]</sup> *Gačanin et al.* incorporated the depsipeptide-kink into the sequence KIKISQINM, which is an amphiphilic peptide with strong tendency to immediately form  $\beta$ -sheet-rich nanofibrils in aqueous solution even at low pH conditions. This short peptide was grafted on a polypeptide backbone to induce hydrogelation through  $\beta$ -sheet formation after pH-dependent peptide linearization. Here, the depsipeptide-kink in the peptide backbone prevented  $\beta$ -sheet formation at pH values lower than 2.<sup>[36]</sup> Therewith, the application of such platforms *in vivo* remains difficult as the physiological pH of 7.4 would immediately lead to linearization of the backbone. To overcome this problem, *Taniguchi et al.* proposed a carbamate based protecting group of the free amino group of the O-acyl isopeptide.<sup>[181,182]</sup> Depending on the molecular design of this caging group the cleavage could be for example triggered *via* external stimuli like peroxides or UV light.<sup>[182–185]</sup>

In particular, photo-triggered stimulation is commonly considered to be beneficial for studying the biological processes of peptides as it provides high spatial and temporal control over their morphology, which is one of the requirements for the creation of smart functional materials.<sup>[98,104,186]</sup> Besides systems with azobenzenes and hydrazones that undergo a *cis-trans* isomerization after irradiation, *ortho*-nitrobenzyl derivatives such as *ortho*-nitrobenzyl esters (*o*-NBE) have been used most extensively and provided precise control over material properties.<sup>[86,104,187–192]</sup> Upon UV irradiation (300–365 nm) the *o*-NBE undergoes a photo-cleavage with a mechanism analogous to the Norrish-type II reaction. Here, one oxygen atom of the excited nitro group (**2**) abstracts a hydrogen from the methylene or methine carbon in  $\gamma$ -position and forms an *aci*-nitro tautomer (**3**) in the ground state. After cyclization into a benzoisoxaline derivative (**4**), which undergoes a cleavage, the products carboxylic acid (**5**) and *o*-nitrosobenzaldehyde (**6**) are formed (Figure 10).<sup>[188–190]</sup>

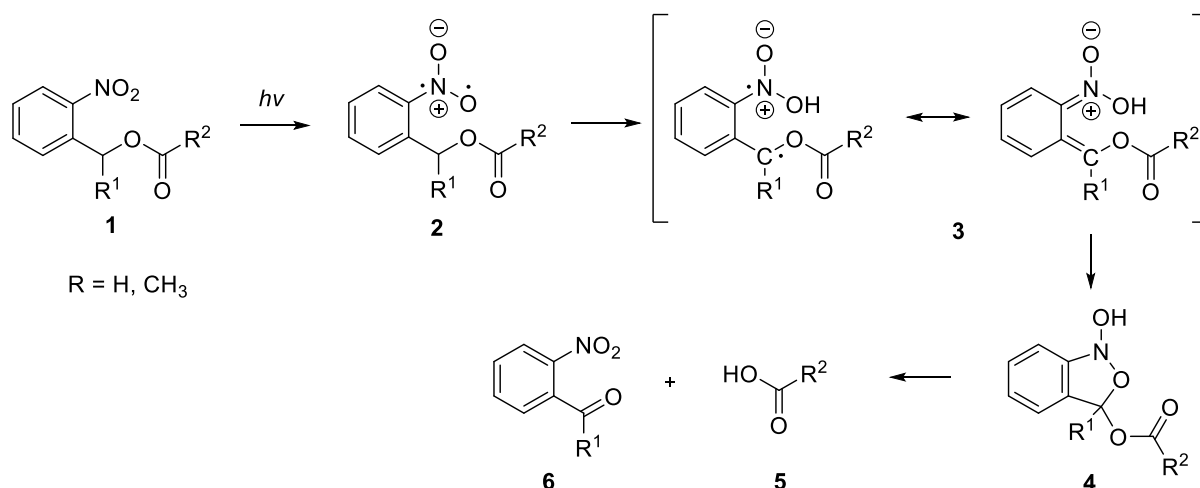


Figure 10: Mechanism of *ortho*-nitrobenzyl derivatives<sup>[188]</sup>.

In the field of amyloid self-assembly *o*-Nitrobenzyl derivatives were used to initiate either self-organization or disassembly by acting as a caging groups of either charged amino acids or depsi-peptides, or as linker molecules of fibril-inhibition or -stabilization units.<sup>[186,193–197]</sup>

For example, *B. Imperiali* and his group temporarily stabilized the solubility of an amyloid forming sequence by introducing the highly charged *N,N*-Dimethylethylenediamine (DMDA) into the peptide design. The group used the peptide (PrP<sub>174-195</sub>), which derived from the human prion protein as an amyloidogenic

sequence. This unmodified PrP<sub>174-195</sub> showed immediate fibril forming tendencies after dilution. Asparagine 174 of the amyloidogenic peptide was then linked through the *o*-Nitrobenzyl group with DMDA. This modified peptide started to form fibrils after 24 h of incubation whereas UV treatment accelerated the conversion and fibril formation occurred after 6 hours.<sup>[195]</sup> Similar to this work, *L. Awad et al.*, caged the glutamine amino acid residue of the amyloid-forming sequence Ac-VQIVYKG (P1) with a trimethylammonium moiety *via* a photoactive *o*-Nitrobenzyl derivative (Q\*). Here, caged glutamine (Q\*) prevented fibril formation by enhancing the solubility of the peptide. After UV irradiation at 406-335 nm for four minutes a complete conversion of Ac-VQ\*IVYKG (P2) into P1 occurred and fibril formation took already place after one hour of UV treatment.<sup>[193]</sup> Both strategies ended up with the temporal controlled assembly in solution by abstracting a solubility stabilizing unit from the designed peptide *via* light treatment. In addition to introducing an extra unit into the sequence that affects the solubility, the *o*-nitrobenzyl group could also act as a caging group of assembly-required charged sequence residues to aim controlled self-assembly like in the work of *L.A. Haines et al.*. She and her colleagues have shown that introducing a hydrophobic caging group on a cysteine of the amyloidogenic sequence named MAX1 created the soluble peptide, here named MAX7CNB. After UV treatment hydrogelation occurred by releasing the caging group and subsequent self-assembling of MAX1.<sup>[198]</sup>

By using the same caging-strategy *T.J. Measey et al.* could demonstrate a controlled disassembly of amyloids. They introduced a hydrophobic *o*-Nitrobenzyl derivate into the amyloid-forming peptide sequence (A $\beta$ <sub>16-22</sub>) at a position where the native side chain is known to play a key role in fibril formation *via* hydrophobic interactions. Thus, they exchanged a phenylalanine residue on sequence position 19 (F19) with *o*-Nitrobenzyl group caged lysine (K\*) to generate the peptide F19K\*. Both, native (A $\beta$ <sub>16-22</sub>) as well as the designed peptide (F19K\*) could form amyloid-like fibrils in aqueous conditions. After seven hours of UV treatment of the fibril solution the caging group cleaved off fibrils and a complete disassembly occurred by conversion of a hydrophobic moiety (K\*) into a charged one (K) whereas the wild-type peptide A $\beta$ <sub>16-22</sub> was not disassembling under same conditions.<sup>[194]</sup> It is important to mention, that all these strategies were designed to disrupt the hydrophilic/hydrophobic balance in the peptide sequence, which is fundamental for fibril formation. This effect could be clearly seen on the investigations of *J.C.M. van Hest* and his group, in which they induced the

disassembly of amphiphilic fibrils composed of a N-terminal linked hydrophobic alkyl tail *via* *o*-NBE to a hydrophilic soluble peptide GANPNAAG.<sup>[197]</sup> He could also show that additional C-terminal hydrophobic residues, here alkylation, could stabilize the fibrillar state of amyloid-forming peptide Ac-KLTVIIE based on the fact that the hydrophobic effect plays a crucial role in amyloid self-assembly.<sup>[199,200]</sup> In contrast, N-terminal PEGylation of Ac-KLTVIIE prevented amyloid formation. The combination of these two modifications ended up in a new design of the amyloidogenic peptide, which was N-terminal PEGylated and C-terminal linked *via* *o*-NBE with a hydrophobic tail. With this design the group was able to create an amyloid-like fibril-forming molecule with photo cleavable characteristics, whose disassembly could be performed on demand.<sup>[196]</sup>

Several strategies were investigated to gain control over the assembly and disassembly of amyloid-like materials mainly by interrupting the amphiphilic character of the amyloidogenic sequence. These strategies included rational design techniques of the peptide sequence by involving chemical modifications that can be triggered by external signals like pH, oxidative conditions or light, which might be supportive in the creation of controllable amyloid-like materials for medical applications. The next chapter gives an overview of the current status of amyloid-like materials in medical applications.



## 1.5. Amyloid-like Materials in Medical Applications

As already described in former chapters, self-assembling amyloid-like materials possess unique mechanical, structural and biological properties such as high mechanical stability, biocompatibility, high loading capacity, e.g., for drugs, improved blood circulation, biodegradability, and the ability to promote cell-attachment and growth without displaying cell toxicity. These characteristics are making them promising candidates for use in medical applications like regenerative medicine, tissue engineering and biomaterial delivery systems such as retroviral gene transfer and drug delivery.<sup>[37,72,122,161,201–203]</sup>

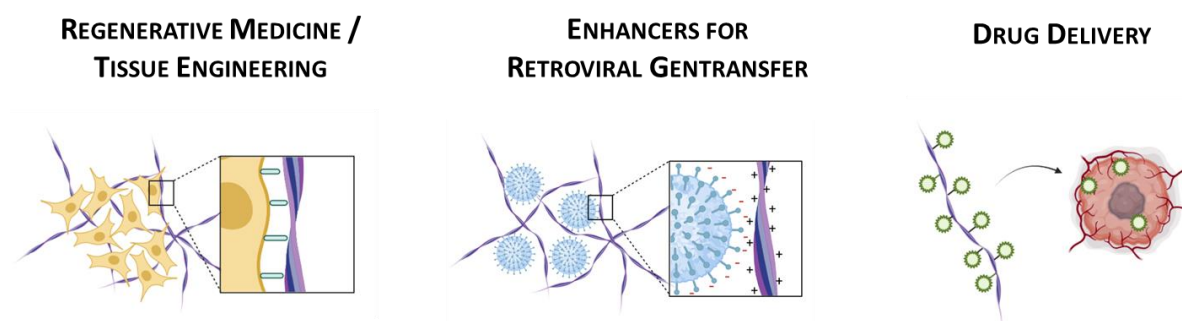


Figure 11: Illustration of potential application areas of amyloid-like scaffolds like Tissue Engineering, Retroviral Gene Transfer and Drug Delivery. The figure was created with BioRender.

### 1.5.1. Amyloid-like Materials in Drug Delivery

Various peptide hormones like glucagon are stored as amyloid-like nanofibrils and are responsible for hormone regulation in the organism. Inspired by this nature-derived design, amyloids can be used either as a vehicle in drug delivery or a drug reservoir itself. This was demonstrated by the design of an amyloidogenic long-term anti-cancer drug, named Degarelix, which is a gonadotropin-releasing hormone. Degarelix is available on the market as Firmagon® and is used for the treatment of prostate cancer by forming an amyloid-depot from which the peptide can be released in a controlled fashion. Here, the slowly and controlled release of the drug from the depot is achieved by amyloids high stability against harsh physical, chemical, and biochemical conditions. The main advantages of amyloids towards other peptide-based therapeutics is their supramolecular self-assembly that is resulting in a prolonged half-life, high stability, resulting in high bioavailability and an improved therapeutic efficiency due to the multivalent effect.<sup>[37,162,204,205]</sup> Hence, several working groups

developed amyloid-like platforms to improve cellular uptake, tissue adhesion and drug loading capacity, long-term-circulation and penetration effect.<sup>[206–210]</sup> For example, *Lei et al.* reported a multivalent platform for a combined chemo- and photodynamic therapy of metastatic melanoma using phenylboronic acid (PBA)-functionalized amyloid-like nanostructures (Figure 12). Indocyanine green (ICG) and a chemotherapeutic drug (SN38) were co-assembled with the amyloid-like forming sequence Ac-KLVFFAL-NH<sub>2</sub> (KL-7). This as I/S-PPNT termed platform was able to precisely target tumor cells through multivalent interaction between PBA and overexpressed sialic acid on the tumor surface to realize imaging-guided combination therapy.<sup>[207]</sup>

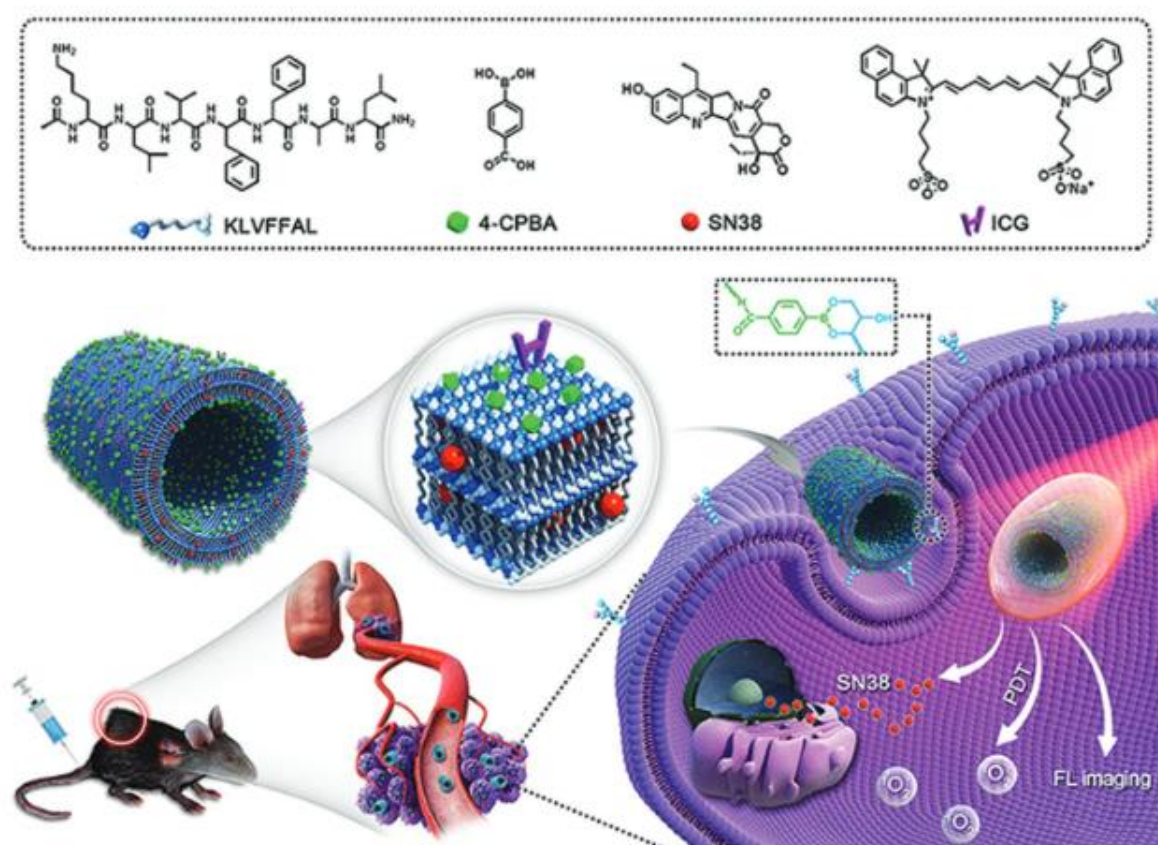


Figure 12: Schematic illustration of a multifunctional platform with four building blocks KL7FFAL (KL-7), 4-CPBA, SN38 and ICG. Here, KL-7 is a self-assembling peptide, 4-CPBA a targeting ligand, SN38 the anticancer drug and ICG a photosensitizer. KL-7, SN38 and ICG were prepared by coassembly. Further functionalization with 4-CPBA leads to active tumor targeting in the treatment of metastatic melanomas. Reprinted from Ref.<sup>[207]</sup> with permission from John Wiley and Sons.

To achieve extended retention times, precise drug release and boost the therapeutic efficiency *H. Wang* and his group designed stimulus-responsive drug delivery with endogenous triggers like pH, reactive oxygen species (ROS) and enzymes as well as exogenous stimuli such as photothermal triggers. Furthermore, they utilized the same

amyloid-like forming peptide core sequence FF to create multivalent platforms.<sup>[179,211–215]</sup> On the one hand, their strategy contained the creation of long-term drug depots with sustained drug release. Here, peptide-based prodrug nanoparticles with favorable tumor targeting sites converted into amyloid-like nanostructures to form long-term drug depots.<sup>[211,215]</sup> On the other hand, they could present nanoparticles morphology transformation into amyloid-like fibrils by photothermic triggers, light or endogenous reactive oxygen species (ROS) within the cells. In comparison to the previous reported results, the internalization and morphological transformations of these nanostructures induced apoptosis through mechanical destruction of mitochondria in tumor cells.<sup>[216–218]</sup>

### **1.5.2. Amyloid-like Materials as Retroviral Enhancers**

Another promising biomaterial delivery application of amyloid-like materials is the retroviral gene transfer, in which amyloids play a crucial role as enhancers for the cellular internalization of the viral cargo. Retroviral gene transfer is a technology that has been fundamental for gene therapy approaches such as chimeric antigen receptor (CAR) T-cell therapy for cancer treatment. Therefore, it is important to overcome its limitation of poor transduction rates caused by low virus concentrations and inefficient cell attachment.<sup>[219,220]</sup> One approach is the complexation of positively charged amyloid fibrils with the negatively charged viral particles that enables a greater co-localization of the complexed viral particles with the cell membrane. This could be explained by the assumption that the highly rigid amyloid fibrils cannot cover virus surfaces thoroughly, but create an excess of positive charges in the virus-fibril complex, which enabled a greater interaction to the negatively charged cell membrane (Figure 13).<sup>[25]</sup>

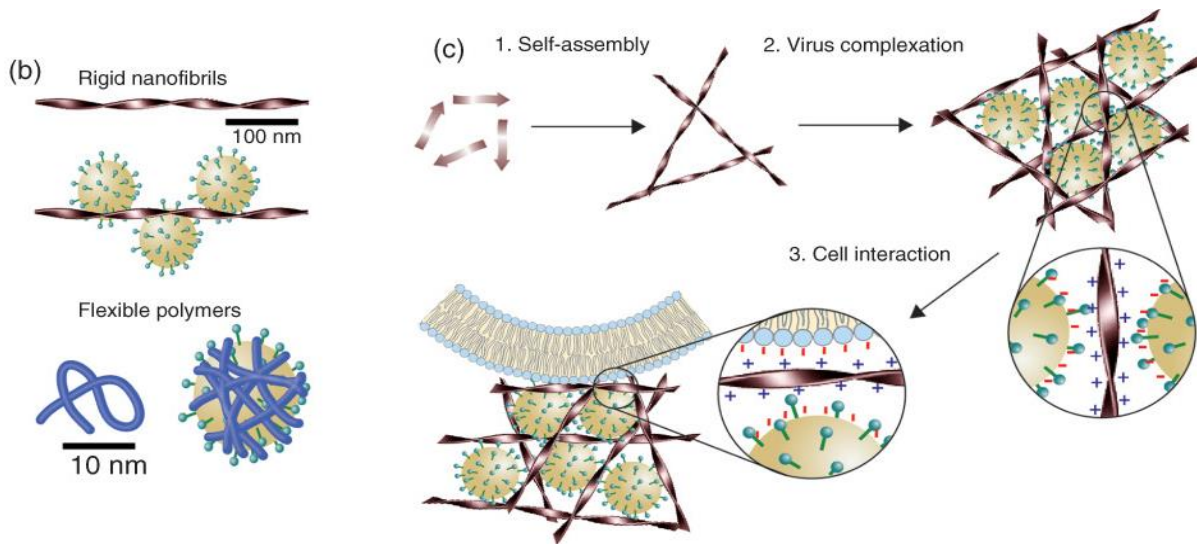


Figure 13: Illustration of the interaction between the virus and the amyloid-like fibril. Reprinted from Ref. [221] with permission from John Wiley and Sons.

Additionally, a study by *Schütz et al.* showed that cellular protrusions engaged amyloid fibrils and pulled them towards the cell body. Here, chemical suppression of protrusion formation showed a lower fibril-cell binding and thus lower virion delivery efficiency. Consequently, they concluded that amyloids superstructure itself has a high contribution to the fibril-cell binding mechanism. This conclusion was surprising as previous reports assumed electrostatic interactions as the main driving force. Furthermore, it was suggested that this mechanism induced invaginations of the plasma membrane resulting in the formation of macropinosomes that may serve as an additional internalization route for complexed viruses. All these results gave a reasonable explanation for the superior activity of amyloids in comparison to other soluble polycationic transduction enhancers like polybrene or DEAE-dextran as the latter ones do not form a fibrillar superstructure.<sup>[142]</sup>

Amyloids characteristics to enhance viral infection was discovered by serendipity. The original goal was to detect a semen-derived component which affects HIV-1 infection. It was revealed that a fragment of the prostatic acid phosphatase ( $PAP_{248-286}$ ), which is an enzyme in the human semen, could form amyloid structures and enhanced the viral uptake drastically. For this reason, it was termed SEVI (semen-derived enhancer of virus infection). Next to  $PAP_{248-286}$  there were other semen-derived amyloid-forming peptides that enhanced viral infection rates such as  $PAP_{85-120}$ , SEM1 and SEM2.<sup>[221,222]</sup> These results additionally underpin the assumption that amyloids can be used as retroviral transduction enhancers as it could be also shown on SEVI, which

boosts retroviral gene transfer more efficiently than conventional additives. Nevertheless, due to obstacles like high production costs of this large polypeptide and difficulties in the achievement of reproducible activities, the use of SEVI as a laboratory tool was limited. This limitations could be overcome by small synthetic amyloid-forming peptides, that can increase the retroviral gene transfer more efficiently and are easy to produce and handle.<sup>[220,221]</sup> Based on previous screening studies *J. Münch* and his group discovered a small amphiphilic 12-mer amyloid-forming peptide (QCKIKQIINMWQ) named enhancing factor C (EF-C) that was equally potent to RetroNectin, which is the reagent of choice to enhance retroviral gene transfer, and was four times more potent than naturally occurring SEVI. One possible explanation for the greater activity could be the strong fibril-forming tendency of EF-C in comparison to SEVI.<sup>[220]</sup> Compared to RetroNectin, EF-C is not only less expensive but it did not require any additional coatings as the activity of EF-C fibrils emerge immediately after addition to the virus stock solution.<sup>[118,220]</sup> EF-C is commercially available as Protransduzin.<sup>[220,223]</sup>

To gain more knowledge about structural features that are responsible for amyloids' distinctive bioactivity *Sieste et al.* performed an extensive sequence optimization study of EF-C by using a multiparameter and multiscale approach. They found the seven-mer amyloid-forming peptide sequence CKFKFQF (PNF18) as the shortest sequence that formed fibrils with high intermolecular  $\beta$ -sheet content, the ability to bind virions and interaction with cellular membranes. Due to these characteristics its retroviral transduction efficiency was higher compared to the original EF-C sequence. Furthermore, it is less expensive to synthesize and its N-terminal thiol group offers additional modification possibilities.<sup>[118]</sup>

### **1.5.3. Amyloid-like Materials as Scaffolds in Tissue Engineering**

Tissue engineering aims for the regeneration of injured tissue by creation artificial materials for transplantation. In the *ex vivo* method, an artificial extracellular matrix (ECM)-mimicking scaffold was linked with the desired cell line in combination with several regulatory signals outside the body.<sup>[83,85,157]</sup> There are only a few simple *ex vivo* biomaterials systems such as skin substitutes on the market like *Apligraf* and *Dermagraft*. As the *ex vivo* approach comprises limitations like the need of complex

culture conditions and occurring immune reactions *in situ* tissue engineering was implemented. This method is using the body's regenerative abilities in combination with engineered biomaterial, which is loaded with bioactive cues that guide functional restoration to the injury through incorporation of additional intracellular reprogramming techniques (Figure 14).<sup>[83,85]</sup>

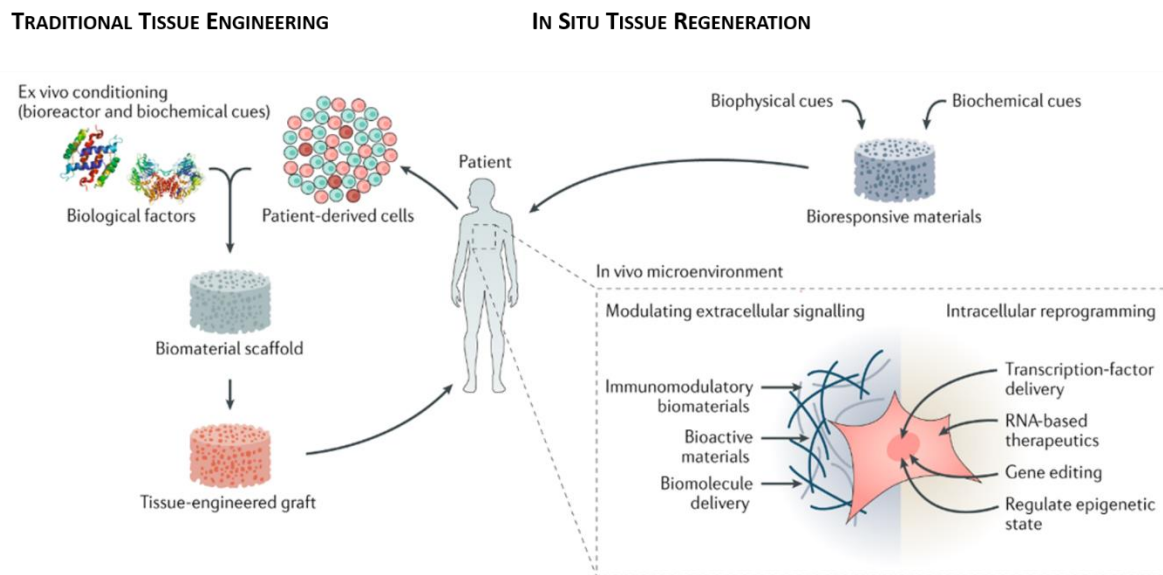


Figure 14: Graphical overview of traditional tissue engineering versus in situ tissue regeneration. Reprinted from Ref. <sup>[83]</sup> with permission from Springer Nature.

There are some requirements for the scaffold material that is used in tissue engineering, specifically a variety of material properties that ensure a recruitment, encapsulation, special organization of cells and avoid cell migration away from the damaged region. Furthermore, the scaffold should stimulate the viability and the regeneration of healthy cells by providing a favourable microenvironment, which mimics the physiological niche of the tissue it is incorporated in.<sup>[83,161,224]</sup> This could be achieved by the modulation of physical, topographical and chemical characteristics of the designed scaffold to the specific type of application.<sup>[224,225]</sup> The variety of 3D scaffold materials ranges from natural derived polymers such as collagen and laminin to synthetic materials such as poly(ethylene glycol) (PEG) or polyvinylidene fluoride (PVDF). Especially natural materials are attractive for tissue engineering applications because of their complex microstructure, biocompatibility, inherent bioactivity and stability that mimics the natural niche to a large degree.<sup>[83,224,225]</sup> The most frequently used natural hydrogel is Matrigel, which is derived from the Engelbreth-Holm-Swarm (EHS) mouse sarcoma cells and contains a complex protein mixture. Unfortunately,

the possibility to shape and control its physico-chemical characteristics is not given due to the high complexity of this scaffold. To avoid this limitation, ECM proteins such as laminin, fibrinogen, or collagen were used as scaffolds. However, their usage is strongly limited by difficulties in purification and immunogenicity of the material.<sup>[226]</sup>

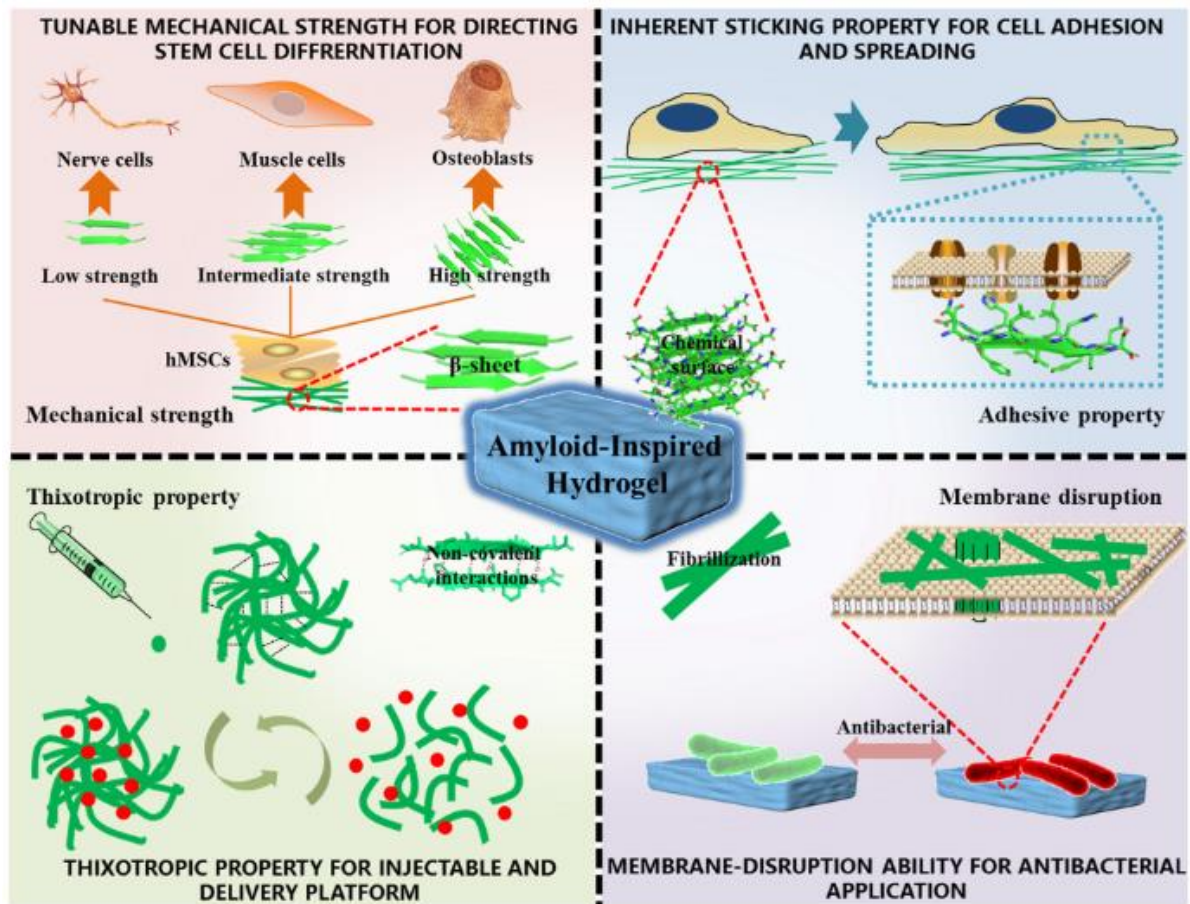


Figure 15: Overview of all structural features of amyloid-like hydrogels with potential in biomedical applications like tissue engineering. Reprinted from Ref.<sup>[227]</sup> with the permission from Frontiers Media S.A.. This work is licensed under a Creative Commons Attribution 4.0 International License.

The before mentioned features of amyloids such as ability to attach cells, improve cell spreading and viability as well as their ECM-mimicking properties, rapid self-assembly kinetics under mild conditions and the ability to act as vehicles for drug delivery make amyloids attractive as scaffolds for tissue engineering (Figure 15).<sup>[72,126,161,227]</sup> Especially designing amyloid-based platforms for stem cell therapy, is attracting more and more attention as amyloids possess tuneable physico-chemical properties like adjustable mechanical strength. This was demonstrated by *Das et al*, who altered amino acid side chains in the original sequence providing a changed number of  $\beta$ -sheets with altering physico-chemical factors of the assembly process.<sup>[227,228]</sup> Interestingly, *Jacob et al*. could show that in a comparability study of collagen and

amyloid fibrils focal adhesion formation on amyloid fibrils was stronger. They also suggested that amyloid fibrils may be even more effective in supporting cell adhesion than native ECM components.<sup>[121]</sup> One example of using amyloid-like materials for tissue engineering purposes is the study of *J. Kisiday et al.*, in which the group developed an amyloid-like hydrogel named KLD-12 for cartilage repair. This hydrogel encapsulated chondrocytes for a time-period of four weeks developing a cartilage-like ECM with proteoglycans and type II collagen. Besides the fact, that within this time-period the chondrocytes retained their morphology, the group indicated a time-dependant increase in scaffold stiffness revealing the deposition of mechanically functional neo-tissue.<sup>[161,229]</sup> In further studies, *Das et al.* investigated a bunch of amyloid-like hydrogel-forming peptides derived from  $\alpha$ -Syn based on the core structure VTAVA. Their various peptidic designs were triggered by different stimuli like heating, cooling and pH changes to induce aggregation and to form supramolecular hydrogels. In this study the tested amyloid-like material was non-toxic, did not induce a massive immune response and supported neuronal differentiation of implanted stem cells. Thus, *Das et al.* provided the first study that used amyloid-like hydrogels for the transplantation of stem cells into the brain.<sup>[228]</sup>

Compared to commonly used synthetic polymers or cross-linked polymer composites such as copolymers of lactic and glycolic acids with PEG, amyloid-based ECM-mimicking hydrogels possess several advantages like: 1) They own a thixotropic character due to their non-covalent self-assembly and have hence chances in future application as injectable hydrogels. 2) Amyloids have an inherent bioactivity like antibacterial properties and cell adhesive character. 3) They avoid the possibility of biological contamination due to their synthesis.<sup>[36,143,161,201,227,230]</sup>

In the following, several synthesis strategies of amyloid-based hydrogels are going to be presented. The creation of amyloidogenic hydrogels was strongly inspired by nature-derived sources with accessible amyloid-forming peptide sequences like lysozyme, amyloid- $\beta$  protein or  $\beta$ -lactoglobulin.<sup>[72,228,231–234]</sup> The two main approaches to access this amyloidogenic peptide sequences are by either determining the sequence using computer-assisted analytical techniques or treatment of the protein with high temperatures and acids to unfold and cleave the sequence, which subsequently self-assembles into amyloid-like fibrils. Here, gelation can be induced through variation of ionic strength and concentration changes of amyloidogenic



peptide solutions. *Yang et al.*, for example, showed a preparation method for an amyloidogenic hydrogel from hydrolyzed hen egg white lysozyme. Another strategy to induce gelation of lysozyme-derived amyloid fibrils was caused by the addition of natural polyphenols such as epigallocatechin gallate (EGCG) as shown by *Hu et al.*<sup>[235]</sup> On the other hand, *de novo* synthesis of hydrogel-forming amyloidogenic peptides could be performed either by rational peptide design or as previously mentioned by identification of sequences from known amyloidogenic proteins or peptides.<sup>[68,161,236]</sup> These *ne novo* synthesized short sequences have the advantages of lower production costs, specific functionalization possibilities and higher purification avoiding cytotoxic off-target assemblies.<sup>[161]</sup> Unfortunately, not every amyloidogenic peptide sequence possesses the capability to form a hydrogel. Thus, intensive research was performed to elucidate the structural motif of amyloids hydrogel formation ability.<sup>[236–238]</sup> For example, *K. Medini et al.* implemented three different modifications of the seven-mer peptide IKHLSVN such as N-terminal Fmoc-functionalization, and exchange of histidine (H) with tyrosine (T) or phenylalanine (F) in order to gain derivatives that easily form gels. All modifications resulted in gel formation and additionally affected fibril morphology and amyloid-like character.<sup>[238]</sup> Especially, Fmoc-based amyloidogenic peptides have been explored intensively in hydrogel systems for cell culturing purposes as they exhibit cell supportive characteristics. It has been found that the occurrence of fluorenyl rings favored the hydrogelation of many amyloid-forming peptides through  $\pi$ - $\pi$  interactions either between two fluorenyl groups or between fluorenyl and phenol groups.<sup>[38,161,238–243]</sup> Another strategy to reach hydrogelation in amyloid-forming peptides is the creation of hybrid materials. For example, *Gaćanin et al.* designed a hybrid amyloid-based hydrogel for tissue engineering purposes by grafting an amyloidogenic peptide and PEG chains onto a polypeptide backbone of Human Serum Albumin (HSA) providing a supramolecular gelator system. The hydrogel was remarkably robust and possessed self-healing as well as thixotropic character.<sup>[36]</sup>

Captivatingly, the occurrence of hydrogelation characteristics in amyloid-like structures does not necessarily provide the material with thixotropic behaviour. *Jacob et al.* could show that there is a lack of thixotropy for Fmoc-FF hydrogels whereas other Fmoc-functionalized amyloidogenic peptides show thixotropic behaviour. They assumed that this could be due to Fmoc-FF peptides higher hydrogel strength (>2

kPa) according to enhanced  $\pi$ - $\pi$  stacking possibilities. Consequently, a subtle balance between the  $\pi$ - $\pi$  stacking forces and the hydrophobicity of the amyloid fibrils could be the driving factor for thixotropy.<sup>[72,243]</sup>

## 1.6. References

- [1] R. Virchow, *Arch. für Pathol. Anat. und Physiol. und für Klin. Med.* **1854**, 6, 135.
- [2] N. Friedreich, A. Kekulé, *Arch. für Pathol. Anat. und Physiol. und für Klin. Med.* **1859**, 16, 50.
- [3] A. B. Mativ, N. P. Trubitsina, A. G. Matveenکو, Y. A. Barbitoff, G. A. Zhouravleva, S. A. Bondarev, *Biochem.* **2020**, 85, 1011.
- [4] A. Giordano, *Current Clinical Pathology*, **2017**.
- [5] K. Nishitsuji, H. Saito, K. Uchimura, *Neural Regen. Res.* **2016**, 11, 408.
- [6] M. Fändrich, *Cell. Mol. Life Sci.* **2007**, 64, 2066.
- [7] P. Westermark, M. D. Benson, J. N. Buxbaum, A. S. Cohen, B. Frangione, S. I. Ikeda, C. L. Masters, G. Merlini, M. J. Saraiva, J. D. Sipe, *Amyloid* **2005**, 12, 1.
- [8] M. S. Rubel, S. A. Fedotov, A. V. Grizel, J. V. Sopova, O. A. Malikova, Y. O. Chernoff, A. A. Rubel, *Functional mammalian amyloids and amyloid-like proteins*, Vol. 10, **2020**.
- [9] S.-Y. Ow, D. E. Dunstan, *Protein Sci.* **2014**, 23, 1315.
- [10] P. H. Nguyen, A. Ramamoorthy, B. R. Sahoo, J. Zheng, P. Faller, J. E. Straub, L. Dominguez, J. E. Shea, N. V. Dokholyan, A. de Simone, B. Ma, R. Nussinov, S. Najafi, S. T. Ngo, A. Loquet, M. Chiricotto, P. Ganguly, J. McCarty, M. S. Li, C. Hall, Y. Wang, Y. Miller, S. Melchionna, B. Habenstein, S. Timr, J. Chen, B. Hnath, B. Strodel, R. Kayed, S. Lesné, G. Wei, F. Sterpone, A. J. Doig, P. Derreumaux, *Chem. Rev.* **2021**, 121, 2545.
- [11] G. Wei, Z. Su, N. P. Reynolds, P. Arosio, I. W. Hamley, E. Gazit, R. Mezzenga, *Chem. Soc. Rev.* **2017**, 46, 4661.
- [12] S. Mankar, A. Anoop, S. Sen, S. K. Maji, *Nano Rev.* **2011**, 2, 6032.
- [13] D. M. Fowler, A. V. Koulov, C. Alory-Jost, M. S. Marks, W. E. Balch, J. W. Kelly, *PLoS Biol.* **2006**, 4, 0100.
- [14] M. Deshmukh, M. L. Evans, M. R. Chapman, *J. Mol. Biol.* **2018**, 430, 3631.
- [15] N. Shanmugam, M. O. D. G. Baker, S. R. Ball, M. Steain, C. L. L. Pham, M. Sunde, .
- [16] P. McCaffrey, *Is It Good for You? Amyloid Shows New Side in Mammalian Cells*, **2005**.
- [17] E. Chuang, A. M. Hori, C. D. Hesketh, J. Shorter, *J. Cell Sci.* **2018**, 131.
- [18] D. Otzen, R. Riek, *Cold Spring Harb. Perspect. Biol.* **2019**, 11.
- [19] D. M. Fowler, A. V. Koulov, W. E. Balch, J. W. Kelly, *Trends Biochem. Sci.* **2007**, 32, 217.
- [20] R. P. McGlinchey, F. Shewmaker, P. McPhie, B. Monterroso, K. Thurber, R. B. Wickner, *Proc. Natl. Acad. Sci. U. S. A.* **2009**, 106, 13731.

- [21] B. Watt, G. van Niel, G. Raposo, M. S. Marks, *Pigment Cell Melanoma Res.* **2013**, 26, 300.
- [22] J. S. Stephan, L. Fioriti, N. Lamba, L. Colnaghi, K. Karl, I. L. Derkatch, E. R. Kandel, *Cell Rep.* **2015**, 11, 1772.
- [23] S. K. Maji, M. H. Perrin, M. R. Sawaya, S. Jessberger, K. Vadodaria, R. A. Rissman, P. S. Singru, K. P. R. Nilsson, R. Simon, D. Schubert, D. Eisenberg, J. Rivier, P. Sawchenko, W. Vale, R. Riek, *Science (80- )*. **2009**, 325, 328.
- [24] Z. Ye, K. C. French, L. A. Popova, I. K. Lednev, M. M. Lopez, G. I. Makhatadze, *Biochemistry* **2009**, 48, 11582.
- [25] K. Kaygisiz, C. V. Synatschke, *Biomater. Sci.* **2020**, 8, 6113.
- [26] J. V. Sopova, E. I. Koshel, T. A. Belashova, S. P. Zadorsky, A. V. Sergeeva, V. A. Siniukova, A. A. Shenfeld, M. E. Velizhanina, K. V. Volkov, A. A. Nizhnikov, D. V. Kachkin, E. R. Gaginskaya, A. P. Galkin, *Sci. Rep.* **2019**, 9, 1.
- [27] O. Kranenburg, B. Bouma, L. M. J. Kroon-Batenburg, A. Reijerkerk, Y. P. Wu, E. E. Voest, M. F. B. G. Gebbink, *Curr. Biol.* **2002**, 12, 1833.
- [28] S. Wnendt, I. Wetzels, W. A. Günzler, *Thromb. Res.* **1997**, 85, 217.
- [29] E. Herczenik, B. Bouma, S. J. A. Korporaal, R. Strangi, Q. Zeng, P. Gros, M. Van Eck, T. J. C. Van Berkel, M. F. B. G. Gebbink, J.-W. N. Akkerman, *Arterioscler. Thromb. Vasc. Biol.* **2007**, 27, 1657.
- [30] A. Soragni, S. Yousefi, C. Stoeckle, A. B. Soriaga, M. R. Sawaya, E. Kozlowski, I. Schmid, S. Radonjic-Hoesli, S. Boutet, G. J. Williams, M. Messerschmidt, M. M. Seibert, D. Cascio, N. A. Zatsepin, M. Burghammer, C. Riek, J.-P. Colletier, R. Riek, D. S. Eisenberg, H.-U. Simon, *Mol. Cell* **2015**, 57, 1011.
- [31] J. Li, T. McQuade, A. B. Siemer, J. Napetschnig, K. Moriwaki, Y.-S. Hsiao, E. Damko, D. Moquin, T. Walz, A. McDermott, F. K.-M. Chan, H. Wu, *Cell* **2012**, 150, 339.
- [32] M. E. Velizhanina, A. P. Galkin, **2022**.
- [33] L. S. Honig, M.-X. Tang, S. Albert, R. Costa, J. Luchsinger, J. Manly, Y. Stern, R. Mayeux, *Arch. Neurol.* **2003**, 60, 1707.
- [34] C. S. Atwood, R. L. Bowen, M. A. Smith, G. Perry, *Brain Res. Rev.* **2003**, 43, 164.
- [35] S. K. Maji, L. Wang, J. Greenwald, R. Riek, *FEBS Lett.* **2009**, 583, 2610.
- [36] J. Gačanin, J. Hedrich, S. Sieste, G. Glaßer, I. Lieberwirth, C. Schilling, S. Fischer, H. Barth, B. Knöll, C. V. Synatschke, T. Weil, *Adv. Mater.* **2019**, 31.
- [37] Y. Lai, F. Li, Z. Zou, M. Saeed, Z. Xu, H. Yu, *Appl. Mater. Today* **2021**, 22, 100966.
- [38] V. Singh, K. Snigdha, C. Singh, N. Sinha, A. K. Thakur, *Soft Matter* **2015**, 11, 5353.
- [39] L. Adler-Abramovich, L. Vaks, O. Carny, D. Trudler, A. Magno, A. Caffisch, D.

- Frenkel, E. Gazit, *Nat. Chem. Biol.* **2012**, *8*, 701.
- [40] A. B. Matiiv, N. P. Trubitsina, A. G. Matveenko, Y. A. Barbitoff, G. A. Zhouravleva, S. A. Bondarev, *Biochem.* **2022**, *87*, 450.
- [41] M. G. Iadanza, M. P. Jackson, E. W. Hewitt, N. A. Ranson, S. E. Radford, *Nat. Rev. Mol. Cell Biol.* **2018**, *19*, 755.
- [42] A. Schmidt, K. Annamalai, M. Schmidt, N. Grigorieff, M. Fändrich, *Proc. Natl. Acad. Sci.* **2016**, *113*, 6200.
- [43] M. G. Iadanza, M. P. Jackson, E. W. Hewitt, N. A. Ranson, S. E. Radford, *Nat. Rev. Mol. Cell Biol.* **2018**, *19*, 755.
- [44] P. C. A. Van Der Wel, J. R. Lewandowski, R. G. Griffin, *J. Am. Chem. Soc.* **2007**, *129*, 5117.
- [45] E. K. Kumar, N. Haque, N. P. Prabhu, *Int. J. Biol. Macromol.* **2017**, *100*, 3.
- [46] Y. Gao, C. Guo, J. O. Watzlawik, P. S. Randolph, E. J. Lee, D. Huang, S. M. Stagg, H.-X. Zhou, T. L. Rosenberry, A. K. Paravastu, *J. Mol. Biol.* **2020**, *432*, 4388.
- [47] F. Meng, J. Yoo, H. S. Chung, *Proc. Natl. Acad. Sci. U. S. A.* **2022**, *119*.
- [48] B. H. Meier, A. Böckmann, *Curr. Opin. Struct. Biol.* **2015**, *30*, 43.
- [49] W.-F. Xue, A. L. Hellewell, W. S. Gosal, S. W. Homans, E. W. Hewitt, S. E. Radford, *J. Biol. Chem.* **2009**, *284*, 34272.
- [50] S. De, D. C. Wirthensohn, P. Flagmeier, C. Hughes, F. A. Aprile, F. S. Ruggeri, D. R. Whiten, D. Emin, Z. Xia, J. A. Varela, P. Sormanni, F. Kundel, T. P. J. Knowles, C. M. Dobson, C. Bryant, M. Vendruscolo, D. Klenerman, *Nat. Commun.* **2019**, *10*.
- [51] W.-C. Chiang, Y.-S. Fang, Y. S. Lye, T.-Y. Weng, K. Ganesan, S.-H. Huang, L.-Y. Chang, S.-C. Chou, Y.-R. Chen, *ACS Chem. Neurosci.* **2022**, *13*, 2599.
- [52] V. Castelletto, I. W. Hamley, (Eds.: Nilsson, B. L.; Doran, T. M.), Springer New York, New York, NY, **2018**, pp. 3–21.
- [53] D. Huang, B. C. Hudson, Y. Gao, E. K. Roberts, A. K. Paravastu, (Eds.: Nilsson, B. L.; Doran, T. M.), Springer New York, New York, NY, **2018**, pp. 23–68.
- [54] J.-M. Ruyschaert, V. Raussens, (Eds.: Nilsson, B. L.; Doran, T. M.), Springer New York, New York, NY, **2018**, pp. 69–81.
- [55] K. Gade Malmos, L. M. Blancas-Mejia, B. Weber, J. Buchner, M. Ramirez-Alvarado, H. Naiki, D. Otzen, *Amyloid* **2017**, *24*, 1.
- [56] P. Frid, S. V Anisimov, N. Popovic, *Brain Res. Rev.* **2007**, *53*, 135.
- [57] D. Shen, J. Coleman, E. Chan, T. P. Nicholson, L. Dai, P. W. Sheppard, W. F. Patton, *Cell Biochem. Biophys.* **2011**, *60*, 173.
- [58] R. Wetzel, S. Chemuru, P. Misra, R. Kodali, S. Mukherjee, K. Kar, *Methods Mol. Biol.* **2018**, *1777*, 121.

- [59] Y. Zou, Y. Li, W. Hao, X. Hu, G. Ma, *J. Phys. Chem. B* **2013**, *117*, 4003.
- [60] M. Groenning, *J. Chem. Biol.* **2010**, *3*, 1.
- [61] J. Raeburn, L. Chen, S. Awhida, R. C. Deller, M. Vatish, M. I. Gibson, D. J. Adams, *Soft Matter* **2015**, *11*, 3706.
- [62] N. Amdursky, Y. Erez, D. Huppert, *Acc. Chem. Res.* **2012**, *45*, 1548.
- [63] R. Khurana, V. N. Uversky, L. Nielsen, A. L. Fink, *J. Biol. Chem.* **2001**, *276*, 22715.
- [64] J. Adamcik, F. S. Ruggeri, J. T. Berryman, A. Zhang, T. P. J. Knowles, R. Mezzenga, *Adv. Sci.* **2021**, *8*, 2002182.
- [65] M. H. Horrocks, S. F. Lee, S. Gandhi, N. K. Magdalinou, S. W. Chen, M. J. Devine, L. Tosatto, M. Kjaergaard, J. S. Beckwith, H. Zetterberg, M. Iljina, N. Cremades, C. M. Dobson, N. W. Wood, D. Klenerman, *ACS Chem. Neurosci.* **2016**, *7*, 399.
- [66] S. Al-Halifa, M. Babych, X. Zottig, D. Archambault, S. Bourgault, *Pept. Sci.* **2019**, *111*, e24095.
- [67] M. López de la Paz, K. Goldie, J. Zurdo, E. Lacroix, C. M. Dobson, A. Hoenger, L. Serrano, *Proc. Natl. Acad. Sci.* **2002**, *99*, 16052.
- [68] A. Bertolani, L. Pirrie, L. Stefan, N. Houbenov, J. S. Haataja, L. Catalano, G. Terraneo, G. Giancane, L. Valli, R. Milani, O. Ikkala, G. Resnati, P. Metrangolo, *Nat. Commun.* **2015**, *6*, 7574.
- [69] C. Liu, M. R. Sawaya, D. Eisenberg, *Nat. Struct. Mol. Biol.* **2011**, *18*, 49.
- [70] M. Gimona, *Nat. Rev. Mol. Cell Biol.* **2006**, *7*, 68.
- [71] T. P. J. Knowles, M. J. Buehler, *Nat. Nanotechnol.* **2011**, *6*, 469.
- [72] S. Das, R. S. Jacob, K. Patel, N. Singh, S. K. Maji, *Biomacromolecules* **2018**, *19*, 1826.
- [73] K. Masters, K. Anseth, *Adv. Chem. Eng.* **2004**, *29*, 7.
- [74] T. G. Vladkova, *Int. J. Polym. Sci.* **2010**, *2010*.
- [75] A. G. Bobylev, R. S. Fadeev, L. G. Bobyleva, M. I. Kobyakova, Y. M. Shlyapnikov, D. V Popov, I. M. Vikhlyantsev, K. Turoverov, **2021**.
- [76] B. Vagaská, L. Bačáková, E. Filová, K. Balík, *Physiol. Res.* **2010**, *59*, 309.
- [77] S. Wu, W. Du, Y. Duan, D. Zhang, Y. Liu, B. Wu, X. Zou, H. Ouyang, C. Gao, *Acta Biomater.* **2018**, *75*, 75.
- [78] E. Zimmerman, B. Geiger, L. Addadi, *Biophys. J.* **2002**, *82*, 1848.
- [79] B. J. Nebe, J. Rychly, *BioNanoMaterials* **2013**, *14*, 153.
- [80] B. G. Keselowsky, D. M. Collard, A. J. García, *Surface chemistry modulates fibronectin conformation and directs integrin binding and specificity to control cell adhesion*, **2003**.

- [81] B. Nebe, *Am. J. Biomed. Sci. Res.* **2020**, 9, 1.
- [82] S. Staehlke, J. Lehnfeld, A. Schneider, J. B. Nebe, R. Müller, *Mater. Sci. Eng. C. Mater. Biol. Appl.* **2019**, 101, 190.
- [83] A. K. Gaharwar, I. Singh, A. Khademhosseini, *Nat. Rev. Mater.* **2020**, 5, 686.
- [84] I. Wheeldon, A. Farhadi, A. G. Bick, E. Jabbari, A. Khademhosseini, *Nanotechnology* **2011**, 22.
- [85] L. Sardelli, D. P. Pacheco, L. Zorzetto, C. Rinoldi, W. Świążzkowski, P. Petriani, *J. Appl. Biomater. Funct. Mater.* **2019**, 17.
- [86] K. Nakamura, W. Tanaka, K. Sada, R. Kubota, T. Aoyama, K. Urayama, I. Hamachi, *J. Am. Chem. Soc.* **2021**, 143, 19532.
- [87] S. SenGupta, C. A. Parent, J. E. Bear, *Nat. Rev. Mol. Cell Biol.* **2021**, 22, 529.
- [88] E. M. Benetti, M. K. Gunnewiek, C. A. Van Blitterswijk, G. Julius Vancso, L. Moroni, *J. Mater. Chem. B* **2016**, 4, 4244.
- [89] M. S. Kim, G. Khang, H. B. Lee, *Prog. Polym. Sci.* **2008**, 33, 138.
- [90] Y. Luo, M. S. Shoichet, *Nat. Mater.* **2004**, 3, 249.
- [91] T. Matsuda, T. Sugawara, *J. Biomed. Mater. Res.* **1995**, 29, 749.
- [92] D. Ryan, B. A. Parviz, V. Linder, V. Semetey, S. K. Sia, J. Su, M. Mrksich, G. M. Whitesides, *Langmuir* **2004**, 20, 9080.
- [93] S. Zhang, L. Yan, M. Altman, M. Lässle, H. Nugent, F. Frankel, D. A. Lauffenburger, G. M. Whitesides, A. Rich, *Biomaterials* **1999**, 20, 1213.
- [94] F. M. Yavitt, B. E. Kirkpatrick, M. R. Blatchley, K. S. Anseth, *ACS Biomater. Sci. Eng.* **2022**, acsbiomaterials.1c01450.
- [95] B. D. Fairbanks, S. P. Singh, C. N. Bowman, K. S. Anseth, *Macromolecules* **2011**, 44, 2444.
- [96] C. Yang, F. W. DelRio, H. Ma, A. R. Killaars, L. P. Basta, K. A. Kyburz, K. S. Anseth, *Proc. Natl. Acad. Sci.* **2016**, 113, E4439.
- [97] A. M. Kloxin, A. M. Kasko, C. N. Salinas, K. S. Anseth, *Science (80-. )*. **2009**, 324, 59.
- [98] N. Muzzio, M. Eduardo Martinez-Cartagena, G. Romero, *Adv. Drug Deliv. Rev.* **2022**, 190, 114554.
- [99] T. B. Dorsey, A. Grath, A. Wang, C. Xu, Y. Hong, G. Dai, *Bioact. Mater.* **2018**, 3, 64.
- [100] J. A. Shadish, A. C. Strange, C. A. Deforest, *J. Am. Chem. Soc.* **2019**, 141, 15619.
- [101] S. N. Nishimura, N. Hokazono, Y. Taki, H. Motoda, Y. Morita, K. Yamamoto, N. Higashi, T. Koga, *ACS Appl. Mater. Interfaces* **2019**, 11, 24577.
- [102] M. Wirkner, J. M. Alonso, V. Maus, M. Salierno, T. T. Lee, A. J. García, A. Del Campo, *Adv. Mater.* **2011**, 23, 3907.

- [103] J. Ricken, R. Medda, S. V. Wegner, *Adv. Biosyst.* **2019**, 3, 1.
- [104] S. V. Wegner, O. I. Sentürk, J. P. Spatz, *Sci. Rep.* **2015**, 5, 1.
- [105] Z. Zhang, N. Chen, S. Li, M. R. Battig, Y. Wang, **2012**.
- [106] J. Boekhoven, C. M. Rubertpérez, S. Sur, A. Worthy, S. I. Stupp, *Angew. Chemie - Int. Ed.* **2013**, 52, 12077.
- [107] B. M. Lamb, M. N. Yousaf, *J. Am. Chem. Soc.* **2011**, 133, 8870.
- [108] W.-S. Yeo, M. N. Yousaf, M. Mrksich, *J. Am. Chem. Soc.* **2003**, 125, 14994.
- [109] A. Motealleh, N. S. Kehr, *Adv. NanoBiomed Res.* **2021**, 1, 2000114.
- [110] R. R. Bhat, M. R. Tomlinson, T. Wu, J. Genzer, *Adv. Polym. Sci.* **2006**, 198, 51.
- [111] J. Genzer, *Annu. Rev. Mater. Res.* **2012**, 42, 435.
- [112] S. Yu, X. Zuo, T. Shen, Y. Duan, Z. Mao, C. Gao, *Acta Biomater.* **2018**, 72, 70.
- [113] M. Arnold, V. C. Hirschfeld-Warneken, T. Lohmüller, P. Heil, J. Blümmel, E. A. Cavalcanti-Adam, M. López-García, P. Walther, H. Kessler, B. Geiger, J. P. Spatz, *Nano Lett.* **2008**, 8, 2063.
- [114] D. H. Kim, L. H. Cui, H. R. Seo, H. J. Joo, S. C. Choi, D. S. Lim, K. B. Lee, *J. Vis. Exp.* **2018**, 2018.
- [115] S. M. Bittner, B. T. Smith, L. Diaz-Gomez, C. D. Hudgins, A. J. Melchiorri, D. W. Scott, J. P. Fisher, A. G. Mikos, *Acta Biomater.* **2019**, 90, 37.
- [116] T. Potyondy, J. A. Uquillas, P. J. Tebon, B. Byambaa, A. Hasan, M. Tavafoghi, H. Mary, G. E. Aninwene, I. Pountos, A. Khademhosseini, N. Ashammakhi, *Biofabrication* **2021**, 13.
- [117] J. Wu, Z. Mao, H. Tan, L. Han, T. Ren, C. Gao, *Interface Focus* **2012**, 2, 337.
- [118] S. Sieste, T. Mack, E. Lump, M. Hayn, D. Schütz, A. Röcker, C. Meier, K. Kaygisiz, F. Kirchhoff, T. P. J. Knowles, F. S. Ruggeri, C. V. Synatschke, J. Münch, T. Weil, *Adv. Funct. Mater.* **2021**, 2009382.
- [119] J. L. Cifelli, C. C. Capule, J. Yang, *ACS Chem. Neurosci.* **2019**, 10, 991.
- [120] C. Kokotidou, S. V. R. Jonnalagadda, A. A. Orr, G. Vrentzos, A. Kretsovali, P. Tamamis, A. Mitraki, *Biomolecules* **2020**, 10, 1.
- [121] R. S. Jacob, E. George, P. K. Singh, S. Salot, A. Anoop, N. N. Jha, S. Sen, S. K. Maji, *J. Biol. Chem.* **2016**, 291, 5278.
- [122] A. Piscitelli, P. Cicatiello, A. M. Gravagnuolo, I. Sorrentino, C. Pezzella, P. Giardina, *Biomolecules* **2017**, 7.
- [123] M. I. Janssen, M. B. M. Van Leeuwen, T. G. Van Kooten, J. De Vries, L. Dijkhuizen, H. A. B. Wösten, *Biomaterials* **2004**, 25, 2731.
- [124] Y. Huang, S. Zhang, B. Niu, D. Wang, Z. Wang, S. Feng, H. Xu, D. Kong, M. Qiao, *Colloids Surfaces B Biointerfaces* **2013**, 101, 361.



- [125] N. P. Reynolds, M. Charnley, R. Mezzenga, P. G. Hartley, *Biomacromolecules* **2014**, *15*, 599.
- [126] C.-O. P. N. as G. S. for R. of P. N. Schilling, T. Mack, S. Lickfett, S. Sieste, F. S. Ruggeri, T. Sneideris, A. Dutta, T. Bereau, R. Naraghi, D. Sinske, T. P. J. Knowles, C. V. Synatschke, T. Weil, B. Knöll, *Adv. Funct. Mater.* **2019**, *29*, 1.
- [127] S. L. Gras, A. K. Tickler, A. M. Squires, G. L. Devlin, M. A. Horton, C. M. Dobson, C. E. MacPhee, *Biomaterials* **2008**, *29*, 1553.
- [128] N. P. Reynolds, K. E. Styan, C. D. Easton, Y. Li, L. Waddington, C. Lara, J. S. Forsythe, R. Mezzenga, P. G. Hartley, B. W. Muir, *Biomacromolecules* **2013**, *14*, 2305.
- [129] S. Kasai, Y. Ohga, M. Mochizuki, N. Nishi, Y. Kadoya, M. Nomizu, *Biopolymers* **2004**, *76*, 27.
- [130] N. P. Reynolds, K. E. Styan, C. D. Easton, Y. Li, L. Waddington, C. Lara, J. S. Forsythe, R. Mezzenga, P. G. Hartley, B. W. Muir, *Biomacromolecules* **2013**, *14*, 2305.
- [131] N. P. Reynolds, M. Charnley, M. N. Bongiovanni, P. G. Hartley, S. L. Gras, *Biomacromolecules* **2015**, *16*, 1556.
- [132] F. Katagiri, K. Takeyama, Y. Ohga, K. Hozumi, Y. Kikkawa, Y. Kadoya, M. Nomizu, *Biochemistry* **2010**, *49*, 5909.
- [133] N. P. Reynolds, M. Charnley, M. N. Bongiovanni, P. G. Hartley, S. L. Gras, *Biomacromolecules* **2015**, *16*, 1556.
- [134] Y. Huang, S. Zhang, B. Niu, D. Wang, Z. Wang, S. Feng, H. Xu, D. Kong, M. Qiao, *Colloids Surfaces B Biointerfaces* **2013**, *101*, 361.
- [135] M. Zhang, Z. Wang, Z. Wang, S. Feng, H. Xu, Q. Zhao, S. Wang, J. Fang, M. Qiao, D. Kong, *Colloids Surfaces B Biointerfaces* **2011**, *85*, 32.
- [136] S. R. Ball, C. L. L. Pham, V. Lo, V. K. Morris, A. H. Kwan, M. Sunde, .
- [137] T. Jin, M. Peydayesh, M. Li, Y. Yao, D. Wu, R. Mezzenga, *Adv. Mater.* **2022**, *34*, 2205072.
- [138] W. Van der Vegt, H. C. Van der Mei, H. A. B. Wosten, J. G. H. Wessels, H. J. Busscher, *Biophys. Chem.* **1996**, *57*, 253.
- [139] K. Wang, Q. Zhang, L. Zhao, Y. Pan, T. Wang, D. Zhi, S. Ma, P. Zhang, T. Zhao, S. Zhang, W. Li, M. Zhu, Y. Zhu, J. Zhang, M. Qiao, D. Kong, **2017**.
- [140] F. Katagiri, Y. Ohga, K. Takeyama, K. Hozumi, Y. Kikkawa, Y. Kadoya, M. Nomizu, *Arch. Biochem. Biophys.* **2010**, *500*, 189.
- [141] F. Katagiri, K. Takeyama, K. Hozumi, Y. Kikkawa, M. Nomizu, *Biochemistry* **2012**, *51*, 8218.
- [142] D. Schütz, S. Rode, C. Read, J. A. Müller, B. Glocker, K. M. J. Sparrer, O. T. Fackler, P. Walther, J. Münch, *Adv. Funct. Mater.* **2021**, *31*, 2104814.
- [143] R. S. Jacob, S. Das, N. Singh, K. Patel, D. Datta, S. Sen, S. K. Maji, *Adv. Exp. Med. Biol.* **2018**, *1112*, 79.

- [144] M. N. Bongiovanni, D. B. Scanlon, S. L. Gras, *Biomaterials* **2011**, 32, 6099.
- [145] A. T. Petkova, R. D. Leapman, Z. Guo, W. M. Yau, M. P. Mattson, R. Tycko, *Science (80-. )*. **2005**, 307, 262.
- [146] A.-M. Fernandez-Escamilla, F. Rousseau, J. Schymkowitz, L. Serrano, *Nat. Biotechnol.* **2004**, 22.
- [147] F. Katagiri, K. Takeyama, Y. Ohga, K. Hozumi, Y. Kikkawa, Y. Kadoya, M. Nomizu, *Biochemistry* **2010**, 49, 5909.
- [148] F. Katagiri, K. Takeyama, K. Hozumi, Y. Kikkawa, M. Nomizu, *Biochemistry* **2012**, 51, 8218.
- [149] F. S. Ruggeri, J. Adamcik, J. S. Jeong, H. A. Lashuel, R. Mezzenga, G. Dietler, .
- [150] N. Kol, L. Adler-Abramovich, D. Barlam, R. Z. Shneck, E. Gazit, I. Rousso, *Nano Lett.* **2005**, 5, 1343.
- [151] E. Gazit, *FASEB J.* **2002**, 16, 77.
- [152] I. Cherny, E. Gazit, *Angew. Chemie - Int. Ed.* **2008**, 47, 4062.
- [153] O. S. Makin, E. Atkins, P. Sikorski, J. Johansson, L. C. Serpell, *Proc. Natl. Acad. Sci. U. S. A.* **2005**, 102, 315.
- [154] S. Marchesan, A. V. Vargiu, K. E. Styan, *Molecules* **2015**, 20, 19775.
- [155] D. Martí, E. Mayans, A. M. Gil, A. Díaz, A. I. Jiménez, I. Yousef, I. Keridou, C. Cativiela, J. Puiggali, C. Alemán, *Langmuir* **2018**, 34, 15551.
- [156] H. Zhang, J. Park, Y. Jiang, K. A. Woodrow, *Acta Biomater.* **2017**, 55, 183.
- [157] R. Pérez-Pedroza, A. Ávila-Ramírez, Z. Khan, M. Moretti, C. A. E. Hauser, *Adv. Polym. Technol.* **2021**, 2021.
- [158] N. Nespovitaya, J. Gath, K. Barylyuk, C. Seuring, B. H. Meier, R. Riek, *J. Am. Chem. Soc.* **2016**, 138, 846.
- [159] A. K. Buell, *Chem. Sci.* **2022**.
- [160] F. U. Hartl, M. Hayer-Hartl, *Nat. Struct. Mol. Biol.* **2009**, 16, 574.
- [161] N. P. Reynolds, *Biointerphases* **2019**, 14, 040801.
- [162] M. M. Ouberai, A. L. G. Dos Santos, S. Kinna, S. Madalli, D. C. Hornigold, D. Baker, J. Naylor, L. Sheldrake, D. J. Corkill, J. Hood, P. Vicini, S. Uddin, S. Bishop, P. G. Varley, M. E. Welland, *Nat. Commun.* 2017 81 **2017**, 8, 1.
- [163] P. A. Rühls, J. Adamcik, S. Bolisetty, A. Sánchez-Ferrer, R. Mezzenga, *Soft Matter* **2011**, 7, 3571.
- [164] D. Lin, J. Lei, S. Li, X. Zhou, G. Wei, X. Yang, *J. Phys. Chem. B* **2020**, 124, 3459.
- [165] G. Son, B. Il Lee, Y. J. Chung, C. B. Park, *Acta Biomater.* **2018**, 67, 147.
- [166] K. Siposova, V. I. Petrenko, O. I. Ivankov, A. Musatov, L. A. Bulavin, M. V.

- Avdeev, O. A. Kyzyma, *ACS Appl. Mater. Interfaces* **2020**, *12*, 32410.
- [167] S. Xiang, J. Wagner, T. Lückerrath, K. Müllen, D. Y. W. Ng, J. Hedrich, T. Weil, *Adv. Healthc. Mater.* **2021**, 2101854.
- [168] N. A. Mavlankar, A. K. Awasthi, J. Ralhan, A. Pal, *ChemNanoMat* **2022**, *n/a*, e202200368.
- [169] J. Gombos, L. Balejčikova, P. Kopcansky, M. Batkova, K. Siposova, J. Kovac, K. Zolochevska, I. Safarik, A. Lokajova, V. M. Garamus, D. Dobrota, O. Strbak, **2022**.
- [170] P. Arosio, T. C. T. Michaels, S. Linse, C. Månsson, C. Emanuelsson, J. Presto, J. Johansson, M. Vendruscolo, C. M. Dobson, T. P. J. Knowles, *Nat. Commun.* **2016**, *7*, 10948.
- [171] A. Franco, P. Gracia, A. Colom, J. D. Camino, J. Á. Fernández-Higuero, N. Orozco, A. Dulebo, L. Saiz, N. Cremades, J. M. G. Vilar, A. Prado, A. Muga, *Proc. Natl. Acad. Sci.* **2021**, *118*, e2105548118.
- [172] M. M. Schneider, S. Gautam, T. W. Herling, E. Andrzejewska, G. Krainer, A. M. Miller, V. A. Trinkaus, Q. A. E. Peter, F. S. Ruggeri, M. Vendruscolo, A. Bracher, C. M. Dobson, F. U. Hartl, T. P. J. Knowles, *Nat. Commun.* **2021**, *12*, 5999.
- [173] A. Franco, L. Velasco-Carneros, N. Alvarez, N. Orozco, F. Moro, A. Prado, A. Muga, *Cells* **2021**, *10*, 2745.
- [174] K. M. Galler, L. Aulisa, K. R. Regan, R. N. D'Souza, J. D. Hartgerink, *J. Am. Chem. Soc.* **2010**, *132*, 3217.
- [175] S. Chagri, D. Y. W. Ng, T. Weil, *Nat. Rev. Chem.* **2022**, *6*, 320.
- [176] J. Herzberger, K. Fischer, D. Leibig, M. Bros, R. Thiermann, H. Frey, *J. Am. Chem. Soc.* **2016**, *138*, 9212.
- [177] D. Spitzer, L. L. Rodrigues, D. Straßburger, M. Mezger, P. Besenius, *Angew. Chemie Int. Ed.* **2017**, *56*, 15461.
- [178] C. M. Berac, L. Zengerling, D. Straßburger, R. Otter, M. Urschbach, P. Besenius, *Macromol. Rapid Commun.* **2020**, *41*, e1900476.
- [179] P. P. Yang, Q. Luo, G. Bin Qi, Y. J. Gao, B. N. Li, J. P. Zhang, L. Wang, H. Wang, *Adv. Mater.* **2017**, *29*.
- [180] Y. Sohma, T. Yoshiya, A. Taniguchi, T. Kimura, Y. Hayashi, Y. Kiso, *Pept. Sci.* **2007**, *88*, 253.
- [181] Y. Sohma, T. Yoshiya, A. Taniguchi, T. Kimura, Y. Hayashi, Y. Kiso, *Pept. Sci.* **2007**, *88*, 253.
- [182] A. Taniguchi, Y. Sohma, M. Kimura, T. Okada, K. Ikeda, Y. Hayashi, T. Kimura, S. Hirota, K. Matsuzaki, Y. Kiso, *J. Am. Chem. Soc.* **2006**, *128*, 696.
- [183] M. Pieszka, S. Han, C. Volkmann, R. Graf, I. Lieberwirth, K. Landfester, D. Y. W. Ng, T. Weil, *J. Am. Chem. Soc.* **2020**, *142*, 15780.
- [184] A. Taniguchi, M. Skwarczynski, Y. Sohma, T. Okada, K. Ikeda, H. Prakash, H.

- Mukai, Y. Hayashi, T. Kimura, S. Hirota, K. Matsuzaki, Y. Kiso, *ChemBioChem* **2008**, *9*, 3055.
- [185] P. Roth, R. Meyer, I. Harley, K. Landfester, I. Lieberwirth, M. Wagner, D. Y. W. Ng, T. Weil, **2023**.
- [186] A. Taniguchi, M. Skwarczynski, Y. Sohma, T. Okada, K. Ikeda, H. Prakash, H. Mukai, Y. Hayashi, T. Kimura, S. Hirota, K. Matsuzaki, Y. Kiso, *ChemBioChem* **2008**, *9*, 3055.
- [187] S. Sur, J. B. Matson, M. J. Webber, C. J. Newcomb, S. I. Stupp, *ACS Nano* **2012**, *6*, 10776.
- [188] A. Romano, I. Roppolo, E. Rossegger, S. Schlögl, M. Sangermano, *Materials (Basel)*. **2020**, *13*, 1.
- [189] A. Romano, I. Roppolo, M. Giebler, K. Dietliker, Možina, P. Šket, I. Mühlbacher, S. Schlögl, M. Sangermano, *RSC Adv.* **2018**, *8*, 41904.
- [190] A. P. Pelliccioli, J. Wirz, **2002**.
- [191] V. Peddie, A. D. Abell, *J. Photochem. Photobiol. C Photochem. Rev.* **2019**, *40*, 1.
- [192] A. A. Deeg, T. E. Schrader, S. Kempter, J. Pfizer, L. Moroder, W. Zinth, *ChemPhysChem* **2011**, *12*, 559.
- [193] L. Awad, N. Jejelava, R. Burai, H. A. Lashuel, *ChemBioChem* **2016**, *17*, 2353.
- [194] T. J. Measey, F. Gai, *Langmuir* **2012**, *28*, 12588.
- [195] C. J. Bosques, B. Imperiali, *J. Am. Chem. Soc.* **2003**, *125*, 7530.
- [196] J. T. Meijer, M. J. A. G. Henckens, I. J. Minten, D. W. P. M. Löwik, J. C. M. Van Hest, *Soft Matter* **2007**, *3*, 1135.
- [197] D. W. P. M. Löwik, J. T. Meijer, I. J. Minten, H. van Kalkeren, L. Heckenmüller, I. Schulten, K. Sliepen, P. Smittenaar, J. C. M. van Hest, *J. Pept. Sci. an Off. Publ. Eur. Pept. Soc.* **2008**, *14*, 127.
- [198] L. A. Haines, K. Rajagopal, B. Ozbas, D. A. Salick, D. J. Pochan, J. P. Schneider, *J. Am. Chem. Soc.* **2005**, *127*, 17025.
- [199] J. T. Meijer, M. Roeters, V. Viola, D. W. P. M. Löwik, G. Vriend, J. C. M. van Hest, *Langmuir* **2007**, *23*, 2058.
- [200] W. Kim, M. H. Hecht, *Proc. Natl. Acad. Sci.* **2006**, *103*, 15824.
- [201] S. Abdelrahman, M. Alghrably, J. I. Lachowicz, A. H. Emwas, C. A. E. Hauser, M. Jaremko, *Molecules* **2020**, *25*, 1.
- [202] K. Sato, M. P. Hendricks, L. C. Palmer, S. I. Stupp, *Chem. Soc. Rev.* **2018**, *47*, 7539.
- [203] A. K. Das, P. K. Gavel, *Soft Matter* **2020**, *16*, 10065.
- [204] P. R. Jadhav, H. Agersø, C. W. Tornøe, J. V. S. Gobburu, *J. Pharmacokinet. Pharmacodyn.* **2006**, *33*, 609.

- [205] S. K. Maji, D. Schubert, C. Rivier, S. Lee, J. E. Rivier, R. Riek, .
- [206] G. Bin Qi, Y. J. Gao, L. Wang, H. Wang, *Adv. Mater.* **2018**, 30.
- [207] L. Lei, Z. Xu, X. Hu, Y. Lai, J. Xu, B. Hou, Y. Wang, H. Yu, Y. Tian, W. Zhang, *Small* **2019**, 15, 1.
- [208] C. Ren, Z. Wang, Q. Wang, C. Yang, J. Liu, *Small Methods* **2020**, 4, 1.
- [209] D.-B. Cheng, D. Wang, Y.-J. Gao, L. Wang, Z.-Y. Qiao, H. Wang, *J. Am. Chem. Soc.* **2019**, 141, 4406.
- [210] A. G. Cheetham, P. Zhang, Y. Lin, L. L. Lock, H. Cui, *J. Am. Chem. Soc.* **2013**, 135, 2907.
- [211] D. B. Cheng, X. H. Zhang, Y. J. Gao, D. Wang, L. Wang, H. Chen, Z. Y. Qiao, H. Wang, *Small* **2019**, 15, 1.
- [212] X.-H. Zhang, D.-B. Cheng, L. Ji, H.-W. An, D. Wang, Z.-X. Yang, H. Chen, Z.-Y. Qiao, H. Wang, *Nano Lett.* **2020**, 20, 1286.
- [213] D.-B. Cheng, X.-H. Zhang, Y.-J. Gao, L. Ji, D. Hou, Z. Wang, W. Xu, Z.-Y. Qiao, H. Wang, *J. Am. Chem. Soc.* **2019**, 141, 7235.
- [214] S. Sun, H.-W. Liang, H. Wang, Q. Zou, *ACS Nano* **2022**, 16, 18978.
- [215] D.-B. Cheng, D. Wang, Y.-J. Gao, L. Wang, Z.-Y. Qiao, H. Wang, *J. Am. Chem. Soc.* **2019**, 141, 4406.
- [216] X.-H. Zhang, D.-B. Cheng, L. Ji, H.-W. An, D. Wang, Z.-X. Yang, H. Chen, Z.-Y. Qiao, H. Wang, *Nano Lett.* **2020**, 20, 1286.
- [217] D.-B. Cheng, X.-H. Zhang, Y.-J. Gao, L. Ji, D. Hou, Z. Wang, W. Xu, Z.-Y. Qiao, H. Wang, *J. Am. Chem. Soc.* **2019**, 141, 7235.
- [218] S. Sun, H.-W. Liang, H. Wang, Q. Zou, *ACS Nano* **2022**, 16, 18978.
- [219] D. Schütz, S. Rode, C. Read, J. A. Müller, B. Glocker, K. M. J. Sparrer, O. T. Fackler, P. Walther, J. Münch, *Adv. Funct. Mater.* **2021**, 31, 2104814.
- [220] M. Yolamanova, C. Meier, A. K. Shaytan, V. Vas, C. W. Bertoncini, F. Arnold, O. Zirafi, S. M. Usmani, J. A. Müller, D. Sauter, C. Goffinet, D. Palesch, P. Walther, N. R. Roan, H. Geiger, O. Lunov, T. Simmet, J. Bohne, H. Schrezenmeier, K. Schwarz, L. Ständker, W.-G. Forssmann, X. Salvatella, P. G. Khalatur, A. R. Khokhlov, T. P. J. Knowles, T. Weil, F. Kirchhoff, J. Münch, *Nat. Nanotechnol.* **2013**, 8, 130.
- [221] C. Meier, T. Weil, F. Kirchhoff, J. Münch, *Wiley Interdiscip. Rev. Nanomed. Nanobiotechnol.* **2014**, 6, 438.
- [222] J. Münch, E. Rücker, L. Ständker, K. Adermann, C. Goffinet, M. Schindler, S. Wildum, R. Chinnadurai, D. Rajan, A. Specht, G. Giménez-Gallego, P. C. Sánchez, D. M. Fowler, A. Koulov, J. W. Kelly, W. Mothes, J.-C. Grivel, L. Margolis, O. T. Keppler, W.-G. Forssmann, F. Kirchhoff, *Cell* **2007**, 131, 1059.
- [223] D. Schütz, C. Read, R. Groß, A. Röcker, S. Rode, K. Annamalai, M. Fändrich, J. Münch, *ACS Omega* **2021**, 6, 7731.

- [224] C. J. Esdaille, K. S. Washington, & Cato, T. Laurencin, .
- [225] D. Ricci, M.-Y. Lee, R. M. Owens, C.-M. Moysidou, C. Barberio, **2021**, 8, 620962.
- [226] J. D. Tang, C. Mura, K. J. Lampe, *J. Am. Chem. Soc.* **2019**, 141, 4886.
- [227] Q. Xuan, Y. Wang, C. Chen, P. Wang, *Front. Bioeng. Biotechnol.* **2021**, 9, 1.
- [228] S. Das, K. Zhou, D. Ghosh, N. N. Jha, P. K. Singh, R. S. Jacob, C. C. Bernard, D. I. Finkelstein, J. S. Forsythe, S. K. Maji, *NPG Asia Mater.* **2016**, 8, 304.
- [229] J. Kisiday, M. Jin, B. Kurz, H. Hung, C. Semino, S. Zhang, A. J. Grodzinsky, *Proc. Natl. Acad. Sci. U. S. A.* **2002**, 99, 9996.
- [230] A. Basu, K. R. Kunduru, S. Doppalapudi, A. J. Domb, W. Khan, *Adv. Drug Deliv. Rev.* **2016**, 107, 192.
- [231] H. Yan, A. Saiani, J. E. Gough, A. F. Miller, *Biomacromolecules* **2006**, 7, 2776.
- [232] L. Yang, H. Li, L. Yao, Y. Yu, G. Ma, **2019**, 14, 36.
- [233] S. Bolisetty, L. Harnau, J. Jung, R. Mezzenga, *Biomacromolecules* **2012**, 13, 3241.
- [234] R. S. Jacob, D. Ghosh, P. K. Singh, S. K. Basu, N. N. Jha, S. Das, P. K. Sukul, S. Patil, S. Sathaye, A. Kumar, A. Chowdhury, S. Malik, S. Sen, S. K. Maji, *Biomaterials* **2015**, 54, 97.
- [235] B. Hu, Y. Shen, J. Adamcik, P. Fischer, M. Schneider, M. J. Loessner, R. Mezzenga, *ACS Nano* **2018**, 12, 3385.
- [236] M. R. Caplan, E. M. Schwartzfarb, S. Zhang, R. D. Kamm, D. A. Lauffenburger, *Biomaterials* **2002**, 23, 219.
- [237] O. V Galzitskaya, O. M. Selivanova, E. Y. Gorbunova, L. G. Mustaeva, V. N. Azev, A. K. Surin, **2021**.
- [238] K. Medini, B. W. Mansel, M. A. K. Williams, M. A. Brimble, D. E. Williams, J. A. Gerrard, *Acta Biomater.* **2016**, 43, 30.
- [239] A. Mahler, M. Rechtes, M. Rechter, S. Cohen, E. Gazit, *Adv. Mater.* **2006**, 18, 1365.
- [240] A. M. Smith, R. J. Williams, C. Tang, P. Coppo, R. F. Collins, M. L. Turner, A. Saiani, R. V. Ulijn, *Adv. Mater.* **2008**, 20, 37.
- [241] V. Jayawarna, M. Ali, T. A. Jowitt, A. F. Miller, A. Saiani, J. E. Gough, R. V. Ulijn, *Adv. Mater.* **2006**, 18, 611.
- [242] K. J. Skilling, F. Citossi, T. D. Bradshaw, M. Ashford, B. Kellam, M. Marlow, *Soft Matter* **2014**, 10, 237.
- [243] R. S. Jacob, D. Ghosh, P. K. Singh, S. K. Basu, N. N. Jha, S. Das, P. K. Sukul, S. Patil, S. Sathaye, A. Kumar, A. Chowdhury, S. Malik, S. Sen, S. K. Maji, *Biomaterials* **2015**, 54, 97.
- [244] X. Zhan, D. M. Desiderio, *Int. J. Mass Spectrom.* **2009**, 287, 77.

- [245] A. Barth, J. E. T. Corrie, M. J. Gradwell, Y. Maeda, W. Mäntele, T. Meier, D. R. Trentham, *J. Am. Chem. Soc.* **1997**, *119*, 4149.
- [246] A. Resemann, L. Liu-Shin, G. Tremintin, A. Malhotra, A. Fung, F. Wang, G. Ratnaswamy, D. Suckau, *MAbs* **2018**, *10*, 1200.

## 2. Motivation, Aims and Conceptual Design

Self-assembling amyloid-like materials, which are formed through supramolecular rearrangement under mild conditions into a typical fibrillar morphology exhibit numerous features such as high rigidity, biocompatibility and -degradability, improved blood circulation and ability to promote cell-attachment and growth without showing cell toxicity towards a variety of cell types. These characteristics make amyloid-like materials outstanding against other synthetic literature-known nanomaterials and emphasizes their importance as supramolecular nanostructures in numerous biomedical applications such as viral gene transduction, drug delivery and regenerative medicine. On the other hand, amyloids are also associated with neurodegenerative disorders, which indicates a huge diversity in amyloid activity towards the living organism. Hence, in the process of the establishment of amyloid-like scaffolds for biomedical purposes, requirements of the materials characteristics must be fulfilled. Here, the amyloid-like material needs to display 1) rapid self-assembly, which prevents the occurrence of pathological oligomers, 2) highly rigid fibrillar morphology given by a high  $\beta$ -sheet content that enhances the cells-supportive character and 3) an external regulation of the supramolecular structure that allows the development of a specific cell response. All these criteria can be covered by rational-sequence design of amyloid-forming peptide sequences, which offers the opportunity for the creation of highly controlled amyloidogenic platforms capable of cell function determination. Here, simple synthesis and functionalization techniques of peptidic structures and the already given knowledge of amyloidogenic peptide self-assembly open new possibilities for the sequential design of scaffolds physico-chemical and topographical characteristics, which can be customized to the desired application.

To expand the scope of applicability of amyloid-like nanofibrils as scaffolds in medical applications such as tissue engineering or drug delivery, the superior objective of this work was the investigation of amyloidogenic sequences with controllable physico-chemical and topographical features and subsequently using them for the creation of a platform capable of controlling cell reactions. To gain controlled physico-chemical characteristics of amyloid-like material the usage of rational sequence design was targeted, which allowed the creation of amyloid-like structures with incorporated motives that were sensitive to external triggers. Next, the creation of patterns and gradients was used to achieve a macroscopic readout of cell-material interactions.



Here, different coating strategies, photo- patterning and gradient- formation techniques were used. Detailed motivation, aims and conceptual design of all three projects are stated in the following sections and illustrated in the subsequent Figure 16.

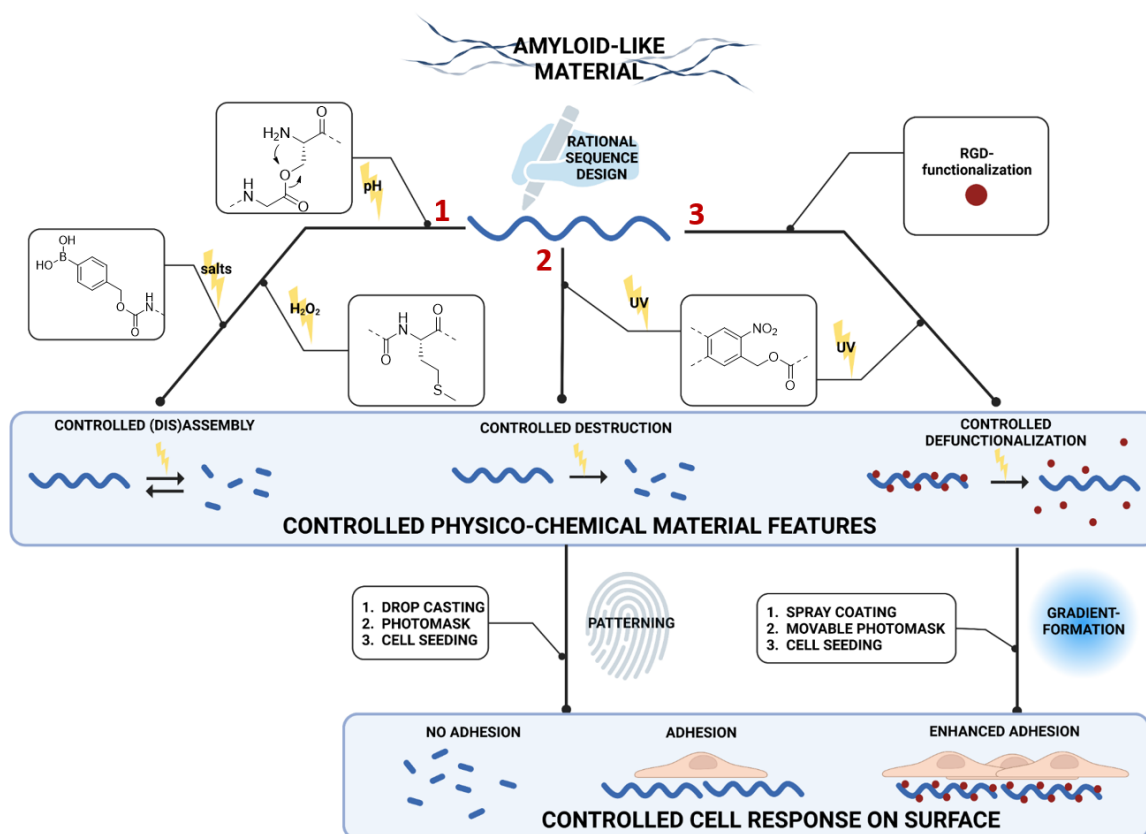


Figure 16: Illustration of the conceptual design of this work with objectives (blue boxes) and used strategies like rational sequence design, patterning and gradient formation. The illustration is divided into 3 project paths marked with red numbers 1, 2 and 3.

Controlled degradation of a scaffold is a prerequisite in tissue engineering as it leads to regulated exchange of the scaffold with regenerated tissue. Here, the regulated degradation of amyloids superstructure provides control over their intrinsic bioactivity, which contributes to achieve predetermined cell-reactions. Hence, the primary goal for the first two projects was the control over amyloids assembly and disassembly/destruction to achieve regulated cell-attachment. To examine the possibilities over controlled assembly and disassembly of amyloid-like peptides, the first project implemented rational molecular design of peptide sequence as the strategy of choice. Hence, the design of an amyloid-forming sequence was targeted with inserted chemical tools, which acted as orthogonal triggers that signaled the self-assembly and disassembly in solution. The use of the amino acid methionine, the so-

called depsi-peptide as well as a carbamate caging group in the peptide sequence was analyzed with regard to amyloids morphology changes *via* activation of specific stimuli like oxidation, pH or hydrolysis. Here, the amyloids secondary structure as well as the morphological changes before and after stimulus application in solution were explored (chapter 3).

The creation of spatiotemporal controlled cell-attachment in the form of patterns is of great importance, for example for the fabrication of bioactive materials in the research field of tissue engineering. It can mimic the natural cell distribution and allows the study of cell migration and communication. Consequently, the goal of the second project was the control over cell-material interactions with a resulting cell growth on predetermined surface areas elicited by the control over the amyloid-fiber destruction. In comparison to the first project, light was used as an external trigger as it gives the possibility to develop the designed platform from solution into the second dimension. Therefore, a new design of an amyloid-forming sequence with an incorporated *o*-Nitrobenzyl group for the controlled light driven fibril destruction was aimed. Along with the destruction of fibrils secondary structure comes the erasing of fibrils bioactivity, which offers the occasion of spatiotemporal controlled cell-attachment on surfaces. This newly designed peptide, its amyloid-like character and morphology with and without the effect of the external stimulus was explored. By transferring the fibrils on a surface and illuminating them through a photomask a patterning of destroyed and preserved fibrils was expected. Here, the effect of the fibril patterns towards cells was examined (chapter 4).

Immobilized gradients of bioactive molecules are highly valued in the environment of the ECM as they are the driving force for several biochemical processes like vascularization, tissue regeneration or immune responses. The in previous project described photo-driven system gave a great opportunity for precise surface patterning by switching the bioactivity on and off. Consequently, the third project showcased its ability to create gradual changes in bioactivity on surfaces with its corresponding cell response. Hence, the design of an amyloid-like fibril forming sequence with a bioactive epitope functionalization *via* a photocleavable linker was applied to study the gradual distribution of regulatory signals on surfaces. Here, the corresponding changes in bioactivity were given by the controlled abstraction of an RGD epitope whereas the scaffold remained unaffected by the external trigger light. Therefore, the fibrils

morphology and secondary structure with and without the influence of the external stimulus were investigated. Furthermore, after applying fibrils on surfaces and processing with the external stimulus a molecular as well as a scaffold gradient on centimeter-landscape was investigated and the effect of the gradual distribution of the bioactive signal towards cells was studied (chapter 5).

Thus, this work could contribute to fundamental understanding of how to influence amyloid self-assembly in order to enable the determination of cell-amyloid interactions and consequently the control over cell behavior. These achievements are essential for biomedical applications like tissue engineering.

### 3. Orthogonally Stimulated Assembly/Disassembly of Depsipeptides by Rational Chemical Design

[REDACTED]

---

[a] [REDACTED]

[b] [REDACTED]

#### Copyright:

Published in ChemBioChem 2019, 20, 1376

The following part is reproduced with permission from John Wiley and Sons.

#### 3.1. Contributions

In this project, I performed the synthesis, purification and characterization of the boronic acid depsipeptide (compound 5), which was partly done during the master thesis as well as during the PhD. The design and development of compound 5 and the oxidized peptide was done by [REDACTED]. She synthesized most of the materials, conducting physicochemical characterization and designed, planned and performed the most experiments including the scientific evaluation of results. She also wrote parts of the manuscripts including figures preparation. [REDACTED] designed, developed, prepared and provided the linear amino acid sequence KIKISQINM. She also provided the depsipeptide version of it and was involved in scientific discussions. [REDACTED] acquired funding for this project, designed and supervised the experiments, was involved in scientific discussions and wrote parts of the manuscript. [REDACTED] designed and supervised experiments, was involved in scientific discussions and wrote the manuscript.

## 3.2. Abstract

Controlling the assembly and disassembly of cross- $\beta$ -sheet-forming peptides is one of the predominant challenges for this class of supramolecular material. As they constitute a continuously propagating material, every atomic change can be exploited to bring about distinct responses at the architectural level. We report herein that, by using rational chemical design, serine and methionine can both be used as orthogonal chemical triggers to signal assembly/disassembly through their corresponding stimuli. Serine is used to construct an ester-bond oligopeptide that can undergo *O,N*-acyl rearrangement, whereas methionine is sensitive to oxidation by  $\text{H}_2\text{O}_2$ . Using the example peptide sequence, KIKISQINM, we demonstrate that assembly and disassembly can be independently controlled on demand.

## 3.3. Results and Discussion

The molecular ordering of small molecules formed by regular and precise intermolecular forces represents one of the leading principles of supramolecular material synthesis.<sup>[1]</sup> Programmed through molecular design, these interactions involve a selection of hydrogen bonds,  $\pi$ -stacks, Van der Waals and electrostatic forces in which the self-association of the molecules is often a thermodynamic minimum.<sup>[1]</sup> Coupled with the release of solvent molecules, the assembly is also driven entropically and hence derives its innate sensitivity towards both temperature and concentration of the monomers.<sup>[2]</sup> Due to these various parameters that can all affect self-assembly, it can often be a challenge to exert direct control over the kinetics and responsiveness of superstructure formation.

Among different self-assembling systems, the cross- $\beta$ -sheet arrangement of many peptides forming so-called amyloid structures has emerged a major class of nanomaterials with several unique features. Amyloid structures are often associated with severe neurodegenerative disorders such as Alzheimer's disease.<sup>[3]</sup> The propagation of the disease stems from several known oligopeptide sequences that exhibit a very strong tendency to form cross- $\beta$ -sheets that subsequently assemble into hierarchical fibrillary networks.<sup>[4]</sup> While the accumulation of these fibrils into larger aggregates can be detrimental towards neurons, they have been exploited as

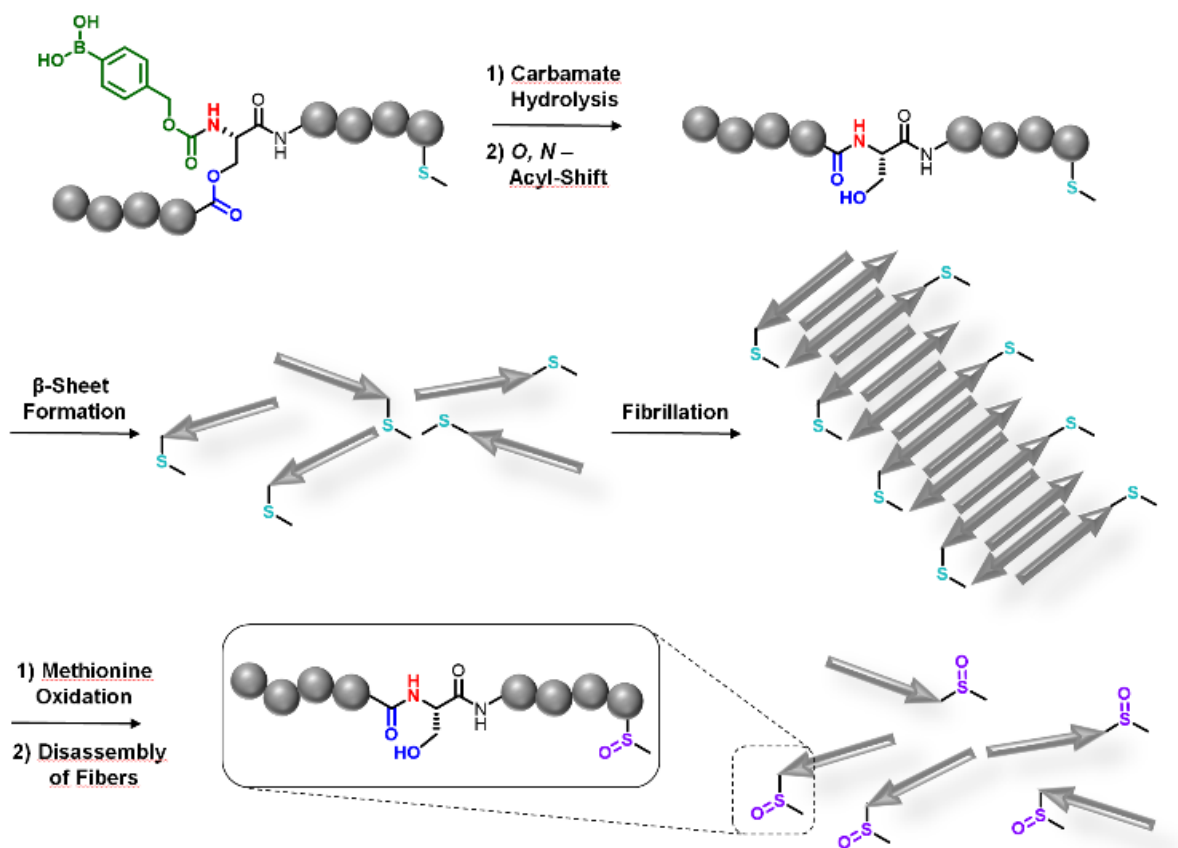


Figure 1. Chemical design and structure of a depsi-oligopeptide controlled by a boronic acid carbamate bond. The carbamate and methionine provide the two orthogonal stimuli.

excellent molecular support in both nano and bulk materials, especially targeted towards biomedical applications.<sup>[3, 5]</sup>

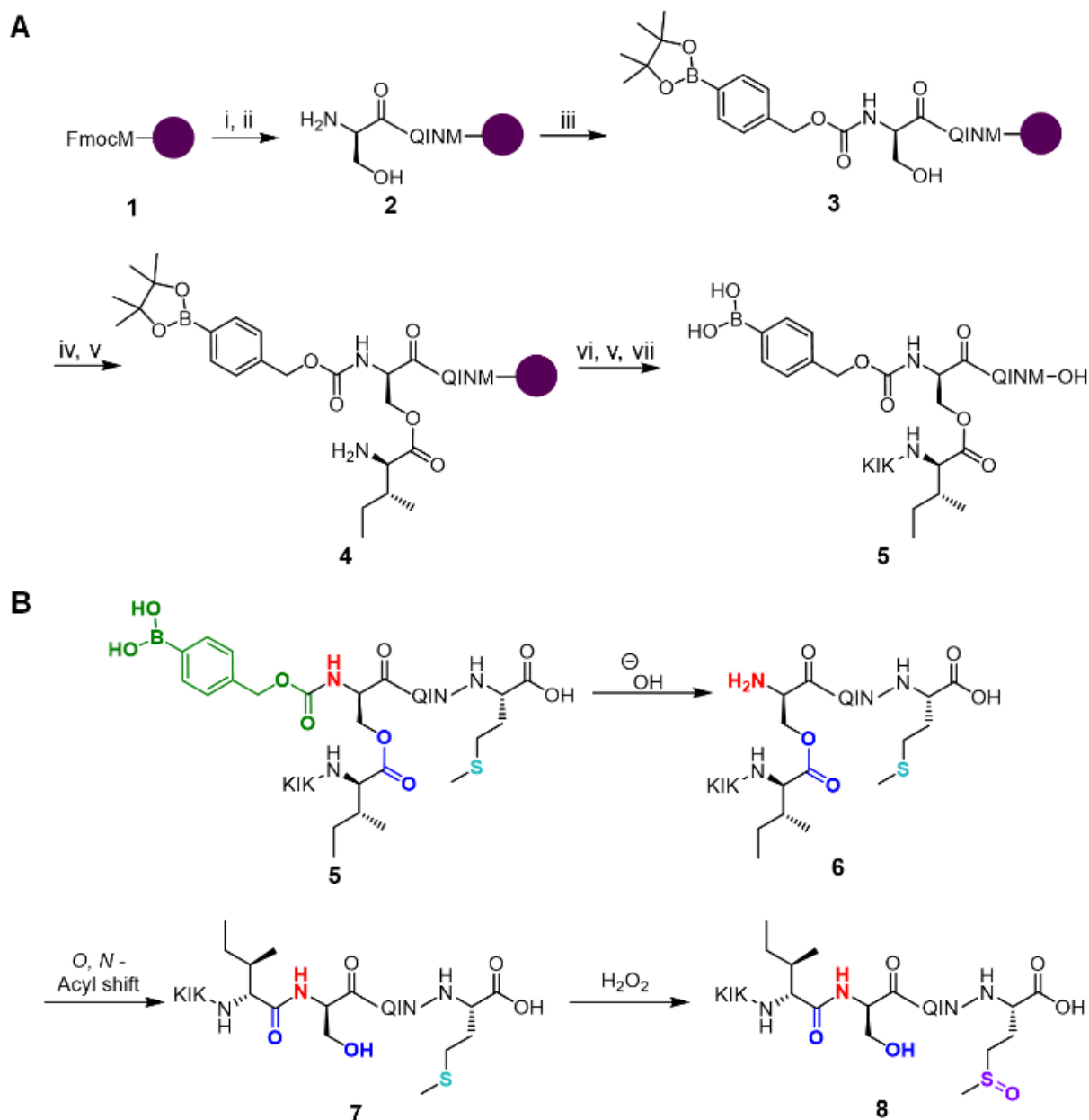
Nonetheless, the processability as well as temporal control over the self-assembly and disassembly of amyloid-like peptides are prominent limitations for use in vivo. Hence, significant efforts have been directed towards the design of oligopeptides to allow a higher level of control towards  $\beta$ -sheet formation.<sup>[6]</sup> Hydrophilic amino acid residues within the sequence such as lysines or glutamic acids can be leveraged to promote or inhibit intermolecular interactions depending on their protonation state.<sup>[7]</sup> On the other hand, depsi-peptides, where a serine residue within the peptide sequence is connected via an ester bond instead, have shown exceptional promise for amyloid fibril formation by an external pH stimulus.<sup>[8]</sup>

Specifically, depsi peptides were originally developed to alleviate solubility issues with ultra-long peptides by providing a kink into the otherwise linear structure.<sup>[9]</sup> This kink, caused by the ester-linked serine residue, would undergo an 5-membered *O,N*-acyl shift due to the higher nucleophilicity of the free amine upon deprotection to furnish

the designated peptide. Hence, depending on the mechanism to release the free amine, we envisioned that the *O,N*-acyl shift can be controlled covalently on demand.

On the other hand, the disassembly of amyloids is likewise a concern for the development of biomaterials, especially for use in vivo.<sup>[10]</sup> The degradation of these systems is essential for its extrusion once its designated purpose has been achieved. However, due to its thermodynamic stability, the disassembly of typical amyloids under physiological conditions are highly unfavourable as they are widely known to be heat and proteolytically resistant.<sup>[11]</sup>

In this respect, we demonstrate that orthogonal chemical triggers can be rationally designed and incorporated within an oligopeptide such that the controlled assembly/disassembly can be controlled independently by external stimuli (Figure 1).



Scheme 1. A) Microwave assisted solid phase peptide synthesis of the target boronic acid caged depsi-peptide 5. B) Mechanism of stimulus responsive *O,N*-acyl rearrangement of 5 and subsequent oxidation of methionine.

We introduce a depsi-peptide sequence containing a boronic acid-carbamate bond caging the amine of the serine. The self-assembling sequence of the oligopeptide contains a methionine residue in which its thioether motif directly imparts sensitivity towards local oxidative conditions. Particularly, an oxidative stimulus is attractive as it is well-known that cancer tissues contain a much higher concentration of hydrogen peroxide and various reactive oxygen species.<sup>[12]</sup> By integrating both aspects, the amyloid self-assembly is directly controlled by the cleavage of the carbamate bond



whereas the disassembly is dictated by the oxidation of the methionine at the C-terminus. In addition, the effects of these triggers produce distinct morphological changes that can be visualized by transmission electron microscopy (TEM). In establishing this concept, we anticipate that the methodology would provide an enormous synergy towards existing amyloid based technology ranging from hydrogels<sup>[13]</sup> to drug delivery<sup>[14]</sup> and viral gene transduction.<sup>[5b]</sup>

The synthesis of the oligopeptide takes place on the solid phase directly with Wang resin preloaded with the first amino acid, methionine 1. Standard microwave-assisted peptide synthesis were used to construct the peptide in sequence with asparagine (Asn), isoleucine (Ile) and glutamine (Gln) using double coupling steps. Following which, 9-fluorenylmethyloxycarbamate(Fmoc)-Ser-OH (Scheme 1) was coupled in a single step in order to prevent side reactions with the free hydroxyl group to form 2. Subsequently, the fmoc group was deprotected followed by the installation of the boronic acid-carbamate caging group using 4-nitrophenyl (4-(4,4,5,5-tetramethyl-1,3,2-dioxaborolan-2-yl)benzyl) carbonate with N,N-diisopropylethylamine in DMF at room temperature overnight. The depside-ester bond of the serine was constructed by reacting 3 with Fmoc-Ile-OH, diisopropylcarbodiimide (DIC) and 4-dimethylaminopyridine (DMAP) to afford 4. Thereafter, the coupling of the next three residues, lysine (Lys), isoleucine (Ile) and lysine (Lys) were conducted at room temperature as the carbamate bond is heat sensitive. The cleavage of the peptide, together with complete deprotection, was accomplished using 95% trifluoroacetic acid (TFA), 2.5% TIPS and 2.5% water to afford the target caged-oligopeptide 5.

The responsiveness of the oligopeptide 5 towards the assembly trigger rests upon the

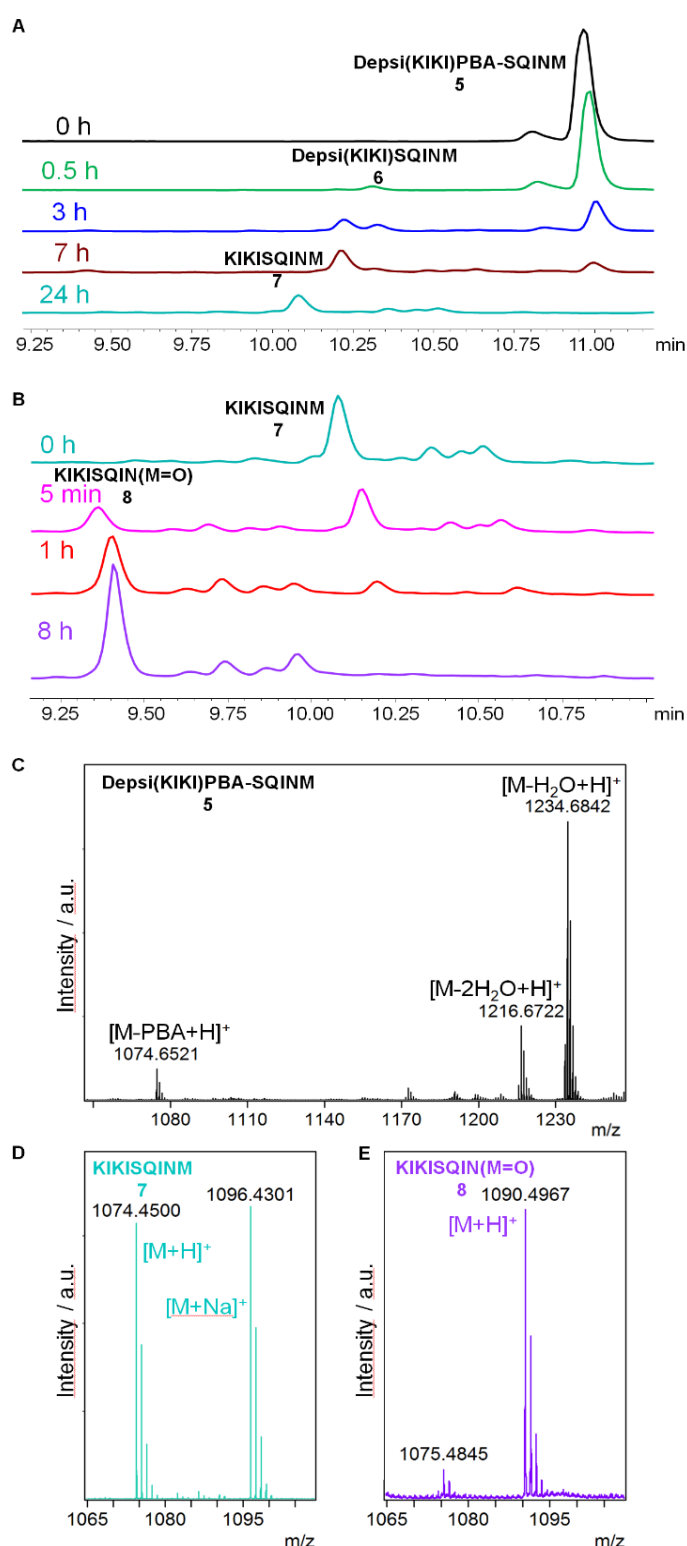


Figure 2. Kinetic profiling of A) Hydrolysis of boronic acid-carbamate 5 with subsequent *O,N*-acyl rearrangement into 7 and B) Oxidation of 7 by  $H_2O_2$ . MALDI-TOF-MS of C) Depsi-peptide 5, D) linearized peptide 7 and E) Oxidation of 7 into 8 by  $H_2O_2$ .

boronic acid-carbamate caging group. Benzylic carbamate bonds are sensitive to hydrolytic conditions and their stability can be tuned over a wide range depending on the aromatic substituents.<sup>[15]</sup> The boronic acid is chosen both as an electron withdrawing group as well as a potential reactive chemical function. Hence, the experiment was designed to monitor the mechanism of bond cleavage by kinetic profiling using analytical HPLC (Figure 2A, Figure S5). We found that the carbamate bond can be cleaved selectively in the presence of kosmotropic agents such as phosphate salts but is stable in pure water alone. In detail, a retention time of 11.0 min was observed for the caged peptide 5. Hydrolysis of the carbamate bond can be gradually observed with time to form the intermediate free depsi-peptide 6 at 10.3 min. It is important to note that the depsi-peptide 6 can be observed to undergo rapid *O,N*-acyl shift to form the linear peptide 7 at 10.2 min. At 24 h, full conversion into the linear peptide

form was attained whereas its formation and spontaneous self-assembly already

occurred after 1 h (Figure S5). In order to confirm these peak assignments, the oligopeptides 6 and 7 were synthesized separately and analyzed as controls in the HPLC (Figure S5).

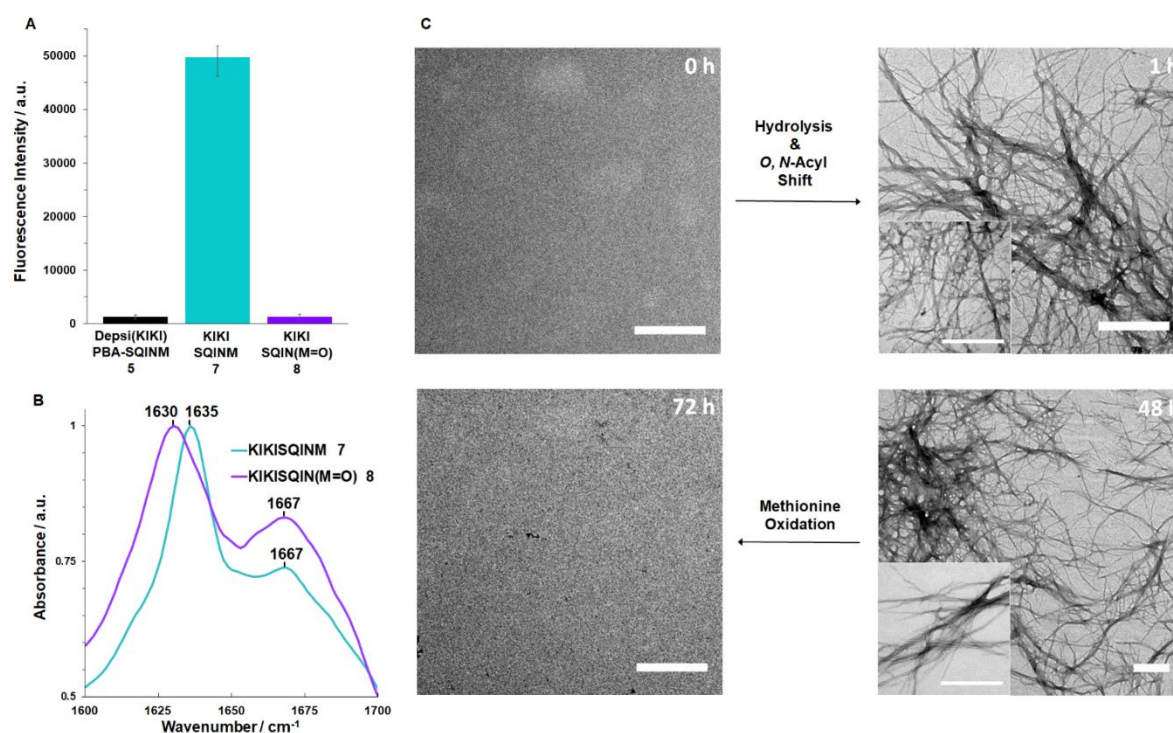


Figure 3. A) Proteostat® assay of depsipeptide 5, hydrolyzed peptide 5 into 7 and oxidized peptide 8. Data represented as mean  $\pm$  SEM,  $n = 4$  B) FTIR spectra of peptide 7 and oxidized peptide 8. C) TEM micrographs of the O,N-Acyl shift triggered fibrillization (top) within 1 h. Complete disassembly of nanofibers by H<sub>2</sub>O<sub>2</sub> oxidation (bottom) over 24 h. Times are represented as cumulative intervals. Scale bar = 500 nm.

In a similar fashion, the disassembly by the oxidation of methionine by applying H<sub>2</sub>O<sub>2</sub> was monitored (Figure 2B, Figure S6). Using the final and linear form of the oligopeptide 7, 100 mM of H<sub>2</sub>O<sub>2</sub> was added. Immediate oxidation of the thioether into a sulfoxide was apparent from the HPLC within 5 min (Figure 2B). A significant shift in the retention time towards higher polarity from 10.2 min to 9.4 min was observed, which is in agreement with the formation of the more polar sulfoxide functional group. The conversion was about 85% within 1 h and shown to be fully complete within 8 h.

While the HPLC studies provide definitive changes of the oligopeptide structure in response to both orthogonal stimuli, a molecular level characterization would reinforce these observations. In this respect, we employed MALDI-TOF-MS to elucidate the peak identities (Figure 2C-E, Figure S7). From the caged-oligopeptide 5 ( $m/z$ : 1234.68 [M-H<sub>2</sub>O+H]<sup>+</sup>), the loss of the carbamate caging motif could be correlated as characterized by the linear peptide 7 ( $m/z$ : 1074.45 [M+H]<sup>+</sup>, 1096.43 [M+Na]<sup>+</sup>). As the molecular weight of 6 and 7 are identical, characterization by MALDI-TOF MS was not

possible. However, by analyzing the transient presence of the peak at RT = 10.3 min, it correlates to the well-reported rapid *O,N*-acyl shift of depsipeptide 6.<sup>[9]</sup> In a complementary fashion, the oxidation of the oligopeptide 7 by H<sub>2</sub>O<sub>2</sub> was confirmed by the addition of oxygen to form the sulfoxide analogue 8 (*m/z*: 1090.50 [M+H]<sup>+</sup>).

Upon the investigation of the molecular mechanisms, the self-assembling behaviour of the caged depsipeptide 5 as a response towards both stimuli was elucidated. As the fundamental linear peptide sequence is known to form strong  $\beta$ -sheet supramolecular nanostructures, the rearrangement reaction could be characterized by Proteostat® staining. The fluorogenic stain produced a large increase in fluorescence intensity upon triggering with phosphate salts, implying the responsive formation of  $\beta$ -sheet structures (Figure 3A, Figure S8). In contrast, the control experiment containing the caged depsipeptide 5 in pure water did not show fluorescence upon staining. Subsequently, upon adding H<sub>2</sub>O<sub>2</sub> as the disassembly stimulus, the fluorescence diminished implying the destruction of the perceived cross- $\beta$ -sheet structures.

These results were further supported by performing FTIR where the literature known vibrational frequencies corresponding to the  $\beta$ -sheet peptidic assemblies were compared.<sup>[16]</sup> The self-assembled peptide 7 showed a distinct absorbance at 1635 cm<sup>-1</sup> and 1667 cm<sup>-1</sup> which corresponds to  $\beta$ -sheet structures and other secondary structures, respectively (Figure 3B, Figure S9). Upon oxidation, while the IR spectrum looks relatively similar, it is important to note that the relative content of other non- $\beta$ -sheet structures are more significant. The higher absorbance at 1667 cm<sup>-1</sup> implies that  $\beta$ -sheet interactions are less dominant after the oxidation reaction. Hence, we speculate that the corresponding increase in other competing secondary structures is detrimental towards self-assembly and interfering the stability of the fibrillar structure. To support the results from IR, circular dichroism spectra of 5, 7 and 8 were recorded (Figure S10). The spectrum of depsi(KIKI)PBA-SQINM 5 showed expected unordered structures, while KIKISQINM 7 was proven to form  $\beta$ -sheets. Upon oxidation of 7 to 8, the spectrum changed considerably with a reduction in  $\beta$ -sheet content and a corresponding increase in unordered structures (Figure S10 and Table S1).<sup>[17]</sup>

To visualize our spectroscopic analysis, we performed a series of transmission electron microscopy (TEM) against both the stimulated assembly of the depsipeptide and disassembly of the nanostructure (Figure 3C). Starting with the caged depsi-

peptide 5, the self-assembly into fibrillar nanostructures was observed to spontaneously occur after the hydrolysis of the carbamate bond in phosphate buffered saline and subsequent rearrangement (Figure 3C). These nanofibers confirm the well-observed characteristic features of amyloid-like peptides that are known to build from continuous  $\beta$ -sheet interactions. The length of the fibers varies between short fibers with around 100 nm in length as well as longer fibers of several micrometers. The diameter of the fibers is  $9.44 \pm 1.59$  nm, yet in some fibers the thickness can be observed to change periodically, indicating a twist of the fiber strand along the fiber axis. As can be seen in Figure S12, the twist is left-handed. Separated fibers as well as dense fiber networks can be observed. Some fiber strands are organized into multistranded assemblies, which appear a lot darker and thicker in TEM compared to solitary fibers.<sup>[18]</sup> In agreement to other reports, a time lapsed study demonstrated that these nanofibers formed rapidly after 1 h, with no observable increase in fiber density for the next 8 h (Figure S11, S13-14). Subsequent oxidation using 100 mM H<sub>2</sub>O<sub>2</sub> successfully demonstrates their disassembly as a response to the stimulus (Figure 3C).

The assembly of the peptides into  $\beta$ -sheets and furthermore into nanofibers is based on an interplay of hydrogen bonds, that are formed by the amide bonds in the peptide backbone and hydrophobic interactions between the non-polar amino acid side chains of isoleucine and methionine.<sup>[19]</sup> Additional stabilization of the structure can be provided by hydrogen bonds formed by the side chains of glutamine and asparagine.<sup>[20]</sup> As shown by FTIR (Figure 3B) parallel  $\beta$ -sheets are formed, which is in accordance with Wang et al. who reported that peptides with strong hydrophobic side chains form parallel instead of anti-parallel  $\beta$ -sheets.<sup>[19c]</sup>

Oxidation of the non-polar thioether in the methionine side chain to the corresponding sulfoxide significantly enhances the polarity of the side chain.<sup>[21]</sup> The dipolar character of sulfoxides is suspected to cause electrostatic repulsion between the methionine sulfoxide residues in the peptide side chains, which leads to disassembly of the fibers.

### **3.4. Conclusion and Outlook**

In summary, we have presented a synthetic methodology that facilitates direct and independent control over the self-assembly of amyloid-like oligopeptides. In the

design, the amino acids, serine and methionine are necessary components to implement the chemical triggers. For serine, it provides a unique handle to control the overall conformation of the peptidic backbone through the depsi-ester bond while methionine is sensitive to oxidation. While the concentration of H<sub>2</sub>O<sub>2</sub> applied within this study still exceeds those in cancer environment, enzymatic triggers such as glucose oxidase may be combined e.g. in a hydrogel to elevate local H<sub>2</sub>O<sub>2</sub> production as a response to glucose. Chemically, different caging groups that introduce other stimulus such as enzymes, light and pH can be tailored to fit a designated application. By providing this facile platform, we envision that the control over self-assembly can be further extended beyond the peptide sequence.

#### Experimental Section

Experimental details, materials and methods can be found within the supporting information.

### **3.5. Acknowledgements**

██  
██

### 3.6. References

- [1] D. B. Amabilino, D. K. Smith, J. W. Steed, *Chem. Soc. Rev.* **2017**, 46, 2404-2420.
- [2] M. J. Webber, E. A. Appel, E. W. Meijer, R. Langer, *Nat. Mater.* **2015**, 15, 13.
- [3] G. Wei, Z. Su, N. P. Reynolds, P. Arosio, I. W. Hamley, E. Gazit, R. Mezzenga, *Chem. Soc. Rev.* **2017**, 46, 4661-4708.
- [4] I. W. Hamley, *Chem. Rev.* **2012**, 112, 5147-5192.
- [5] a) D. Straßburger, N. Stergiou, M. Urschbach, H. Yurugi, D. Spitzer, D. Schollmeyer, E. Schmitt, P. Besenius, *ChemBioChem* **2018**, 19, 912-916; b) M. Yolamanova, C. Meier, A. K. Shaytan, V. Vas, C. W. Bertoncini, F. Arnold, O. Zirafi, S. M. Usmani, J. A. Müller, D. Sauter, C. Goffinet, D. Palesch, P. Walther, N. R. Roan, H. Geiger, O. Lunov, T. Simmet, J. Bohne, H. Schrezenmeier, K. Schwarz, L. Ständker, W.-G. Forssmann, X. Salvatella, P. G. Khalatur, A. R. Khokhlov, T. P. J. Knowles, T. Weil, F. Kirchhoff, J. Münch, *Nat. Nanotechnol.* **2013**, 8, 130.
- [6] a) Y. Liu, Y. Yang, C. Wang, X. Zhao, *Nanoscale* **2013**, 5, 6413-6421; b) S. J. Sigg, V. Postupalenko, J. T. Duskey, C. G. Palivan, W. Meier, *Biomacromolecules* **2016**, 17, 935-945; c) E. Lump, L. M. Castellano, C. Meier, J. Seeliger, N. Erwin, B. Sperlich, C. M. Stürzel, S. Usmani, R. M. Hammond, J. von Einem, G. Gerold, F. Kreppel, K. Bravo-Rodriguez, T. Pietschmann, V. M. Holmes, D. Palesch, O. Zirafi, D. Weissman, A. Sowislok, B. Wettig, C. Heid, F. Kirchhoff, T. Weil, F.-G. Klärner, T. Schrader, G. Bitan, E. Sanchez-Garcia, R. Winter, J. Shorter, J. Münch, *eLife* **2015**, 4, e05397.
- [7] P. Ahlers, H. Frisch, R. Holm, D. Spitzer, M. Barz, P. Besenius, *Macromol. Biosci.* **2017**, 17, 1700111.
- [8] a) J. Gačanin, J. Hedrich, S. Sieste, G. Glaßer, I. Lieberwirth, C. Schilling, S. Fischer, H. Barth, B. Knöll, C. V. Synatschke, T. Weil, *Adv. Mater.* **2019**, 0, 1805044; b) A. Taniguchi, Y. Sohma, Y. Hirayama, H. Mukai, T. Kimura, Y. Hayashi, K. Matsuzaki, Y. Kiso, *ChemBioChem* **2009**, 10, 710-715.
- [9] I. Coin, R. Dölling, E. Krause, M. Bienert, M. Beyermann, C. D. Sferdean, L. A. Carpino, *J. Org. Chem.* **2006**, 71, 6171-6177.
- [10] L. Sun, C. Zheng, T. J. Webster, *Int. J. Nanomed.* **2016**, 12, 73-86.
- [11] A. Dehsorkhi, V. Castelletto, I. W. Hamley, *J. Pept. Sci.* **2014**, 20, 453-467.
- [12] C. Lennicke, J. Rahn, R. Lichtenfels, L. A. Wessjohann, B. J. C. Seliger, Signaling, *Cell Commun. Signal.* **2015**, 13, 39.
- [13] S. Das, K. Zhou, D. Ghosh, N. N. Jha, P. K. Singh, R. S. Jacob, C. C. Bernard, D. I. Finkelstein, J. S. Forsythe, S. K. Maji, *NPG Asia Mater.* **2016**, 8, e304.

- [14] N. Habibi, N. Kamaly, A. Memic, H. Shafiee, *Nano Today* **2016**, 11, 41-60.
- [15] A. K. Ghosh, M. Brindisi, *J. Med. Chem.* **2015**, 58, 2895-2940.
- [16] G. Zandomenighi, M. R. H. Krebs, M. G. McCammon, M. Fändrich, *Protein Sci.* **2004**, 13, 3314-3321.
- [17] a) Y. Liu, L. Zhang, W. Wei, *International of Journal Nanomedicine* **2017**, 12, 659-670; b) R. Xing, C. Yuan, S. Li, J. Song, J. Li, X. Yan, *Angew. Chem. Int. Ed.* **2018**, 57, 1537-1542.
- [18] K. Pagel, S. C. Wagner, K. Samedov, H. von Berlepsch, C. Böttcher, B. Kokschi, *J. Am. Chem. Soc.* **2006**, 128, 2196-2197.
- [19] a) K. Liu, R. Xing, C. Chen, G. Shen, L. Yan, Q. Zou, G. Ma, H. Möhwald, X. Yan, *Angew. Chem. Int. Ed.* **2015**, 54, 500-505; b) N. R. Lee, C. J. Bowerman, B. L. Nilsson, *Biomacromolecules* **2013**, 14, 3267-3277; c) J. Wang, K. Liu, R. Xing, X. Yan, *Chem. Soc. Rev.* **2016**, 45, 5589-5604; d) C. Yuan, S. Li, Q. Zou, Y. Ren, X. Yan, *Phys. Chem. Chem. Phys.* **2017**, 19, 23614-23631.
- [20] S. Sieste, T. Mack, C. V. Synatschke, C. Schilling, C. Meyer zu Reckendorf, L. Pendi, S. Harvey, F. S. Ruggeri, T. P. J. Knowles, C. Meier, D. Y. W. Ng, T. Weil, B. Knöll, *Adv. Healthcare Mater.* **2018**, 7, 1701485.
- [21] D. Spitzer, L. L. Rodrigues, D. Straßburger, M. Mezger, P. Besenius, *Angew. Chem. Int. Ed.* **2017**, 56, 15461-15465.



## **3.7. Supporting Information**

### **3.7.1. Materials and instruments**

#### **Materials**

All solvents and reagents were bought from commercial sources (Sigma Aldrich, GL Biochem, Carl Roth, Fisher Scientific, Acros Organics, Merck Novabiochem) and used without any further purification. All reagents used for peptide synthesis were used in Peptide Synthesis grade. HPLC was performed using HPLC grade acetonitrile. Water for HPLC and reactions was obtained from a Millipore purification system. Thin-layer chromatography (TLC) was performed on Macherey-Nagel Alugram Sil G/UV254 plates and visualized under UV light at 254 nm. Column chromatography was carried out using Macherey-Nagel silica gel 0.04 – 0.063 mm.

#### **Instruments**

##### **Nuclear Magnetic Resonance Spectroscopy (NMR)**

NMR spectra were recorded on a Bruker Avance II 300 MHz and Avance III 700 MHz NMR spectrometer. The solvent signal was used as a reference (deuterated chloroform  $\delta = 7.26$  ppm for  $^1\text{H}$ , 77.16 ppm for  $^{13}\text{C}$ ). The data was processed in MestReNova.

##### **Microwave Peptide Synthesizer**

Peptide Synthesis was performed in a Liberty Blue Automated Microwave Peptide Synthesizer by CEM.

##### **High-Performance Liquid Chromatography (HPLC)**

Purification of the peptides was done on a preparative HPLC setup by Shimadzu. An Agilent ZORBAX Eclipse XDB-C18 HPLC column (9.4 x 250 mm, 5  $\mu\text{m}$ ) was used for the purification at a flowrate of 4 mL/min. Analytical HPLC measurements were performed on a semi-preparative HPLC by Shimadzu using an Atlantis T3 column (4.6

x 100 mm, 5  $\mu$ m) with a flowrate of 1 mL/min. Acetonitrile and MilliQ water, each acidified to 0.1% TFA were used as solvents. Absorbance was measured at 190, 214 and 254 nm. Spectra were processed with the software LabSolutions.

### **Liquid Chromatography - Mass Spectrometry (LC-MS)**

HPLC-ESI-MS was measured on the device LC-MS 2020 by Shimadzu using a Kinetex 2.6  $\mu$ m EVO C18 100 Å LC 50 x 2.1 mm column. The solvents were MilliQ water + 0.1% formic acid and acetonitrile. Samples were prepared in methanol. The solvent gradient started at 5% ACN content, which was increased to 95% within 12 min. The data was processed with LabSolutions.

### **Matrix-Assisted Laser Desorption/Ionization - Time of Flight Mass Spectrometry (MALDI-TOF)**

MALDI-TOF spectra were measured on a rapifleX MALDI-TOF/TOF from Bruker and MALDI Synapt G2-SI from Waters. Samples were prepared by mixing with a saturated  $\alpha$ -cyano-4-hydroxycinnamic acid (CHCA) solution in water/ACN 1/1 + 0.1% TFA. The data was processed in mMass.

### **Fluorescence Spectroscopy**

Fluorescence intensity was measured using a SPARK 20M microplate reader by the company Tecan Group Ltd. A Greiner 384 flat black wellplate was used and the data was processed with Excel.

### **Fourier-Transform Infrared Spectroscopy (FTIR)**

FTIR spectra were measured using a Bruker TENSOR II spectrometer equipped with a PLATINUM ATR single reflection diamond ATR accessory. The data was processed using Excel.

### **Circular Dichroism Spectroscopy (CD)**

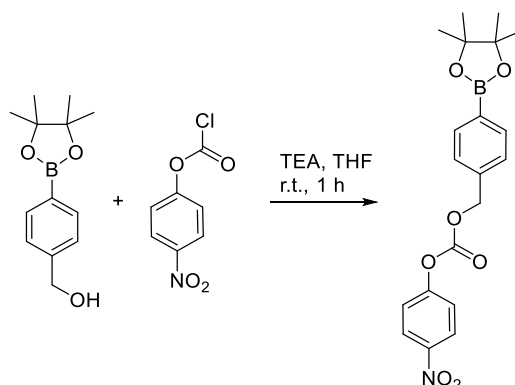
CD was measured on a JASCO J-1500 spectrometer in a 1 mm High Precision Cell by HellmaAnalytics. The data was processed in the software's Spectra Analysis and CD Multivariate SSE by JASCO.

### Transmission Electron Microscopy (TEM)

TEM pictures were taken on a JEOL 1400 transmission electron microscope. Formvar/carbon-film coated copper grids (300 mesh) were purchased from Plano GmbH. The pictures were processed in ImageJ.

### 3.7.2. Synthesis

#### Synthesis of 4-Nitrophenyl (4-(4,4,5,5-tetramethyl-1,3,2-dioxaborolan-2-yl)benzyl) carbonate



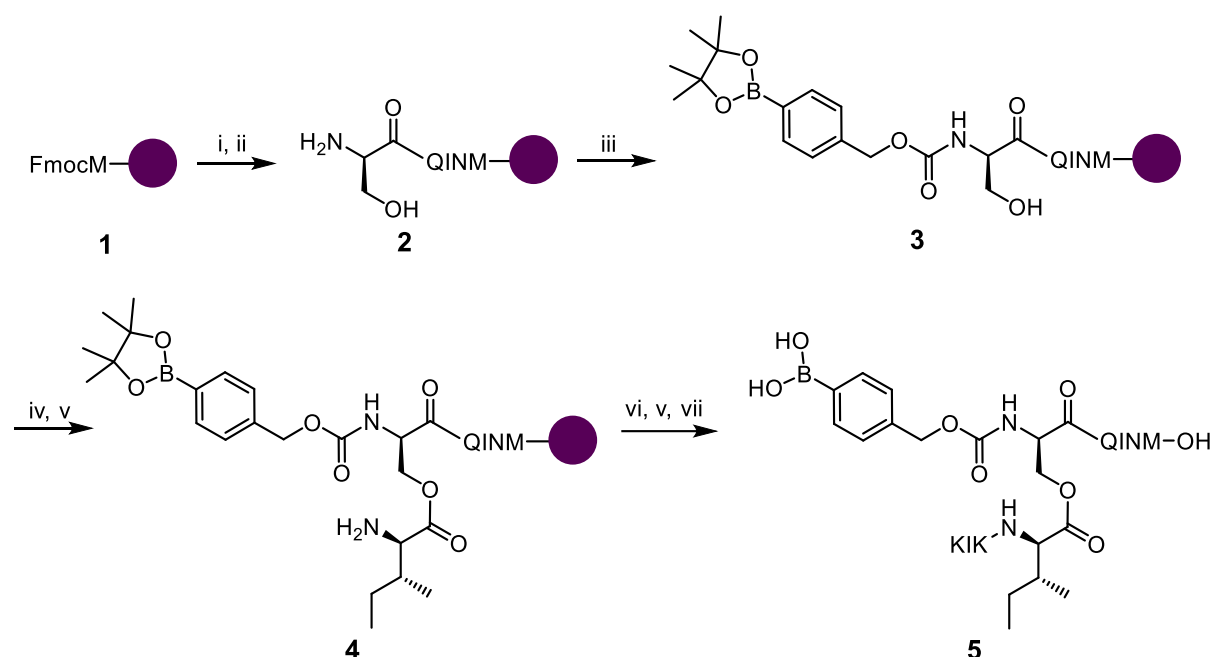
4-Hydroxymethylphenylboronic acid pinacol ester (3.00 g, 12.81 mmol) was dissolved in 30 mL dry THF under argon atmosphere. After triethylamine (3.6 ml, 25.97 mmol) was added to the reaction flask, the flask was cooled in an ice bath. 4-Nitrophenyl chloroformate (2.84 g, 14.10 mmol) was added in portions and the reaction mixture was stirred for one hour at room temperature, then the solvent was removed *in vacuo*. The mixture was suspended in ethylacetate and washed with 1 M HCl<sub>aq</sub>, saturated sodium bicarbonate solution and brine. Ethylacetate was removed *in vacuo* and the reaction mixture was purified by silica chromatography (1:4 ethylacetate:n-hexane). After drying *in vacuo* 5.11 g (8.97 mmol, 70% yield) of 4-nitrophenyl (4-(4,4,5,5-tetramethyl-1,3,2-dioxaborolan-2-yl)benzyl) carbonate was received as a white crystalline powder.<sup>[1]</sup>

<sup>1</sup>H-NMR (300 MHz, CDCl<sub>3</sub>) δ [ppm] = 8.27 (d, J = 9.1 Hz, 2H), 7.85 (d, J = 7.6 Hz, 2H), 7.41 (m, 4H), 5.31 (s, 2H), 1.35 (s, 12H).

$^{13}\text{C-NMR}$  (176 MHz,  $\text{CDCl}_3$ )  $\delta$  [ppm] = 155.67, 152.57, 145.57, 137.20, 135.34, 127.77, 125.45, 121.92, 84.14, 70.95, 25.01.

## Peptide Synthesis

### Depsi(KIKI)PBA-SQINM



Peptide synthesis was performed according to the solid phase peptide synthesis Fmoc strategy by Merrifield. The peptide was synthesized from the C to the N-terminus in a microwave peptide synthesizer. After Fmoc-Methionine Wang resin 1 (147 mg, 0.1 mmol) was swollen in DMF for one hour at room temperature, the Fmoc protecting group was removed by two deprotection steps with 20% piperidine in DMF (3 mL) at 75 °C for 2 and 5 min (i). Fmoc-Asn(Trt)-OH, Fmoc-Ile-OH and Fmoc-Gln(Trt)-OH (5 eq in 2.5 mL DMF) were double coupled consecutively for 10 min at 75 °C (ii). PyBOP (5 eq in 1 mL DMF) and DIPEA (10 eq in 0.5 mL DMF) were added in every coupling step. Each coupling was followed by two deprotection steps (2 and 5 min) and three washes with DMF. Fmoc-Ser-OH was also coupled for 10 min (ii), but not double coupled to prevent side reactions on its unprotected hydroxyl group. After the deprotection of the N-terminal protecting group of serine (i), 0.025 mmol of the resin were modified on the N-terminus with 4-nitrophenyl 4-(4,4,5,5-tetramethyl-1,3,2-dioxaborolan-2-yl)benzyl) carbonate (99.79 mg, 0.25 mmol) in DMF and DIPEA (87  $\mu\text{L}$ , 0.5 mmol) overnight at room temperature (iii). After the resin was thoroughly

washed with DMF and DCM, the depsi ester bond was formed by a reaction of the serine side chain hydroxyl group with Fmoc-Ile-OH (88.35 mg, 0.25 mmol) using DIC (39  $\mu$ L, 0.25 mmol) and 4-DMAP (3.05 mg, 0.025 mmol) in 1 mL DMF for two hours at room temperature (iv). The reagents were removed and the same amount of Fmoc-Ile-OH, DIC, 4-DMAP and DMF was added to the resin, which was stirred overnight afterwards. After washing the resin with DMF and DCM, Fmoc-Lys(Boc)-OH, Fmoc-Ile-OH and Fmoc-Lys(Boc)-OH were double coupled, while every coupling step was performed for 60 min at room temperature (vi). In between the couplings, double Fmoc deprotection was performed at room temperature for 10 min each (v). After final Fmoc-deprotection (2x10 min, room temperature) the resin was washed with DMF and stirred in a cleavage cocktail containing trifluoroacetic acid/triisopropylsilane/water 95/2.5/2.5% (2 mL) for 2 h to cleave the peptide from the resin (vii). This also removed the side chain protecting groups and the pinacol protecting group of the PBA modification. The crude peptide was precipitated in 20 mL of cold diethylether, centrifuged (4 °C, 3800 rpm, 10 min), dissolved in ACN/water and purified by HPLC. The gradient started with 5% ACN, which was kept constant for 1 min, then the ACN content was increased linearly to 100% within 15 min. The retention time of the product was 13.25 min. After lyophilization Depsi(KIKI)PBA-SQINM 5 was received as a white powder.

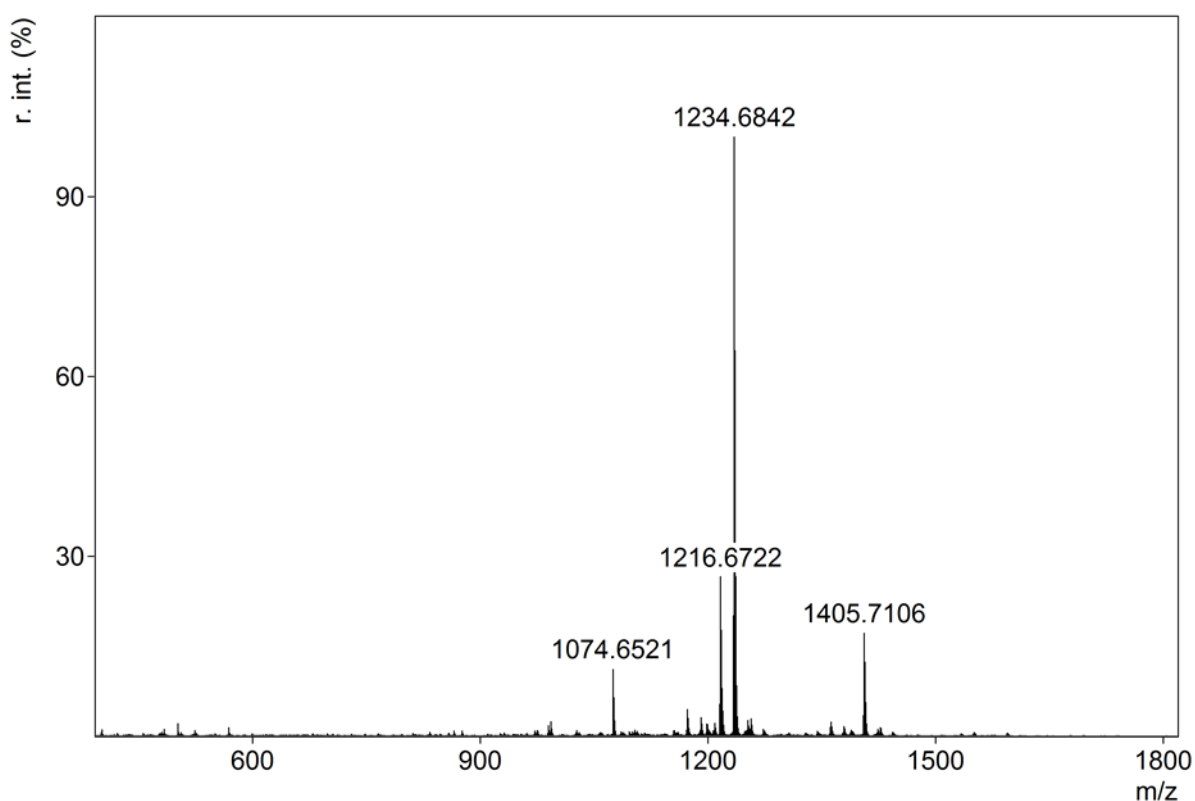


Figure S1: MALDI-TOF MS of Depsi(KIKI)PBA-SQINM 5 using  $\alpha$ -cyano-4-hydroxycinnamic acid as matrix.  $m/z$  calculated:  $[M+H]^+ = 1251.67$  g/mol, found:  $[M-PBA]^+ = 1074.6521$  g/mol,  $[M-OH-H_2O]^+ = 1216.6722$  g/mol,  $[M-OH]^+ = 1234.6842$  g/mol,  $[M+K+TFA]^+ = 1405.7106$  g/mol. Note: Due to the instability of the carbamate bond, some PBA is cleaved during the measurement.

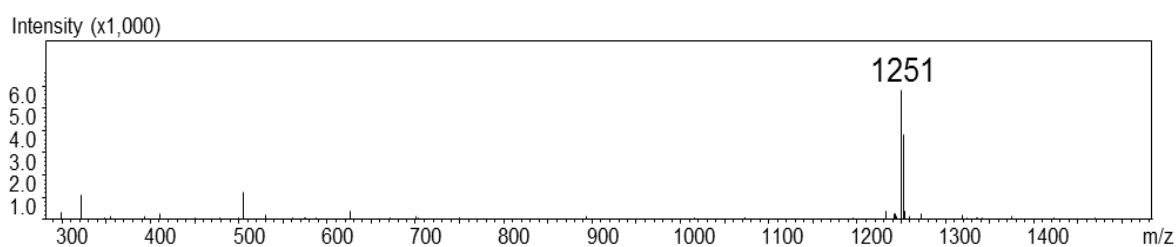


Figure S2: LCMS-ESI spectrum of the Depsi(KIKI)PBA-SQINM 5 calculated,  $[M-H]^- = 1250.67$  g/mol, found:  $[M-H]^- = 1251$  g/mol.

## Depsi(KIKI)SQINM 6

Depsi(KIKI)SQINM 6 was synthesized following the protocol of Gačanin *et al.*<sup>[2]</sup>

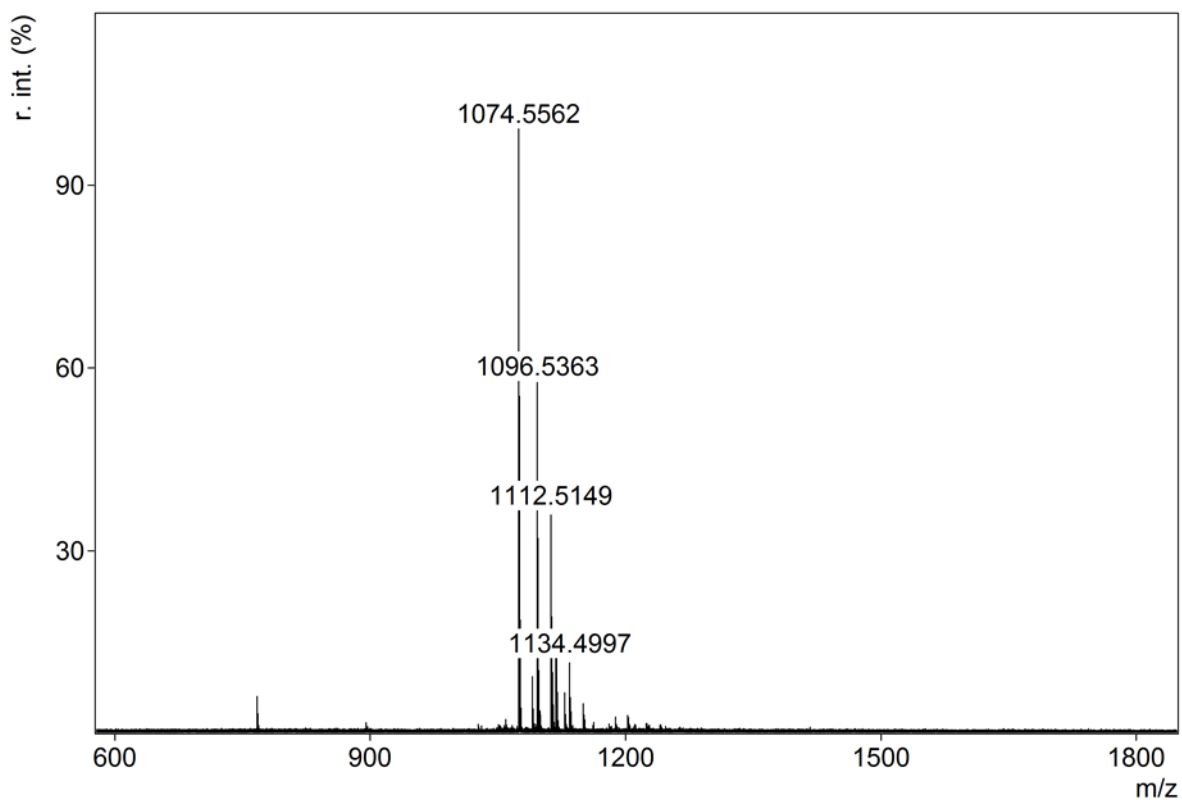


Figure S3: MALDI-TOF MS of Depsi(KIKI)SQINM 6 using  $\alpha$ -cyano-4-hydroxycinnamic acid as matrix.  $m/z$  calculated:  $[M+H]^+ = 1074.35$  g/mol, found:  $[M+H]^+ = 1074.5562$  g/mol,  $[M+Na]^+ = 1096.5363$  g/mol,  $[M+K]^+ = 1112.5149$  g/mol,  $[M+Na+K-H]^+ = 1134.4997$  g/mol.

## KIKISQINM 7

KIKISQINM 7 was synthesized following the protocol of *Gaćanin et al.*<sup>[2]</sup>

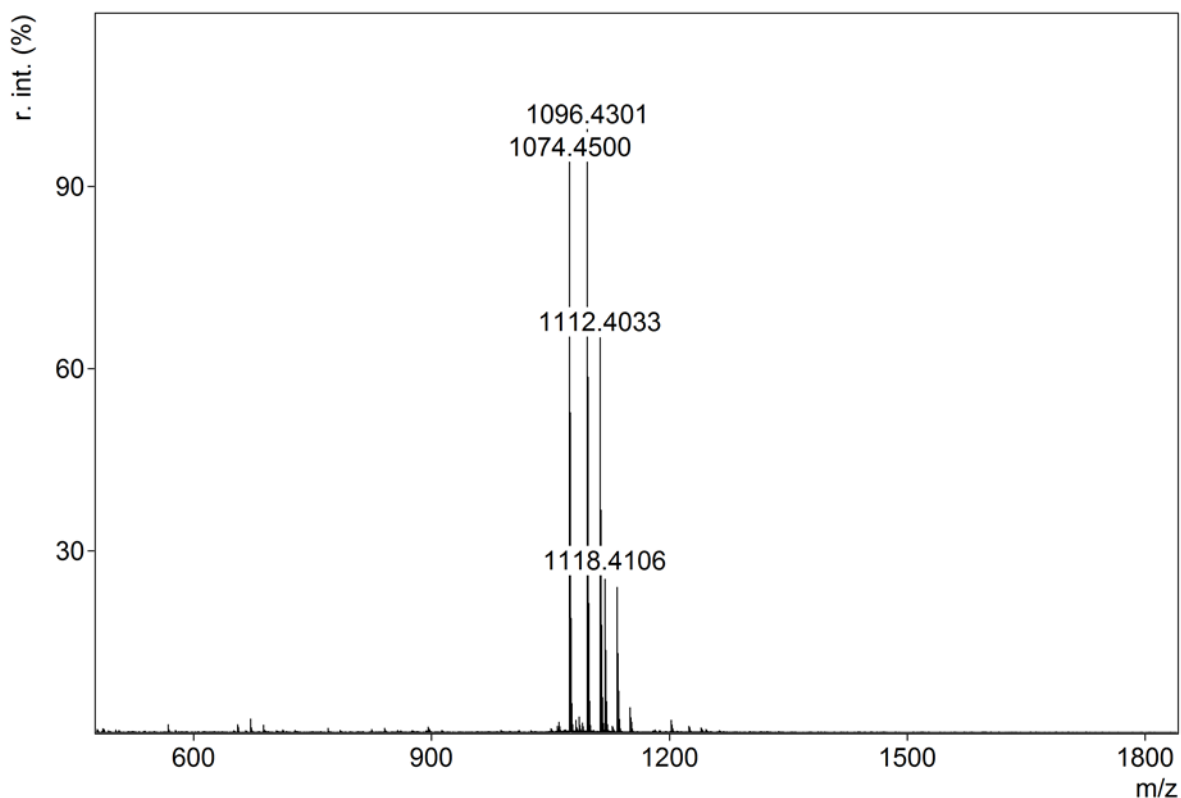


Figure S4: MALDI-TOF MS of KIKISQINM 7 using  $\alpha$ -cyano-4-hydroxycinnamic acid as matrix.  $m/z$  calculated:  $[M+H]^+ = 1074.35$  g/mol, found:  $[M+H]^+ = 1074.4500$  g/mol,  $[M+Na]^+ = 1096.4301$  g/mol,  $[M+K]^+ = 1112.4033$  g/mol,  $[M+2Na-H]^+ = 1118.4106$  g/mol.

### 3.7.3. Characterization

#### HPLC Study

Depsi(KIKI)PBA-SQINM 5 (0.2 mg) was dissolved in 400  $\mu$ L tetrahydrofuran and diluted to 0.1 mg·ml<sup>-1</sup> with 1.6 mL PBS (Dulbecco's phosphate buffered saline). HPLC spectra were measured by injection of 50  $\mu$ L of the reaction solution at certain time points using an analytical column (see HPLC section) with a flowrate of 1 mL/min (Figure S5). The gradient started at 5% ACN, which was kept constant for 1 min, then the acetonitrile content was increased linearly to 100% ACN within 15 min. After 24 h incubation time the hydrolysis and O, N - acyl shift was completed, therefore 35% H<sub>2</sub>O<sub>2</sub> solution was added to receive a concentration of 100 mM. HPLC spectra were taken until completion of the oxidation reaction (Figure 6).



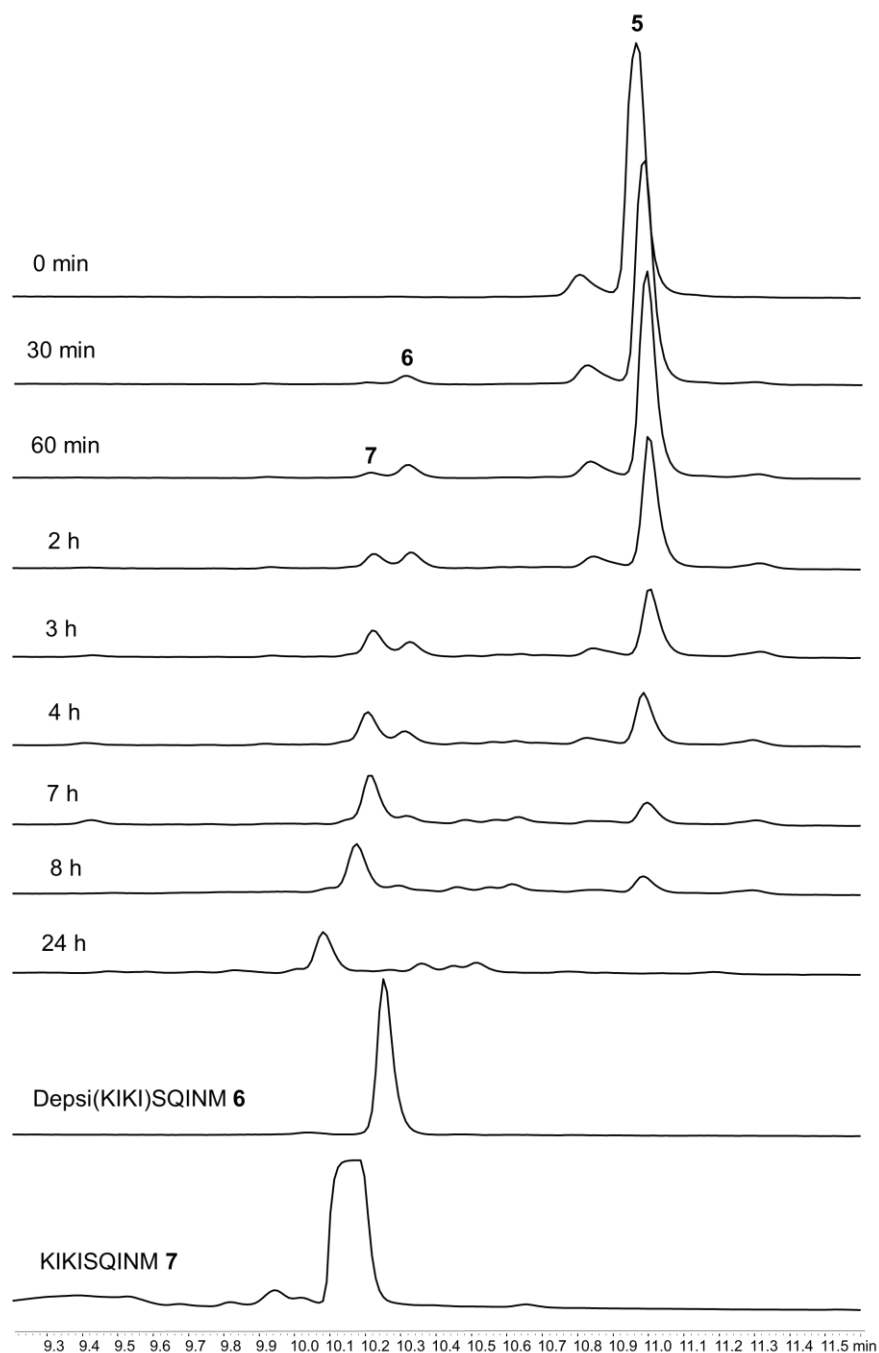


Figure S5: HPLC spectra at 190 nm taken after certain time points to observe the carbamate hydrolysis and O, N-acyl shift. The peak at 11 min is the educt Depsi(KIKI)PBA-SQINM 5. After 30 min the peak of Depsi(KIKI)SQINM 6 is observed at 10.3 min. KIKISQINM 7 is observed after 10.2 min. Note: the retention time of KIKISQINM and its depsi form shifts slightly upon increasing its concentration.

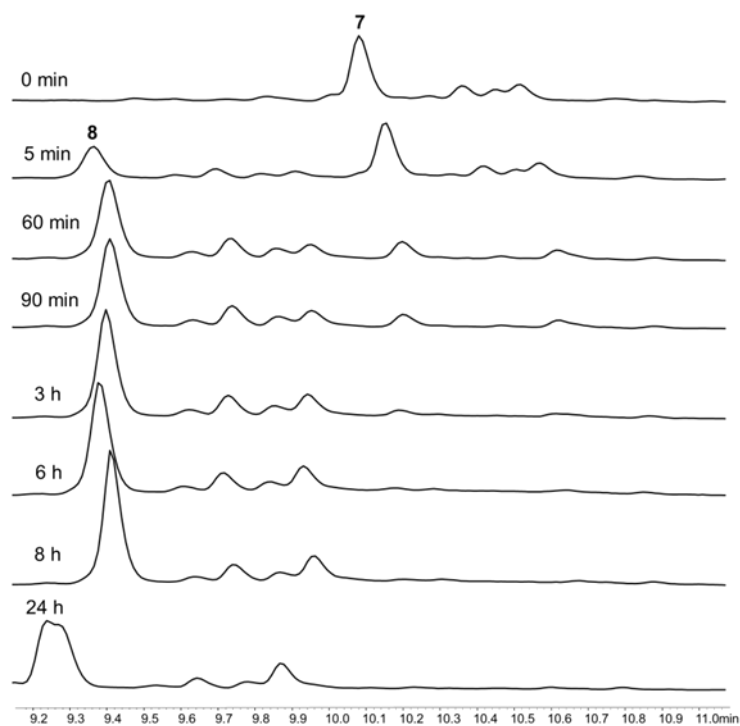


Figure 6: HPLC spectra at 190 nm taken after certain time points to observe methionine oxidation in KIKISQINM (retention time 10.15 min) to KIKISQIN(M=O) 8 (9.40 min).

## MALDI-TOF

MALDI spectra of the educt Depsi(KIKI)PBA-SQINM 5, KIKISQINM 7 and KIKISQIN(M=O) 8, resulting from the HPLC study were recorded to prove methionine oxidation.

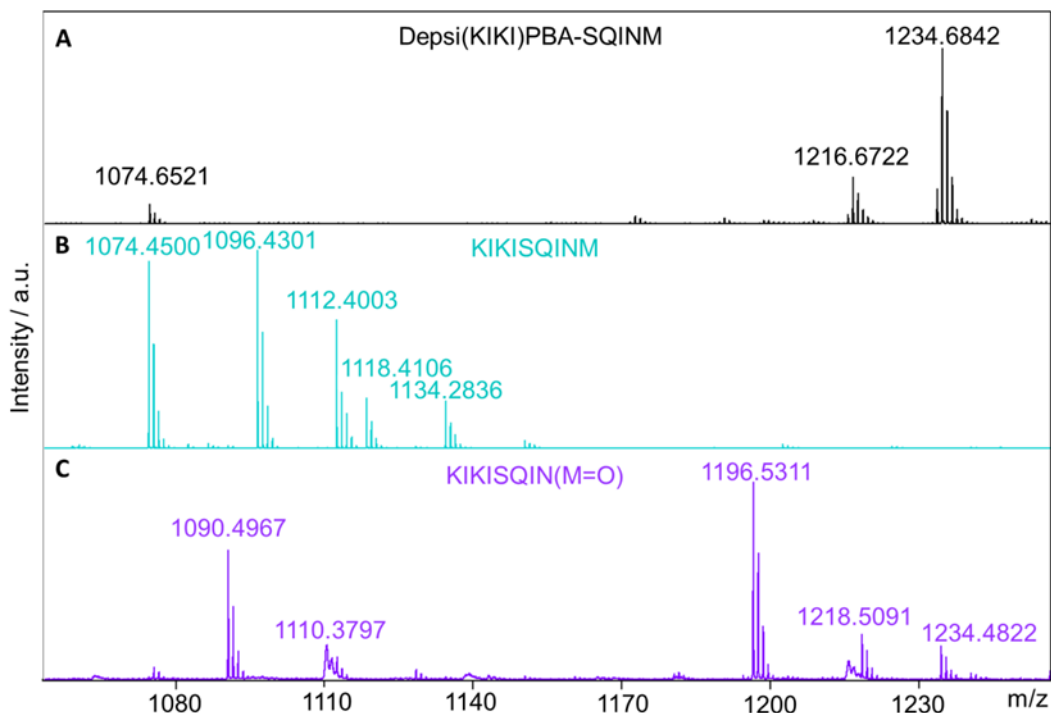


Figure S7: MALDI-TOF MS of Depsi(KIKI)PBA-SQINM 5, KIKISQINM 7 and KIKISQIN(M=O) 8 using  $\alpha$ -cyano-4-hydroxycinnamic acid as matrix. A: Depsi(KIKI)PBA-SQINM  $m/z$  calculated:  $[M+H]^+ = 1251.67$  g/mol, found:  $[M-PBA]^+ = 1074.6521$  g/mol,  $[M-OH-H_2O]^+ = 1216.6722$  g/mol,  $[M-OH]^+ = 1234.6842$  g/mol, Note: Due to the instability of the carbamate bond, some PBA is cleaved during the measurement. B: KIKISQINM  $m/z$  calculated:  $[M+H]^+ = 1074.63$  g/mol, found:  $[M+H]^+ = 1074.4500$  g/mol,  $[M+Na]^+ = 1096.4301$  g/mol,  $[M+K]^+ = 1112.4003$  g/mol,  $[M+2 Na-H]^+ = 1118.4106$  g/mol,  $[M+Na+K-H]^+ = 1134.2836$  g/mol. C: KIKISQIN(M=O)  $m/z$  calculated:  $[M+H]^+ = 1089.62$  g/mol, found:  $[M+H]^+ = 1090.4967$  g/mol,  $[M+Na+2ACN]^+ = 1196.5311$  g/mol,  $[M+2Na+2ACN-H]^+ = 1218.5091$  g/mol,  $[M-Na+K+2ACN-H]^+ = 1234.4822$  g/mol.

## Peptide Fibrillation

Peptide fibers were formed by dissolving the peptide in DMSO at a concentration of 10 mg/ml and diluting with Dulbecco's phosphate buffered saline (PBS) to receive a final concentration of 1 mg/ml (0.8 mM). The peptides were incubated at room temperature for 24 h in an orbital shaker. In order to destroy the fibers by oxidation of methionine to methionine sulfoxide, hydrogen peroxide was added as a 35% solution to receive a concentration of 100 mM of  $H_2O_2$  and incubated for further 24 h.

## Proteostat Assay

The Proteostat Protein Aggregation Assay Kit was purchased from Enzo Life Sciences, Inc. 0.13  $\mu$ L of the Proteostat stock solution was diluted with 24.62  $\mu$ L MilliQ water and 0.25  $\mu$ L assay buffer. 1  $\mu$ L of this solution was added to 9  $\mu$ L peptide solution (see peptide fibrillation) in a Greiner 384 flat black wellplate. The solutions were

incubated in the dark for 15 min while shaking at 510 rpm. The fluorescence intensity was measured with an excitation and emission bandwidth of 20 nm and an emission wavelength of 600 nm after excitation with light at 550 nm. The experiment was done four times. Control measurements were done by incubating Proteostat solution in MilliQ water, PBS and PBS with 100 mM H<sub>2</sub>O<sub>2</sub>.

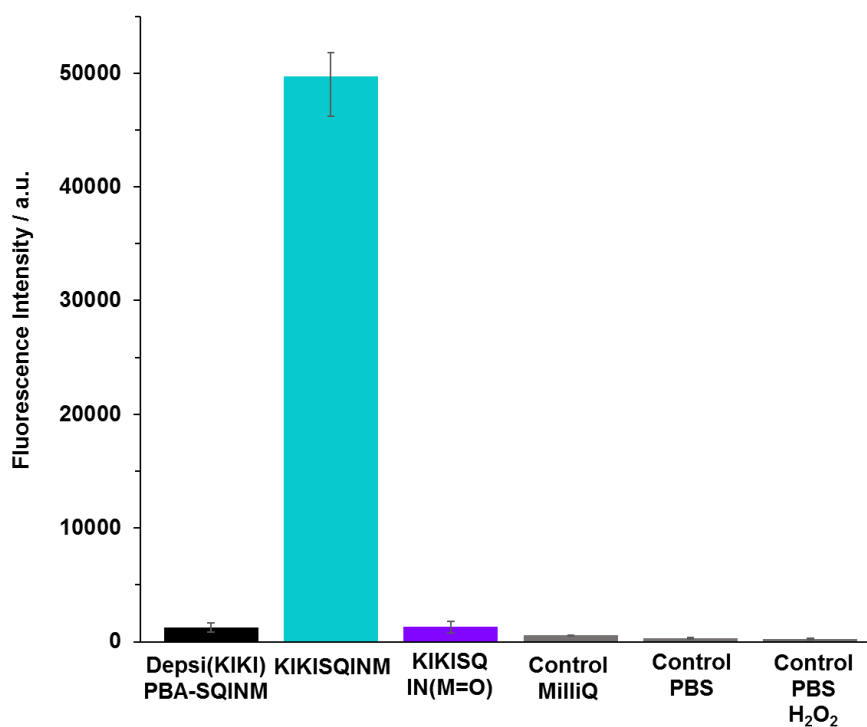


Figure S8: Fluorescence intensity spectra of peptides incubated with Proteostat, measured at 600 nm after irradiation with 550 nm. Depsi(KIKI)PBA-SQINM 5 was incubated in water/DMSO 9:1 for 48 h. KIKISQINM was fibrillized by dissolving Depsi(KIKI)PBA-SQINM 5 in PBS:DMSO 9:1 and incubating for 48 h. KIKISQIN(M=O) 8 was formed by adding 100 mM hydrogen peroxide to KIKISQINM 7 fiber solution and further incubation for 24 h.

### Fourier-Transform Infrared Spectroscopy

100  $\mu$ L of peptide solution (see peptide fibrillation) were lyophilized. FT-IR spectra of the lyophilized peptides were measured at wavenumbers from 400 to 4000  $\text{cm}^{-1}$ .

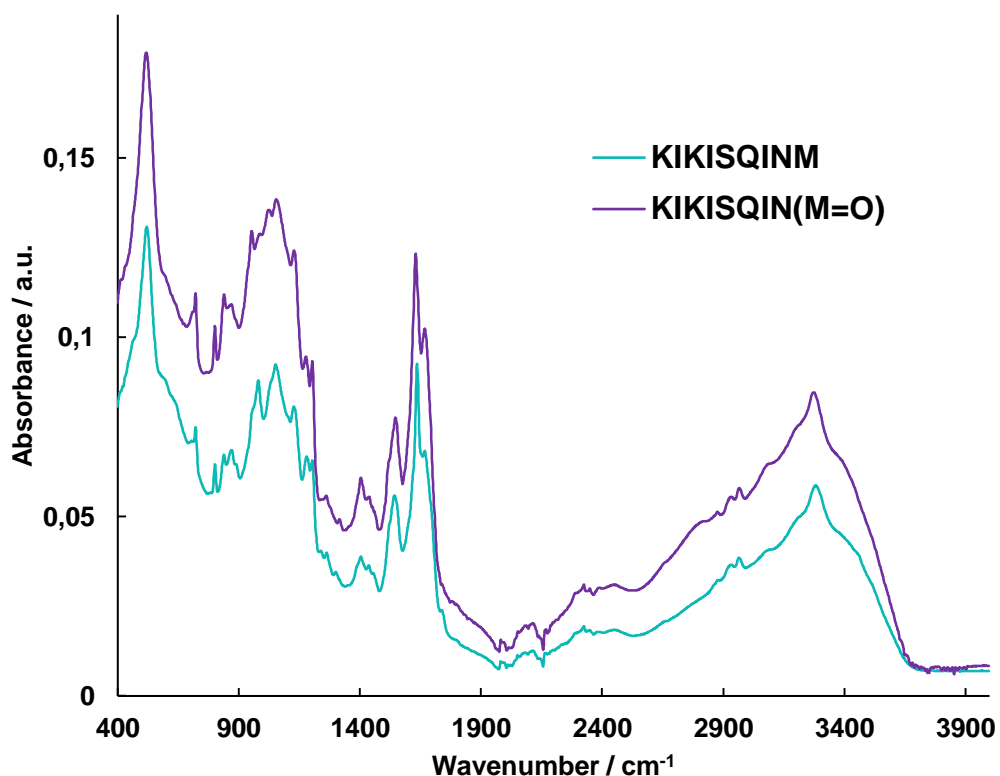


Figure S9: FT-IR spectra of KIKISQINM 7 and the oxidized derivative KIKISQIN(M=O) 8.

### Circular Dichroism

After KIKISQINM 7 was dissolved in 40  $\mu\text{L}$  MilliQ water (1 mg/mL), the pH was adjusted to 7 with a 1 M NaOH solution. After 2 h incubation time at room temperature the sample was divided in two and 35% hydrogen peroxide solution was added to one sample to achieve a 100 mM concentration of  $\text{H}_2\text{O}_2$ . After incubation overnight both samples were further diluted with 240  $\mu\text{L}$  MilliQ water and circular dichroism was measured at room temperature from 260 to 190 nm with a bandwidth of 1 nm. The data pitch was set to 0.2 nm, while the scanning speed was 5 nm/min. Each sample was measured three times and the data accumulated. For comparison Depsi(KIKI)PBA-SQINM 5 was dissolved in MilliQ water and CD spectra were measured at the same concentration and the same settings as 7 and 8.

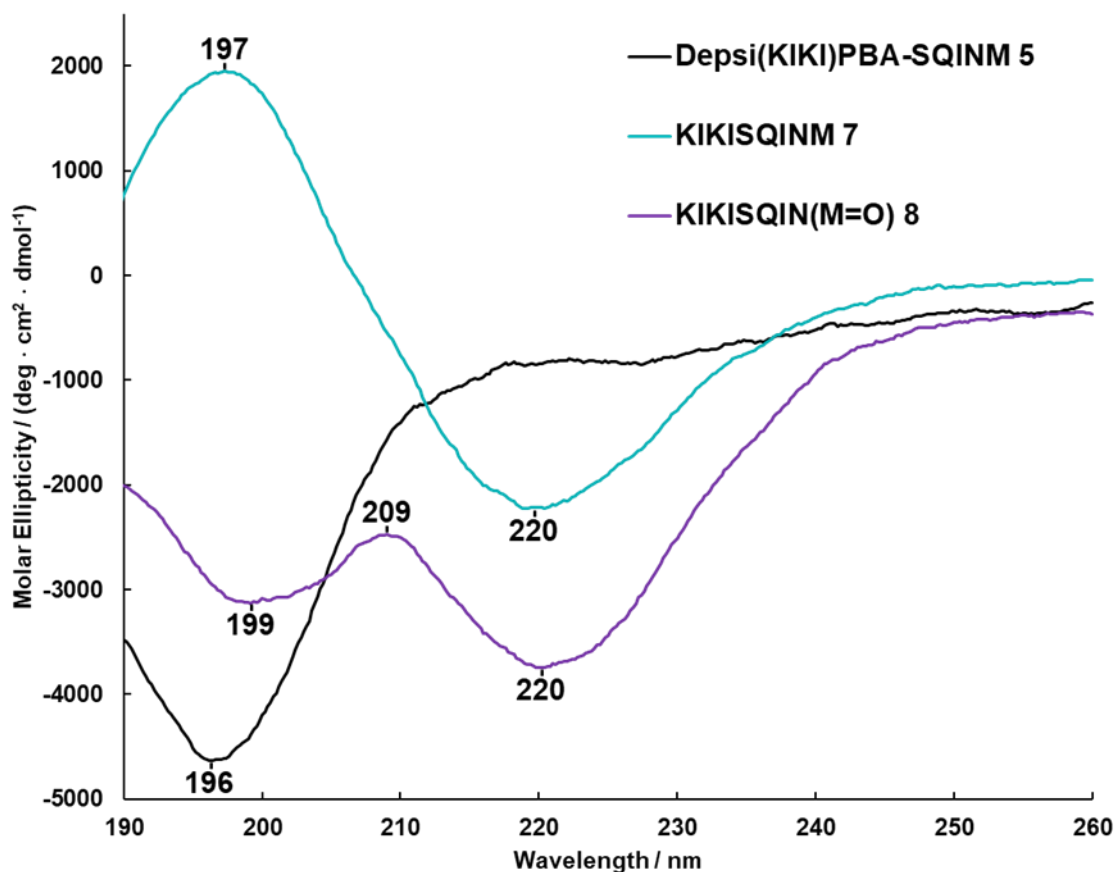


Figure S10: CD spectra of Depsi(KIKI)PBA-SQINM 5, KIKISQINM 7 and the oxidized derivative KIKISQIN(M=O) 8.

The spectra were used to calculate the content of each secondary structure with the software CD Multivariate SSE by JASCO.

Table S1: Content of secondary structures calculated based on CD.

	Helix	Sheet	Turn	Unordered
DEPSI(KIKI)PBA-SQINM 5	0.0%	38.1%	13.6%	50.0%
KIKISQINM 7	4.7%	42.6%	13.4%	39.3%
KIKISQIN(M=O) 8	2.7%	36.9%	15.1%	45.2%

### Transmission Electron Microscopy

4  $\mu$ L of peptide fiber solution (see peptide fibrillation) were pipetted onto freshly etched Formvar coated copper grids and incubated for 5 min. The solutions were removed with filter paper and the grids were stained with 4% uranyl acetate solution for 2.5 min.

After washing with MilliQ water three times the grids were left to dry before they were measured.

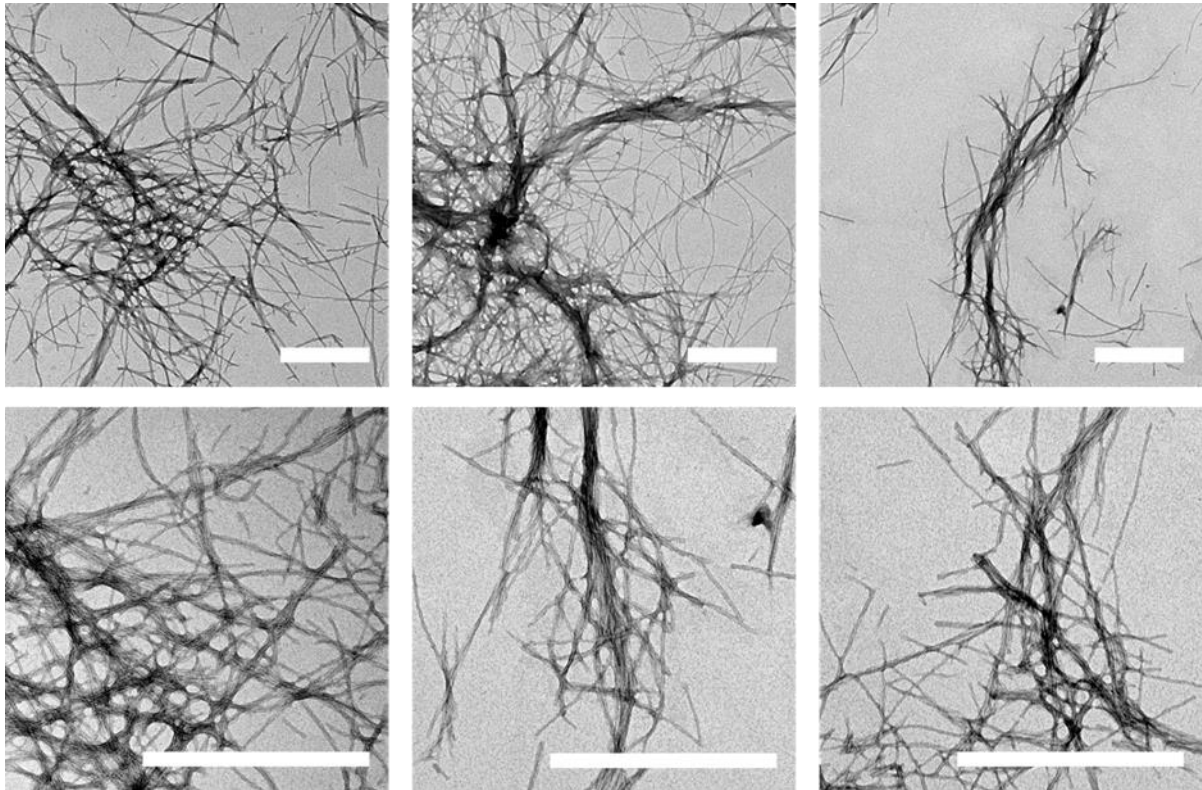
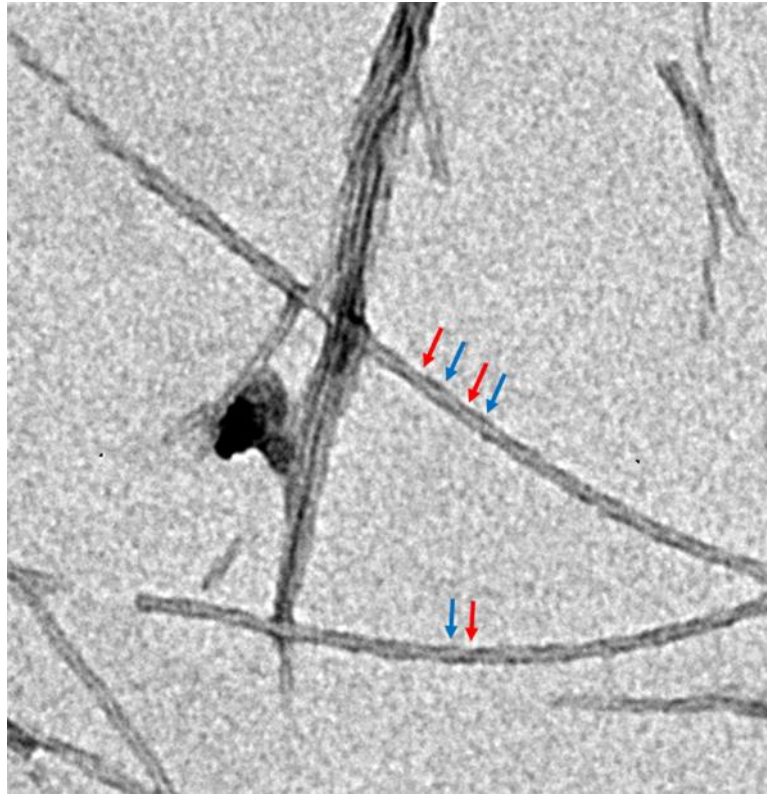


Figure S11: TEM after hydrolysis and O, N-acyl shift of Depsi(KIKI)PBA-SQINM 5 to KIKISQINM 7 in PBS after 48 h incubation. Scale bar = 500 nm.



*Figure S12: TEM of left-handed twisted peptide fibers formed by KIKISQINM. The red arrow indicates the thinner part of the peptide fiber with a diameter of 9 nm, the blue arrow shows the thicker one with a diameter of 11 nm.*

In order to determine how long it takes till fibers are formed and how the fibers change upon time, TEM grids were prepared as described above at certain time points after adding PBS (45  $\mu$ L) to the peptide stock solution in DMSO (50  $\mu$ g in 5  $\mu$ L).



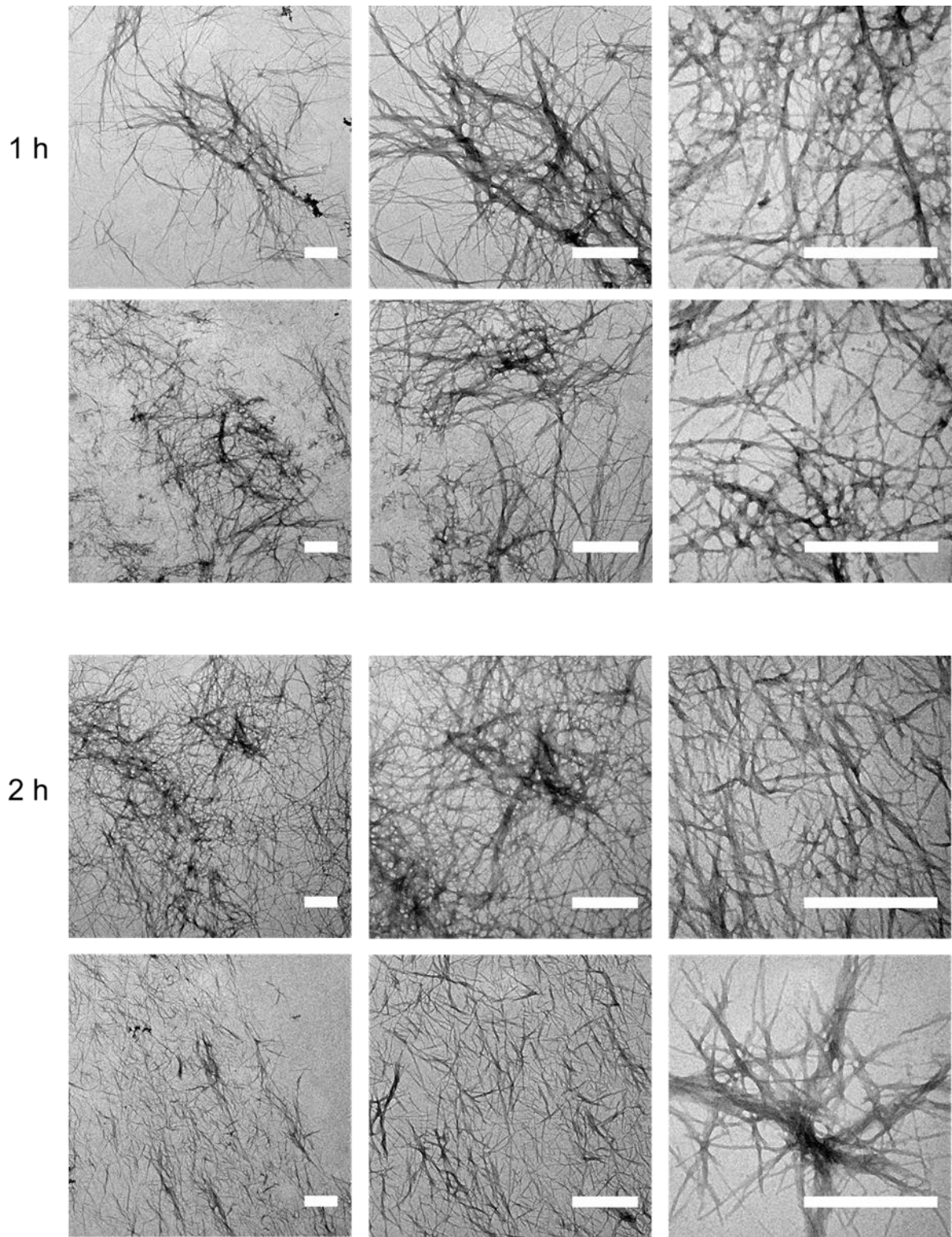


Figure S13: TEM after hydrolysis and O, N-acyl shift of Depsi(KIKI)PBA-SQINM 5 to KIKISQINM 7 in PBS after one and two hours. Scale bar = 500 nm.

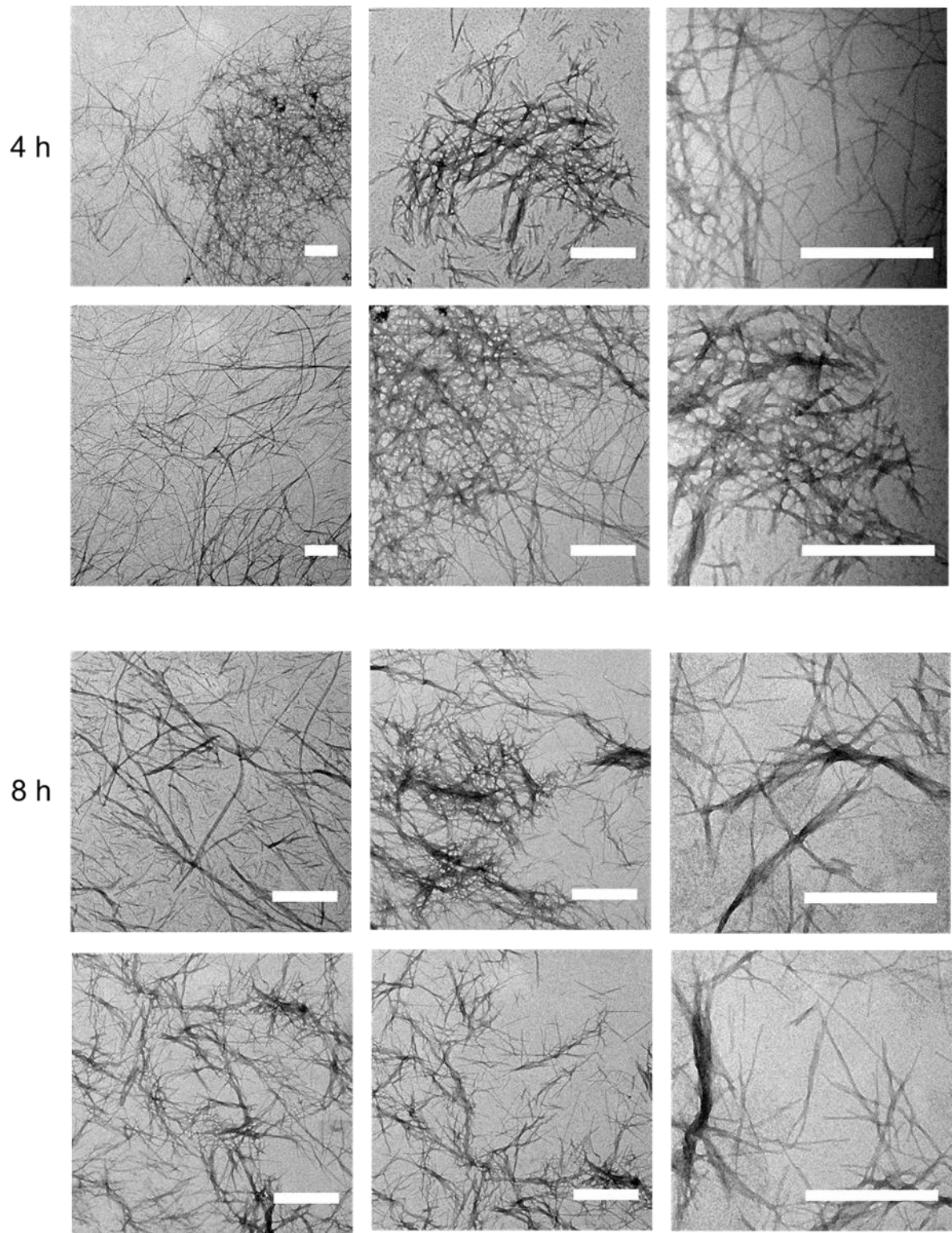


Figure S14: TEM after hydrolysis and O, N-acyl shift of Depsi(KIKI)PBA-SQINM 5 to KIKISQINM 7 in PBS after four and eight hours. Scale bar = 500 nm.




### 3.7.4. Literature

- [1] J. Li, Y. Li, Q. He, Y. Li, H. Li, L. Liu, *Org. Biomol. Chem.* **2014**, 12, 5435–5441.
- [2] J. Gačanin, J. Hedrich, S. Sieste, G. Glaßer, I. Lieberwirth, C. Schilling, S. Fischer, H. Barth, B. Knöll, C. V. Synatschke, T. Weil, *Adv. Mater.* **2018**, 1805044.

## 4. Photoinduced Amyloid Fibril Degradation for Controlled Cell Patterning



# denotes equal contribution





- [a] 
- [b] 
- [c] 

### Copyright:

Published in *Macromol. Biosci.* 2023, 23, 2200294

The following part is reproduced with permission from John Wiley and Sons. This work is licensed under a Creative Commons Attribution 4.0 International License.

### 4.1. Contributions

Together with , I designed and wrote the manuscript, prepared the figures, interpreted the data and incorporated them into the manuscript. We conceptualized the idea of a photo-responsive amyloid-like peptides together that reveal controllable bioactivity with further using as scaffold for patterning in tissue engineering. Moreover, I introduced the photomasks for light-controlled fibril as well as cell patterning. I performed parts of cell adhesion assays and established the agarose and fiber coating techniques. Furthermore, I performed the Cell-Titer Glo Assay, Zeta-Potential measurements, parts of the TEM measurements and parts of the ThT-Assays and I interpreted the results. I supervised the performance of the linker and peptide synthesis, characterization and its cleavage kinetics, as well as FT-IR-, AFM sample preparation-, SEM- and CD- studies, which were performed by . .  designed the peptide sequences and validated the photoresponsive destruction of the fibril morphology. She applied the drop-casting

method as a fibril coating strategy. She synthesized and characterized the NCL linker, PCL linker, NCL peptide and parts of the PCL peptide and performed parts of the cleavage kinetics. Moreover, she performed parts of the TEM measurements and ThT-Assays and established the turbidity and Proteostat Assays and she interpreted the results. She designed the photomasks, optimized coating techniques of agarose and peptide fibrils, optimized cell-culturing conditions, performed parts of the imaging of the cells and validated thereby the cell-patterning. [REDACTED] investigated the cell patterning and performed the imaging of the proteostat pattern. Therefore, she developed the methodology and performed the experiments, analysed and validated the results. She was involved in scientific discussions, she wrote parts and revised the manuscript. MALDI-Imaging was investigated, validated and analyzed by [REDACTED] and [REDACTED]. [REDACTED] designed the photomasks and revised the manuscript. [REDACTED] optimized the agarose coatings and performed the majority of the agarose coatings. [REDACTED] performed the AFM measurements. [REDACTED] and [REDACTED] provided funding, supervised the agarose coating investigation and revised the manuscript. [REDACTED] and [REDACTED] designed and supervised the project, discussed all experimental data, provided funding, and revised the manuscript.

## 4.2. Abstract

Amyloid-like fibrils are a special class of self-assembling peptides that have emerged as a promising nanomaterial with rich bioactivity for applications such as cell adhesion and growth. Unlike the extracellular matrix, the intrinsically stable amyloid-like fibrils do not respond nor adapt to stimuli of their natural environment. Here, we designed a self-assembling motif (CKFKFQF), in which a photosensitive *o*-nitrobenzyl linker (PCL) is inserted. This peptide (CKFK-PCL-FQF) assembles into amyloid-like fibrils comparable to the unsubstituted CKFKFQF and reveals a strong response to UV-light. After UV irradiation, the secondary structure of the fibrils, fibril morphology and bioactivity are lost. Thus, coating surfaces with the pre-formed fibrils and exposing them to UV-light through a photomask generates well-defined areas with patterns of intact and destroyed fibrillar morphology. The unexposed, fibril-coated surface areas retain their ability to support cell adhesion in culture, in contrast to the light-exposed

regions, where the cell-supportive fibril morphology is destroyed. Consequently, the photoresponsive peptide nanofibrils provide a facile and efficient way of cell patterning, exemplarily demonstrated for A549, CHO and Raw Dual type cells. This study introduces photoresponsive amyloid-like fibrils as adaptive functional materials to precisely arrange cells on surfaces.

### 4.3. Introduction

Nature creates function through complex self-organization processes. In the past few decades, great progress has been made in mimicking these ordered nanostructures with synthetic biomaterials.<sup>[1]</sup> To mimic natural cell distribution and to study cell migration and communication, the spatial control of cell-attachment (cell patterning) is of great interest.<sup>[2–4]</sup> The most frequently used approaches for cell-patterning focus on controlling the stiffness and texture of substrates or the position of cell attractive molecules on inorganic substrates or biomaterials.<sup>[2,5–8]</sup> However, these methods usually lack spatiotemporal control of the morphology of the cellular environment, which plays an essential part in natural matrices that are constantly reshaped by various stimuli.<sup>[9]</sup> For instance, directed cell alignment is controlled by patterning of fibrillar structures from self-assembling peptides (SAPs).<sup>[10]</sup> These fibrillar morphologies have crucial functions in living cells and are thus highly prevalent in the extracellular matrix to enhance material—cell interactions to support proliferation and cell infiltration at the mesoscopic length scale.<sup>[11–13]</sup>

Amyloid fibrils are a subclass of SAPs and Nature's intrinsically bioactive nanofibrils. They are characterized by their high cross  $\beta$ -sheet content, mechanical stiffness, stability towards enzymatic degradation, and strong adhesion to various substrates.<sup>[14]</sup> The best known are amyloid structures in misfolded proteins that lead to insoluble plaques associated with several neurodegenerative diseases.<sup>[15–17]</sup> However, naturally occurring amyloids fulfil various purposes in organisms as scaffold materials.<sup>[18,19]</sup> For example, they are involved in the formation of bacteria biofilms<sup>[20,21]</sup> or as scaffolds for hormone storage<sup>[22]</sup> and melanin polymerization.<sup>[23]</sup> Recently, the potential of amyloid nanostructures serving in beneficial roles have been exploited in 3D cell culture, gene delivery, tissue and neuronal regeneration, as well as drug delivery.<sup>[24–26]</sup> This is due

to the cell adhesive properties that were found for some artificial amyloid fibrils. However, because of the inherent stability of the amyloid fibrils, they cannot readily be quantitatively disassembled in a short time,<sup>[27]</sup> which would be a prerequisite to study morphology dependent cell-adhesive properties, e.g. for the application as adaptive scaffold biomaterials. Synthetic amyloid-like short SAPs that spontaneously form  $\beta$ -sheet-rich nanofibrils through noncovalent interactions<sup>[25,28]</sup> are not related to amyloids found in neurodegenerative diseases and exhibit several distinctively different features. They can be chemically customized to design next generation functional biomaterials with controllable stability and bioactivity.<sup>[17,29,30]</sup>

To gain control over the formation of amyloid structures and thereby their bioactivities, several groups have established strategies to disassemble already formed fibrils. Changing environmental parameters such as peptide concentration and pH can lead to disassembly, as these parameters affect the equilibrium of fibril formation.<sup>[31]</sup> Furthermore, additives such as ruthenium(II)-complexes,<sup>[32]</sup> fullerenes,<sup>[33]</sup> water—ethanol mixtures,<sup>[34]</sup> amphiphilic polyphenylene dendrimers,<sup>[35]</sup> PEG-chains,<sup>[36]</sup> carbon nanotubes,<sup>[37]</sup> and molecular chaperons<sup>[38,39]</sup> have been applied to disassemble amyloid fibrils. However, these methods cannot be applied for controlled spatiotemporal modification after fibrils are embedded in complex environments. Instead, stimulus-sensitive reactive groups have been incorporated in the peptide sequence to initiate morphological changes of fibrils.<sup>[40]</sup> For example, azobenzene and hydrazone groups that undergo a cis-trans isomerization after irradiation<sup>[41–43]</sup> or depsipeptides that reveal a pH-induced structural transition from a kinked to a linear structure<sup>[44,45]</sup> have been proposed to control peptide assembly and disassembly. In these instances, highest spatiotemporal control can only be achieved with light. Since the first pioneering works on photoresponsive manipulation of the cell environment,<sup>[46–49]</sup> a variety of spatial cell-patterning techniques have been applied.<sup>[50]</sup> The overwhelming amount of reports modulate cell attachment by introducing or removing bioactive molecules<sup>[51–54]</sup> or locally changing stiffness of the polymeric (bio)material by crosslinking or bond scission.<sup>[55–57]</sup> Photoresponsive approaches for modulating structural changes in self-assembly of peptides are rarely reported<sup>[58]</sup> and not applied for cell-patterning. *o*-Nitrobenzyl ester is a well-established photoresponsive molecule and can be combined with peptides to attach bioactive molecules.<sup>[11,59]</sup> For example,

using this photocleavable linker (PCL) attached to amyloid-like fibrils, we previously created functional cell-gradients by photocleavage of a bioactive moiety from the fibrillar backbone.<sup>[60]</sup> It is important to note that in these published reports, the fibrillar backbone of the nanofibrils remained intact and also cell-adherent to some extent, limiting the generation of unique cell patterns.

In this work, we solve this limitation by introducing the PCL cleavage motif into the backbone of an amphiphilic self-assembling peptide sequence. UV-irradiation fully destroys the amyloid-like fibrillar morphology, resulting in a complete loss of bioactivity. Consequently, cell-patterning is achieved by coating the fibrils on surfaces and irradiating them with UV-light through a photomask. Our strategy demonstrates a direct connection between amyloid morphology and bioactivity, which is exploited to study cell attachment and migration in artificial cell-matrices. We envision that the spatiotemporal control over structural integrity gives access to tailored and customizable 4D cell-culture.



## 4.4. Results and Discussion

### 4.4.1. Design, Synthesis, and Characterization of the Photoresponsive Self-Assembling Peptide.

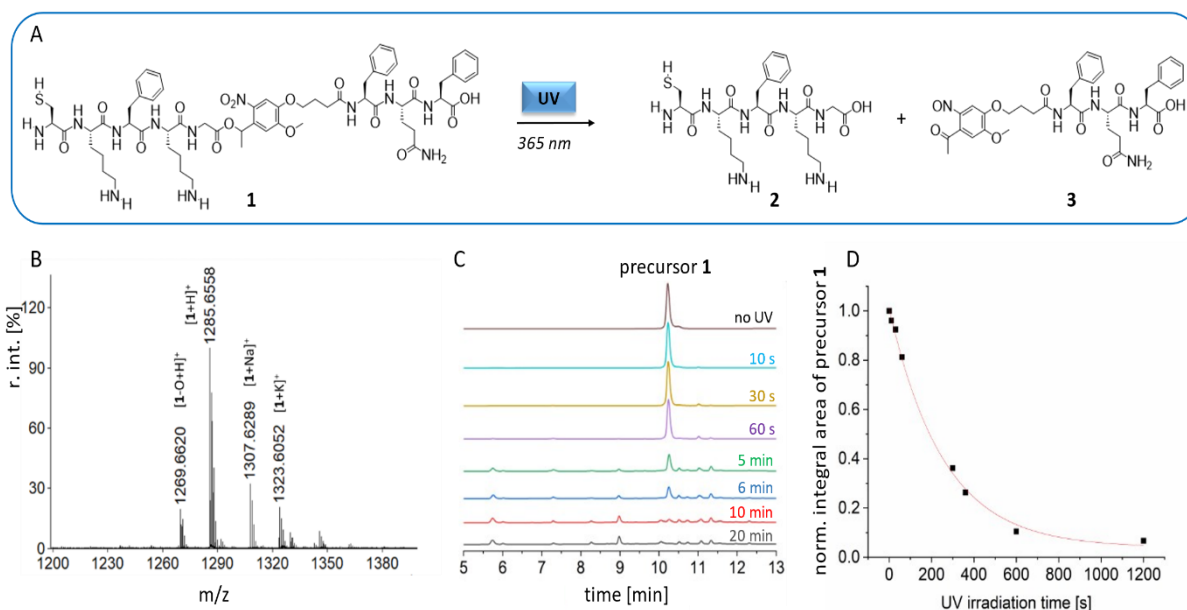


**Figure 17** **A** Scheme of molecular cleavage of the designed peptide CKFK-PCL-FQF **1** under UV-irradiation. **B** MALDI-ToF-MS spectra of the purified peptide CKFK-PCL-FQF, **1**, MS calcd. for  $[1+H]^+$ , 1285.59 g/mol; found  $m/z$  1285.66, calcd for  $[1+Na]^+$ , 1307.57 g/mol; found 1307.63  $m/z$ ., calcd. for  $[1-O+H]^+$ , 1269.60 g/mol found  $m/z$  1269.66. The loss of oxygen ascribed with the mass 1269.66  $[1-O+H]^+$  is caused by high laser power of the MALDI-ToF-MS measurement in HCCA matrix.<sup>[244]</sup> **C** HPLC spectra of CKFK-PCL-FQF peptide after different UV-irradiation times in aqueous solution. After 10 min irradiation, the precursor molecule **1** is completely cleaved. Several decomposition products of **1** were detected via LC-MS (Figure S3). Absorbance detected at 254 nm. **D** first-order kinetics of the integral area from LC traces of the precursor molecule **1** at  $t_{Ret}$  10.2 min normalized to **1** without irradiation (no UV).

The peptide sequence CKFKFQF assembles into cell-adhesive nanofibrils in aqueous media (Figure S1) and was used as scaffold for the design of photocleavable nanofibrils that provide the capacity to disintegrate upon irradiation. CKFKFQF forms biocompatible amyloid-like structures, which were previously shown to enhance neuronal outgrowth *in vitro*.<sup>[61]</sup> We hypothesized that the bioactivity can be traced back to the fibril morphology and speculated that changes in sequence length or amphiphilicity will affect the assembly and bioactivity for short sequences like CKFKFQF. Furthermore, due to its amphiphilic sequence composed of hydrophobic, noncharged Phenylalanine (F) and hydrophilic, cationic Lysine (K) amino acids this peptide represents an ideal starting point to study the effect on assembly by cleaving the hydrophilic charged peptide part from the lipophilic part. In our concept, a photocleavable linker (PCL) was implemented between the third (F) and fourth (K) amino acid of this sequence, resulting in CKFK-PCL-FQF **1**. Even after integration of the PCL linker, this sequence formed amyloid-like nanofibrils serving as bioactive scaffold and stimulating cell adhesion and growth. UV-irradiation leads to a molecular

scission of PCL, resulting in the disintegration of the nanofibrils and the formation of fragments **2** and **3** (Figure 1A), which cannot form fibrils (Figure S1). Additionally, the non-photoreactive control peptide CKFK-NCL-FQF (**4**, Scheme S1) was synthesized and characterized (Figure S8, S9).

Peptide synthesis of **1** and **4** was conducted via SPPS (Scheme S1) using Wang resin. The PCL as well as NCL linkers were synthesized and conjugated to the solid phase bound peptides as described previously.<sup>[60]</sup> Purification of the peptides was accomplished applying reversed-phase HPLC. Successful synthesis and purity (>95%) were validated by MALDI-ToF-MS and LC-MS, respectively (Figure 1B, Figure S2). Next, the photocleavage kinetics were determined by time-dependent measurements, in which aliquots of **1** (1 mg/mL in water) were analyzed by HPLC starting with a non-irradiated sample and irradiation times of up to 20 min (Figure 1C). Using LC-MS measurements (Figure S3), the signal with the retention time of 10.2 min was assigned to the intact peptide showing a mass-to-charge ratio ( $m/z$ ) of 1285.70, matching the protonated  $[1+H]^+$  adduct. After 10 min UV treatment at 365 nm, less than 10% of the intact peptide was detected (Figure 1D). An additional kinetic study was performed, by incubating **1** in DMSO. After one minute of UV-irradiation, complete photocleavage of the peptide CKFK-PCL-FQF was observed (Figure S4), indicating that the cleavage kinetics strongly depend on the selected solvent.<sup>[62]</sup> In contrast, UV-irradiation of the non-cleavable control peptide CKFK-NCL-FQF did not alter its structure nor its elution time after 10 minutes of irradiation in water (Figure S10 – S12) or DMSO (Figure S1).

#### 4.4.2. Secondary Structure and Morphology of Amyloid-like Fibrils is Altered after Irradiation.

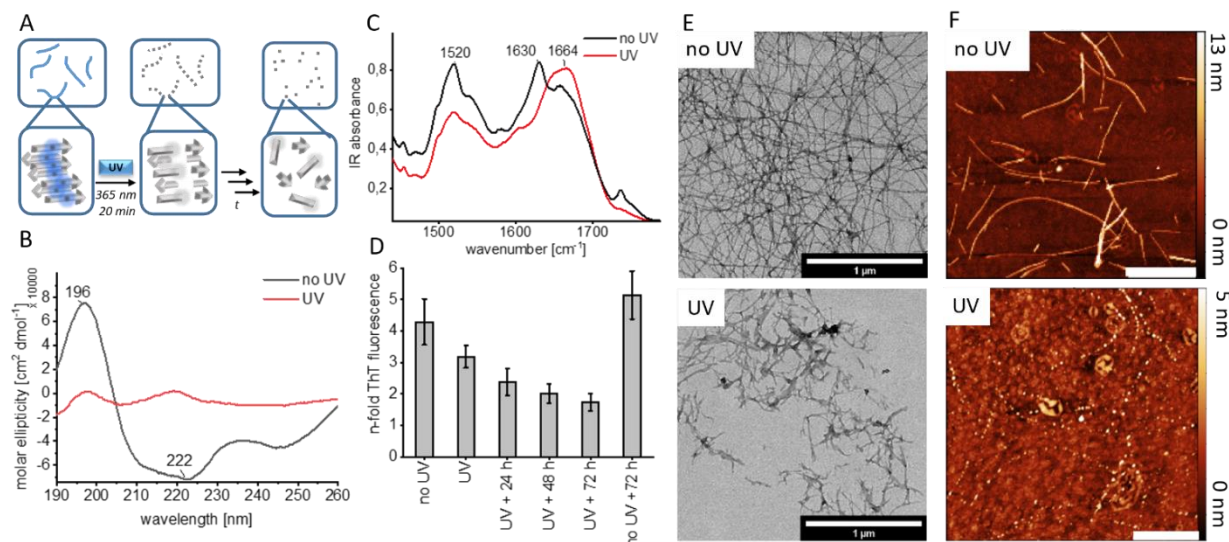


**Figure 18** Secondary structure and morphology of CKFK-PCL-FQF fibrils before and after UV irradiation for 20 min. **A** Schematic illustration of photocleavage of the peptide sequence upon irradiation, which destabilizes the amyloid-like fibrils. **B** Circular Dichroism spectra of non-irradiated versus irradiated fibrils reveal loss of secondary structure after irradiation. **C** ATR-FTIR spectra of non-irradiated and irradiated fibril samples indicate loss of  $\beta$ -sheet structures in the amide I and II regions. **D** Thioflavin-T Assay of non-irradiated fibrils as well as fibrils irradiated for 20 min at 365 nm and incubated at room temperature for 24 h, 48 h, and 72 h. The bar plot shows the n-fold fluorescence relative to ThT fluorescence in water at pH 7.4, excitation 440/10 nm, emission 488/10 nm. **E** TEM micrographs of fibrils before (top) and after irradiation (bottom) displaying morphological changes, scalebar 1  $\mu$ m. **F** Liquid AFM measurements of the fibrils (top) after in situ irradiation for 20 min (bottom) showing destabilization of fibrils into fragments, scalebar 500 nm.

We designed CKFK-PCL-FQF to form amyloid-like fibrils in water at pH 7.4 with similar morphology (Figure 2E) as the original bioactive peptide sequence CKFKFQF (Figure S1).<sup>[63]</sup> The only difference in the structure is the PCL linker, which serves as cleavage site for controlled linker degradation (Figure 2A). After UV irradiation of the CKFK-PCL-FQF nanofibrils, the  $\beta$ -sheet secondary structure is lost, as evidenced by the decrease of the characteristic Cotton peaks for  $\beta$ -sheet structure<sup>[64]</sup> elements at 196 nm and 222 nm in circular dichroism measurements (Figure 2B).

The photoinduced cleavage and disintegration of the  $\beta$ -sheet structures was further supported by ATR-FTIR measurements of lyophilized peptides (Figure 2C). Here, the non-irradiated fibrils showed absorbance maxima in the amide I region at 1630 and 1664  $\text{cm}^{-1}$  corresponding to  $\beta$ -sheet and  $\beta$ -turn structures, respectively, as well as absorbance in the amide II region at around 1520  $\text{cm}^{-1}$ , corresponding to  $\beta$ -sheet structures.<sup>[65]</sup> Upon irradiation of the fibrils in solution, the peak at 1630  $\text{cm}^{-1}$  in the amide I region disappeared, whereas the peak at 1664  $\text{cm}^{-1}$  increased and the amide II band at 1520  $\text{cm}^{-1}$  decreased compared to the non-irradiated sample. These

experimental results indicated loss of  $\beta$ -sheet structures and increase of non-ordered and  $\alpha$ -helical structural elements.<sup>[44,66]</sup>

To elucidate, whether the  $\beta$ -sheet structures of the fibrils dispersed in aqueous media, the ThT assay was conducted, which indicates the presence of amyloid structures by an increase in fluorescence intensity of the ThT molecule after binding to ordered  $\beta$ -sheets structures.<sup>[67]</sup> In this assay, fluorescence intensity of ThT decreased after irradiation of CKFK-PCL-FQF fibrils (Figure 2D), revealing the reduction of  $\beta$ -sheet-rich amyloid-like structures. Interestingly, the ThT fluorescence further decreased, when incubating the irradiated sample in solution for 72h. In contrast to the non-irradiated sample, which shows no decrease in ThT-fluorescence after 72h. The time-dependent decrease in ThT-fluorescence indicates a hysteretic degradation of irradiated fibrils. TEM images that were recorded directly after irradiation for 20 min (Figure 2E) revealed fragments of broken fibrils, which further transformed to irregular aggregates during the selected observation time of 72h (Figure S5). Fragments of broken fibrils may retain the ability to bind ThT to a certain extent, whereas the irregular aggregates cannot. Obviously, the supramolecular structures were destabilized over a prolonged period of time, whereas the intermolecular changes altering the packing of the peptide monomers within the nanofibrils already occurred during the irradiation process.

Liquid AFM measurements of in situ irradiated nanofibrils allowed us to directly study the fragmentation of the nanofibril during irradiation. A clear transition from elongated nanofibrils into spherical aggregates (Figure 2F) was observed. The degradation of the fibrillar morphology was also supported by turbidity measurements of the fibril solution, which increased directly after irradiation and further over the following three days. We interpret the increased turbidity by the formation of a large number of aggregates of the newly formed peptide fragments, indicated by enhanced light scattering of the dispersed sample (Figure S6). The degradation of the nanofibrils did not result in a complete disassembly and solvation of the peptide as shown by microscopy measurements (Figure S5) and by a conversion assay which quantifies aggregated monomers (Figure S7).<sup>[63]</sup> We trace the aggregated structures back to the peptide fragment **3**, which is highly lipophilic due to the phenylalanine side chain

residues and the N-terminal nitrosobenzyl group. Noteworthy, these aggregated peptide fragments do not have  $\beta$ -sheet secondary order as shown by CD and FTIR (Figure 2B, 2C).

In contrast, the integrity of the control peptide CKFK-NCL-FQF was not affected by photoirradiation (TEM, Figure S11, AFM Figure S12 and ThT-assay Figure S13), confirming that the observed structural changes of CKFK-PCL-FQF were due to the photoinduced bond cleavage of the PCL. Photoirradiation of the CKFK-PCL-FQF nanofibrils therefore resulted in immediate loss of the  $\beta$ -sheet structures because of the scission of the peptide backbone in a cationic, hydrophilic (CKFK) and lipophilic (FQF) part. The resulting destabilization of the intermolecular interactions between peptide monomers further lead to fragmentation of the fibrillar assembly into aggregates with no  $\beta$ -sheet secondary order.

### 4.4.3. Photopatterning of Fibril-Coated Surfaces.

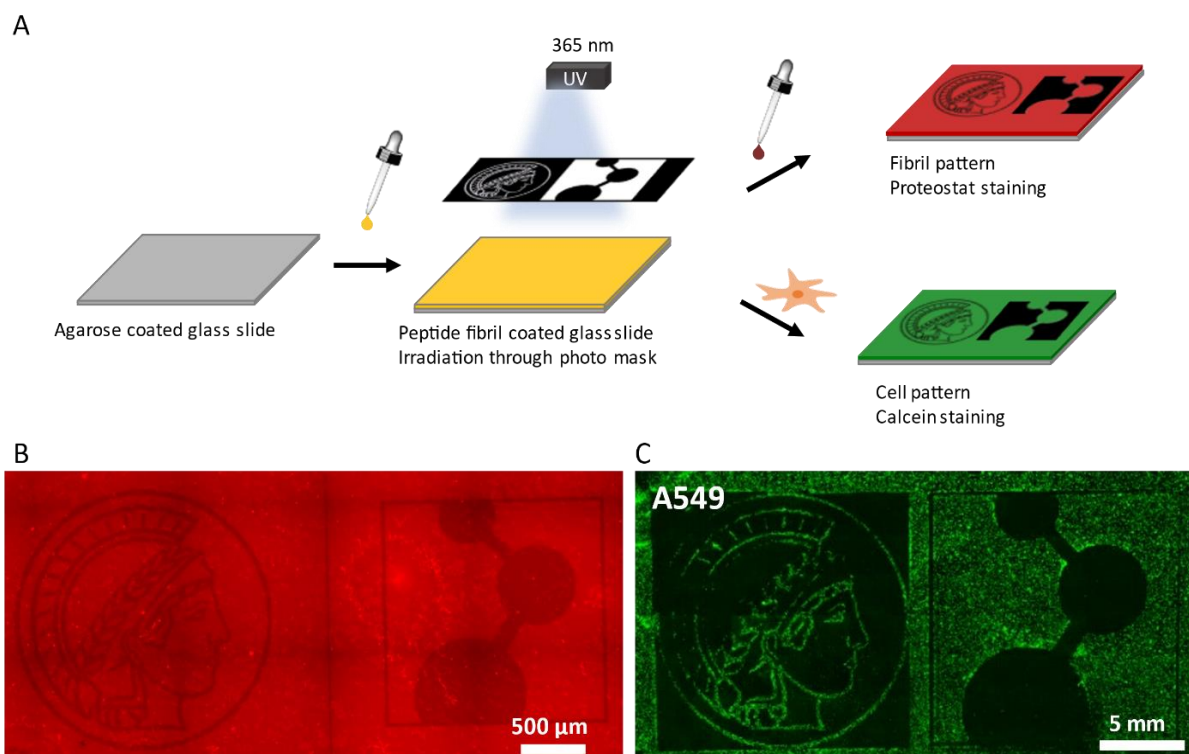


**Figure 19** Patterning of glass slides coated with photocleavable amyloid-like fibrils. **A** Schematic representation of the workflow. The peptide layer is applied on an agarose pre-treated glass slide and exposed to UV-light through a photomask. The fibril morphology is destroyed where UV-light can reach the surface, which is visualized via fluorescence microscopy of Proteostat-stained samples. Before seeding the cells, the photopatterned surface is stored for 5 h in water to allow morphology change of the irradiated parts. Cells seeded for 15 h on the patterns only attach to the non-irradiated regions, where fibrils remained intact. **B** Fluorescence microscope image of Proteostat-stained photopatterned peptide layer depicting the head of Minerva and MPIP logo (scalebar 500 μm). **C** Fluorescence microscopy image of A549 cells seeded on photopatterned peptide layer. The UV-exposure alters the ability of the amyloid-like fibrils to sustain cell culturing and results in cell patterning (scalebar 5 mm).

Next, we investigated whether photolithography could be used to create defined patterns of intact and degraded amyloid-like nanofibrils to create distinct cell-adhesive regions on substrates (Figure 3A). Initially, optical microscope glass slides were covered with a thin agarose layer<sup>[60]</sup> using a dip coating technique. The agarose layer of approximately 50 nm thickness (Figure S14) shows a cell-repellent character and is applied to suppress nonspecific cell adhesion.<sup>[61,68–70]</sup> Subsequently, the slides were coated with an amyloid-like fibril layer via drop casting. As agarose forms gels by physical crosslinks via hydrogen bonds, these interactions may also stabilize the attachment of the peptide fibrils coating and agarose layer.<sup>[71–73]</sup> A photolithography mask was used to cover parts of the peptide film, leaving the rest of it exposed to UV-light. Thereby, a pattern of choice can be imbedded on the substrate that was previously coated with CKFK-PCL-FQF.

We applied different photomasks with different resolution for the photopatterning of peptide nanofibrils (Figure S15). We established MALDI-MSI (mass spectrometry imaging) for characterizing the identity of the formed fragments on the surface. MALDI-MSI directly determines the chemical species on the surface and reveals the distribution of the fragmented peptide **2** with a spatial resolution up to 100  $\mu\text{m}$  (Figure S17). Moreover, photopatterning was visually demonstrated by the Proteostat assay that only stains intact amyloid structures, which can then be detected by fluorescence microscopy. The surface areas that were directly exposed to UV-light reveal less fluorescence and appear darker compared to the non-exposed regions. Via this photopatterning technique resolutions down to 10  $\mu\text{m}$  could be achieved (Figure 3B, Figure S16), which is in the size-range of a single A549 cell and thereby suitable for accurate cell patterning.

#### **4.4.4. Spatially Controlled Cell Pattern.**

We have reported previously that bioactive amyloid-like nanofibrils, which bind to cellular membranes<sup>[63]</sup> and support neuronal outgrowth<sup>[61]</sup> require a positive net charge, fibrillar morphology, as well as high content of  $\beta$ -sheet structures. As demonstrated in the previous sections, the intact CKFK-PCL-FQF peptide can provide these features in regard to their morphology (Figure 2) and charge (Figure S22), but loses them upon irradiation. We therefore aimed to create spatial cell patterns by photoinduced degradation of these fibril properties and applied A549, Chinese Hamster Ovary (CHO) and Raw-Dual type cells as model cell-lines. The cell distribution was analyzed by fluorescence microscopy and attached viable cells were stained in green with calcein (Figure S18). The CellTiter-Glo assay confirmed the nontoxic character of irradiated and non-irradiated fibril regions (Figure S19). A549 cells (Figure 3C), CHO and Raw-Dual cells (Figure S20) did not attach to irradiated areas, whereas non-irradiated areas with intact fibril-coating showed robust cell attachment, which were due to differences in morphology and secondary structure of irradiated and non-irradiated fibril areas. Control experiments without peptide coating and with the non-photoresponsive CKFK-NCL-FQF fibrils did not show any cell attachment and cell patterning, respectively (Figure S21). To determine the resolution

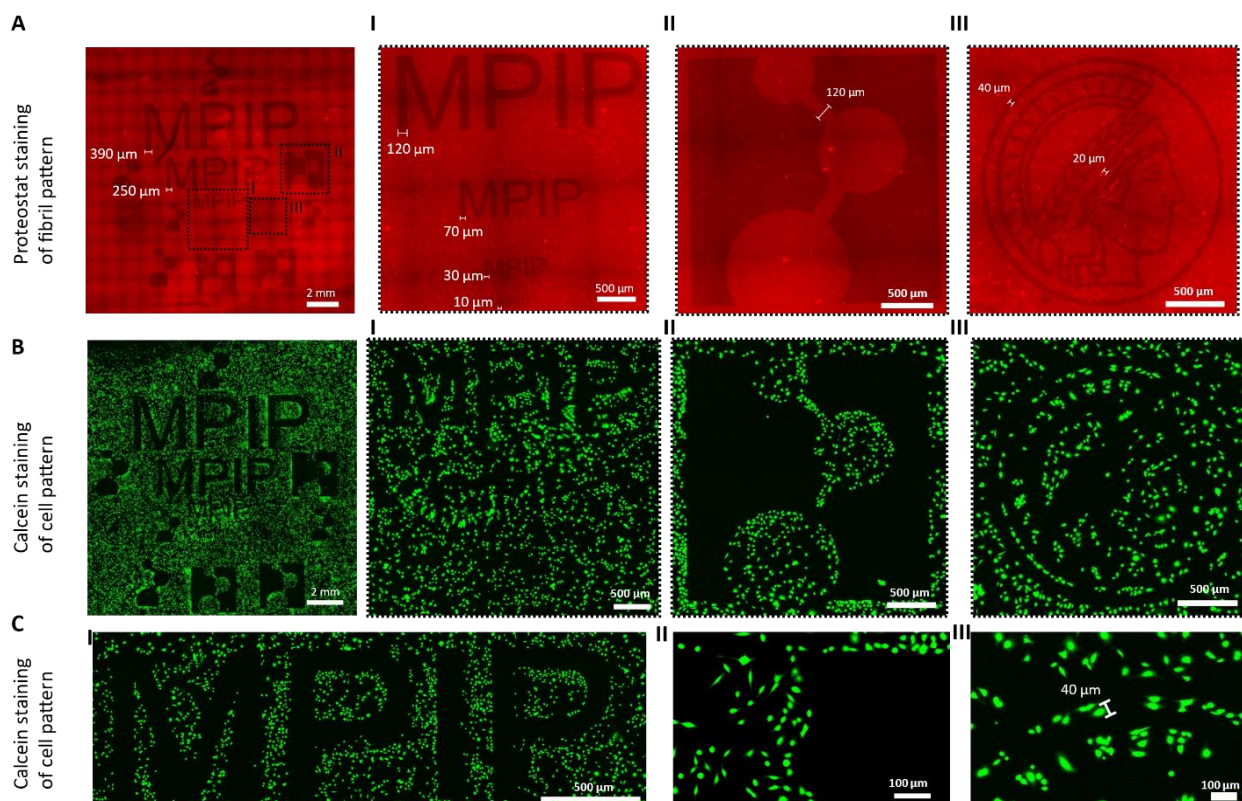


Figure 20 Cell pattern resolution limit shown for A549 cells, which were incubated on a photopatterned peptide fibril surface. A The photomask (Figure S15B) enables the creation of motifs of various size as shown via Proteostat staining (scalebar 2 mm). I-III show regions of interest depicting the smallest resolvable motif, which is 10  $\mu\text{m}$  as part of the letter “M” (scalebar 500  $\mu\text{m}$ ). B Cells seeded on this photopatterned surface (I, scalebar 2 mm) show that cell pattern can be clearly observed for motifs with a size larger than 100  $\mu\text{m}$  (I and II, scalebar 500  $\mu\text{m}$ ) but not for motifs smaller than 40  $\mu\text{m}$  (III, scalebar 500  $\mu\text{m}$ ). C Enlarged details of B-I (scalebar 500  $\mu\text{m}$ ), B-II and B-III (scalebar 100  $\mu\text{m}$ ) show cell alignment at the borders of the patterning motifs. Distance bars show width of indicated patterning elements.

limit for cell-patterning, we applied a photomask with elements of different size down to 10  $\mu\text{m}$  (Figure S15B, Figure 4A). Cell patterns could be clearly identified for fibril patterned elements larger than 100  $\mu\text{m}$  (Figure 4B-I and B-II). Motifs smaller than 40  $\mu\text{m}$  (Figure 4B-III and C-III) cannot be resolved. In summary, cell patterning was achieved by photopatterning of photocleavable peptides on surfaces. Intact fibrillar morphology induced cellular attachment, whereas photocleavage of irradiated fibril surface areas resulted in complete loss of their ability to support cell adhesion.

## 4.5. Conclusion

We have successfully demonstrated the synthesis of a photoreactive self-assembling peptide sequence that forms cell-adhesive fibrillar surface coatings supporting spatially controlled cell attachment. Positioning the photocleavable linker at a critical position within the self-assembling sequence resulted after the irradiation process in



the formation of a positively charged and a lipophilic fragment that were no longer able to form ordered, cell-adhesive nanofibrils. Fibril morphology was locally destroyed through UV-light irradiation as an external trigger resulting in immediate loss of  $\beta$ -sheet structures, nanofibril morphology and cell adhesiveness of the SAPs. Using photomasks, cell-adhesive and cell-repulsive areas were fabricated with resolutions of up to 10  $\mu\text{m}$  precision. We envision that this method could be applied to create UV-treatable peptide layers on various substrates and various cell-types to realize a versatile cell patterning technique and establish amyloid-like fibrils as adaptive functional materials in biologically relevant model environments. Embedding these photoresponsive peptide fibrils into a 3D cell-matrix for spatiotemporal control over structural integrity may provide access to tailored and customizable 4D cell culture materials. More broadly, these findings are important beyond biomaterials applications by providing a direct correlation between morphology and cell-interactions and for understanding bioactivity of amyloid fibrils in general.

## **4.6. Experimental Section/Methods**

### **4.6.1. Materials**

For peptide synthesis, OxymaPure®, Fmoc-Cys(Trt)-OH, Fmoc-Gln(Trt)-OH, Fmoc-Gly-OH, Boc-Gly-OH and Fmoc-Phe-Wang resin and (2-(1H-benzotriazol-1yl)-1,1,3,3-tetramethyluronium hexafluorophosphate (HBTU) were purchased from Novabiochem®, Merck. Fmoc-Lys(Boc)-OH, Fmoc-Phe-OH, piperidine, trifluoroacetic acid (TFA), N,N-diisopropylethylamine (DIPEA) and N,N'-diisopropylcarbodiimide were purchased from Carl Roth GmbH + Co. KG. Peptide-synthesis-grade solvents (dichloromethane, dimethylformamide) were acquired from Acros Organics. Solvents used for synthesis were purchased in HPLC grade purity or higher from Sigma-Aldrich (diethyl ether, dimethylsulfoxide (DMSO), ethanol), Fisher Scientific (dichloromethane, chloroform, hexane, dimethylformamide, acetone, acetonitrile, ethyl acetate, tetrahydrofuran), or VWR Chemicals (methanol). Proteostat® was purchased from Enzo Life Sciences. Thioflavin-T was purchased from Sigma-Aldrich. Dulbecco's modified eagle medium (DMEM), F-12K Nutrient Mixture Kaighns's Modification (Nut Mix (1X)), heat-inactivated (30 min at 56 °C) fetal bovine serum (FBS), MEM non-essential amino acid solution, penicillin (10.000 U/mL) and streptomycin (10.000

µg/mL) were purchased from Gibco (Darmstadt, Germany). Normocin and Zeocin were purchased from InvivoGen.

## 4.6.2. Methods

### Linker-Synthesis

The photocleavable (PCL, 4-(4-(1-((9H-fluoren-9-ylmethoxy)carbonyl)glycyl)oxy)ethyl)-2-methoxy-5-nitrophenoxy) butanoic acid) and non-photocleavable (NCL, 4-(4-(2-(2-((9H-fluoren-9-ylmethoxy)carbonyl)amino)acetamido)ethyl) phenoxy)butanoic acid) linkers were synthesized according to literature.<sup>[11,60]</sup>

### Solid-Phase Peptide Synthesis and Characterization of CKFK-PCL-FQF 1 and CKFK-NCL-FQF 4 (Scheme S1)

Peptides were synthesized using an automated microwave peptide synthesizer (CEM, Liberty Blue™) from C to N-terminus according to fluorenylmethyloxycarbonyl (Fmoc) solid phase peptide synthesis (SPPS) strategy by Merrifield using the Fmoc-L-Phe-Wang resin (Scheme S1). The coupling reaction of the PCL<sup>[60]</sup> (5 equiv) or NCL<sup>[60]</sup> (5 equiv) to the peptide sequence FQF on solid phase was performed manually in DMF with HBTU (5 equiv) and DIPEA (10 equiv) for 24 h at room temperature. Successive coupling of the following amino acids (CKFK) was carried out using an automated microwave peptide synthesizer as described in detail in the supporting information (SI) section 4.9.1. Cleavage from the resin was performed by shaking in a solution of TFA containing 2.5% water and 2.5% triisopropylsilane for 2 h at room temperature. This solution was added to cold diethyl ether (40 mL) to afford a white precipitate and afterward centrifuged three times at 4 °C, 4000 rpm for 15 min. The precipitate was dissolved in water with 0.1% TFA and purified via high performance liquid chromatography (HPLC) (Shimadzu modules DGU-20A5R, LC-20AP, CBM-20A, SPD-M20A, SIL-10AP, FRC-18A with Phenomenex Gemini® 5 µm NX-C18, 110 Å, 150 x 30 mm) using a gradient of water and acetonitrile containing 0.1% TFA as the mobile phase at a flow rate of 25 mL/min. Chromatography was monitored with an UV absorption detector at 214 nm and 254 nm. After lyophilization, a white solid (yield 10%) was obtained. The peptides were identified via matrix assisted laser desorption/ionization time of flight (MALDI-ToF) mass spectrometry and purity (>95%)

was confirmed by liquid chromatography mass spectrometry (LC-MS). MALDI-ToF was conducted on a Bruker rapifleX MALDI-TOF/TOF and a Waters MALDI Synapt G2-SI instrument. The samples were mixed with a saturated  $\alpha$ -cyano-4-hydroxycinnamic acid (HCCA) solution in water/ACN 1:1 + 0.1% TFA before measurement and applied to the target via dried droplet method.<sup>[74]</sup> The data was evaluated with mMass software. LC-MS was conducted on a Shimadzu LC-2020 Single Quadrupole MS instrument with the modules LC-20AD, SIL-20A, SPD-20A, CTO-using a Kinetex EVO and C18 100 Å LC 50 × 2.1 mm column with 2.6 μm pore size. A gradient of acetonitrile/water mixture with 0.1% formic acid (5% ACN to 95% ACN over 20 min) was used as eluent. Samples were dissolved either in methanol or MilliQ water to a concentration of 0.01 mg/mL and monitored at 214 nm absorption. The data was processed with LabSolutions and Origin.

### **Photocleavage Kinetics in Solution**

The photocleavage kinetics in solution were conducted analogous to a previous report.<sup>[60]</sup> Briefly, the peptides were predissolved in DMSO to a concentration of 10 mg/mL and subsequently diluted to a concentration of 1 mg/mL with pure MilliQ water. Irradiation was conducted using an LED by Oplulent Americas (Starboard Luminus SST-10-UV-A130,  $\lambda = 365$  nm) operating at a current of 1 A and a radiant flux of 875 mW with varying exposure times ranging from 0—20 min. 50 μL of the samples were injected per run in a Shimadzu system (modules DGU-20A5R, LC-20AT, CBM-20A, SPD-M20A, SIL-10A, CTO-20AC) with an Agilent ZORBAX Eclipse XDB-C18, 80 Å, 5 μm, 9.4 x 250 mm column at a flow rate of 4 mL/min and MilliQ water and ACN with 0.1% TFA as a gradual eluent from 5 to 80% ACN in 15 min.

### **Nanofibril-Formation**

The peptides were predissolved in DMSO to a concentration of 10 mg/mL. The solution was immediately diluted to 1 mg/mL using MilliQ water. The pH was adjusted to  $7.4 \pm 0.4$  using 0.1 M NaOH and 0.1 M HCl solutions and checked with a pH electrode. To complete fibril formation, the pH-adjusted peptide solution was incubated 24 h at room temperature.

### **Amyloid-like Fibril Characterization from Solution**

Transmission electron microscopy (TEM) measurements, ThioflavinT (ThT) measurements, and attenuated total reflection fourier transform infrared (ATR-FTIR) spectra for nanofibril characterization were prepared and conducted analogous to a previous report.<sup>[60]</sup> Monomer to fibril conversion were determined as previously reported.<sup>[63]</sup> Circular dichroism measurements were conducted on a JASCO 1500 instrument in a 1 mm quartz cuvette (HellmaAnalytics) from 190– 260 nm with preformed fibrils diluted to 0.1 mg/mL. For the characterization of irradiated samples, the preformed fibrils were irradiated in solution with an LED by Opulent Americas (Starboard Luminus SST-10-UV-A130) operated at 365 nm at a current of 1 A and a radiant flux of 875 mW. Unless indicated otherwise, the characterization was conducted immediately after irradiation. The characterization of irradiated fibrils was conducted analogous to non-irradiated samples.

### **Precoating of Microscope Slides with Agarose**

Glass slides were precleaned with acetone and isopropanol. An aqueous agarose solution (1 wt%) was cooked 1 h in order to obtain a fully dissolved and transparent solution. The slides were then dipped in the hot (90°C) agarose solution for 3 min and thereafter slowly (800  $\mu\text{m/s}$ ) lifted up from the solution with an automated stage. The slides were air-dried before further usage.

### **Fabrication of Nanofibril-Coated Surfaces**

Surface coatings of SAPs were achieved by homogenous distribution and incubation of 300  $\mu\text{L}$ , 0.25 mg/mL preformed fibrils on agarose coated microscopy slides (75 by 26 mm) over night. Excess solvent was removed by flipping and the slides were dried. After photo-patterning the slides were stored in MilliQ for 5 h before conducting cell studies.

### **Irradiation of Surface with Photomask**

In order to create patterns of irradiated photoresponsive SAP a photolithography mask (SELBA) was applied. UV exposure was realized with an LED by Opulent Americas (Starboard Luminus SST-10-UV-A130, 20 min,  $\lambda=365$  nm, 1 A, 875 mW) for the patterning of motifs Figure S15A or with a SÜSS MicroTec MA6 mask aligner (10s,  $\lambda=365$  nm, 9 mW/cm<sup>2</sup> 350 W Hg) for the photopatterning of motif Figure S15B.

### **Atomic Force Microscopy**

Atomic force microscopy (AFM) was conducted in liquid state with a JPK NW III atomic force microscope for compound 1 or with a Bruker Dimension FastScan Bio™ atomic force microscope for compound 4. AFM probes with a nominal force constant of 2 N/m or 0.25 N/m were used, respectively and operated in tapping mode with a resonance frequency of 70 kHz (OLTESPA-R3, Bruker). Samples were irradiated in situ by using an LED by Opulent Americas (Starboard Luminus SST-10-UV-A130) operating at a current of 1 A, 875 mW at 365 nm for 20 min while being measured. Images were processed with Gwyddion 2.59.

### **Pattern Analysis by Proteostat Assay**

Proteostat-staining was applied as an amyloid-sensitive dye to detect intact fibrils after UV treatment of 1. A Proteostat Kit by Enzo Lifesciences was used for analysis. 1 µL of the assay buffer was diluted in 99 µL MilliQ water. 0.1 µL of the Proteostat stock solution were added, thoroughly mixed and 500 µL of the solution was placed on the sample to cover the peptide-coated area as well as a part of the non-coated area for reference. After incubation in the dark for 15 min, the solution was removed, and samples were dried. The measurement was conducted on a Leica Thunder DMI8 microscope coupled to a Leica DFC9000 GTC VSC-12365 camera with HC PL FLUOTAR 10x/0.32 DRY objective. The fluorescence emission was detected at 550 nm upon excitation at 475 nm. Images were processed with Leica Application Suite X (LAS X).

### **Cell Culture**

A549 human wild-type cells, a human alveolar basal epithelial carcinoma cell line (obtained from Abcam), were cultivated in DMEM supplemented with 10% heat-inactivated (30 min at 56 °C) FBS, 1% MEM non-essential amino acid solution as well as 1% penicillin (10.000 U/mL) and 1% streptomycin (10.000 µg/mL) at 37 °C under a humidified atmosphere with 5% CO<sub>2</sub>. Chinese Hamster Ovary (CHO) type cells, an epithelial cell line derived from hamster ovaries were cultivated in F-12K Nut Mix supplemented with 10% heat-inactivated (30 min at 56 °C) FBS, 1% penicillin (10.000 U/mL) and 1% streptomycin (10.000 µg/mL). The RAW-Dual reporter cell line (264.7) was purchased from InvivoGen (San Diego, CA, USA) and were cultured in DMEM-GlutaMAX™ medium, which was supplemented with 10% fetal bovine serum, 1%

penicillin/streptomycin, 0.02% normocin, and 0.01% zeocin at 37°C with 5% CO<sub>2</sub> saturation. Cells were reseeded at least twice weekly. For splitting of A549 and CHO cells, the cells were washed with DPBS, trypsinated and resuspended in supplemented culture medium. Splitting of Raw-Dual cells was conducted by scratching cells and resuspending in supplemented culture medium.

For the cell patterning, A549 and CHO cells were washed with PBS, trypsinated, centrifuged (4 min, RT, 500 rpm), resuspended in supplemented medium and Raw-Dual cells were scratched, centrifuged (4 min, RT, 500 rpm) and resuspended prior to, seeding on the respective surfaces with a density of 5x10<sup>4</sup> cells per petri dish (8 cm diameter) in 16 mL medium. This was followed by overnight (15 h) incubation in the respective supplemented culture medium at 37 °C under a humidified atmosphere with 5% CO<sub>2</sub>. Cells were then treated with calcein-AM staining. To this end, cells were washed three times with PBS. The cell-culture medium was then replaced by 15—16 mL supplemented medium containing 1µM calcein-AM solution (prepared from 10 mg/mL solution in DMSO) and cells were incubated at 37°C under a humidified atmosphere with 5% CO<sub>2</sub> for 30 min. Live imaging was performed subsequently on a Leica Thunder DMI8 microscope coupled to a Leica DFC9000 GTC VSC-12365 camera with a N PLAN 5x/0.12 DRY objective. The fluorescence emission was detected using a 519 nm filter upon excitation at 475 nm. Images were processed with Leica Application Suite X (LAS X). All cell-culture experiments were repeated at least in triplicates.

## 4.7. Acknowledgements

[REDACTED]



## 4.8. References

- [1] T. Aida, E. W. Meijer, S. I. Stupp, *Science* **2012**, 335, 813.
- [2] Y. Li, Y. Xiao, C. Liu, *Chem. Rev.* **2017**, 117, 4376.
- [3] J. d'Alessandro, A. Barbier--Chebbah, V. Cellerin, O. Benichou, R. M. Mège, R. Voituriez, B. Ladoux, *Nat. Commun.* **2021**, 12, 4118.
- [4] D. B. Brückner, N. Arlt, A. Fink, P. Ronceray, J. O. Rädler, C. P. Broedersz, *Proc. Natl. Acad. Sci.* **2021**, 118, e2016602118.
- [5] P. Premnath, A. Tavangar, B. Tan, K. Venkatakrishnan, *Exp. Cell Res.* **2015**, 337, 44.
- [6] M. Ventre, C. F. Natale, C. Rianna, P. A. Netti, *J. R. Soc. Interface* **2014**, 11, 20140687.
- [7] C. M. Kelleher, J. P. Vacanti, *J. R. Soc. Interface* **2010**, 7, S717.
- [8] Y. Lin, M. M. Mazo, S. C. Skaalure, M. R. Thomas, S. R. Schultz, M. M. Stevens, *Chem. Sci.* **2019**, 10, 1158.
- [9] C. T. Mierke, *Front. Phys.* **2021**, 9, 619.
- [10] E. C. Wu, S. Zhang, C. A. E. Hauser, *Adv. Funct. Mater.* **2012**, 22, 456.
- [11] S. Sur, J. B. Matson, M. J. Webber, C. J. Newcomb, S. I. Stupp, *ACS Nano* **2012**, 6, 10776.
- [12] I. Wheeldon, A. Farhadi, A. G. Bick, E. Jabbari, A. Khademhosseini, *Nanotechnology* **2011**, 22, 212001.
- [13] G. Ye, F. Bao, X. Zhang, Z. Song, Y. Liao, Y. Fei, V. Bunpetch, B. C. Heng, W. Shen, H. Liu, J. Zhou, H. Ouyang, *Nanomedicine* **2020**, 15, 1995.
- [14] J. Adamcik, F. S. Ruggeri, J. T. Berryman, A. Zhang, T. P. J. Knowles, R. Mezzenga, *Adv. Sci.* **2021**, 8, 2002182.
- [15] G. G. Glenner, C. W. Wong, *Biochem. Biophys. Res. Commun.* **1984**, 122, 1131.
- [16] A. V. Maltsev, S. Bystryak, O. V. Galzitskaya, *Ageing Res. Rev.* **2011**, 10, 440.
- [17] I. Cherny, E. Gazit, *Angew. Chem. Int. Ed.* **2008**, 47, 4062.
- [18] V. A. Iconomidou, G. Vriend, S. J. Hamodrakas, *FEBS Lett.* **2000**, 479, 141.
- [19] J. E. Podrabsky, J. F. Carpenter, S. C. Hand, *Am. J. Physiol. Integr. Comp. Physiol.* **2001**, 280, R123.



- [20] D. Romero, C. Aguilar, R. Losick, R. Kolter, *Proc. Natl. Acad. Sci. U. S. A.* **2010**, 107, 2230.
- [21] A. Taglialegna, I. Lasa, J. Valle, *J. Bacteriol.* **2016**, 198, 2579.
- [22] S. K. Maji, M. H. Perrin, M. R. Sawaya, S. Jessberger, K. Vadodaria, R. A. Rissman, P. S. Singru, K. P. R. Nilsson, R. Simon, D. Schubert, D. Eisenberg, J. Rivier, P. Sawchenko, W. Vale, R. Riek, *Science* **2009**, 325, 328.
- [23] B. Watt, G. van Niel, G. Raposo, M. S. Marks, *Pigment Cell Melanoma Res.* **2013**, 26, 300.
- [24] K. Sato, M. P. Hendricks, L. C. Palmer, S. I. Stupp, *Chem. Soc. Rev.* **2018**, 47, 7539.
- [25] A. K. Das, P. K. Gavel, *Soft Matter* **2020**, 16, 10065.
- [26] N. P. Reynolds, *Biointerphases* **2019**, 14, 040801.
- [27] E. Chuang, A. M. Hori, C. D. Hesketh, J. Shorter, *J. Cell Sci.* **2018**, 131.
- [28] Lee, Trinh, Yoo, Shin, Lee, Kim, Hwang, Lim, Ryou, *Int. J. Mol. Sci.* **2019**, 20, 5850.
- [29] N. Balasco, C. Diaferia, G. Morelli, L. Vitagliano, A. Accardo, *Front. Bioeng. Biotechnol.* **2021**, 9, 130.
- [30] M. Jackson, E. Hewitt, *Biomolecules* **2017**, 7, 71.
- [31] N. Nespovitaya, J. Gath, K. Barylyuk, C. Seuring, B. H. Meier, R. Riek, *J. Am. Chem. Soc.* **2016**, 138, 846.
- [32] G. Son, B. Il Lee, Y. J. Chung, C. B. Park, *Acta Biomater.* **2018**, 67, 147.
- [33] K. Siposova, V. I. Petrenko, O. I. Ivankov, A. Musatov, L. A. Bulavin, M. V. Avdeev, O. A. Kyzyma, *ACS Appl. Mater. Interfaces* **2020**, 12, 32410.
- [34] S. Jordens, J. Adamcik, I. Amar-Yuli, R. Mezzenga, *Biomacromolecules* **2011**, 12, 187.
- [35] S. Xiang, J. Wagner, T. Lückerrath, K. Müllen, D. Y. W. Ng, J. Hedrich, T. Weil, *Adv. Healthcare Mater.* **2022**, 11, 2101854.
- [36] P. A. Rühls, J. Adamcik, S. Bolisetty, A. Sánchez-Ferrer, R. Mezzenga, *Soft Matter* **2011**, 7, 3571.
- [37] D. Lin, J. Lei, S. Li, X. Zhou, G. Wei, X. Yang, *J. Phys. Chem. B* **2020**, 124, 3459.
- [38] P. Arosio, T. C. T. Michaels, S. Linse, C. Månsson, C. Emanuelsson, J. Presto, J. Johansson, M. Vendruscolo, C. M. Dobson, T. P. J. Knowles, *Nat. Commun.* **2016**, 7, 10948.

- [39] A. Franco, P. Gracia, A. Colom, J. D. Camino, J. Á. Fernández-Higuero, N. Orozco, A. Dulebo, L. Saiz, N. Cremades, J. M. G. Vilar, A. Prado, A. Muga, *Proc. Natl. Acad. Sci.* **2021**, 118, e2105548118.
- [40] S. Chagri, D. Y. W. Ng, T. Weil, *Nat. Rev. Chem.* **2022**, 6, 320.
- [41] V. Peddie, A. D. Abell, *J. Photochem. Photobiol. C Photochem. Rev.* **2019**, 40, 1.
- [42] A. A. Deeg, T. E. Schrader, S. Kempter, J. Pfizer, L. Moroder, W. Zinth, *ChemPhysChem* **2011**, 12, 559.
- [43] K. Nakamura, W. Tanaka, K. Sada, R. Kubota, T. Aoyama, K. Urayama, I. Hamachi, *J. Am. Chem. Soc.* **2021**, 143, 19532.
- [44] M. Pieszka, A. M. Sobota, J. Gačanin, T. Weil, D. Y. W. Ng, *ChemBioChem* **2019**, 20, 1376.
- [45] J. Gačanin, J. Hedrich, S. Sieste, G. Glaßer, I. Lieberwirth, C. Schilling, S. Fischer, H. Barth, B. Knöll, C. V. Synatschke, T. Weil, *Adv. Mater.* **2019**, 31, 1805044.
- [46] Y. Luo, M. S. Shoichet, *Nat. Mater.* **2004**, 3, 249.
- [47] T. Matsuda, T. Sugawara, *J. Biomed. Mater. Res.* **1995**, 29, 749.
- [48] D. Ryan, B. A. Parviz, V. Linder, V. Semetey, S. K. Sia, J. Su, M. Mrksich, G. M. Whitesides, *Langmuir* **2004**, 20, 9080.
- [49] S. Zhang, L. Yan, M. Altman, M. Lässle, H. Nugent, F. Frankel, D. A. Lauffenburger, G. M. Whitesides, A. Rich, *Biomaterials* **1999**, 20, 1213.
- [50] F. M. Yavitt, B. E. Kirkpatrick, M. R. Blatchley, K. S. Anseth, *ACS Biomater. Sci. Eng.* **2022**, acsbiomaterials.1c01450.
- [51] C. A. DeForest, K. S. Anseth, *Angew. Chem. Int. Ed.* **2012**, 51, 1816.
- [52] R. J. Wade, E. J. Bassin, W. M. Gramlich, J. A. Burdick, *Adv. Mater.* **2015**, 27, 1356.
- [53] D. S. Hernandez, E. T. Ritschdorff, S. K. Seidlits, C. E. Schmidt, J. B. Shear, *J. Mater. Chem. B* **2016**, 4, 1818.
- [54] I. Batalov, K. R. Stevens, C. A. DeForest, *Proc. Natl. Acad. Sci.* **2021**, 118, e2014194118.
- [55] B. D. Fairbanks, S. P. Singh, C. N. Bowman, K. S. Anseth, *Macromolecules* **2011**, 44, 2444.
- [56] C. Yang, F. W. DelRio, H. Ma, A. R. Killaars, L. P. Basta, K. A. Kyburz, K. S. Anseth, *Proc. Natl. Acad. Sci.* **2016**, 113, E4439.

- [57] A. M. Kloxin, A. M. Kasko, C. N. Salinas, K. S. Anseth, *Science* **2009**, 324, 59.
- [58] J. B. Matson, Y. Navon, R. Bitton, S. I. Stupp, *ACS Macro Lett.* **2015**, 4, 43.
- [59] S. V. Wegner, O. I. Sentürk, J. P. Spatz, *Sci. Rep.* **2016**, 5, 18309.
- [60] A. M. Ender, K. Kaygisiz, H.-J. Räder, F. J. Mayer, C. V. Synatschke, T. Weil, *ACS Biomater. Sci. Eng.* **2021**, 7, 4798.
- [61] C. Schilling, T. Mack, S. Lickfett, S. Sieste, F. S. Ruggeri, T. Sneideris, A. Dutta, T. Bereau, R. Naraghi, D. Sinske, T. P. J. Knowles, C. V. Synatschke, T. Weil, B. Knöll, *Adv. Funct. Mater.* **2019**, 29, 1809112.
- [62] M. E. Lee, E. Gungor, A. M. Armani, *Macromolecules* **2015**, 48, 8746.
- [63] S. Sieste, T. Mack, E. Lump, M. Hayn, D. Schütz, A. Röcker, C. Meier, K. Kaygisiz, F. Kirchhoff, T. P. J. Knowles, F. S. Ruggeri, C. V. Synatschke, J. Münch, T. Weil, *Adv. Funct. Mater.* **2021**, 31, 2009382.
- [64] N. J. Greenfield, *Nat. Protoc.* **2007**, 1, 2876.
- [65] A. Adochitei, G. Drochioiu, *Rev. Roum. Chim.* **2011**, 56, 783.
- [66] M. Jackson, H. H. Mantsch, *Crit. Rev. Biochem. Mol. Biol.* **1995**, 30, 95.
- [67] C. Xue, T. Y. Lin, D. Chang, Z. Guo, *R. Soc. Open Sci.* **2017**, 4, 160696.
- [68] J. Jeong, Y. Lee, Y. Yoo, M. K. Lee, *Colloids Surf. B. Biointerfaces* **2018**, 162, 306.
- [69] W. Y. Seow, K. Kandasamy, G. S. L. Peh, J. S. Mehta, W. Sun, *ACS Biomater. Sci. Eng.* **2019**, 5, 4067.
- [70] F. Topuz, A. Nadernezhad, O. S. Caliskan, Y. Z. Menciloglu, B. Koc, *Carbohydr. Polym.* **2018**, 201, 105.
- [71] R. Armisen, *Hydrobiologia* **1991**, 221, 157.
- [72] S. Arnott, A. Fulmer, W. E. Scott, I. C. M. Dea, R. Moorhouse, D. A. Rees, *J. Mol. Biol.* **1974**, 90, 269.
- [73] K. Nakamura, R. Kubota, I. Hamachi, *ChemRxiv* **2022**, 10.26434/chemrxiv.
- [74] A. A. Patil, C.-K. Chiang, C.-H. Wen, W.-P. Peng, *Anal. Chim. Acta* **2018**, 1031, 128.
- [75] X. Zhan, D. M. Desiderio, *Int. J. Mass Spectrom.* **2009**, 287, 77.
- [76] A. Barth, J. E. T. Corrie, M. J. Gradwell, Y. Maeda, W. Mäntele, T. Meier, D. R. Trentham, *J. Am. Chem. Soc.* **1997**, 119, 4149.
- [77] A. Resemann, L. Liu-Shin, G. Tremintin, A. Malhotra, A. Fung, F. Wang, G. Ratnaswamy, D. Suckau, *MABs* **2018**, 10, 1200.

## 4.9. Supporting Informations

### 4.9.1. Methods

#### Microwave assisted solid phase peptide synthesis

Peptides were synthesized using an automated microwave peptide synthesizer (CEM, Liberty Blue™) from C to N terminus according to fluorenylmethyloxycarbonyl (Fmoc) solid phase peptide synthesis (SPPS) strategy by Merrifield (Scheme S1). N,N'-Diisopropylcarbodiimide (0.5 M in DMF) and ethyl cyano(hydroxyimino)acetate (1.0 M in DMF) were used as activator and base, a piperidine solution (20 vol% in N,N'-dimethylformamide (DMF)) was used for deprotection and DMF as the main washing agent. The preloaded polystyrene (PS) based Fmoc-L-Phe-Wang resin (Novabiochem®, loading: 0.68 mmol/g, 100–200 mesh) and side-chain functionality protected L-amino acids were used for coupling. Depending on the reaction scale, reagents were prepared as suggested by CEM in the Liberty Blue™ User Guide.

For 0.1 mmol synthesis scale, Fmoc-L-Phe-Wang resin (0.1 mmol, 0.65 mmol/g) was swelled in DMF for an hour before synthesis. In the automated peptide synthesizer (Liberty Blue, CEM), another short swelling in 10 mL DMF for 5 min was carried out. Fmoc-deprotection was carried out with 3 mL of a 20% piperidine in DMF solution while heating to 75 °C (155 W) for 15 s and 90 °C (30 W) for 50 s. Subsequently, the resin was washed with DMF twice with 2 mL and once with 3 mL for 5 min each. Coupling of the amino acids was conducted using 2.5 mL of a 0.2 M solution of the respective amino acid in DMF, 1 mL of a 0.5 M DIC in DMF solution and 0.5 mL of a 1.0 M Oxyma in DMF solution, followed by heating to 75 °C (170 W) for 15 s and 90 °C (30 W) for 110 s and flushing with 2 mL DMF. Final deprotection was carried out using 20% piperidine in DMF as previously described. The synthesized linkers were coupled to the FQF sequence on the resin in a separate reaction vessel. Successive coupling of CKFK to the resin was carried out using the same cycle as previously described. Cleavage from the resin was carried out by shaking in a solution of TFA (95%), TIPS (2.5%) and MilliQ water (2.5%) for 2 h at room temperature. Subsequently, the solution was transferred into ice-cold diethyl ether for precipitation and the mixture was centrifuged three times at 4 °C, 4000 rpm for 15 min. The remaining liquid was disposed, and the pellet stored in the freezer.

## **Turbidity measurements**

Turbidity measurements were conducted with a Zetasizer Nano S instrument (Malvern Panalytic) in a micro cuvette (ZEN0040) with 70  $\mu\text{L}$  of the undiluted nanofibril sample at room temperature. The derived count rate of scattered light provided information on turbidity of the sample before and after irradiation.

## **MALDI-MSI**

For the matrix assisted laser desorption ionization mass spectrometry imaging (MALDI-MSI) measurements the peptide layer was coated on an agarose pre-treated indium tin oxide (ITO) slide. The peptide layer was photopatterned and spray-coated with a solution of MALDI matrix  $\alpha$ -cyano-4-hydroxycinnamic acid (HCCA, 10 mg/mL in 70% ACN, 30%  $\text{H}_2\text{O}$ , 0.2% TFA, Sigma-Aldrich, Germany) analogous to a previous report.[60] Acquisition of the MALDI MSI spectra were carried on a MALDI-TOF mass spectrometer (rapifleX TOF/TOF, Bruker, Bremen, Germany) in the reflection mode using the software Compass 2.0 (Bruker GmbH, Bremen, Germany) and FlexImaging 5.0, (Bruker GmbH Bremen, Germany). An area of 60 mm  $\times$  3.5 mm was scanned in steps of 10  $\mu\text{m}$  using a laser profile M5.<sup>[59]</sup> A pixel size of 10  $\mu\text{m}$   $\times$  10  $\mu\text{m}$ , 26% laser intensity, 1000 shots/pixel and a laser pulse repetition rate of 10 kHz was used. Distribution of peak intensities were visualized with the software Scils Lab Pro 2019 (Bruker, Germany) with a color gradient of ion signal intensities<sup>[2]</sup> normalized to total ion current (TIC).

## **Cell Viability Analysis (CellTiter-Glo Assay)**

A549 cell viability in presence of peptide nanofibrils was tested using a CellTiter-Glo Assay (Promega G7571). A549 cells were seeded with a density of 18000 cells/mL in 96-well plates before treatment and incubated for 24 h. 5  $\mu\text{L}$  of the prepared samples were added to 45  $\mu\text{L}$  cell culture medium to a final concentration of 0.1 mg/mL. 1  $\mu\text{M}$  staurosporine was added as a negative control, pure cell culture medium served as positive control. The plates were incubated for 24 h at 37  $^\circ\text{C}$ . The wells were washed with DPBS, and the CellTiter-Glo Assay was performed according to manufacturer's instructions. Luminescence was detected using a GloMax Multi 96-well plate reader (Promega). All samples were measured in sextuplicates.

## **Zeta Potential**

To reveal surface charges, the electrophoretic mobility of fibrils was measured and converted to  $\zeta$ -potentials. Here, 60  $\mu\text{L}$  of preformed fibrils (10 mg/mL DMSO solution diluted in PBS to obtain a 1 mg/mL concentration and subsequently incubated for 24 h) were diluted in 600  $\mu\text{L}$  of 1 mM KCl solution. The measurement was conducted in 1 mL disposable DTS1070 folded capillary cells (Zetasizer Nano series, Malvern Panalytical) on a Zetasizer Nano ZS (Malvern Panalytical) at 25°C. The  $\zeta$ -potential values were converted via Zetasizer Nano Software (Malvern Panalytical).

#### 4.9.2. Additional Characterization CKFK-PCL-FQF 1

#### Comparison of fibril morphology via TEM of CKFKFQF, CKFK-PCL-FQF 1 and CKFK-NCL-FQF 4 after irradiation of monomers in DMSO

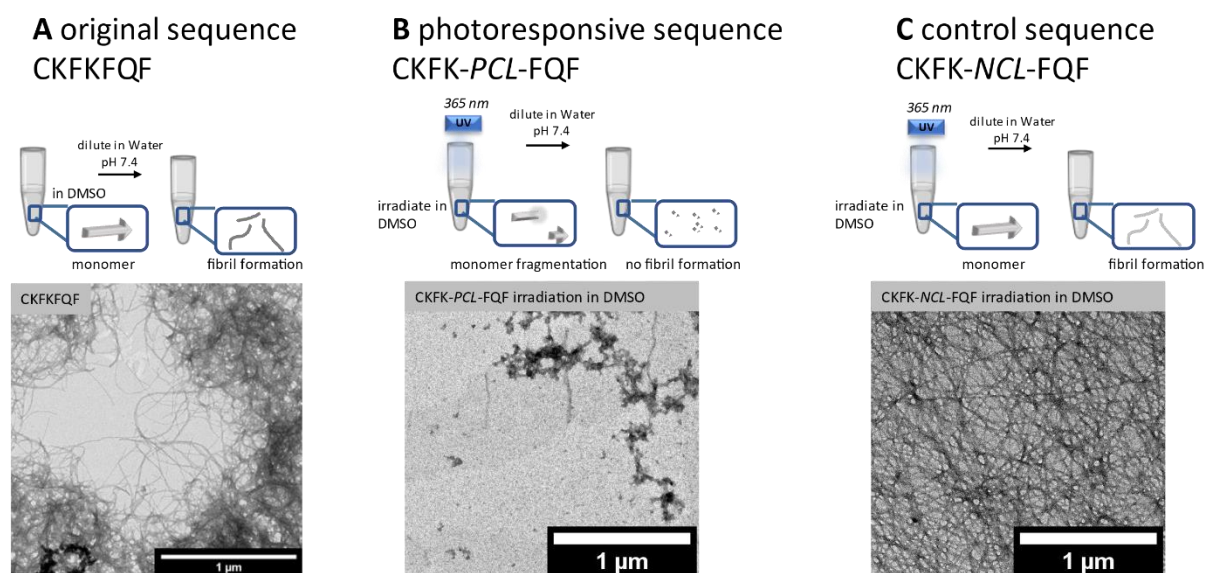


Figure S1: TEM micrographs of CKFKFQF,<sup>[61]</sup> CKFK-PCL-FQF 1 and CKFK-NCL-FQF 4. A Fibril morphology of the original sequence CKFKFQF<sup>[61]</sup> diluted from DMSO (10 mg/mL) in water (1 mg/mL) at pH 7.4. B UV irradiation of monomeric CKFK-PCL-FQF in DMSO (10 mg/mL) for 10 min and subsequent incubation in water (1 mg/mL) at pH 7.4. C UV irradiation of monomeric CKFK-NCL-FQF in DMSO (10 mg/mL) for 10 min and subsequent incubation in water (1 mg/mL) at pH 7.4, scalebar 1 $\mu\text{m}$ .

## LC-MS

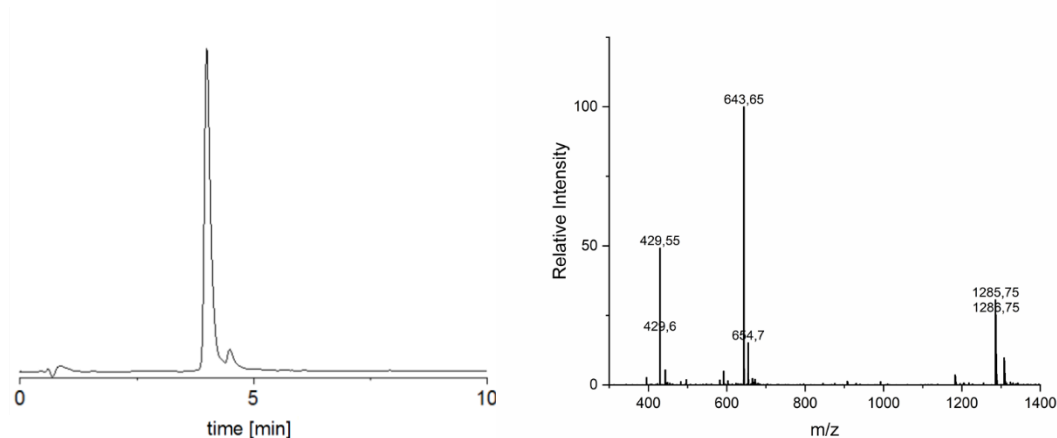


Figure S2: A LC-MS chromatogram (detector: 214 nm) of CKFK-PCL-FQF 1 B MS (ESI+)  $m/z$  calc. for CKFK-PCL-FQF  $[1+3H]^{3+}$ , 429.19 g/mol; found  $m/z$  429.55,  $[1+2H]^{2+}$ , 643.29 g/mol; found  $m/z$  643.65 and  $[1+H]^+$ , 1285.58 g/mol; found  $m/z$  1285.75.

## Photocleavage kinetics of CKFK-PCL-FQF 1 in water

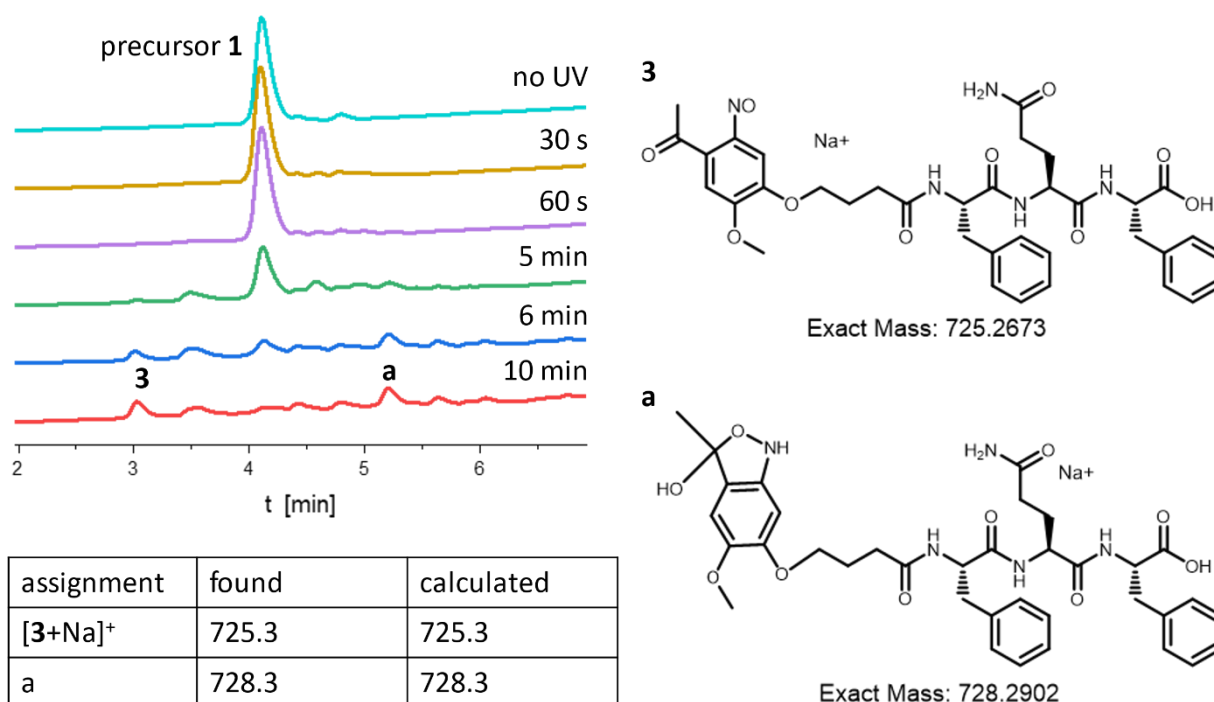


Figure S21: LC-MS traces of CKFK-PCL-FQF before UV and after UV exposure for 30 s, 60 s, 5 min, 6 min and 10 min in water. Absorbance detected at 254 nm. Photocleavage of 1  $t_{Ret}$  4.1 min result in several decomposition products because the photocleavage reaction is driven by radical reaction. Two main peaks which can be assigned to the proposed main fragment 3  $t_{Ret}$  3.0 min can be found with another by-product a  $t_{Ret}$  5.2 min caused by thiol-side reactions as detected and assigned via ESI-MS.<sup>[245]</sup> a is a ring-chain tautomer of 3, the ratio between the main fragment 3 and a is 49:51.

## Photocleavage kinetics of CKFK-PCL-FQF 1 in DMSO

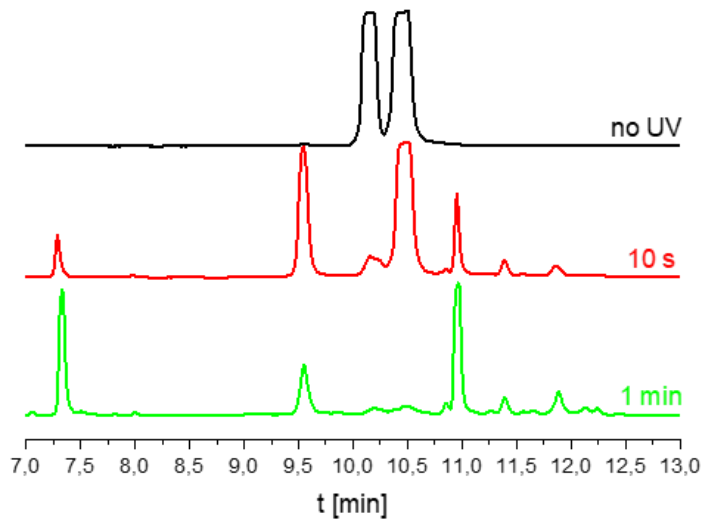


Figure S4: HPLC traces of CKFK-PCL-FQF 1 before UV and after UV exposure for 10 s and 60 s after 24 h incubation time in pure DMSO. Absorbance detected at 190 nm. After 60 s of irradiation, the precursor molecule is completely photocleaved. The two peaks visible in the non-irradiated sample can be assigned to CKFKF-PCL-FQF in its monomeric and dimerized form. Incubation in pure DMSO for 24 h results in disulfide bond formation as identified by mass spectrometry of the respective peaks (data not shown).

## TEM

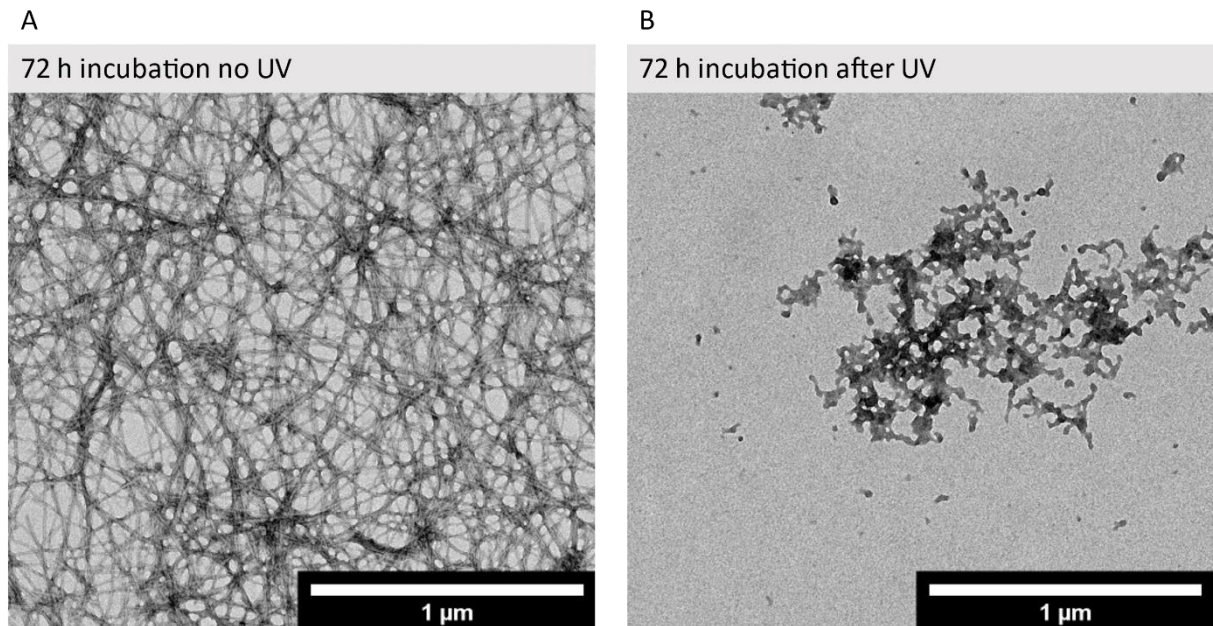


Figure S22: TEM micrographs of CKFK-PCL-FQF 1 after 72 h of incubation in water at pH 7.4. A without UV irradiation and B with UV irradiation of the peptide fibrils in solution for 20 min.



## Turbidity of CKFK-PCL-FQF 1 before and after irradiation by DLS

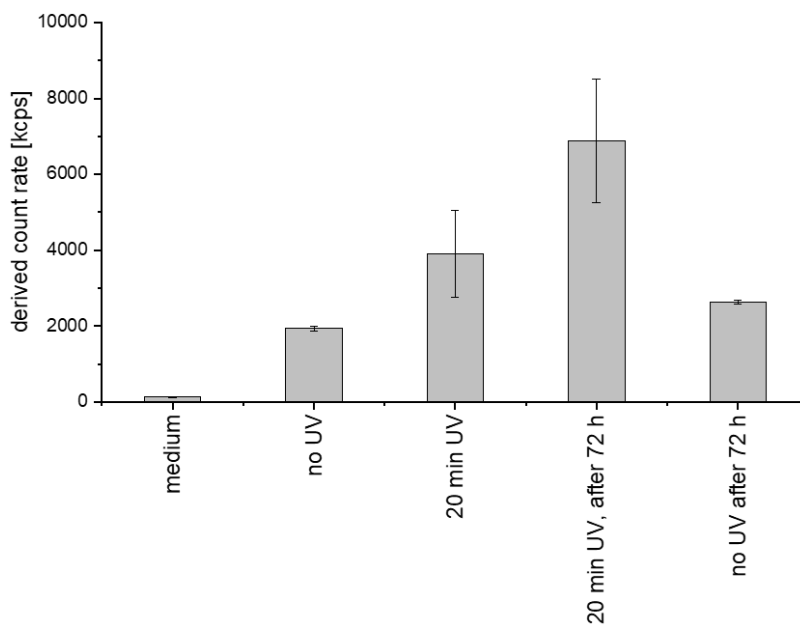


Figure S23: DLS count rate of scattered light (600 nm) of CKFK-PCL-FQF 1 solution 1 mg/mL before and after irradiation at 365 nm and after incubation at rt for 72 h.

## Conversion of monomers to aggregated monomers before and after irradiation of CKFK-PCL-FQF 1

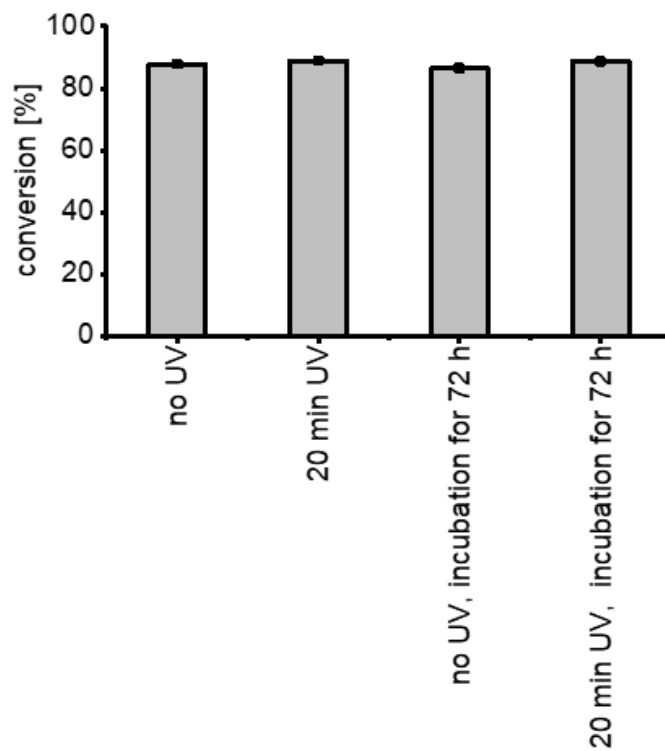


Figure S7: Conversion rate assay. Irradiated and non-irradiated CKFK-PCL-FQF 1 solution at 1 mg/mL before and after incubation at rt for 72 h.

### 4.9.3. Additional Characterization CKFK-NCL-FQF 4

#### LC-MS

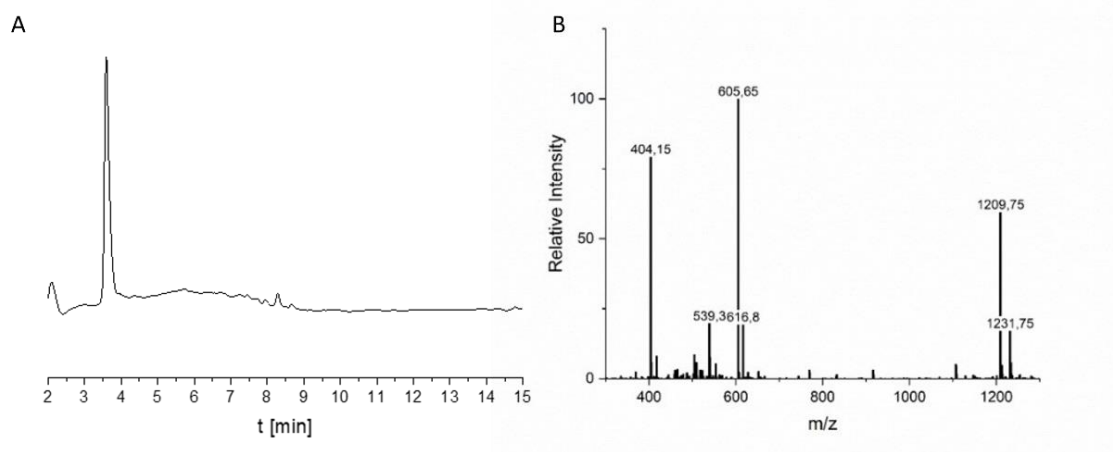


Figure S8: A LC-MS chromatogram (detector: 214 nm) of CKFK-NCL-FQF 4. B MS (ESI+)  $m/z$  calc. for  $[4+3H]^{3+}$ , 403.87 g/mol; found  $m/z$  404.15,  $[4+2H]^{2+}$ , 605.31 g/mol; found  $m/z$  605.65,  $[4+H]^+$ , 1209.61 g/mol; found  $m/z$  1209.75 and  $[4+Na]^+$ , 1231.61 g/mol; found  $m/z$  1231.75.

#### MALDI-ToF-MS

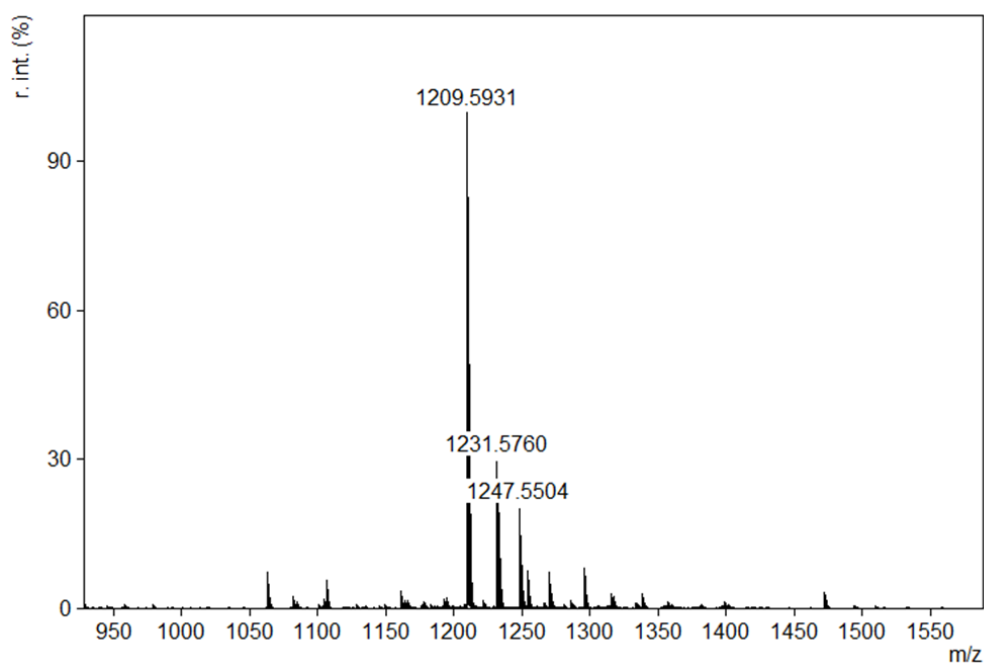


Figure S9: MALDI-ToF-MS of CKFK-NCL-FQF 4 with  $m/z$  calc. for  $[4+H]^+$ , 1209.61 g/mol; found  $m/z$  1209.59,  $[4+Na]^+$ , 1231.61 g/mol; found  $m/z$  1231.57 and  $[4+K]^+$ , 1247.61 g/mol; found  $m/z$  1247.55.

## HPLC study of CKFK-NCL-FQF

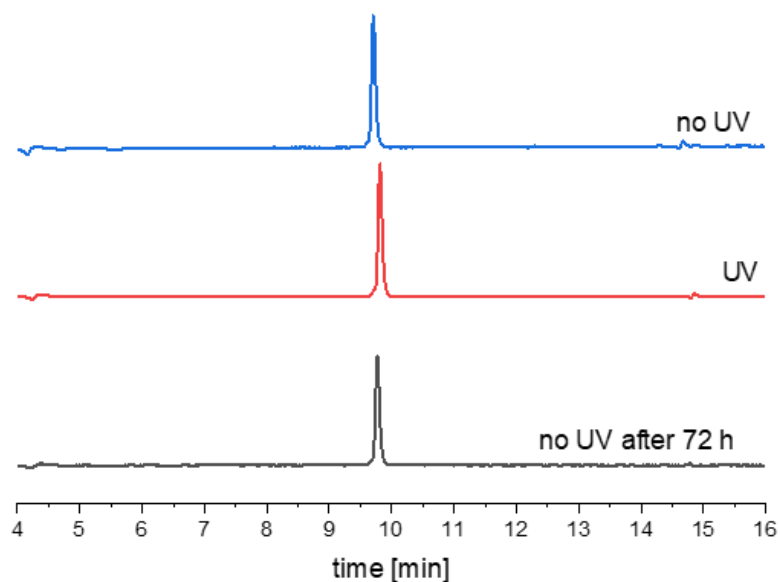


Figure S10: HPLC traces of CKFK-NCL-FQF 4 fibrils after no UV (24 h and 72 h incubation time) and UV exposure for 10 min after 24 h incubation time. Absorbance detected at 254 nm.

## TEM of CKFK-NCL-FQF fibrils before and after irradiation

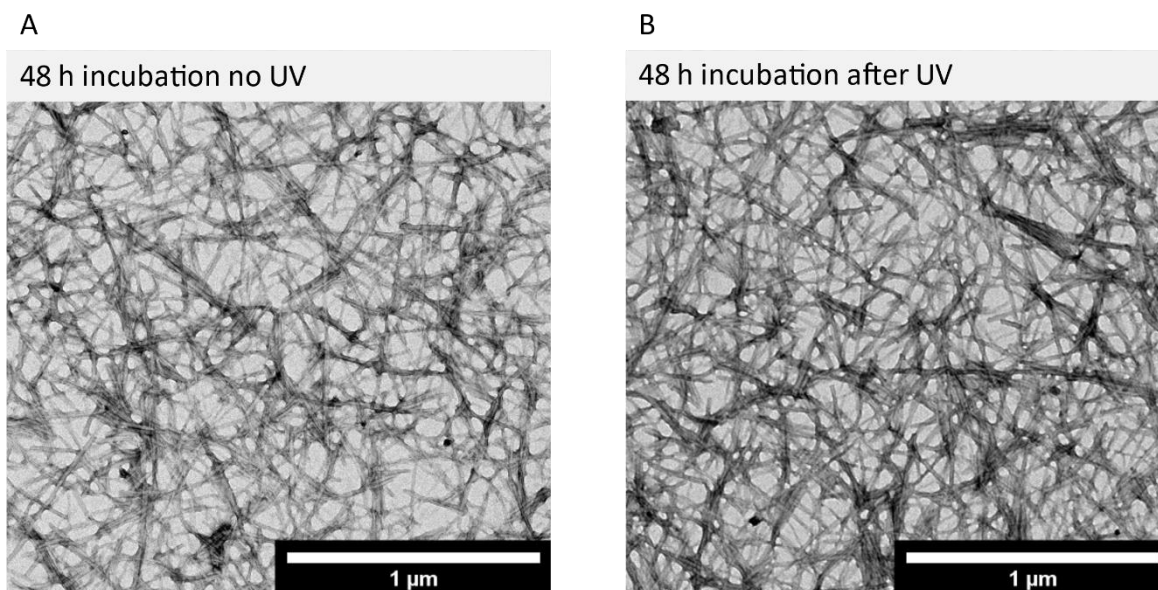


Figure S11: TEM micrographs of CKFK-NCL-FQF 4 after 48 h of incubation in water at pH 7.4. A without UV irradiation and B with UV irradiation of the peptide solution for 20 min.

## AFM of in situ irradiated CKFK-NCL-FQF 4

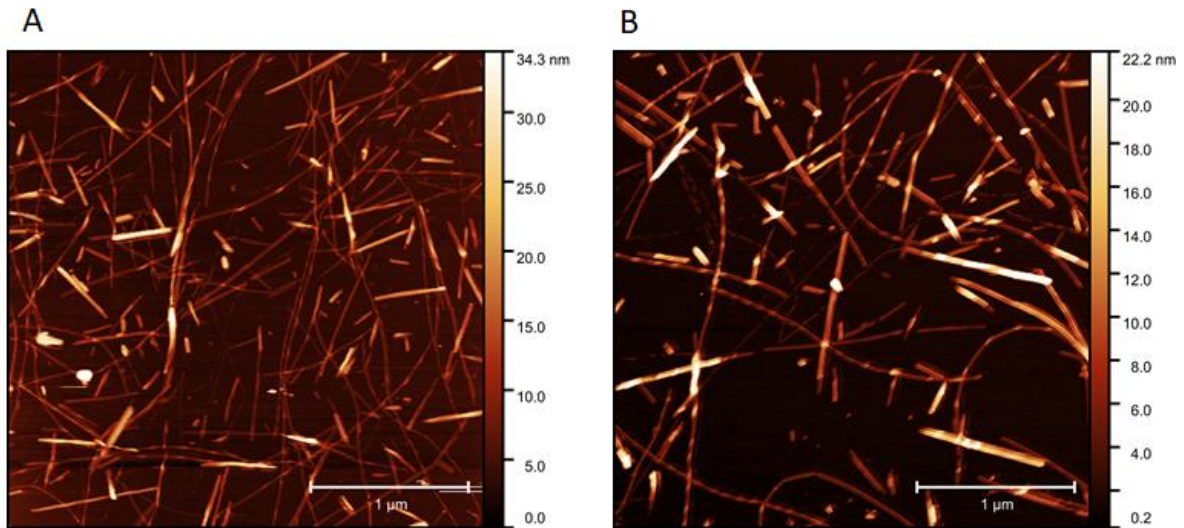


Figure S12: Liquid AFM measurement of CKFK-NCL-FQF 4 after of incubation in water at pH 7.4. A without UV irradiation and B with in situ UV irradiation of the peptide solution for 20 min.

### ThT-Assay of CKFK-NCL-FQF 4

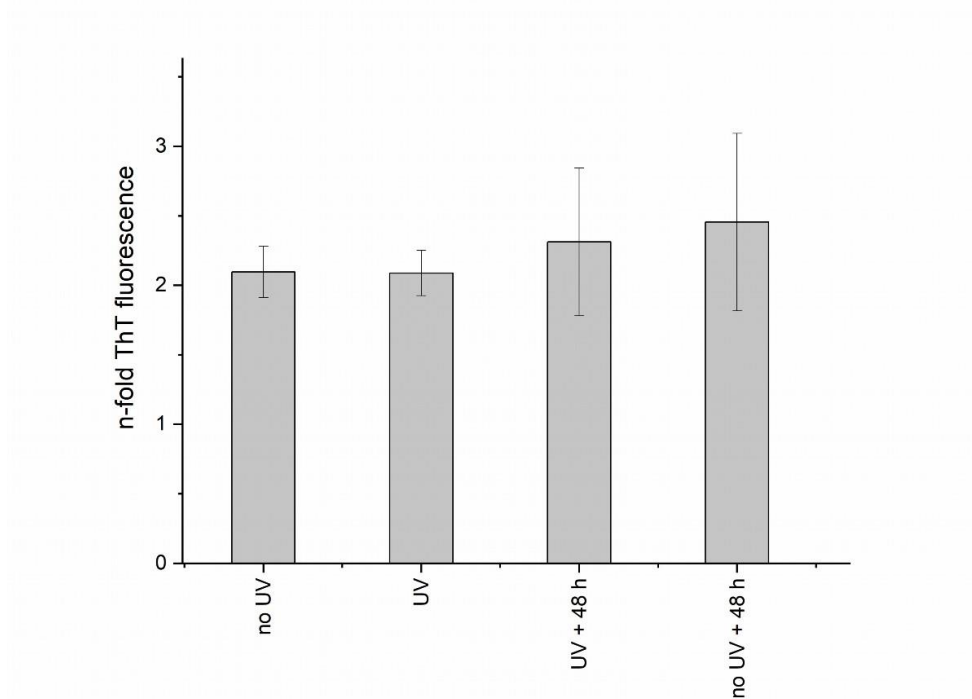


Figure S13: N-fold ThT fluorescence for CKFK-NCL-FQF nanofibrils before and after UV irradiation for 20 min and after 48 h incubation before and after UV irradiation for 20 min.

#### 4.9.4. Peptide Coating and Patterning

##### Photomasks for patterning peptide fibrils

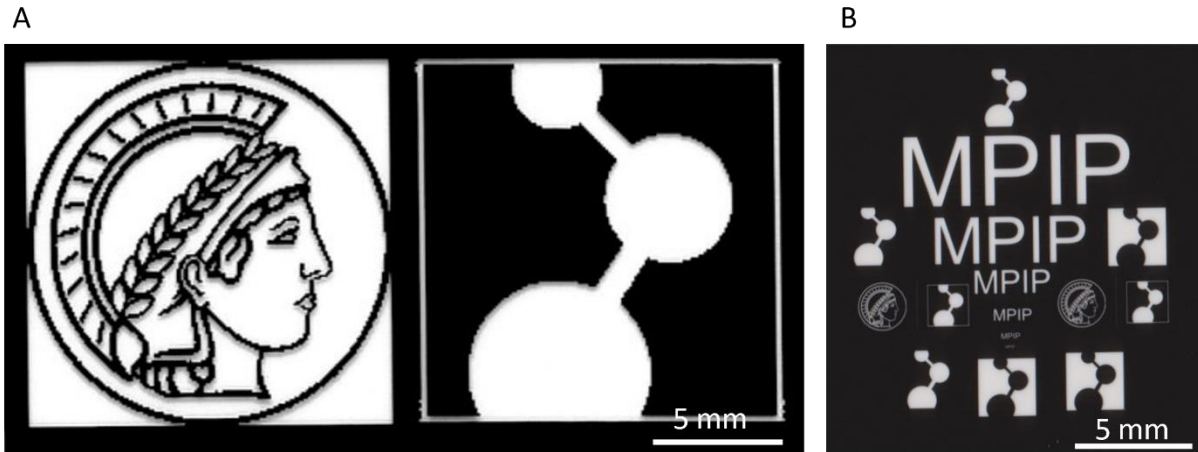


Figure S15: Overview of photomasks for patterning of peptide fibrils and cells. A Photomasks for patterning cells, scalebar 5 mm. B Photomask with smallest elements line thickness 10 - 40  $\mu\text{m}$ , scalebar 5 mm.

## Proteostat staining of photopatterned surface

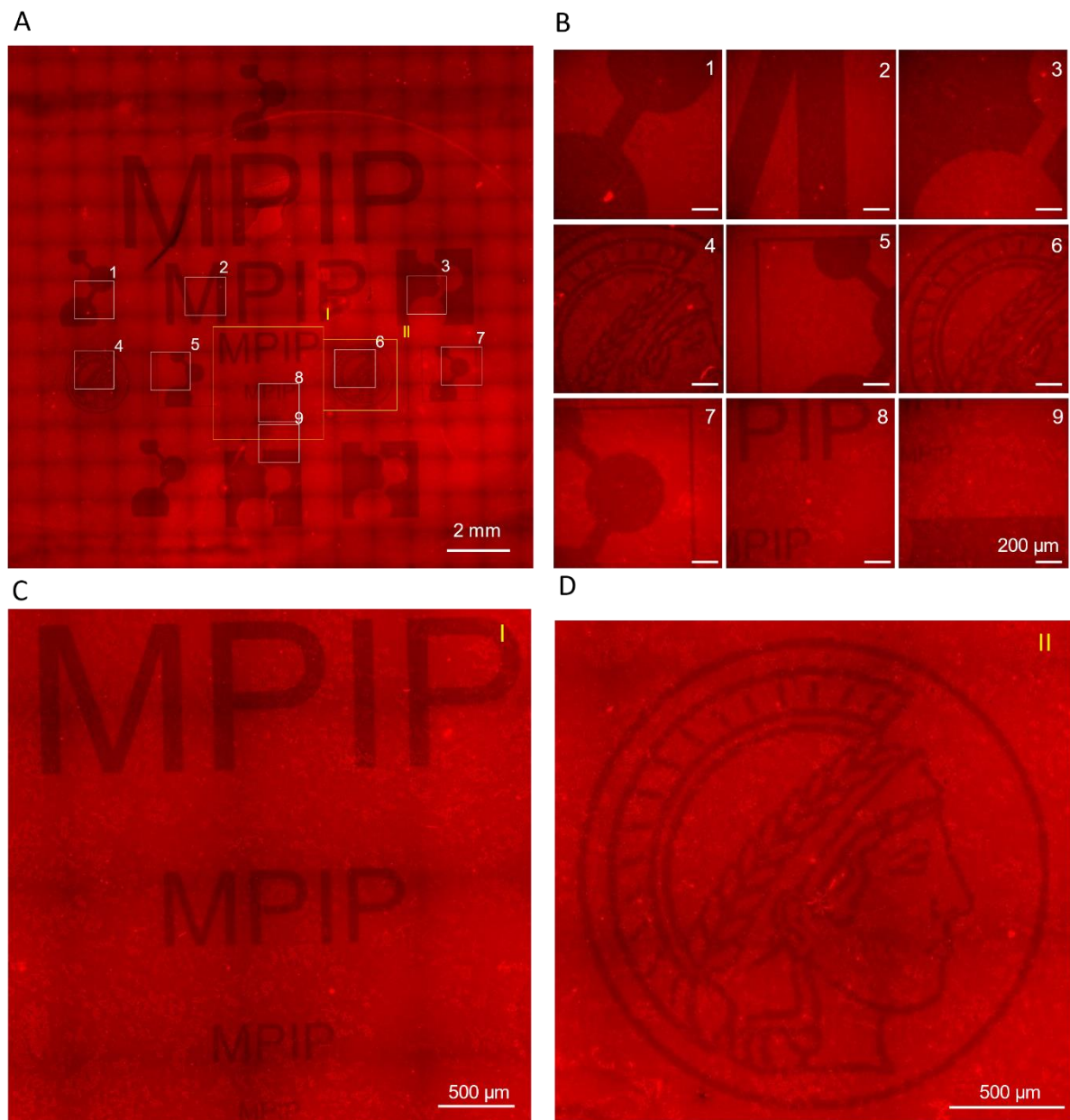
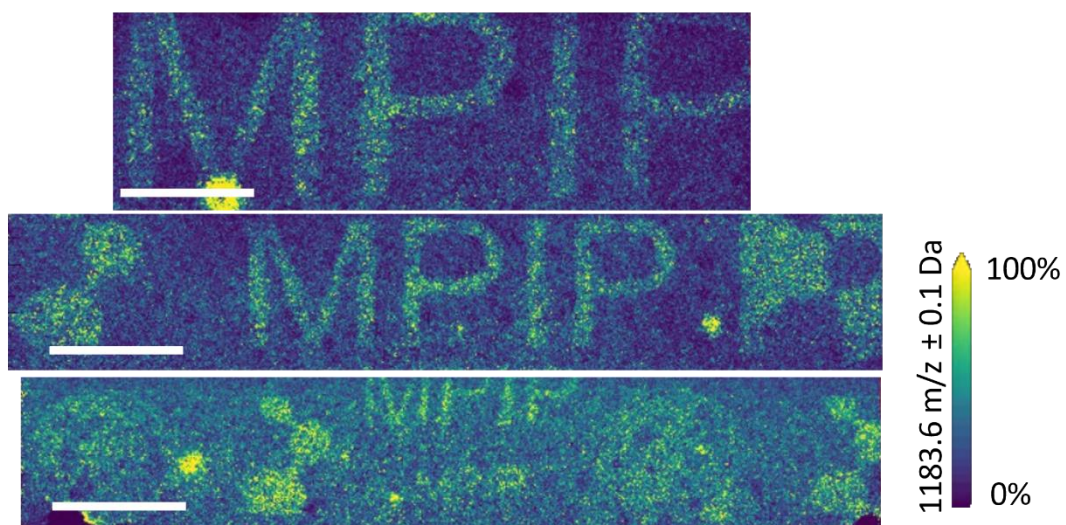


Figure S16: Fluorescence microscopy of photopatterned peptide layer of 1 after Proteostat-staining. Detailed overview of photopatterned surface: A tile scan over irradiated area (scale bar 2 mm), B ROI 1-9: single images of specific areas (scale bar 200  $\mu\text{m}$ ), C Region of interest (ROI) I: „MPIP“ tile scan (scale bar 500  $\mu\text{m}$ ) (MPIP: Max Planck Institute for Polymer Research ), D ROI II: Head of Minerva, a trademark of the Max Planck Society tile scan (scale bar 500  $\mu\text{m}$ ).

## MALDI MSI of photopatterned peptide layer

A  $[2M_f(\text{DSB})+\text{Na}]^+ 1183.57\text{Da}$



B  $[M_f(\text{DSB})+\text{H}]^+ 616.26\text{Da}$

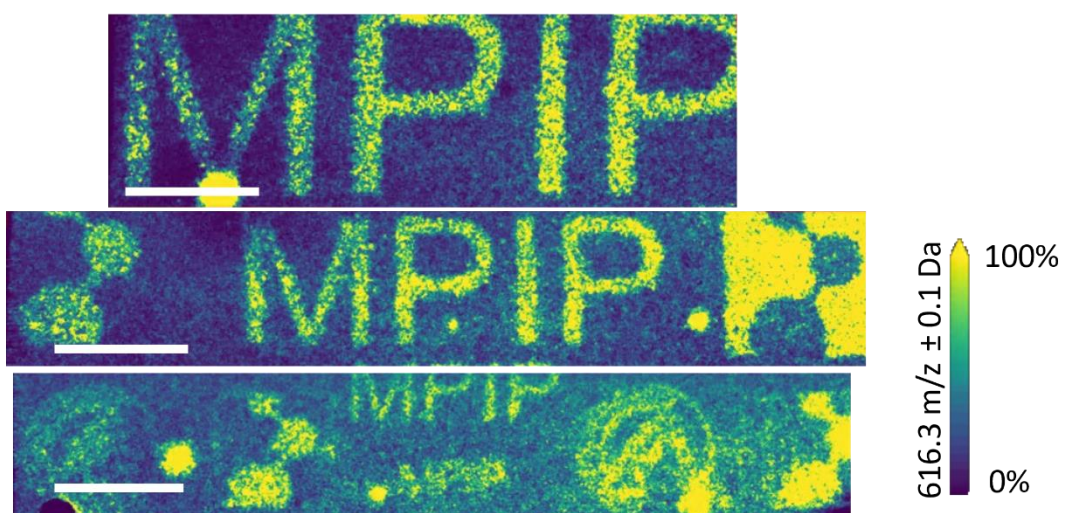
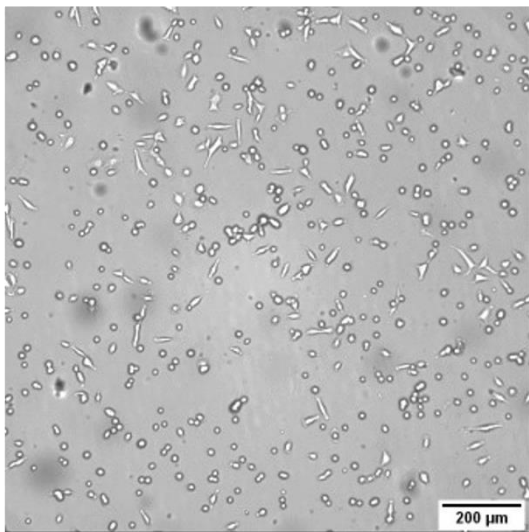


Figure S17: MALDI-MSI of photopatterned peptide layer of 1. A MALDI-MSI results visualize the photopatterning via distribution of the mass intensity of the disulfide bonded peptide (DSB)<sup>[246]</sup> of the fragment (Mf (DSB): 2+S) with sodium counter ion  $[2M_f(\text{DSB})\text{Na}^+] = 1183.57\text{Da}$  and B with the fragment peptide of  $[M_f(\text{DSB}) + \text{H}]^+ = 616.26\text{Da}$  (In-Source-Decay fragment of the disulfide bonded peptide of  $2M_f(\text{DSB})$ <sup>[246]</sup> Scalebars 2 mm.

## Cell-Viability of A549 on photopatterned surface

A



B

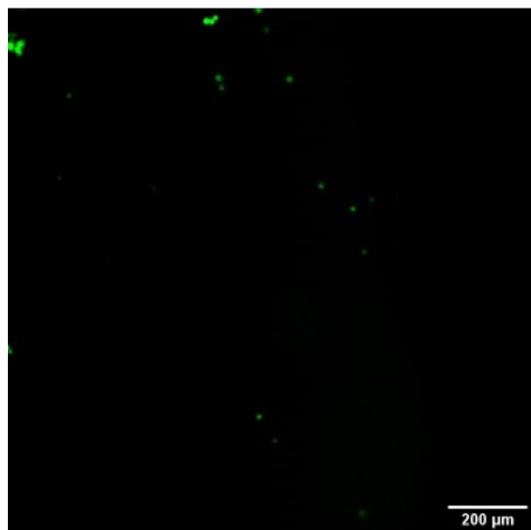
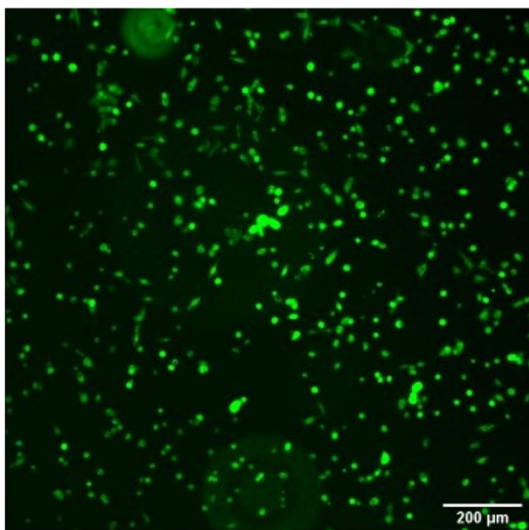
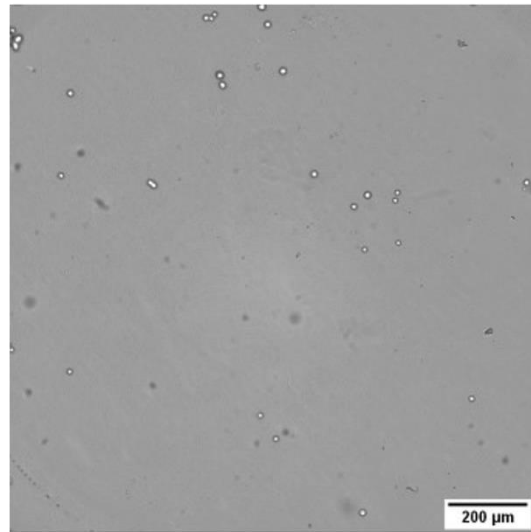


Figure S18: Imaging of calcein staining of A549 cells on CKFK-PCL-FQF peptide coated agarose slides A before irradiation with UV and B after UV-irradiation for 20 min. Top brightfield, bottom UV fluorescence image. Cells were seeded after irradiation. Scalebar 200 μm.



### Cell Titer Glo Assay of CKFK-PCL-FQF fibrils

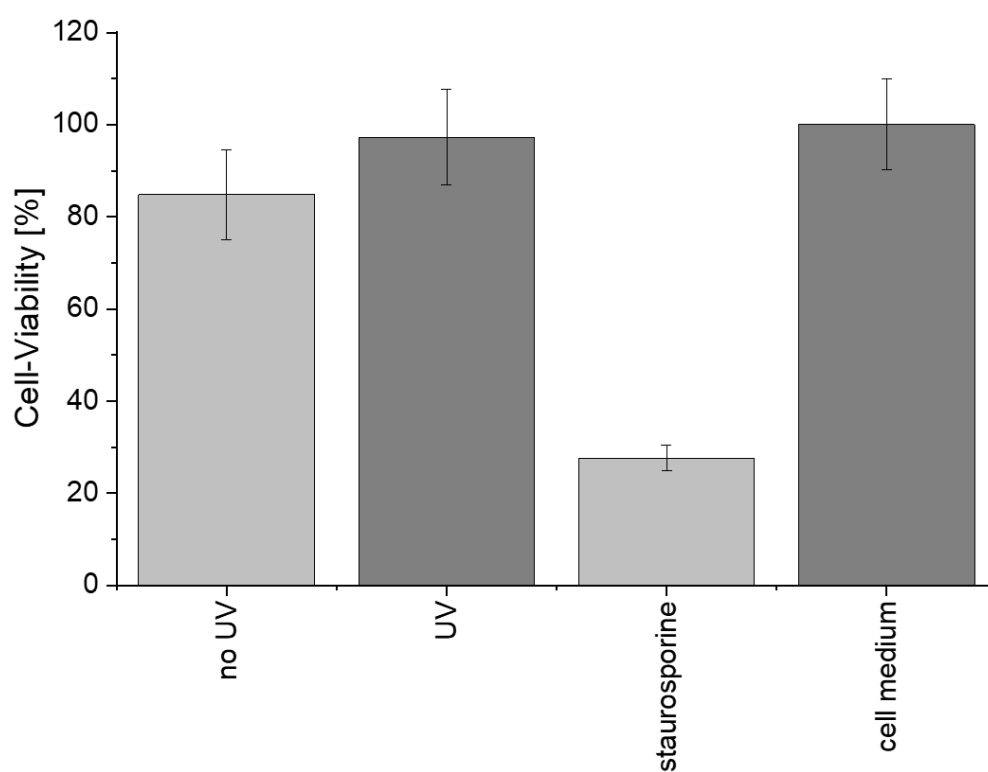


Figure S19: CellTiter-Glo Assay of preformed fibrils from CKFK-PCL-FQF 1 with and without UV irradiation for 10 minutes. 1  $\mu$ M staurosporine was added for a negative control, pure cell culture medium served as positive control.

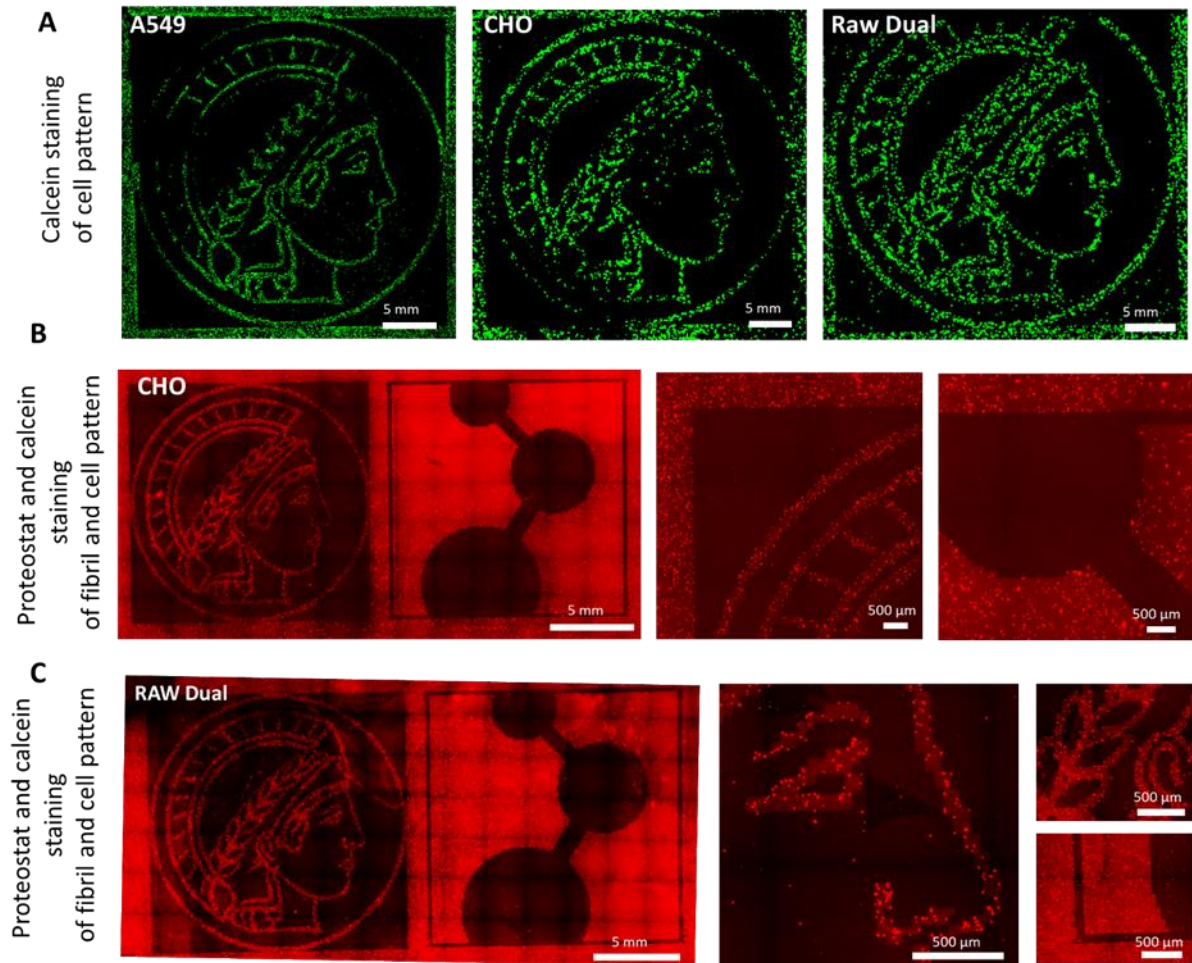
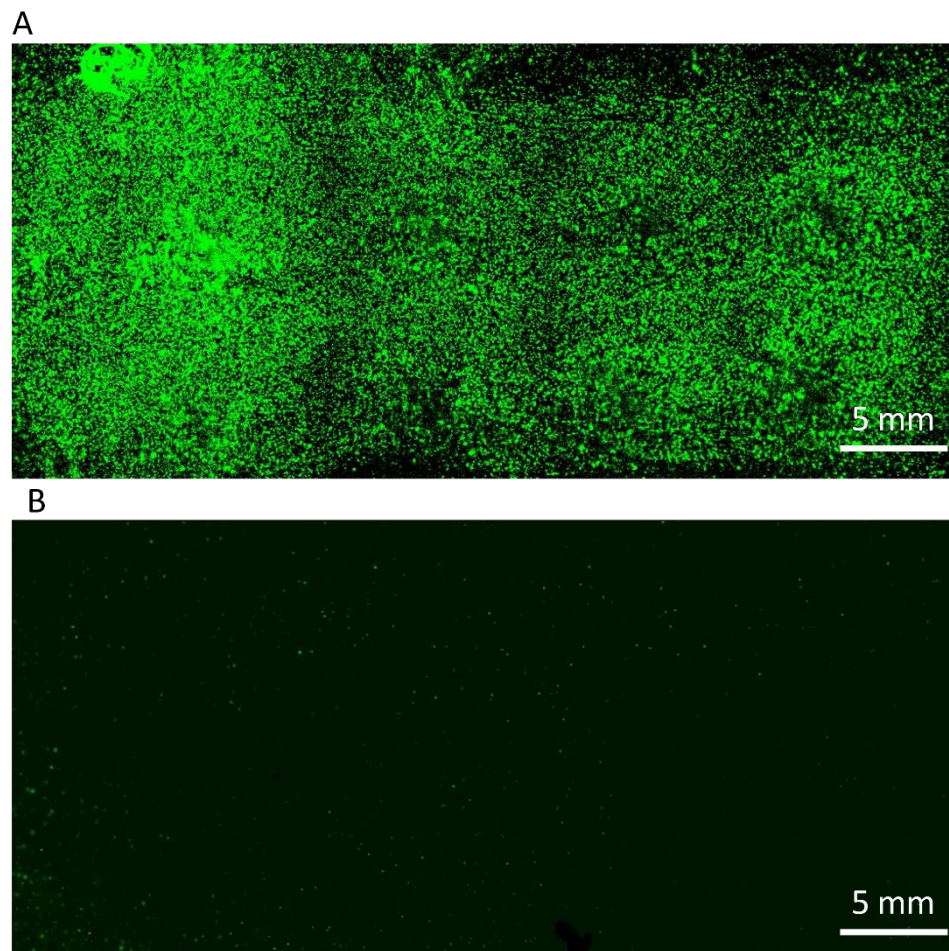


Figure S20: Cell patterning with three different cell types on surfaces irradiated with photo mask shown in Figure S15A. A Fluorescence microscopy measurement of calcein stained A549, CHO and Raw Dual cells display the head of Minerva, a trademark of the Max Planck Society, scalebar 5 mm. B Simultaneous calcein and Proteostat staining of CHO cells and C Raw Dual cells show that cells attach to intact peptide fibrils, which appear brighter upon Proteostat staining, whereas non-fibrillar parts, which are less fluorescent, cannot maintain cell attachment, scalebar left 5 mm, right 500  $\mu\text{m}$ .

**Control patterning experiments with non-responsive peptide fibrils CKFKF-NCL-FQF and with agarose coated slide without peptide fibrils.**



*Figure S24: Control patterning study with A549 cells seeded on non-responsive CKFKF-NCL-FQF 4 fibrils and agarose treated slide without peptide fibrils, which were irradiated with MPI-P logo motif Figure S15A. A As expected, no cell patterning can be observed for CKFKF-NCL-FQF fibrils and B cells cannot attach well to agarose coated slide if peptide fibrils are not applied (scalebar 5 mm).*

## Zeta Potential

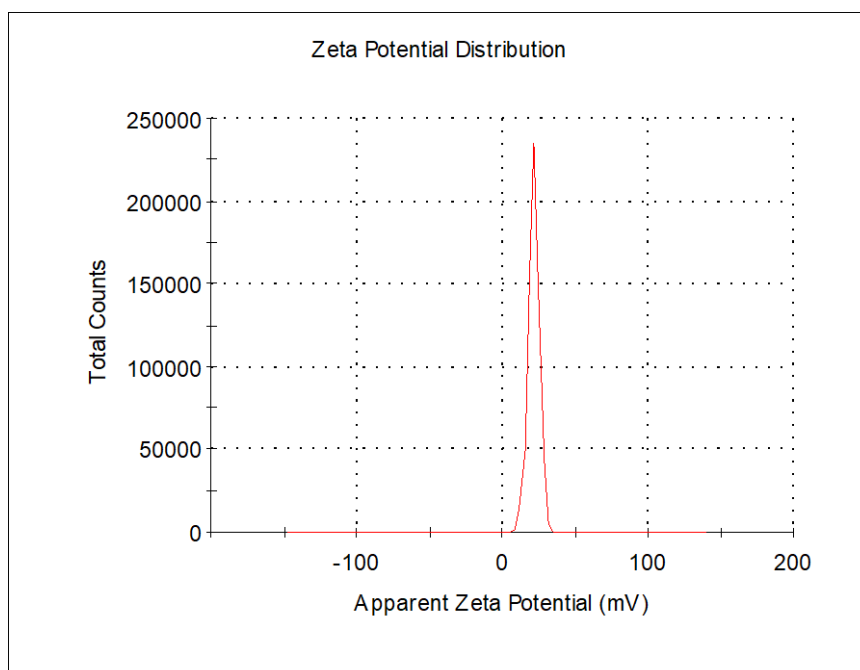


Figure S22:  $\zeta$ -Potential distribution of fibrils from CKFK-PCL-FQF (1) peptide. The calculated mean value ( $21.0 \pm 0.8$  mV) for the  $\zeta$ -potential was achieved by six independent measurements à 20 runs.  $\zeta$ -potential of CKFKFQF is  $22.3 \pm 1.4$  mV.<sup>[61]</sup>

#### 4.9.5. References

- [1] T. Aida, E. W. Meijer, S. I. Stupp, *Science* **2012**, 335, 813.
- [2] Y. Li, Y. Xiao, C. Liu, *Chem. Rev.* **2017**, 117, 4376.
- [3] J. d'Alessandro, A. Barbier--Chebbah, V. Cellerin, O. Benichou, R. M. Mège, R. Voituriez, B. Ladoux, *Nat. Commun.* **2021**, 12, 4118.
- [4] D. B. Brückner, N. Arlt, A. Fink, P. Ronceray, J. O. Rädler, C. P. Broedersz, *Proc. Natl. Acad. Sci.* **2021**, 118, e2016602118.
- [5] P. Premnath, A. Tavangar, B. Tan, K. Venkatakrishnan, *Exp. Cell Res.* **2015**, 337, 44.
- [6] M. Ventre, C. F. Natale, C. Rianna, P. A. Netti, *J. R. Soc. Interface* **2014**, 11, 20140687.
- [7] C. M. Kelleher, J. P. Vacanti, *J. R. Soc. Interface* **2010**, 7, S717.
- [8] Y. Lin, M. M. Mazo, S. C. Skaalure, M. R. Thomas, S. R. Schultz, M. M. Stevens, *Chem. Sci.* **2019**, 10, 1158.
- [9] C. T. Mierke, *Front. Phys.* **2021**, 9, 619.
- [10] E. C. Wu, S. Zhang, C. A. E. Hauser, *Adv. Funct. Mater.* **2012**, 22, 456.
- [11] S. Sur, J. B. Matson, M. J. Webber, C. J. Newcomb, S. I. Stupp, *ACS Nano* **2012**, 6, 10776.
- [12] I. Wheeldon, A. Farhadi, A. G. Bick, E. Jabbari, A. Khademhosseini, *Nanotechnology* **2011**, 22, 212001.
- [13] G. Ye, F. Bao, X. Zhang, Z. Song, Y. Liao, Y. Fei, V. Bunpetch, B. C. Heng, W. Shen, H. Liu, J. Zhou, H. Ouyang, *Nanomedicine* **2020**, 15, 1995.
- [14] J. Adamcik, F. S. Ruggeri, J. T. Berryman, A. Zhang, T. P. J. Knowles, R. Mezzenga, *Adv. Sci.* **2021**, 8, 2002182.
- [15] G. G. Glenner, C. W. Wong, *Biochem. Biophys. Res. Commun.* **1984**, 122, 1131.
- [16] A. V. Maltsev, S. Bystryak, O. V. Galzitskaya, *Ageing Res. Rev.* **2011**, 10, 440.
- [17] I. Cherny, E. Gazit, *Angew. Chem. Int. Ed.* **2008**, 47, 4062.
- [18] V. A. Iconomidou, G. Vriend, S. J. Hamodrakas, *FEBS Lett.* **2000**, 479, 141.
- [19] J. E. Podrabsky, J. F. Carpenter, S. C. Hand, *Am. J. Physiol. Integr. Comp. Physiol.* **2001**, 280, R123.

- [20] D. Romero, C. Aguilar, R. Losick, R. Kolter, *Proc. Natl. Acad. Sci. U. S. A.* **2010**, 107, 2230.
- [21] A. Taglialegna, I. Lasa, J. Valle, *J. Bacteriol.* **2016**, 198, 2579.
- [22] S. K. Maji, M. H. Perrin, M. R. Sawaya, S. Jessberger, K. Vadodaria, R. A. Rissman, P. S. Singru, K. P. R. Nilsson, R. Simon, D. Schubert, D. Eisenberg, J. Rivier, P. Sawchenko, W. Vale, R. Riek, *Science* **2009**, 325, 328.
- [23] B. Watt, G. van Niel, G. Raposo, M. S. Marks, *Pigment Cell Melanoma Res.* **2013**, 26, 300.
- [24] K. Sato, M. P. Hendricks, L. C. Palmer, S. I. Stupp, *Chem. Soc. Rev.* **2018**, 47, 7539.
- [25] A. K. Das, P. K. Gavel, *Soft Matter* **2020**, 16, 10065.
- [26] N. P. Reynolds, *Biointerphases* **2019**, 14, 040801.
- [27] E. Chuang, A. M. Hori, C. D. Hesketh, J. Shorter, *J. Cell Sci.* **2018**, 131.
- [28] Lee, Trinh, Yoo, Shin, Lee, Kim, Hwang, Lim, Ryou, *Int. J. Mol. Sci.* **2019**, 20, 5850.
- [29] N. Balasco, C. Diaferia, G. Morelli, L. Vitagliano, A. Accardo, *Front. Bioeng. Biotechnol.* **2021**, 9, 130.
- [30] M. Jackson, E. Hewitt, *Biomolecules* **2017**, 7, 71.
- [31] N. Nespovitaya, J. Gath, K. Barylyuk, C. Seuring, B. H. Meier, R. Riek, *J. Am. Chem. Soc.* **2016**, 138, 846.
- [32] G. Son, B. Il Lee, Y. J. Chung, C. B. Park, *Acta Biomater.* **2018**, 67, 147.
- [33] K. Siposova, V. I. Petrenko, O. I. Ivankov, A. Musatov, L. A. Bulavin, M. V. Avdeev, O. A. Kyzyma, *ACS Appl. Mater. Interfaces* **2020**, 12, 32410.
- [34] S. Jordens, J. Adamcik, I. Amar-Yuli, R. Mezzenga, *Biomacromolecules* **2011**, 12, 187.
- [35] S. Xiang, J. Wagner, T. Lückerrath, K. Müllen, D. Y. W. Ng, J. Hedrich, T. Weil, *Adv. Healthcare Mater.* **2022**, 11, 2101854.
- [36] P. A. Rühls, J. Adamcik, S. Bolisetty, A. Sánchez-Ferrer, R. Mezzenga, *Soft Matter* **2011**, 7, 3571.
- [37] D. Lin, J. Lei, S. Li, X. Zhou, G. Wei, X. Yang, *J. Phys. Chem. B* **2020**, 124, 3459.
- [38] P. Arosio, T. C. T. Michaels, S. Linse, C. Månsson, C. Emanuelsson, J. Presto, J. Johansson, M. Vendruscolo, C. M. Dobson, T. P. J. Knowles, *Nat. Commun.* **2016**, 7, 10948.

- [39] A. Franco, P. Gracia, A. Colom, J. D. Camino, J. Á. Fernández-Higuero, N. Orozco, A. Dulebo, L. Saiz, N. Cremades, J. M. G. Vilar, A. Prado, A. Muga, *Proc. Natl. Acad. Sci.* **2021**, 118, e2105548118.
- [40] S. Chagri, D. Y. W. Ng, T. Weil, *Nat. Rev. Chem.* **2022**, 6, 320.
- [41] V. Peddie, A. D. Abell, *J. Photochem. Photobiol. C Photochem. Rev.* **2019**, 40, 1.
- [42] A. A. Deeg, T. E. Schrader, S. Kempter, J. Pfizer, L. Moroder, W. Zinth, *ChemPhysChem* **2011**, 12, 559.
- [43] K. Nakamura, W. Tanaka, K. Sada, R. Kubota, T. Aoyama, K. Urayama, I. Hamachi, *J. Am. Chem. Soc.* **2021**, 143, 19532.
- [44] M. Pieszka, A. M. Sobota, J. Gačanin, T. Weil, D. Y. W. Ng, *ChemBioChem* **2019**, 20, 1376.
- [45] J. Gačanin, J. Hedrich, S. Sieste, G. Glaßer, I. Lieberwirth, C. Schilling, S. Fischer, H. Barth, B. Knöll, C. V. Synatschke, T. Weil, *Adv. Mater.* **2019**, 31, 1805044.
- [46] Y. Luo, M. S. Shoichet, *Nat. Mater.* **2004**, 3, 249.
- [47] T. Matsuda, T. Sugawara, *J. Biomed. Mater. Res.* **1995**, 29, 749.
- [48] D. Ryan, B. A. Parviz, V. Linder, V. Semetey, S. K. Sia, J. Su, M. Mrksich, G. M. Whitesides, *Langmuir* **2004**, 20, 9080.
- [49] S. Zhang, L. Yan, M. Altman, M. Lässle, H. Nugent, F. Frankel, D. A. Lauffenburger, G. M. Whitesides, A. Rich, *Biomaterials* **1999**, 20, 1213.
- [50] F. M. Yavitt, B. E. Kirkpatrick, M. R. Blatchley, K. S. Anseth, *ACS Biomater. Sci. Eng.* **2022**, acsbiomaterials.1c01450.
- [51] C. A. DeForest, K. S. Anseth, *Angew. Chem. Int. Ed.* **2012**, 51, 1816.
- [52] R. J. Wade, E. J. Bassin, W. M. Gramlich, J. A. Burdick, *Adv. Mater.* **2015**, 27, 1356.
- [53] D. S. Hernandez, E. T. Ritschdorff, S. K. Seidlits, C. E. Schmidt, J. B. Shear, *J. Mater. Chem. B* **2016**, 4, 1818.
- [54] I. Batalov, K. R. Stevens, C. A. DeForest, *Proc. Natl. Acad. Sci.* **2021**, 118, e2014194118.
- [55] B. D. Fairbanks, S. P. Singh, C. N. Bowman, K. S. Anseth, *Macromolecules* **2011**, 44, 2444.
- [56] C. Yang, F. W. DelRio, H. Ma, A. R. Killaars, L. P. Basta, K. A. Kyburz, K. S. Anseth, *Proc. Natl. Acad. Sci.* **2016**, 113, E4439.

- [57] A. M. Kloxin, A. M. Kasko, C. N. Salinas, K. S. Anseth, *Science* **2009**, 324, 59.
- [58] J. B. Matson, Y. Navon, R. Bitton, S. I. Stupp, *ACS Macro Lett.* **2015**, 4, 43.
- [59] S. V. Wegner, O. I. Sentürk, J. P. Spatz, *Sci. Rep.* **2016**, 5, 18309.
- [60] A. M. Ender, K. Kaygisiz, H.-J. Räder, F. J. Mayer, C. V. Synatschke, T. Weil, *ACS Biomater. Sci. Eng.* **2021**, 7, 4798.
- [61] C. Schilling, T. Mack, S. Lickfett, S. Sieste, F. S. Ruggeri, T. Sneideris, A. Dutta, T. Bereau, R. Naraghi, D. Sinske, T. P. J. Knowles, C. V. Synatschke, T. Weil, B. Knöll, *Adv. Funct. Mater.* **2019**, 29, 1809112.
- [62] M. E. Lee, E. Gungor, A. M. Armani, *Macromolecules* **2015**, 48, 8746.
- [63] S. Sieste, T. Mack, E. Lump, M. Hayn, D. Schütz, A. Röcker, C. Meier, K. Kaygisiz, F. Kirchhoff, T. P. J. Knowles, F. S. Ruggeri, C. V. Synatschke, J. Münch, T. Weil, *Adv. Funct. Mater.* **2021**, 31, 2009382.
- [64] N. J. Greenfield, *Nat. Protoc.* **2007**, 1, 2876.
- [65] A. Adochitei, G. Drochioiu, *Rev. Roum. Chim.* **2011**, 56, 783.
- [66] M. Jackson, H. H. Mantsch, *Crit. Rev. Biochem. Mol. Biol.* **1995**, 30, 95.
- [67] C. Xue, T. Y. Lin, D. Chang, Z. Guo, *R. Soc. Open Sci.* **2017**, 4, 160696.
- [68] J. Jeong, Y. Lee, Y. Yoo, M. K. Lee, *Colloids Surf. B. Biointerfaces* **2018**, 162, 306.
- [69] W. Y. Seow, K. Kandasamy, G. S. L. Peh, J. S. Mehta, W. Sun, *ACS Biomater. Sci. Eng.* **2019**, 5, 4067.
- [70] F. Topuz, A. Nadernezhad, O. S. Caliskan, Y. Z. Menciloglu, B. Koc, *Carbohydr. Polym.* **2018**, 201, 105.
- [71] R. Armisen, *Hydrobiologia* **1991**, 221, 157.
- [72] S. Arnott, A. Fulmer, W. E. Scott, I. C. M. Dea, R. Moorhouse, D. A. Rees, *J. Mol. Biol.* **1974**, 90, 269.
- [73] K. Nakamura, R. Kubota, I. Hamachi, *ChemRxiv* **2022**, 10.26434/chemrxiv.
- [74] A. A. Patil, C.-K. Chiang, C.-H. Wen, W.-P. Peng, *Anal. Chim. Acta* **2018**, 1031, 128.
- [75] X. Zhan, D. M. Desiderio, *Int. J. Mass Spectrom.* **2009**, 287, 77.
- [76] A. Barth, J. E. T. Corrie, M. J. Gradwell, Y. Maeda, W. Mäntele, T. Meier, D. R. Trentham, *J. Am. Chem. Soc.* **1997**, 119, 4149.
- [77] A. Resemann, L. Liu-Shin, G. Tremintin, A. Malhotra, A. Fung, F. Wang, G. Ratnaswamy, D. Suckau, *MABs* **2018**, 10, 1200.



## 5. Cell-instructive surface gradients of photo-responsive amyloid-like fibrils

# denotes equal contribution

[1]

Correspondence to be addressed to:

### Copyright:

Published in ACS Biomater. Sci. Eng. 2021, 7,4798.

The following part is reproduced with permission from American Chemical Society. This work is licensed under a Creative Commons Attribution 4.0 International License. Further permissions related to the material excerpted should be directed to the ACS.

### 5.1. Contributions

My contributions were the conceptualization of the manuscript and the design of project aims. I integrated the linker molecule as an external trigger molecule into the amyloid-like structure and proposed, performed and established the spray-coating method as a new technique for coating of amyloid-like fibrils. Furthermore, I established a Proteostat-Assay protocol for amyloid-like fiber identification on surfaces. In addition, I synthesized, purified and characterized the PCL-peptide, performed all surface coatings, TEM measurements, ThT-Assays, SEM sample preparation, Proteostat-Assay, MALDI-sample preparation, gradient fabrication and all cell assays and interpreted the results. I supervised the photocleavage kinetics in solution, which were performed by [REDACTED]. Furthermore, I interpreted most experimental data and visualized the results for publication. I wrote large parts of the manuscript and the supporting information and prepared all figures. [REDACTED] synthesized, purified and characterized the NCL and PCL linker molecules and NCL- and PCL-peptides. She performed the initial cleavage kinetics studies in solution and on surface and she established the fibril formation protocol in pure water, proposed and evaluated different gradient fabrication techniques. She proposed and evaluated

the usage of the agarose coating as cell repellent agent and investigated the gradient forming technique via MALDI-Imaging. She curated some of the data, edited the figures and wrote parts of the manuscript and the supporting information. MALDI-Imaging was investigated, validated and analyzed by [REDACTED] and [REDACTED]. [REDACTED] carried out the IR measurements and [REDACTED] the SEM measurements. [REDACTED] and [REDACTED] designed and supervised the project, discussed all experimental data, provided funding, and revised the manuscript.

## 5.2. Abstract

Gradients of bioactive molecules play a crucial role in various biological processes like vascularization, tissue regeneration or cell migration. In order to study these complex biological systems, it is necessary to control the concentration of bioactive molecules on their substrates. Here, we created a photochemical strategy to generate gradients using amyloid-like fibrils as scaffolds functionalized with a model epitope, i.e. the integrin-binding peptide RGD, to modulate cell adhesion. The self-assembling  $\beta$ -sheet forming peptide (CKFKFQF) was connected to the RGD epitope via a photo-sensitive nitrobenzyl linker and assembled into photo-responsive nanofibrils. The fibrils were spray-coated on glass substrates and macroscopic gradients were generated by UV-light over a cm-scale. We confirmed the gradient formation using matrix assisted laser desorption ionization mass spectroscopy imaging (MALDI-MSI), which directly visualized the molecular species on the surface. The RGD gradient was used to instruct cells. In consequence, A549 adapted their adhesion properties in dependence of the RGD-epitope density.

## 5.3. Introduction

Concentration gradients in the physiochemical environment of the extra cellular matrix (ECM) play a crucial role for cell adhesion and growth.<sup>[1],[2]</sup> Gradual alterations of biochemical signals are the driving force for events like directed cell migration i.e. during nerve- and skin regeneration, vascularization and immune responses.<sup>[3],[4]</sup> Since these cell-material interactions occur at the mesoscopic length scale, and the

ECM is composed of a dense network of fibrillar structures,<sup>[5],[6],[7],[8]</sup> self-assembling peptides that form fibrils are promising biomaterials serving as scaffolds for cellular growth, adhesion, spreading and migration.<sup>[9,10]</sup>

Amyloid-forming peptides are a special group of peptides assembling into highly ordered fibrils with a characteristic cross  $\beta$ -sheet structure and characteristic physical properties such as long-term stability in physiological environments, mechanical stiffness, and strong adhesion to various substrates.<sup>[11]</sup> Many amyloid-forming peptides also exhibit intrinsic bioactivity and have recently evolved from a class exclusively associated with pathology<sup>[12,13]</sup> to functional materials<sup>[14,15]</sup> with applications such as stimulating nerve growth for tissue engineering<sup>[16–18]</sup> and increased retroviral cell uptake for gene therapy.<sup>[19,20]</sup> In Nature, the intrinsic adhesiveness and high aspect ratio of amyloid fibrils provide structural integrity to bacteria biofilms<sup>[21,22]</sup> and allow material-efficient substrate coverage.

Therefore, amyloid-like peptides featuring these favorable nanomechanical properties as well as an intrinsic bioactivity could be appropriate scaffolds for mimicking concentration gradients of the ECM.<sup>[23]</sup> Functionalization of the amyloid-scaffold e.g. with certain ECM protein-derived epitopes such as the laminin-derived peptide sequence RGD can further increase their bioactivity.<sup>[5,24]</sup> The RGD-motif is involved in regulating several cellular processes such as cell attachment, spreading, orientation, proliferation, differentiation and even directional cell migration, and it is therefore widely applied to facilitate cell-substrate interactions.<sup>[4],[25]</sup>

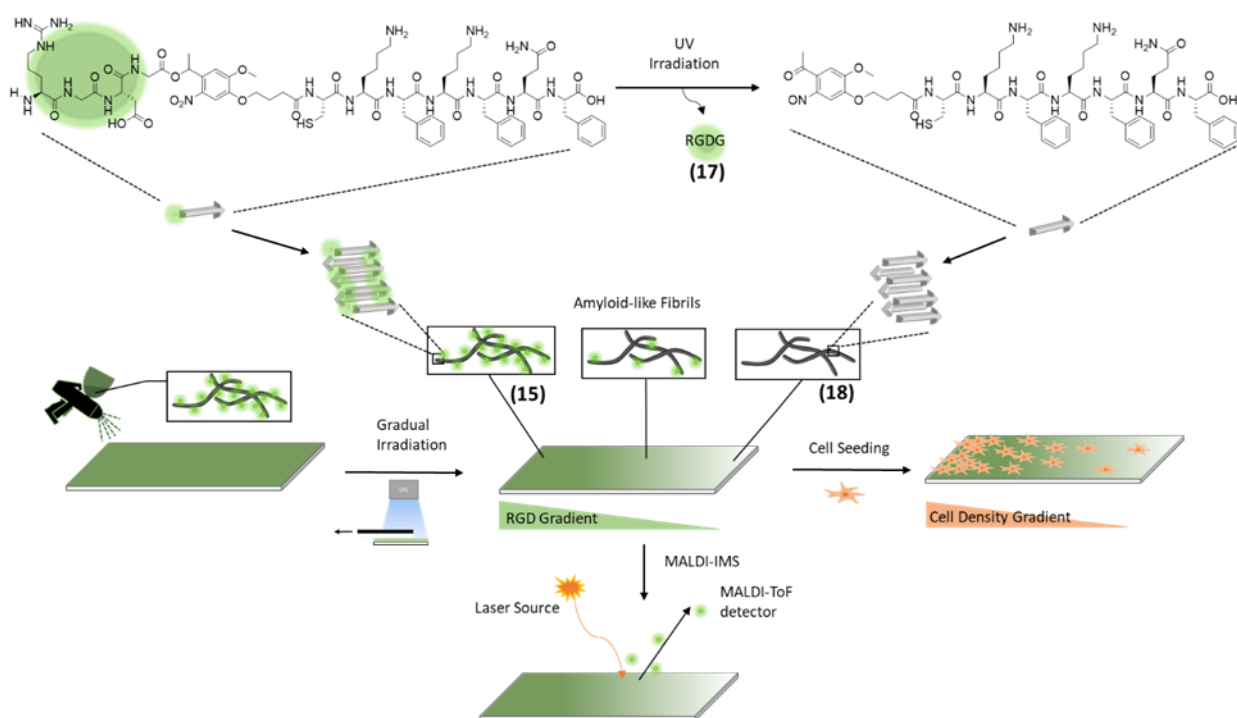
Several examples of RGD-carrying amyloids have been reported in the literature. For example Gras et al. could alter cell attachment<sup>[26]</sup> and cell compatibility<sup>[27,28]</sup> on coatings from RGD-modified YTIAALLSPYS peptide.<sup>[29]</sup> Neuronal cells in culture also benefited from incorporating the RGD motif into amyloids in terms of cell attachment and neurite outgrowth.<sup>[30,31]</sup> The accessibility of the RGD motif is an important parameter when designing a self-assembled nanomaterial. This was studied in a combined theoretical and experimental study for different RGD-carrying hexapeptides.<sup>[32]</sup> Supramolecular coassembly of non-functional and RGD-modified peptides provides easy access to bioactive materials with adjustable epitope concentrations as demonstrated for peptide hydrogels.<sup>[33]</sup>

While fibrous scaffolds are versatile supramolecular biomaterials, very few examples for molecular gradients within this material class exist.<sup>[34]</sup> Contemporary strategies to create molecular gradients on surfaces that can direct or guide cellular behavior<sup>[4],[35],[36]</sup> include bipolar electrochemistry, microfluidic systems, and dip coating techniques.<sup>[37],[38]</sup> However, many of these techniques require a laborious setup and create large gradient sizes in the millimeter regime.<sup>[37–39]</sup> In contrast, photoreactive chemistry is an extremely versatile tool providing high spatial resolution only limited by the wavelength of light<sup>[40]</sup> and experimental setup, e.g. by a photomask.<sup>[41,42]</sup> Photoinduced spatial release of bioactive substances<sup>[43]</sup> and precise positioning of molecules and cells on various surfaces has been achieved and applied down to a sub-micrometer level.<sup>[5,44–47]</sup> Nitrobenzyl esters are well established as a class of light-responsive groups that undergo a photocleavage reaction upon irradiation with UV light. For example, Del Campo et al. and Wegner et al. created patterned cell distributions on coatings of covalently-bound bioactive molecules on glass surfaces that were photo-released on demand.<sup>[46,48]</sup> Stupp et al. were able to control the bioactivity of peptide amphiphile nanofibers by using the nitrobenzyl group as a light-sensitive linker to remove attached RGDS-epitopes from fiber surfaces.<sup>[5]</sup> Furthermore, by using the nitrobenzyl as a caging group, Yousaf et al. accomplished a gradual distribution of RGD (Arg-Gly-Asp) bound to gold-coated glass surfaces, which resulted in signal-driven cell migration.<sup>[49]</sup>

While fluorescence microscopy is the most commonly used method for the validation of surface gradient formation, it requires fluorophore-labeling, which can be labor intensive and may interfere with structure and activity of the bioactive gradient. An alternative and label-free method for analyzing molecular compositions directly on surfaces is matrix assisted laser desorption ionization mass spectrometry imaging (MALDI-MSI).<sup>[50]</sup> This technique represents a unique characterization strategy that is well-established for tissue samples, but is gaining more interest in the biomaterials community.<sup>[51–55]</sup> This soft-ionization technique<sup>[51–55]</sup> provides spatially resolved mass spectra of molecules with a lateral resolution of approximately 10 micrometers. By scanning the surface and post processing the mass spectra, images can be obtained depicting the two-dimensional intensity distribution of individual components, such as bioactive moieties or their precursor molecules. Consequently, this technique has several benefits by rapidly identifying intact chemical species on coated surfaces, in

contrast to other surface detection methods like Raman or fluorescence spectroscopy.<sup>[56]</sup> MALDI-MSI measurements for the characterization of different surface coatings rather than tissue and cell samples are scarce.<sup>[57]</sup> Our study demonstrates the great potential of the MALDI-MSI technique for characterizing and quantifying molecular surface gradients to control cellular attachment.

Herein, we present a straight-forward method to generate substrates coated with amyloid-like nanofibrils that present gradual concentrations of bioactive epitopes to control cell adhesion with low spatial resolution. By connecting the RGD-motif via a photocleavable linker (PCL) to the bioactive self-assembling peptide CKFKFQF<sup>[9]</sup>, a photo-controllable peptide RGD-PCL-CKFKFQF was designed. CKFKFQF nearly quantitatively (95%) assembles into amyloid-like nanofibrils in physiological environment and supports cellular adhesion and growth<sup>[9]</sup> as well as enhanced viral transduction<sup>[20]</sup> The PCL-attached RGD motif is cleaved in a dose-dependent manner upon exposure to UV-light, thus generating a gradual distribution of the RGD moiety over cm-length scales. Homogenous distribution of the nanofibrils on different substrates was achieved by simple spray-coating. The molecular gradients were imaged directly, without the need for additional labels by MALDI-MSI. A two-dimensional map of the epitope-presenting substrate was achieved and cells adjusted their adhesion behavior according to the density of the RGD-epitope on the substrate (Scheme 1). This versatile platform could be employed for bio and tissue engineering, in which spatial control over cell growth can be achieved on an anisotropic distribution of bioactive molecules, mimicking the ECM in certain aspects.<sup>[58–61]</sup>



*Scheme 1: Overview of the workflow: RGD-PCL-CKFKFQF peptides (15) form amyloid-like fibrils. After cleavage of the RGD-moiety (17), the remaining peptide maintains its amyloid-like fibril morphology (18) Spray-coating of glass-surfaces with amyloid-fibril solution (15) and gradual irradiation with UV-light of the-fibril (15)-coated surface. Direct characterization of the gradual distribution of cleaved RGDG (17) and the precursor-fibril (15) via MALDI-MSI is feasible. A549 cell seeding on the RGD-gradient surface and incubation for 24h leads to a gradual cell distribution.*

## 5.4. Materials and Methods

### 5.4.1. Materials

OymaPure®, Arg(Pbf)-OH, Fmoc-Gly-OH, Fmoc-Asp(OtBu)-OH, Fmoc-Cys(Trt)-OH, Fmoc-Lys(Boc)-OH, Fmoc-Phe-OH, Fmoc-Gln(Trt)-OH, Fmoc-Phe-Wang resin were purchased from Novabiochem®. N-Ethyl-diisopropylamine (DIPEA), piperidine ( $\geq 99.5\%$  for peptide synthesis) and trifluoroacetic acid (TFA,  $\geq 99.9\%$ ) were obtained from Carl Roth. Dimethylformamide (DMF for peptide synthesis), diethyl ether and dimethyl sulfoxide (DMSO,  $\geq 99.97\%$ ) was purchased from Acros Organics. Acetonitrile (HPLC grade) was purchased from Fisher Scientific. Syringe filters Minisart SRP (0.20  $\mu\text{m}$ ) were obtained from Sartorius. Glass cover slips (24  $\times$  50 mm) were obtained from Hirschmann® and glass cover slips ( $\varnothing = 13$  mm) were purchased from Fisher Scientific. ITO coated glass slides for scanning electron microscope (SEM) (15  $\times$  20 mm) were obtained from Ossila and for MALDI-MSI (25  $\times$  75 mm) were purchased from Bruker Daltonics. LE Agarose was obtained from Biozym Scientific.

A549 cells, Dulbecco's Modified Eagle's Medium (DMEM, 4.5 g/L glucose/glutamine), penicillin/streptavidin, Fetal Bovine Serum (FBS) and Minimum Essential Medium Non-Essential Amino Acids (MEM NEAA, 100x) were purchased from Thermo Fisher Scientific. The ProteoStat® Amyloid Plaque detection Kit was purchased from Enzo Life Sciences, Inc.  $\alpha$ -Cyano-4-hydroxycinnamic acid (HCCA) was purchased from Sigma Aldrich.

#### 5.4.2. Methods

**Linker-Synthesis.** Photocleavable (PCL, (8)) and non-photocleavable (NCL, (14)) linkers were synthesized according to a literature procedure (Scheme S1 and Scheme S2).<sup>[5]</sup>

**Solid-Phase Peptide Synthesis and Characterization of RGD-PCL-CKFKFQF (15) and RGD-NCL-CKFKFQF (16).** Peptides were synthesized by using an automated microwave peptide synthesizer (CEM, Liberty Blue™) at a 0.1 mmol scale using the Fmoc-L-Phe-Wang resin according to the standard coupling strategy (Supporting Information, standard peptide synthesis strategy). The coupling reaction of the PCL (5 equiv.; 290 mg) or NCL (5 equiv., 251 mg) to the peptide was performed manually in 1 mL of DMF with HBTU (5 equiv.; 190 mg) and DIPEA (10 equiv.; 175  $\mu$ L) for 48 h at room temperature. The peptide was cleaved off the resin through treatment with 2 mL of TFA containing 2.5% water and 2.5% triisopropylsilane (TIPS) for 2 h. This solution was added to cold diethyl ether (40 mL) and afterwards centrifuged at 3000 rpm for 15 min to afford a white precipitate. The precipitate was dissolved in water and 0.1% TFA and purified via HPLC using a gradient of water and acetonitrile containing 0.1% TFA as the mobile phase. After lyophilization overnight, a white solid was obtained (47 mg; yield = 29%). The MALDI spectrum is shown in Figure 1, B: theoretical  $[M+H]^+=$  1613.74 g/mol; found  $[M+H]^+=$  1613.82 g/mol.

**Photocleavage Kinetics in Solution.** The kinetic study was performed using an analytical HPLC system by Shimadzu equipped with the following modules: DGU-20A5R, LC-20AT, CBM-20A, SPD-M20A, SIL-10ACHT, CTO-20AC. In the analytical scale, the column Zorbax XDB-C18, 9.4  $\times$  250 mm, 5  $\mu$ m pore size was used. The eluent was a gradient from 5% ACN in water with 0.1% TFA to 80 % ACN in 45 min. The peptide was dissolved in DMSO at a concentration of 10 mg/mL. This solution was diluted in water to a concentration of 1 mg/mL and irradiated with UV light (365

nm). 50  $\mu\text{L}$  of each sample ( $t_0$  = no irradiation,  $t_1$  = 10 s,  $t_2$  = 30 s,  $t_3$  = 60 s,  $t_4$  = 5 min,  $t_5$  = 6 min,  $t_6$  = 10 min,  $t_7$  = no irradiation and incubation for 24 h) was injected.

**Nanofibril-Formation.** Peptides were dissolved in DMSO to obtain a 10 mg/mL stock solution, which was further diluted in MilliQ water to 1 mg/mL. The pH value of this solution was adjusted to pH 7.4 with 0.1 M NaOH or 0.1 M HCl. The solution was incubated at room temperature for 24 h to facilitate fibril formation.<sup>[9]</sup>

**Amyloid Fibril Characterization from Solution.** For **TEM** measurements the nanofibril formation was performed as previously described. Carbon-film coated copper grids were plasma-etched for 30 s at 20% intensity, before 4  $\mu\text{L}$  of the pre-incubated peptide solution was pipetted on the grid and incubated for 5 min. Then, the solution was removed with filter paper and the grid was stained with 4% uranyl acetate solution for 2.5 min. The grids were washed three times with MilliQ water and left to dry before measurement. TEM measurements were conducted using a Jeol 1400 electron microscope operated at 120kV voltage and equipped with a CCD camera. ImageJ software was used for image processing. ThioflavinT (**ThT**) assay was performed by using nanofibril solutions that were prepared as previously described. 10  $\mu\text{L}$  (50  $\mu\text{M}$ ) of a ThT solution was pipetted in a black 384 well-plate and 2  $\mu\text{L}$  of the nanofibril solution (1 mg/mL) were added. For reference PBS (2  $\mu\text{L}$ ) instead of fibril solution was added. The solutions were mixed and incubated for 15 min at room temperature to allow intercalation of ThT dye with potential cross- $\beta$ -sheet structures.<sup>[16]</sup> Subsequently, fluorescence emission was recorded  $\lambda_{\text{em}} = 488$  nm upon excitation at  $\lambda_{\text{ex}} = 440$  nm with 10 nm bandwidth and multiple reads per well (3 $\times$ 3). Fluorescence intensity was measured using a Spark® 20M microplate reader by the company Tecan Group Ltd. Data processing was performed with Origin software. **FT-IR** spectra of solid samples were recorded after lyophilization of fibril solutions using a Bruker Tensor II spectrometer equipped with a diamond crystal as ATR element with a spectral resolution of 2  $\text{cm}^{-1}$ , each spectrum was an average of 40 scans. The data was processed with Origin software.

**Characterization of Amyloid Fibril-coated Surfaces.** For **SEM** measurements the ITO coated glass slides were spray-coated with an aqueous solution of preformed nanofibrils (see standard protocol) with the concentration of 0.1 mg/mL. Scanning electron measurements were performed on a Hitachi SU8000 instrument using the



declaration mode with the top-detector. Various spots on the whole sample were evaluated while measuring. Unless stated otherwise the acceleration voltage was 0.1 kV. **Proteostat-Assay.** 1  $\mu$ L of the ProteoStat® stock solution was diluted with 10  $\mu$ L assay buffer and 990  $\mu$ L MilliQ water and pipetted on the fibril-coated surfaces. The samples were then incubated in the dark for 15 min. Images were taken with Leica DM2500 microscope coupled to a Leica DFC2000GT camera with the Rhodamine filter (fluorescence emission was recorded  $\lambda_{em}$ = 585/40 nm upon excitation at  $\lambda_{ex}$ =546/10 nm) and processed with the software ImageJ.

**Pre-coating with Agarose.** Glass slides, that were pre-cleaned with isopropanol and MilliQ water, were then immersed in a hot aqueous agarose solution (1wt%) and airdried before further usage.

**Fabrication of Nanofibril-coated Surfaces.** Nanofibrils were formed according to the standard protocol. Directly before usage, the solution was diluted to a concentration of 0.1 mg/mL solution with MilliQ water and spray-coated with an air-brush (nozzle size 0.3 mm) on diverse surfaces. Here, 1 mL of the peptide solution was used for an agarose coated glass slide (24 x 50 mm) and 2 mL of the peptide solution for agarose coated glass slides ( $\varnothing$  = 13 mm) for cell tests. 2 mL of the peptide solution was used for an ITO-coated glass slide for MALDI-MSI (25 x 75 mm) and 1mL peptide solution for 4 ITO-coated glass slides for SEM measurements (15 x 20 mm).

**Atomic Force Microscopy.** Atomic force microscopy was conducted in dry state with a Bruker Dimension FastScan Bio™ atomic force microscope, which was operated in Tapping mode. AFM probes with a nominal force constant of 26 N/m and resonance frequency of 300 kHz (OTESPA-R3, Bruker) were used. Samples were scanned with scan rates between 0.6 and 1 Hz. Images were processed with NanoScope Analysis 1.8.

**Fabrication of RGD-gradients.** Fibril-coated surfaces were gradually irradiated (365nm) using a programmable moving stage. (0.083 mm/s) The dried samples were placed in a distance of 2 cm to the lamp in a radiation-insulated chamber at room temperature. Irradiation of samples was conducted with LED from Opulent Americas (Starboard Luminus SST-10-UV-A130) with a peak wavelength at 365 nm and a current of 1 A and radiant flux of 875 mW. The emission spectrum of the LED was measured via an Ulbricht sphere (Figure S3).

A549 Cell Culture. A549 cells were cultured in DMEM (4.5 g/L Glucose/Glutamin) supplemented with 1% penicillin/streptavidin, 10% FBS, 1% MEM NEAA. During cultivation, the medium was changed every 2-3 days. Round, 13 mm-diameter glass coverslips coated with agarose were transferred to a 6-well plate (3 glass coverslips per well), and cells were seeded at a density of  $4 \times 10^5$  cells/well. For the RGD-gradient, a coated glass cover slip (2.4 × 5.0 cm) was transferred to a 15 cm petri dish, and cells were seeded at a density of  $1 \times 10^6$  cells/dish. After 24 h, the surfaces were washed with fresh DMEM and imaged using a Leica DM2500 microscope coupled to a Leica DFC2000GT camera. An average of three fields of view per coverslip were imaged. The number of adherent cells on the surface were analyzed by ImageJ software. All experiments were performed in biological triplicates with three technical replicates. For calceine staining 1 mL of a 1 mg/mL Calceine-AM solution was added to the medium and incubated for 30 min. The images were taken with a FITC filter (fluorescence emission was recorded  $\lambda_{em} = 527/30$  nm upon excitation at  $\lambda_{ex} = 480/40$  nm) and processed with ImageJ.

**Cell Viability Analysis.** The cell viability against peptide nanofibrils was quantified using the CellTiter-Glo Assay (Promega G7571). Prior treatment, cells were seeded with a density of 9.000 cells/well. Peptides were pre-incubated via standard protocol to form fibrils and the solution was diluted with DMEM medium to create final concentrations of 0.1 mg/mL, 0.02 mg/mL and 0.01 mg/mL. Staurosporine (1  $\mu$ M) was added as negative control, while medium alone was used as positive control and were applied 24h after cell seeding, followed by incubation with cells for 24 h. The CellTiter Glo Assay was performed 48h after cell seeding according to manufacturer's instructions. Luminescence was detected using a GloMax Multi 96-well plate reader (Promega).

**MALDI-ToF-MSI.** Relative label-free quantitation of precursor (RGD-PCL-CKFKFQF (15)) and fragment ions (RGDG (17)) were carried out by comparison of the corresponding ion signal intensities in mass spectra recorded by a MALDI-TOF mass spectrometer (rapiflex TOF/TOF, Bruker, Bremen, Germany). Acquisition of spectra were carried out in the reflection mode using the software Compass 2.0 (Bruker GmbH, Bremen, Germany) and FlexImaging 5.0, (Bruker GmbH Bremen, Germany). Utilizing a TM-Sprayer (HTX-Imaging, HTX Technologies LLC) prior to the analysis the fibril-coated and UV-irradiated surface of the ITO slide was spray-coated with a

solution of MALDI matrix  $\alpha$ -cyano-4-hydroxycinnamic acid (HCCA) (Sigma, Germany), which was in a concentration of 10 mg/mL in a solution of 70% ACN, 30% H<sub>2</sub>O and 0.2% TFA. The spray method utilized was provided by the manufacturer featuring the following parameters: nozzle temperature 75°C, nozzle height 40 mm, solvent flow 0.12 mL/min, z-arm velocity 1200 mm/min, N<sub>2</sub> pressure 10 psi, four passes subsequently in a crisscross moving pattern and a track spacing of 3 mm. The matrix-coated slide was introduced into the mass spectrometer by placing it into a glass slide adapter II target. An area of 60 mm × 3.5 mm was scanned in steps of 100  $\mu$ m using a laser profile M5.<sup>[62]</sup> A pixel size of 100  $\mu$ m × 100  $\mu$ m, 35% laser intensity and a laser pulse repetition rate of 10 kHz was used.

In order to visualize the distribution of peak intensities across the measured area, we used the software FlexImaging 5.0 (Bruker, Germany). A color gradient displays the distribution of ion signal intensities<sup>[4]</sup> normalized to total ion count (TIC) (Figure 4F, G).

**Photocleavage Kinetic on Surfaces.** The cleavage kinetic was performed by using MALDI-ToF-MSI. Here, the ITO-coated glass slides were washed with MilliQ water and isopropanol and dried. A fibril solution (RGD-PCL-CKFKFQF (15); 0.1 mg) was prepared using the standard protocol. After 24 h of incubation, these preformed fibrils were spray-coated on the ITO glass slides and irradiated for increasingly longer times (0 min, 1 min, 2 min, 3 min, 4 min, 5 min, 6 min, 8 min, 10 min) with UV light (365 nm) by using a photomask. Since the wavelength of the UV light used for the photocleavage experiment is very close to the one of the Nd-YAG-laser (355 nm) used for desorption/ionization in the MALDI process, it is expected that some photocleavage can occur. In order to minimize this effect to both precursor (15) as well as fragment (17) ion yields the laser power was set to a value very close to the desorption threshold of the precursor (35%) so that no substantial ion yield of RGDG (17) on the non-irradiated side of the ITO glass slide was detected.

## 5.5. Results and Discussion

### 5.5.1. Design and Synthesis of a Photoresponsive Self-assembling Peptide

In order to manufacture biocompatible coatings with controllable bioactivity, we chose a short peptide motif, CKFKFQF, as a supramolecular backbone.<sup>[9,20]</sup> The fibril-forming sequence was extended at the N-terminus by a photocleavable nitrobenzyl linker (PCL) to connect bioactive epitopes to the surface of the nanofibrils. A short RGD sequence served as a model epitope, resulting in the RGD-PCL-CKFKFQF peptide (15). Synthesis of this molecule was achieved through Merrifield solid phase synthesis (Figure 1), and a subsequent purification was performed on a reversed phase high performance liquid chromatography (RP-HPLC, see Supporting Information). Successful synthesis was confirmed by MALDI-ToF-MS ( $m/z$ : 1613.82 [M+H]<sup>+</sup>,  $m/z$ : 1635.79 [M+Na]<sup>+</sup>,  $m/z$ : 1651.77 [M+K]<sup>+</sup>) and LCMS (Figure S13) with a total yield of 29%. The loss of an oxygen atom of the nitrobenzyl group that emerges due to the high laser intensity during the MALDI measurement is found as well ( $m/z$ : 1597.82 [M-O+H]<sup>+</sup>).<sup>[63]</sup>

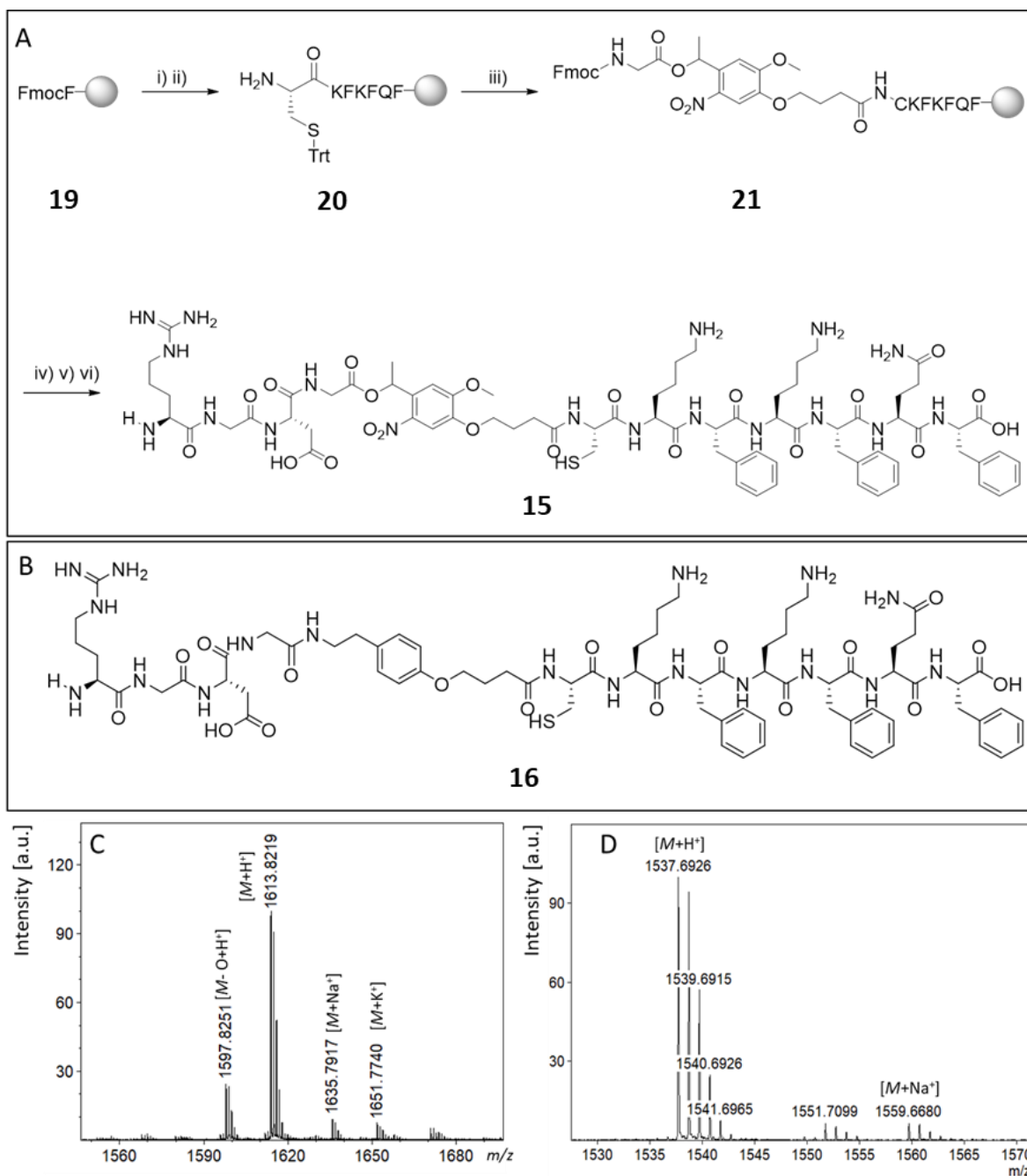


Figure 1: A) Microwave assisted solid-phase peptide synthesis of the photo-cleavable peptide RGD-PCL-CKFKFQF (**15**). i) Fmoc deprotection; ii) Coupling of Fmoc-Gln(Trt)-OH/Fmoc-Phe-OH/Fmoc-Lys(Boc)-OH/Fmoc-Cys(Trt)-OH iii) coupling of PCL iv) Coupling of Fmoc-Asp(OtBu)-OH/Fmoc-Gly-OH/Fmoc-Arg(Pbf)-OH v) Fmoc deprotection; vi) resin cleavage B) non-photocleavable peptide RGD-NCL-CKFKFQF (**16**) C) MALDI-ToF-MS spectra of the purified peptide (**15**) confirming successful synthesis, calc. for  $[M+H]^+$ , 1613.74 g/mol; found 1613.82 m/z, calc. for  $[M+Na]^+$ , 1635.72 g/mol; found 1635.79 m/z., calc. for  $[M+K]^+$ , 1651.694 g/mol found 1651.77m/z. D). MALDI-ToF-MS spectra of the purified peptide (**16**), calc. for  $[M+H]^+$ , 1537.76 g/mol; found 1537.69 m/z., calc. for  $[M+Na]^+$ , 1559.74 g/mol; found 1559.66 m/z.

RGD-PCL-CKFKFQF (**15**) forms amyloid nanostructures very similar as the literature-known peptide sequence CKFKFQF<sup>[9]</sup> after incubation for 24 hours in water at pH 7.4 (Figure 2B). After UV-irradiation of the preformed fibrils, the RGD epitope (**17**) is cleaved off and released (**18**) while fibril morphology is maintained (Figure 2A). In order to determine, whether these nanofibrils have  $\beta$ -sheet structures, the fibril solution

was stained with Thioflavin T (ThT). The so-called ThT-assay can indicate the presence of amyloid structures by an increase in fluorescence intensity of the ThT molecule after binding to the beta-sheets of amyloids.<sup>[64]</sup> A distinct increase in the fluorescence intensity is observed for RGD-PCL-CKFKFQF (15) (Figure 2D), indicating that  $\beta$ -sheet-rich amyloid fibrils are formed. The existence of  $\beta$ -sheet structures was further supported by Fourier transform infrared spectroscopy (FT-IR) measurements (Figure 2E). Here, the fibril containing samples showed absorbance at 1628 and 1661  $\text{cm}^{-1}$  that correspond to  $\beta$ -sheet (1628  $\text{cm}^{-1}$  in the amyloid A  $\beta$ 1-40 peptide), and  $\beta$ -turn structures (1662  $\text{cm}^{-1}$  in A  $\beta$ 1-40 peptide), respectively.<sup>[65]</sup> The short peptide (15) as well as its fragment (18) can rearrange to a larger structure with characteristic FT-IR absorbance similar to the amyloid structure of the A  $\beta$ 1-40 peptide.

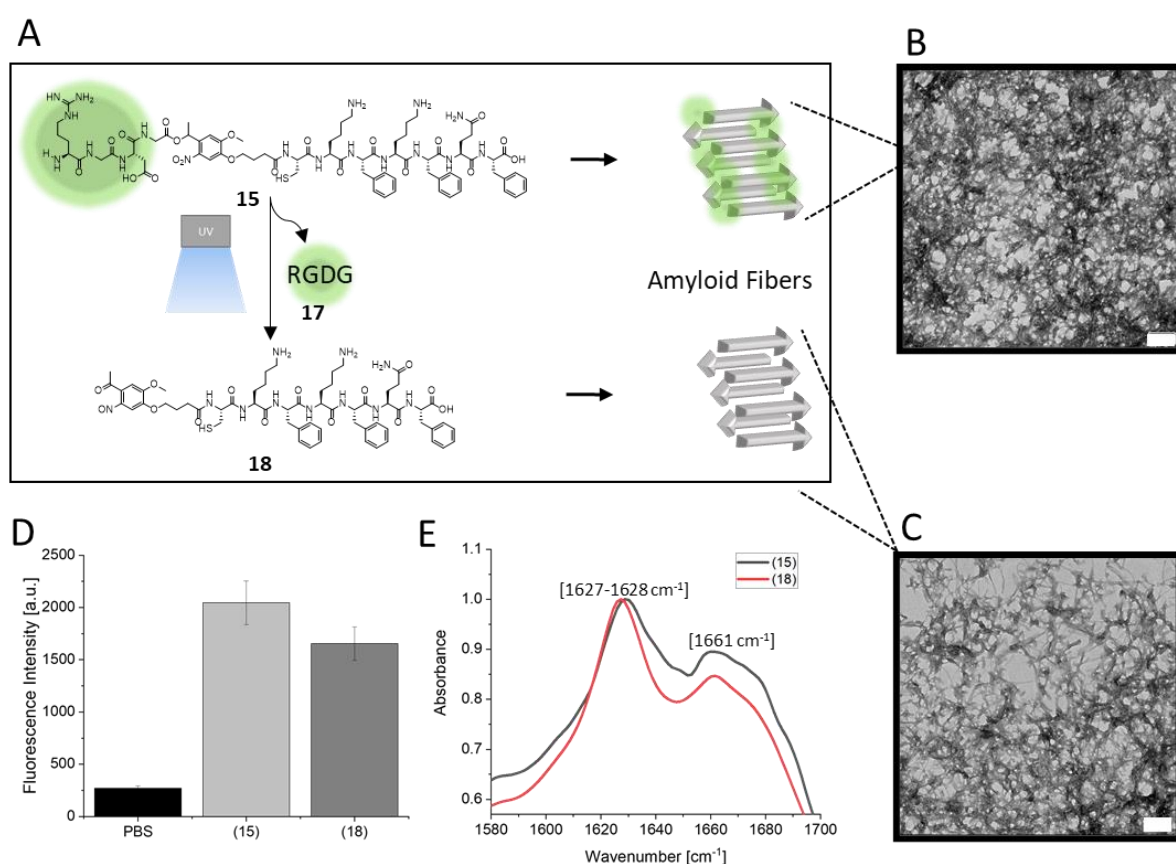


Figure 2: Peptide nanofibrils with photocleavable epitopes. A) Schematic illustration of peptide nanofibril formation and UV-induced cleavage of RGDG (17) from peptide (15) resulting in (18). B) TEM images (scale bars = 0.2  $\mu\text{m}$ ) of peptide nanofibrils after 24 h incubation of a 1 mg/mL peptide solution in the dark. C) Peptide nanofibrils after UV-irradiation for 10 min. D) ThT assay shows high fluorescence for nanofibrils before and after UV irradiation. PBS served as control. E) FT-IR spectra of peptide structures show characteristic amyloid signals for both UV treated (18, red line) and untreated (15, black line) samples.

In order to assess whether photocleavage of the nitrobenzyl linker affects fibril formation, a freshly prepared solution of peptide (15) was UV-treated for 10 min and subsequently incubated for 24 hours similar to the standard fibril formation procedure to yield the irradiated peptide (18). The TEM measurements of (18) reveal fibrillar structures that reveal similar morphologies as (15) (Figure 2C). Likewise, the ThT-assay displayed an increased fluorescence intensity indicating the presence of amyloid structures for non-irradiated (15) and irradiated (18) structures (Figure 2D). Finally, FT-IR spectra of both, irradiated and non-irradiated samples, exhibit absorbance at 1627 (18), 1628 (15) and 1661  $\text{cm}^{-1}$  (15 and 18) confirming that the UV irradiation does not affect the secondary structures, especially the high  $\beta$ -sheet content of the nanostructures (Figure 2E). The results on the assembly both peptide sequences are comparable to CKFKFQF,<sup>[9]</sup> indicating that the presence of the photocleavable group and RGD does not interfere with CKFKFQF assembly.

The photocleavage kinetics of (15) were determined in time-dependent measurements (Figure 3). Aliquots from a solution of (15) were withdrawn at intervals ranging from 0 s up to 10 min of UV-irradiation and they were analyzed by HPLC. The signal at a retention time of 19.67 min, corresponding to the intact peptide (15), decreases in favor of a new signal at a retention time of 20.34 min with increasing irradiation time (Figure 3A). Using LC-MS measurements (Figure 3B, Figure S15), the new signal at 20.34 min retention time was assigned to the fragment (18) with  $[\text{M}+\text{H}]^+ = 1226 \text{ m/z}$  that occurs after photocleavage. The UV-irradiation treatment rapidly cleaves the RGD motif off peptide (15) as a clear signal for (18) is visible after 10 s, and the initial peptide (15) has been almost completely consumed after 6 min (Figure 3A). The half-life of (15) under UV irradiation was determined to be  $t_{1/2} = 1.66 \text{ min}$  (Figure S16). In the absence of light, (15) remains stable for a minimum of 24 h, as shown by HPLC (Figure 3A, beige line), confirming that the UV-irradiation triggers the cleavage reaction.

The control peptide RGD-NCL-CKFKFQF (16) containing a non-photocleavable linker did not show any changes in HPLC elution time after UV exposure (Figure S4, S8) (16) and had the same fibrous morphology and amyloid characteristics as peptide (15) (Figure S5-S7). In summary, our data suggests that peptide (15) can release the RGD motif by UV irradiation, and the degree of cleavage can be controlled by adjusting the irradiation time without affecting fibril morphology. Consequently, this peptide nanofibril platform combines stability under ambient conditions and dose-dependent

UV-induced cleavage making the system suitable for generating biofunctional gradients.

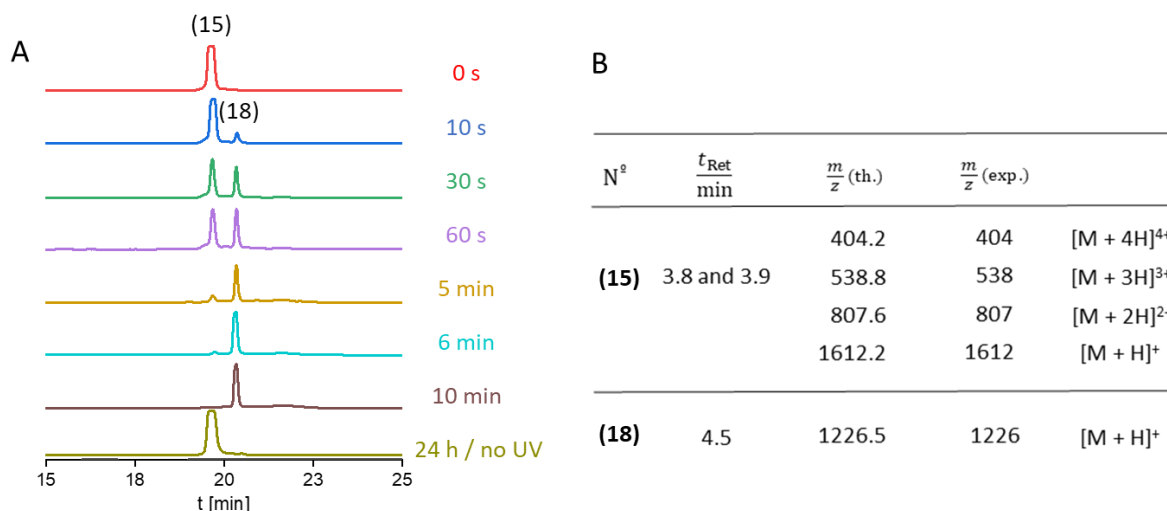


Figure 3: A) HPLC spectra of peptide (15) after different UV-treatment times in aqueous solution. After 6 min of irradiation the precursor molecule (15) is completely converted to (18). B) Assignment of signals found in LC-MS measurements of samples before and after UV treatment.  $t_{Ret}$  is the retention time,  $m/z$  (th.) is the theoretical molecular weight and  $m/z$  (exp.) is the experimental molecular weight.

### 5.5.2. Functional Gradients on Surfaces

Next, surface coatings for the preparation of cell instructive gradients were prepared (Figure 4). In order to accomplish surface-bound gradients of the bioactive epitope RGD, the peptide nanofibrils (15) were first coated on glass slides using a simple spray coating method. In principle, this method can be used to deposit bioactive fibrils on any substrate including non-flat geometries. Beside glass substrates, indium tin oxide (ITO)-coated glass slides for SEM and MALDI-MSI measurements as well as agarose-coated glass slides for further cell adhesion tests were spray-coated analogously. The homogeneity of the fibril coating was analyzed by fluorescence microscopy of ProteoStat® Amyloid Plaque detection Kit stained substrates. The increased fluorescence signal over the entire surface confirms the presence of amyloid-like surface structures (Figure 4B) indicating that a homogeneous fibril coating from peptide (15) was achieved. These results were further supported by SEM measurements, in which the deposition of a thin layer of single fibrils is clearly visible (Figure 4C). The thickness of the coatings was determined to be  $25 \pm 5$  nm by atomic force microscopy (Figure S17). The amyloid-like structures of the fibrils also remain after UV exposure of 10 min on the surface (Figure 4C, bottom). In summary, this spray-coating method provides a fast and easy fabrication route for homogeneous coatings of peptide fibrils on various substrates.



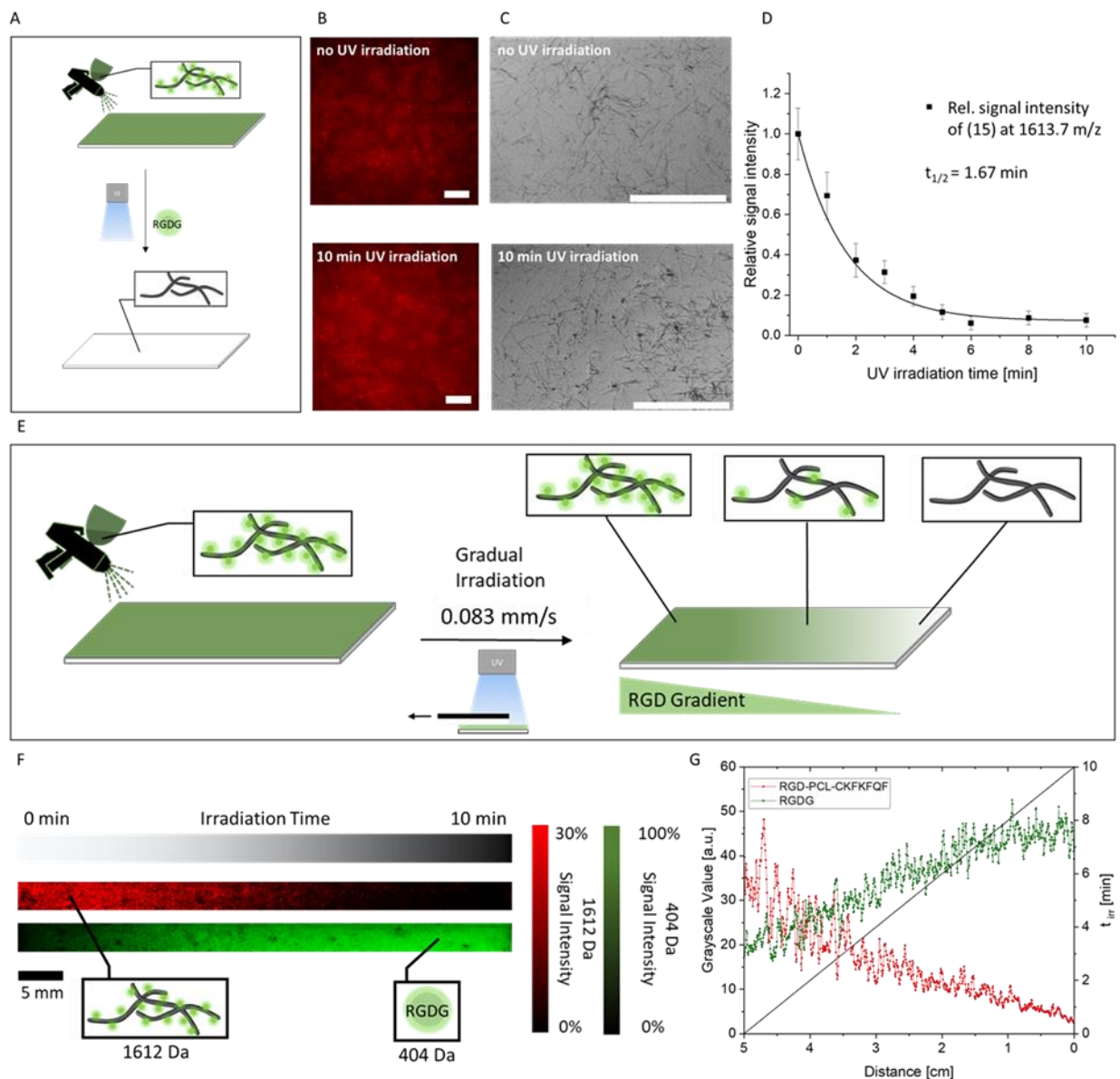


Figure 4: A) Illustration of the spray-coating procedure with fibrils on surfaces and the subsequent UV-treatment of the dried sample to cleave off the bioactive RGD epitope from the fibrils. B) Fluorescence microscopy images of Proteostat stained, fibril coatings before (top) and after a 10-minute UV treatment (bottom) (scale bar = 200  $\mu\text{m}$ ) show homogeneous coverage with Proteostat active structures. C) SEM images show the homogenous fibril coatings before (top) and after a 10-minute UV treatment (bottom) (scale bar = 5  $\mu\text{m}$ ). D) MALDI-ToF-MS measurement of UV-irradiation induced degradation of (15). The sample was irradiated for 0, 1, 2, 3, 4, 5, 6, 8 and 10 min on a dried state coated on ITO-glass substrate. The MALDI signal intensities at 1613.7 m/z corresponding to RGD-PCL-CKFKFQF ((15), black data points) were set relative to non-irradiated (15) at time 0 and fitted (black line) to first-order kinetics ( $t_{1/2} = 1.67 \text{ min}$ ). E) Scheme of the preparation of the RGD-bound fibril gradient on the surface. F) MALDI-MSI results show a gradual distribution of the intact RGD-fibrils (15), red) and the corresponding inverse gradient from the cleaved fragment RGDG ((17), green) over a 5 cm distance. G) The Grayscale plot of MALDI-MSI results from B) showcases an irradiation time dependent decrease of precursor signal ((15), 1612 Da) and increase of RGDG-fragment ((17), 404 Da).

To evaluate the cleavage kinetics of (15) in the dry state, the peptide fibril coated ITO-glass substrates were exposed to UV light for various time durations. HCCA was applied as a matrix prior to MALDI measurements on substrates. The relative signal intensity at 1613.7 m/z of irradiated fibrils to the non-irradiated fibrils indicates the

quantity of remaining precursor (15) on the surface. The results show an exponential decay with first-order kinetics and a photolysis half-life of 1.67 min (Figure 4D), which is in very good agreement to the value determined by HPLC ( $t_{1/2} = 1.66$  min, Figure S16) and comparable to a literature report ( $t_{1/2} = 1.9$  min) measured via a fluorescence-based approach with the same photolinker group.[5] In addition, no further decrease in signal intensity was observed after 6 min of irradiation time, indicating that the photocleavage reaction is completed. Interestingly, a residual signal for the intact peptide (15) at about 7% relative intensity remains after 10 min of UV irradiation, which can be traced back to the previously reported photoreduction of the nitro group in the photo linker in presence of amines. This competing reaction of the nitro groups hinders complete photocleavage reaction of self-assembled samples on substrates.<sup>[66]</sup>

### 5.5.3. Fabrication of RGD-Gradient on Glass Substrates

A gradual distribution of the RGD-motif over a 5 cm-length scale was prepared by exposing nanofibril coated glass slides to UV-light by continuously removing a UV-impermeable cover (Figure 4). The resulting substrates were analyzed in MALDI-MSI, where signals for both the intact RGD-PCL-CKFKFQF (15) and the smaller RGDG (17) fragment which results after photocleavage could be detected. A gradual change in the signal intensities of the corresponding  $m/z$  values were observed. Here, the intact precursor molecule ((15), 1612 Da, illustrated in red, Figure 4F) is detected with the highest signal intensity in the areas that are non-irradiated and gradually decreases with increasing irradiation time. Vice versa, the signal intensity of the cleaved fragment RGDG ((17), 404 Da, illustrated in green) occurs more strongly in regions of long UV irradiation (Figure 4G) and decreases with decreasing irradiation time, as expected. Plotting the grayscale values of precursor (red) and cleaved fragment (green) against the length of the irradiated sample showcases an opposite trend of decrease of precursor signal ((15), 1612 Da) and increase of RGDG-fragment ((17), 404 Da) with longer UV irradiation. The MALDI-MSI signal value fluctuations, especially for precursor at lower UV irradiation areas, can be explained by the setting of desorption (Figure 4G). Since the applied laser power is close to the desorption threshold of the precursor, the ion yield is very vulnerable to small fluctuations of laser power as well as changes of the threshold of ionization itself due to contamination in

the irradiated area i.e. salts, as on suppression of ionization due to co-desorbing species.

Our data shows that, the cleavage reaction occurs analogue to the conditions in solution and conversion from the intact molecule (15) to the fragment (17) can be controlled simply through irradiation time with a given light intensity on surfaces. In principle, bioactive patterns could also be prepared, when an appropriate photomask or a UV projector are used.

#### **5.5.4. A549 Cell-Gradient formation**

The biological response to the RGD-gradients was tested in cell culture (Figure 5). To this end, a cell-repellent pre-coating with agarose was applied on glass slides prior to fibril coating and irradiation, to avoid unwanted cellular adhesion of A549 cells (Figure S14). These surfaces were subsequently spray-coated with nanofibril solution and gradually irradiated as previously described, thus creating an RGD-gradient. After incubation with a suspension of A549-cells for 24 hours, the substrates were analyzed for cell-attachment in three distinct regions (low, medium and high UV irradiation) using fluorescence microscopy. Attached and alive cells were stained with calceine (Figure 5A). A significant difference in cell density is visible when comparing the three regions of the substrate (Figure 5B). As expected, the sections exposed to longer UV irradiation time show less cell attachment than those with shorter exposure times, indicating that a bioactive gradient is achieved that cells can respond to. Noteworthy, some cell attachment and spreading are observed also for fully photocleaved peptides at 100% UV irradiation site (Figure 5B, S14). This observation is in accordance with previous reports on the backbone peptide fibril CKFKFQF stimulating cell adhesion<sup>[9]</sup> and further emphasizes the maintenance of the amyloid-like morphology after UV irradiation. A cell-viability assay confirmed the non-toxic character of both the non-UV-treated and UV-treated fibrils (Figure 5C). As a control, surfaces with the non-cleavable peptide (16) were exposed to UV irradiation and subsequently seeded with A549 cells. As expected, no change in the adhesion behavior of the cells on irradiated and non-irradiated samples were detected (Figure S11). The cell-viability assay was likewise carried out and shows no toxic behavior of peptide (16) before and after UV irradiation (Figure S12). The cell adhesion results and the cell viability data confirming

negligible toxicity, demonstrate that the designed amyloid-like fibrils are a promising scaffold for controlling epitope presentation and displaying cell density gradients.

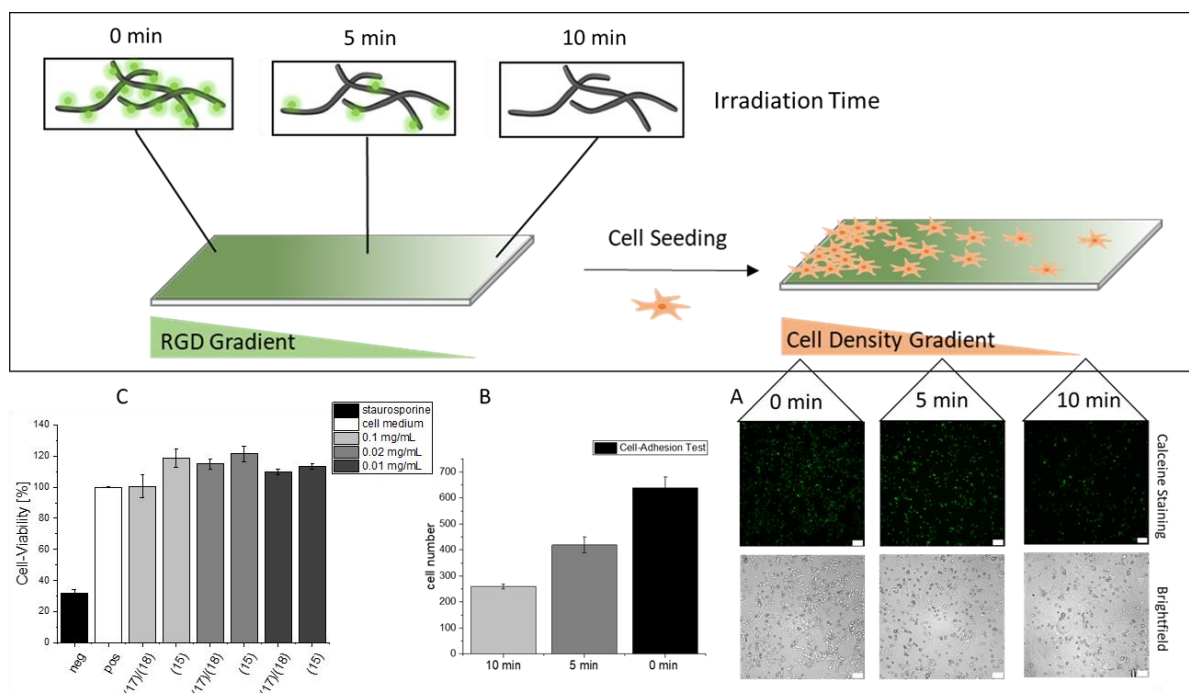


Figure 5: A) Gradual irradiation of fibril coated agarose glass slide and subsequent A549 cell seeding results in a cell density gradient after incubation for 24 h. The calceine staining shows in comparison to the brightfield images that only alive cells attach to the surface. B) Three images of three regions (0 min, 5 min and 10 min) were selected and the cell number was counted. The result is a decrease of the cell number with an increase of irradiation. C) The Cell-Viability Assay confirms the non toxic character of the used fibrils with (17)/(18) and without (15) irradiation for 10 min. negative control is a toxic staurosporine solution and positive control are cells without additive Scale bar: 100  $\mu$ m.

## 5.6. Conclusion

In summary, we developed an easy and fast strategy to create bioactive spatial gradients by spray-coating UV-sensitive, epitope functionalized amyloid-like peptide fibrils on glass slides. The bottom-up approach of the designed photocleavable peptide (15) requires the usage of a nitrobenzyl linker that allows the RGD-epitope cleavage of fibrils after the coating procedure. The cleavage was performed by irradiating the samples with 365 nm UV light. Gradients of irradiated photocleavable peptide (15) on ITO-coated glass slides were visualized by MALDI-MSI measurements, which is a facile method for precise and direct mass characterization of 2D samples covering multiple length scales (micrometers–centimeters). Exemplarily, A549 cell density gradients could be achieved by spray-coating peptide (15) on agarose coated glass slides. In addition, the amyloid fibril coatings before and after UV irradiation were non-

toxic when tested *in vitro*. The amyloid-like fibrils show a high tendency for cell adhesion and spreading. In areas of high RGD concentrations, the number of attached cells is further enhanced three-fold compared to areas of low RGD concentration, enabling a precise control over cell density through the underlying coating. By replacing the RGD epitope with other motifs like bioactive peptide sequences, DNA aptamers, nano- or even antibodies, different cells and their responses may be studied in regard to the gradual distribution of the respective signal. For incorporating larger epitopes, optimized self-assembling peptide sequences as well as other bioconjugation strategies, such as a post-assembly-conjugation i.e. strain-promoted cycloaddition reactions, may become necessary, to ensure correct spatial presentation necessary for biological function. We envision that our strategy can be used for tissue engineering in regenerative medicine, especially considering peptide nanofibrils as ECM mimicking materials.

## 5.7. Acknowledgements

[REDACTED]

## 5.8. References

- [1] S. Lee, T. H. T. Trinh, M. Yoo, J. Shin, H. Lee, J. Kim, E. Hwang, Y. B. Lim, C. Ryou, *Int. J. Mol. Sci.* **2019**, 20.
- [2] K. Sato, M. P. Hendricks, L. C. Palmer, S. I. Stupp, *Chem. Soc. Rev.* **2018**, 47, 7539.
- [3] Y. Li, Y. Xiao, C. Liu, *Chem. Rev.* **2017**, 117, 4376.
- [4] S. Wu, W. Du, Y. Duan, D. Zhang, Y. Liu, B. Wu, X. Zou, H. Ouyang, C. Gao, *Acta Biomater.* **2018**, 75, 75.

- [5] S. Sur, J. B. Matson, M. J. Webber, C. J. Newcomb, S. I. Stupp, *ACS Nano* **2012**, 6, 10776.
- [6] I. Wheeldon, A. Farhadi, A. G. Bick, E. Jabbari, A. Khademhosseini, *Nanotechnology* **2011**, 22.
- [7] T. W. Chung, D. Z. Liu, S. Y. Wang, S. S. Wang, *Biomaterials* **2003**, 24, 4655.
- [8] C. Frantz, K. M. Stewart, V. M. Weaver, *J. Cell Sci.* **2010**, 123, 4195.
- [9] C. Schilling, T. Mack, S. Lickfett, S. Sieste, F. S. Ruggieri, T. Sneideris, A. Dutta, T. Bereau, R. Naraghi, D. Sinske, T. P. J. Knowles, C. V. Synatschke, T. Weil, B. Knöll, *Adv. Funct. Mater.* **2019**, 29.
- [10] X. Chen, Y. D. Su, V. Ajeti, S. J. Chen, P. J. Campagnola, *Cell. Mol. Bioeng.* **2012**, 5, 307.
- [11] J. Adamcik, F. S. Ruggieri, J. T. Berryman, A. Zhang, T. P. J. Knowles, R. Mezzenga, *Adv. Sci.* **2021**, 8, 2002182.
- [12] G. G. Glenner, C. W. Wong, *Biochem. Biophys. Res. Commun.* **1984**, 122, 1131.
- [13] J. Collinge, *Nature* **2016**, 539, 217.
- [14] I. Cherny, E. Gazit, *Angew. Chemie - Int. Ed.* **2008**, 47, 4062.
- [15] G. Wei, Z. Su, N. P. Reynolds, P. Arosio, I. W. Hamley, E. Gazit, R. Mezzenga, *Chem. Soc. Rev.* **2017**, 46, 4661.
- [16] J. Gačanin, J. Hedrich, S. Sieste, G. Glaßer, I. Lieberwirth, C. Schilling, S. Fischer, H. Barth, B. Knöll, C. V. Synatschke, T. Weil, *Adv. Mater.* **2019**, 31.
- [17] S. M. Pilkington, S. J. Roberts, S. J. Meade, J. A. Gerrard, *Biotechnol. Prog.* **2010**, 26, 93.
- [18] N. P. Reynolds, *Biointerphases* **2019**, 14, 040801.
- [19] K. Kaygisiz, C. V. Synatschke, *Biomater. Sci.* **2020**, 8, 6113.
- [20] S. Sieste, T. Mack, E. Lump, M. Hayn, D. Schütz, A. Röcker, C. Meier, K. Kaygisiz, F. Kirchhoff, T. P. J. Knowles, F. S. Ruggieri, C. V. Synatschke, J. Münch, T. Weil, *Adv. Funct. Mater.* **2021**, 2009382.
- [21] D. Romero, C. Aguilar, R. Losick, R. Kolter, *Proc. Natl. Acad. Sci. U. S. A.* **2010**, 107, 2230.
- [22] P. C. Ke, R. Zhou, L. C. Serpell, R. Riek, T. P. J. Knowles, H. A. Lashuel, E. Gazit, I. W. Hamley, T. P. Davis, M. Fändrich, D. E. Otzen, M. R. Chapman, C. M. Dobson, D. S. Eisenberg, R. Mezzenga, *Chem. Soc. Rev.* **2020**, 49, 5473.

- [23] S. Jamous, A. Comba, P. R. Lowenstein, S. Motsch, *PLoS Comput. Biol.* **2020**, 16, 1.
- [24] S. L. Gras, A. K. Tickler, A. M. Squires, G. L. Devlin, M. A. Horton, C. M. Dobson, C. E. MacPhee, *Biomaterials* **2008**, 29, 1553.
- [25] D. B. Gehlen, L. C. De Lencastre Novaes, W. Long, A. J. Ruff, F. Jakob, T. Haraszti, Y. Chandorkar, L. Yang, P. Van Rijn, U. Schwaneberg, L. De Laporte, *ACS Appl. Mater. Interfaces* **2019**, 11, 41091.
- [26] N. P. Reynolds, M. Charnley, M. N. Bongiovanni, P. G. Hartley, S. L. Gras, *Biomacromolecules* **2015**, 16, 1556.
- [27] M. N. Bongiovanni, D. B. Scanlon, S. L. Gras, *Biomaterials* **2011**, 32, 6099.
- [28] M. N. Bongiovanni, S. L. Gras, *Biomaterials* **2015**, 46, 105.
- [29] S. L. Gras, A. K. Tickler, A. M. Squires, G. L. Devlin, M. A. Horton, C. M. Dobson, C. E. MacPhee, *Biomaterials* **2008**, 29, 1553.
- [30] Y. Ohga, F. Katagiri, K. Takeyama, K. Hozumi, Y. Kikkawa, N. Nishi, M. Nomizu, *Biomaterials* **2009**, 30, 6731.
- [31] C.-O. P. N. as G. S. for R. of P. N. Schilling, T. Mack, S. Lickfett, S. Sieste, F. S. Ruggeri, T. Sneideris, A. Dutta, T. Bereau, R. Naraghi, D. Sinske, T. P. J. Knowles, C. V. Synatschke, T. Weil, B. Knöll, *Adv. Funct. Mater.* **2019**, 29, 1.
- [32] G. Deidda, S. V. R. Jonnalagadda, J. W. Spies, A. Ranella, E. Mossou, V. T. Forsyth, E. P. Mitchell, M. W. Bowler, P. Tamamis, A. Mitraki, *ACS Biomater. Sci. Eng.* **2017**, 3, 1404.
- [33] P. J. S. King, M. Giovanna Lizio, A. Booth, R. F. Collins, J. E. Gough, A. F. Miller, S. J. Webb, *Soft Matter* **2016**, 12, 1915.
- [34] S. G. Ricoult, T. E. Kennedy, D. Juncker, *Front. Bioeng. Biotechnol.* **2015**, 3.
- [35] J. Roy, J. Mazzaferri, J. G. Filep, S. Costantino, *Sci. Rep.* **2017**, 7, 1.
- [36] A. D. Doyle, R. J. Petrie, M. L. Kutys, K. M. Yamada, *Curr. Opin. Cell Biol.* **2013**, 25, 642.
- [37] E. M. Benetti, M. K. Gunnewiek, C. A. Van Blitterswijk, G. Julius Vancso, L. Moroni, *J. Mater. Chem. B* **2016**, 4, 4244.
- [38] S. Inagi, *Polym. J.* **2016**, 48, 39.
- [39] K. Chatterjee, S. Lin-Gibson, W. E. Wallace, S. H. Parekh, Y. J. Lee, M. T. Cicerone, M. F. Young, C. G. Simon, *Biomaterials* **2010**, 31, 5051.
- [40] S. C. P. Norris, P. Tseng, A. M. Kasko, *ACS Biomater. Sci. Eng.* **2016**, 2, 1309.

- [41] J. Lee, K. H. Ku, J. Kim, Y. J. Lee, S. G. Jang, B. J. Kim, *J. Am. Chem. Soc.* **2019**, 141, 15348.
- [42] R. A. Marklein, J. A. Burdick, *Soft Matter* **2009**, 6, 136.
- [43] M. K. Gupta, D. A. Balikov, Y. Lee, E. Ko, C. Yu, Y. W. Chun, D. B. Sawyer, W. S. Kim, H. J. Sung, *J. Mater. Chem. B* **2017**, 5, 5206.
- [44] M. Wirkner, J. M. Alonso, V. Maus, M. Salierno, T. T. Lee, A. J. García, A. Del Campo, *Adv. Mater.* **2011**, 23, 3907.
- [45] J. Ricken, R. Medda, S. V. Wegner, *Adv. Biosyst.* **2019**, 3, 1.
- [46] S. V. Wegner, O. I. Sentürk, J. P. Spatz, *Sci. Rep.* **2015**, 5, 1.
- [47] J. Cui, V. S. Miguel, A. Del Campo, *Macromol. Rapid Commun.* **2013**, 34, 310.
- [48] M. Wirkner, J. M. Alonso, V. Maus, M. Salierno, T. T. Lee, A. J. García, A. Del Campo, *Adv. Mater.* **2011**, 23, 3907.
- [49] W. Luo, M. N. Yousaf, *J. Am. Chem. Soc.* **2011**, 133, 10780.
- [50] S. Schulz, M. Becker, M. R. Groseclose, S. Schadt, C. Hopf, *Curr. Opin. Biotechnol.* **2019**, 55, 51.
- [51] M. R. L. Paine, P. C. Kooijman, G. L. Fisher, R. M. A. Heeren, F. M. Fernández, S. R. Ellis, *J. Mater. Chem. B* **2017**, 5, 7444.
- [52] K. Medini, B. West, D. E. Williams, M. A. Brimble, J. A. Gerrard, *Chem. Commun.* **2017**, 53, 1715.
- [53] M. A. Touve, A. S. Carlini, N. C. Gianneschi, *Nat. Commun.* **2019**, 10, 1.
- [54] J. Hall-Andersen, S. G. Kaasgaard, C. Janfelt, *Chem. Phys. Lipids* **2018**, 211, 100.
- [55] D. M. Anderson, M. G. Nye-Wood, K. L. Rose, P. J. Donaldson, A. C. Grey, K. L. Schey, *J. Mass Spectrom.* **2019**.
- [56] C. Li, J. P. Armstrong, I. J. Pence, W. Kit-Anan, J. L. Puetzer, S. Correia Carreira, A. C. Moore, M. M. Stevens, *Biomaterials* **2018**, 176, 24.
- [57] J. Lee, I. Choi, W. S. Yeo, *Chem. - A Eur. J.* **2013**, 19, 5609.
- [58] M. Kuzucu, G. Vera, M. Beaumont, S. Fischer, P. Wei, V. P. Shastri, A. Forget, *ACS Biomater. Sci. Eng.* **2021**, 7, 2192.
- [59] T. M. Keenan, A. Folch, *Lab Chip* **2008**, 8, 34.
- [60] J. Zonderland, S. Rezzola, P. Wieringa, L. Moroni, *Biomed. Mater.* **2020**, 15.
- [61] S. Khorshidi, A. Karkhaneh, *J. Tissue Eng. Regen. Med.* **2018**, 12, e1974.



- [62] A. Holle, A. Haase, M. Kayser, J. Höndorf, *J. Mass Spectrom.* **2006**, 41, 705.
- [63] X. Zhan, D. M. Desiderio, *Int. J. Mass Spectrom.* **2009**, 287, 77.
- [64] N. Amdursky, Y. Erez, D. Huppert, *Acc. Chem. Res.* **2012**, 45, 1548.
- [65] A. Adochitei, G. Drochioiu, *Rev. Roum. Chim.* **2011**, 56, 783.
- [66] K. Critchley, L. Zhang, H. Fukushima, M. Ishida, T. Shimoda, R. J. Bushby, S. D. Evans, *J. Phys. Chem. B* **2006**, 110, 17167.

## 5.9. Supporting Information

### 5.9.1. Materials for Linker Synthesis

Dimethylformamide (DMF, for peptide synthesis), dimethylsulfoxide (DMSO) and 4-dimethylaminopyridine (DMAP) were purchased from Acros Organics. EDC hydrochloride, tyramine hydrochloride, 3,4-dihydro-2H pyrane, pyridinium p-toluenesulfonate, potassium iodide (KI), acetovanillone, acetic anhydride, nitric acid (HNO<sub>3</sub>, 65%), ethanol (EtOH, abs.), Boc anhydride and tert-butanol were obtained from Sigma Aldrich. Diethyl ether, tetrahydrofuran (THF, abs.), dichloromethane (DCM), and acetonitrile (ACN) were obtained from Fisher Scientific. Potassium carbonate, sodium sulfate, trifluoroacetic acid (TFA) and triethylamine were purchased from Carl Roth. Sodium borohydride, 4-bromobutyric acid ethyl-4-bromobutyrate were obtained from TCI chemicals. Methanol, acetone and sodium hydroxide were obtained from VWR chemicals.

### 5.9.2. Instruments

#### Nuclear Magnetic Resonance Spectroscopy (NMR)

NMR measurements were recorded either on an Avance 300 or Avance III 250 spectrometer (Bruker) (300 MHz for <sup>1</sup>H-NMR and 75 MHz for <sup>13</sup>C-NMR or 250 MHz for <sup>1</sup>H-NMR and 63 MHz for <sup>13</sup>C-NMR). The chemical shifts are given in parts per million (ppm) relating to the solvent peak of CD<sub>3</sub>Cl or DMSO-d<sub>6</sub> for <sup>1</sup>H-NMRs. The signal splittings are listed as s (singlet), d (doublet), t (triplet), dd (doublet of doublet), m (multiplet), br (broad singlet). The coupling constant (J) is stated in Hz. All spectra were analyzed using MestReNova 14.0.0-23239.

### **High-Performance Liquid Chromatography (HPLC)**

HPLC runs for purification were conducted in preparative scale using a Shimadzu system with the following modules: DGU-20A5R, LC-20AP, CBM-20A, SPD-M20A, SIL-10AP, FRC-18A. The column Gemini NX-C18-110Å, Phenomenex, 150 mm × 30 mm, 5 μm pore size and a flow rate of 25 mL/min was used. An acetonitrile/water mixture with additional 0.1%TFA was used as eluent with a programmed gradient running from 0% to 100% ACN in water in 45 min (PCL) and 35 min (NCL). The peptides were dissolved in MilliQ water with 0.1% TFA to a concentration of approx. 0.1–0.01 mg/mL and filtered via a PES syringe filter with a pore size of 0.45 μm before injecting approx. 10 mL per run in HPLC and were detected at 214 nm and 254 nm.

Analytical scale HPLC was performed using a Shimadzu system with following modules: DGU-20A5R, LC-20AT, CBM-20A, SPD-M20A, SIL-10ACHT, CTO-20AC. In analytical scale, the column Zorbax XDB-C18, 9.4 × 250 mm, 5 μm pore size was used. The eluent was a gradient from 5% to 80% ACN in water over 22 min (NCL). The peptides were dissolved in MilliQ water with 0.1% TFA to a concentration of 1 mg/mL and filtered via a PES syringe filter with a pore size of 0.45 μm before injecting approx. 50 μL per run in HPLC.

### **Liquid Chromatography - Mass Spectrometry (LC-MS)**

HPLC-ESI-MS was measured on a Shimadzu LC-2020 Single Quadrupole MS instrument equipped with the modules LC-20AD, SIL-20ACHT, SPD-20A, CTO-using a Kinetex EVO C18 100 Å LC 50 × 2.1 mm column with 2.6 μm pore size. An acetonitrile/water mixture with additional 0.1% formic acid was used as eluent. The gradient was from 5% ACN to 95% ACN over 20 min. The data was processed with LabSolutions and Origin. Samples were dissolved either in methanol or MilliQ water to a concentration of 0.1 mg/mL.

### **Matrix-Assisted Laser Desorption/Ionization - Time of Flight Mass Spectrometry (MALDI-ToF MS)**

MALDI-ToF measurements were measured on a rapifleX MALDI-TOF/TOF from Bruker and MALDI Synapt G2-SI from Waters. The samples were prepared via dried droplet method by mixing with a saturated α-cyano-4-hydroxycinnamic acid (HCCA)

solution in water/ACN 1:1+0.1% TFA before measurement. Appr. 1  $\mu$ L of the solution was added to the target plate and allowed to dry. The data was evaluated with mMass software.

### **Matrix-Assisted Laser Desorption/Ionization - Time of Flight Mass Spectrometry (MALDI-ToF MS)-Setup**

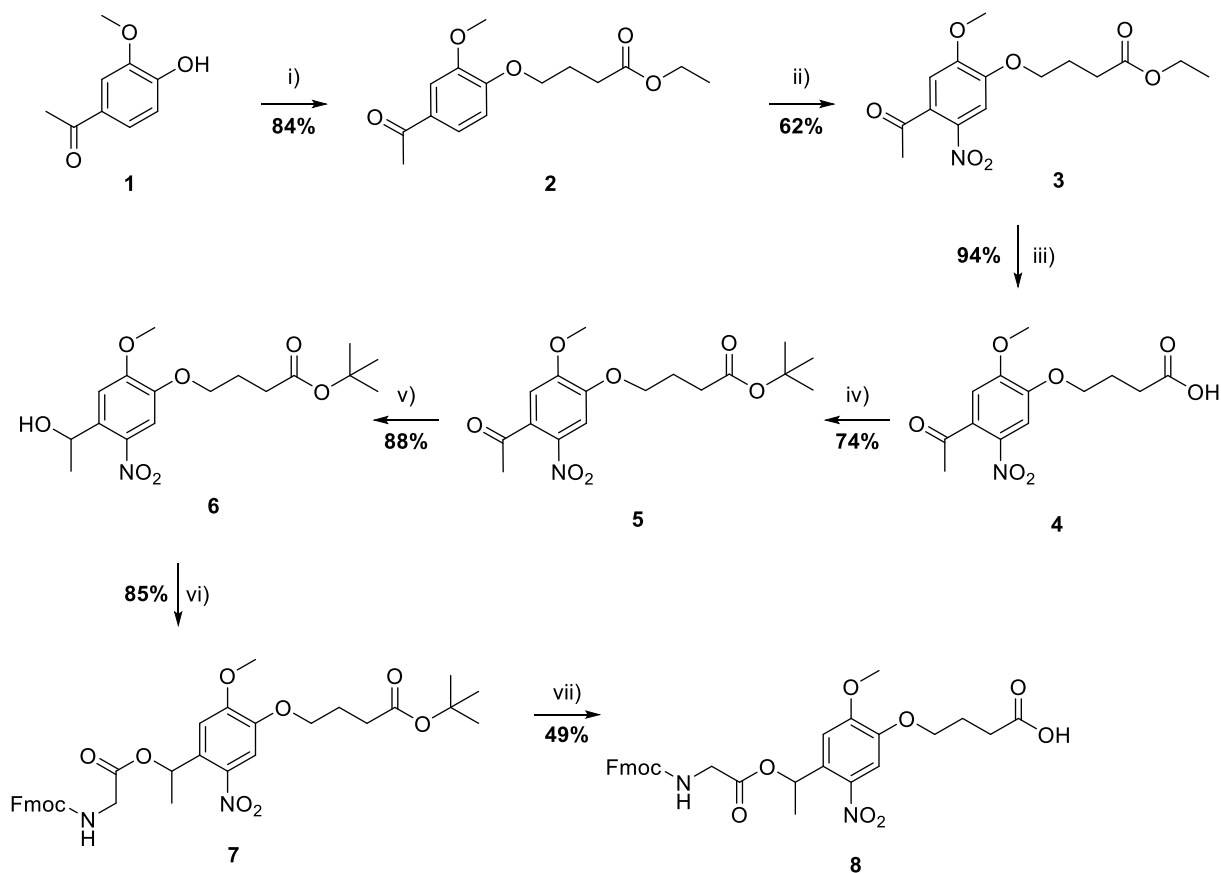
Since the wavelength of the laser (355 nm) is close to the UV-radiation used for fragmentation of the PCL (365 nm), particular care was taken in adjusting the laser intensity. The laser power, which is typically applied for MALDI-MSI of  $10^8$ W resulted in in-source-fragmentation and a significant contribution to the yield of the RGD-fragment signal was observed. The reduction of the laser intensity to 35%, which is close to desorption/ionization threshold of the HCCA matrix, suppressed in-source fragmentation almost completely.

### **Microwave Peptide Synthesizer**

Peptides were synthesized using an automated microwave peptide synthesizer (CEM, Liberty Blue™) according to the standard coupling strategy (see chapter 5.9.3.).

### 5.9.3. Synthesis

Synthesis of Photo-cleavable Linker, PCL (8), according to Sur et al.<sup>[1]</sup>



Scheme S1: Synthesis of 8: i) Ethyl 4-bromobutanoate,  $K_2CO_3$ , DMF, 24 h, rt; ii)  $HNO_3$ ,  $Ac_2O$ , 4 min, 0 °C; iii) EtOH, 1 h, 40 °C; iv) Di-tert-butylpyrocarbonate, DMAP, tBuOH/THF (3:1, v/v), 21 h, rt; v)  $NaBH_4$ , EtOH, 5 h, rt; vi) ((9H-fluoren-9-ylmethoxy)carbonyl]glycine), EDC, DMAP, 1.5 h, rt; vii) TFA,  $CH_2Cl_2$ , 4 h, rt.

#### (2) Ethyl 4-(4-(2-acetyl-3-methoxyphenoxy)butanoate

To a solution of ethyl 4-bromobutanoate (5.60 mL, 39.23 mmol) in DMF (50 mL) was added 1-(4-hydroxy-3-methoxyphenyl)ethan-1-one (8.03 g, 48.36 mmol) and  $K_2CO_3$  (12.55 g, 90.88 mmol). The reaction mixture was stirred overnight at room temperature and was diluted with water (50 mL) and EtOAc (50 mL). The aqueous phase was extracted three times with EtOAc (50 mL). The combined organic phase was washed three times with water (25 mL) and with brine (25 mL). The organic phase was dried over  $Na_2SO_4$ , filtered, and the solvent was removed under reduced pressure to yield a white solid (11.40 g, 40.70 mmol, 84% yield).

Chemical formula  $C_{15}H_{20}O_5$ ,  $M = 280.32$  g/mol

$R_f$  (n-hexane/ EtOAc, 5/3) = 0.5

<sup>1</sup>H-NMR (250 MHz, CDCl<sub>3</sub>, 25 °C) δ/ppm: 7.57 – 7.50 (m, 2H, H1, H3), 6.88 (d, J = 8.2 Hz, 1H, H4), 4.18 - 4.09 (m, 4H, H14, H19), 3.90 (s, 3H, H8), 2.55 (s, 3H, H11), 2.53 (s, 2H, H15), 2.18 (q, J = 6.8 Hz, 2H, H13), 1.25 (t, J = 7.1 Hz, 3H, H20).

<sup>13</sup>C-NMR (63 MHz, CDCl<sub>3</sub>, 25 °C) δ/ppm: 196.97, 173.15, 152.72, 149.35, 130.58, 123.34, 111.30, 110.49, 67.89, 60.63, 56.10, 30.68, 26.36, 24.38, 14.34.

LC-MS: (ESI+) m/z calc. for C<sub>15</sub>H<sub>20</sub>O<sub>5</sub> [M+H]<sup>+</sup>, 281.32 g/mol; found 281.15 g/mol.

### (3) Ethyl 4-(4-acetyl-2-methoxy-5-nitrophenoxy)butanoate

To a solution of ethyl 4-(4-acetyl-2-methoxyphenoxy)butanoate (2 (10.35 g, 36.92 mmol) in 175 mL acetic anhydride at 0 °C was added 65% HNO<sub>3</sub> (6 mL) dropwise over 2 min. The brownish-yellow solution was added to ice-water (1500 mL) 4 min. after starting to add HNO<sub>3</sub>. The reaction mixture was stirred for further 30 min. The yellow solid was filtered and dissolved in dichloromethane. The organic phase was washed three times with sat. aq. NaHCO<sub>3</sub> (150 mL) and water (150 mL). The organic phase was dried over Na<sub>2</sub>SO<sub>4</sub>, filtered, and the solvent was removed under reduced pressure. The crude product showed 30% of side product due to nitration side reactions and was purified via column chromatography eluting with 1.5% MeOH in CH<sub>2</sub>Cl<sub>2</sub> to yield a yellow solid (7.52 g, 23.1 mmol, 63% yield).

Chemical formula C<sub>15</sub>H<sub>19</sub>N<sub>5</sub>O<sub>7</sub>. M = 325.11 g/mol.

R<sub>F</sub> (CH<sub>2</sub>Cl<sub>2</sub> with 1.5% MeOH) = 0.20

<sup>1</sup>H-NMR (250 MHz, CDCl<sub>3</sub>, 25 °C) δ/ppm: 7.61 (s, 1H, H1), 6.74 (s, 1H, H4), 4.22 – 4.10 (m, 4H, H14, H19), 3.96 (s, 3H, H8), 2.55 (t, J = 7.2 Hz, 2H, H13), 2.49 (s, 3H, H10), 2.20 (q, J = 6.7 Hz, 2H, H15), 1.27 (t, J = 7.1 Hz, 3H, H20).

<sup>13</sup>C-NMR (63 MHz, CDCl<sub>3</sub>, 25 °C) δ/ppm: 200.17, 172.82, 154.30, 148.85, 132.87, 108.72, 107.95, 68.46, 60.63, 56.61, 30.51, 30.44, 24.17, 14.24.

LC-MS: (ESI+) m/z calc. for C<sub>15</sub>H<sub>19</sub>N<sub>5</sub>O<sub>7</sub> [M+H]<sup>+</sup>, 326.12 g/mol; found 326.15 g/mol.

### (4) 4-(4-Acetyl-2-methoxy-5-nitrophenoxy)butanoic acid

To a suspension of ethyl-4-(4-acetyl-2-methoxy-5-nitrophenoxy)butanoate (3) (3.65 g, 11.22 mmol) in EtOH (50 mL) was given 1M aq. NaOH (20 mL). The reaction mixture was stirred at 40 °C for 1.5h. The solvent was removed under reduced pressure, and the aqueous residue was taken up in sat. aq. NaHCO<sub>3</sub>. The aqueous layer was washed three times with CH<sub>2</sub>Cl<sub>2</sub> (50 mL) and acidified with conc. HCl to pH 1. A brown-yellow precipitation was observed. The aqueous layer was extracted three times with CH<sub>2</sub>Cl<sub>2</sub> (150 mL), and the organic layer was washed two times with 0.5 N HCl (100 mL). The organic phase was dried over Na<sub>2</sub>SO<sub>4</sub>, filtered and the solvent was removed under reduced pressure to obtain a yellow solid (3.19 g, 10.75 mmol, 94% yield).

Chemical formula C<sub>13</sub>H<sub>15</sub>NO<sub>7</sub>. M = 297.08 g mol<sup>-1</sup>.

R<sub>F</sub> (CH<sub>2</sub>Cl<sub>2</sub> with 10% MeOH) = 0.62.

<sup>1</sup>H-NMR (250 MHz, CDCl<sub>3</sub>, 25 °C) δ/ppm: 7.62 (s, 1H, H1), 6.75 (s, 1H, H4), 4.18 (t, J = 6.1 Hz, 2H, H14), 3.95 (s, 3H, H8), 2.63 (t, J = 7.1 Hz, 2H, H13), 2.50 (s, 3H, H10), 2.22 (p, J = 6.7 Hz, 2H, H15).

<sup>13</sup>C-NMR (63 MHz, CDCl<sub>3</sub>, 25 °C) δ/ppm: 201.05, 175.23, 154.28, 148.85, 138.09, 132.51, 108.53, 107.90, 77.67, 77.16, 76.65, 68.34, 56.41, 30.16, 30.01, 23.97.

LC-MS: (ESI+) m/z calc. for C<sub>13</sub>H<sub>15</sub>NO<sub>7</sub> [M+Na]<sup>+</sup>, 320.07 g/mol; found 320.10 g/mol.

#### *(5) tert-Butyl 4-(4-acetyl-2-methoxy-5-nitrophenoxy)butanoate*

To a suspension of 4-(4-acetyl-2-methoxy-5-nitrophenoxy)butanoic acid (4) (3.00 g, 10.43 mmol) in 80 mL tBuOH/THF solution (3:1 v/v) was added DMAP (382 mg, 3.13 mmol). Di-tert-butylpyrocarbonate (6.83 g, 31.29 mmol) was added portion wise over 1.5 h. Bubbling was observed, and the flask was equipped with a balloon under argon atmosphere. After stirring for 21 h, TLC (10% MeOH in CH<sub>2</sub>Cl<sub>2</sub>) showed complete conversion. The solvent was removed under reduced pressure to obtain an orange oil. The residue was taken up in CH<sub>2</sub>Cl<sub>2</sub> (100 mL), washed twice with 0.2 N HCl (50 mL) and three times with sat. aq. NaHCO<sub>3</sub> (50 mL). The organic layer was then dried over Na<sub>2</sub>SO<sub>4</sub>. The solvent was removed under reduced pressure to afford an orange oil, which was further purified through column chromatography eluting with 2% MeOH in CH<sub>2</sub>Cl<sub>2</sub> to afford a yellow viscous oil (2.76g, 7.81 mmol, 74% yield).

Chemical formula  $C_{17}H_{23}NO_7$ .  $M = 353.17$  g/mol.

$R_F$  ( $CH_2Cl_2$  with 2% MeOH) = 0.56.

$^1H$ -NMR (250 MHz,  $CDCl_3$ , 25 °C)  $\delta$ /ppm: 7.61 (s, 1H, H1), 6.74 (s, 1H, H4), 4.14 (t,  $J = 6.4$  Hz, 2H, H14), 3.96 (s, 3H, H11), 2.47 (d,  $J = 9.6$  Hz, 5H, H15, H8), 2.15 (p,  $J = 6.9$  Hz, 2H, H16), 1.45 (s, 9H, H21–H23).

$^{13}C$ -NMR (63 MHz,  $CDCl_3$ , 25 °C)  $\delta$ /ppm: 200.18, 172.12, 154.30, 148.92, 138.37, 132.83, 108.73, 107.99, 80.68, 77.54, 77.04, 76.53, 68.63, 56.62, 31.69, 30.44, 28.12, 24.31.

LC-MS: (ESI-)  $m/z$  calc. for  $C_{17}H_{23}NO_7 [M]^-$ , 353.14 g/mol; found 353.15 g/mol.

*(6) tert-Butyl 4-(4-(1-hydroxyethyl)-2-methoxy-5-nitrophenoxy)butanoate*

$NaBH_4$  (1.03 g, 27.2 mmol) was added to a suspension of tert-butyl-4-(4-acetyl-2-methoxy-5-nitrophenoxy)butanoate (5) (2.76 g, 7.81 mmol) in EtOH (45 mL). After 5 h the reaction was quenched by adding a citric acid solution (600 mg/mL) until pH 4 is reached. The solution was then diluted with  $CH_2Cl_2$  (100 mL) and water (50 mL). The organic layer was washed with brine and dried over  $Na_2SO_4$ . The solvent was removed under reduced pressure to yield a viscous orange oil (2.46 g, 6.98 mmol, 88%).

Chemical formula  $C_{17}H_{25}NO_7$ .  $M = 355.16$  g/mol.

$R_F$  ( $CH_2Cl_2$  with 2% MeOH) = 0.32.

$^1H$ -NMR (250 MHz,  $CDCl_3$ , 25 °C)  $\delta$ /ppm: 7.55 (s, 1H, H1), 7.28 (s, 1H, H4), 5.54 (q,  $J = 6.3$  Hz, 1H, H9), 4.08 (t,  $J = 6.4$  Hz, 2H, H15), 3.96 (s, 3H, H8), 2.46 (dt,  $J = 14.5, 7.3$  Hz, 2H, H14), 2.13 (q,  $J = 6.6$  Hz, 2H, H16), 1.53 (d,  $J = 6.2$  Hz, 3H, H10), 1.44 (s, 9H, H21–H23)..

$^{13}C$ -NMR (63 MHz,  $CDCl_3$ , 25 °C)  $\delta$ /ppm: 172.27, 154.12, 146.96, 139.51, 136.94, 109.05, 108.65, 80.60, 77.56, 77.05, 76.54, 68.42, 65.75, 56.36, 31.82, 28.11, 24.42, 24.29, 21.85.

LC-MS: (ESI+)  $m/z$  calc. for  $C_{17}H_{25}NO_7 [M+Na]^+$ , 378.15 g/mol; found 378.15 g/mol.

*(7) tert-Butyl 4-(4-(1-(((9H-fluoren-9-ylmethoxy)carbonyl)glycyl)oxy)ethyl)-2-methoxy-5-nitrophenoxy)butanoate*

To [(9H-fluoren-9-ylmethoxy)carbonyl]glycine (3.18 g, 10.5 mmol), EDC × HCl (2.38 g, 12.3 mmol) and DMAP (90 mg, 0.7 mmol) was added dry CH<sub>2</sub>Cl<sub>2</sub> (20 mL). The suspension becomes clear solution after stirring for 5 min and tert-butyl 4-(4-(1-hydroxyethyl)-2-methoxy-5-nitrophenoxy)butanoate (6) (2.40 g, 6.75 mmol) was added in CH<sub>2</sub>Cl<sub>2</sub> (13 mL). After stirring for 4 h at room temperature, the reaction mixture was washed twice with water (50 mL) and twice with sat. aq. NaHCO<sub>3</sub> (100 mL). The organic layer was dried over Na<sub>2</sub>SO<sub>4</sub>. The solvent was removed under reduced pressure to afford a yellow powder that was further purified via column chromatography, eluting with 2% MeOH in CH<sub>2</sub>Cl<sub>2</sub>, yielding a light yellow solid with small amount of impurities (3.65 g, 5.76 mmol, 85%).

Chemical formula C<sub>34</sub>H<sub>38</sub>N<sub>2</sub>O<sub>10</sub>. M = 634.24 g/mol.

R<sub>F</sub> (CH<sub>2</sub>Cl<sub>2</sub> with 2% MeOH) = 0.54, R<sub>F</sub> (Cyclohexane/ EtOAc, 5/3) = 0.52.

<sup>1</sup>H-NMR (250 MHz, CDCl<sub>3</sub>, 25 °C) δ/ppm: 7.75 (d, J = 7.5 Hz, 2H, H36, H37), 7.57 (d, J = 6.7 Hz, 3H, H33, H40), 7.44 – 7.20 (m, 4H, H34, H35, H38, H39), 6.98 (s, 1H, H1), 6.55 (q, J = 6.2 Hz, 1H, H4), 5.30 (d, J = 5.2 Hz, 1H, H9), 4.47 – 4.27 (m, 2H, H41), 4.23 – 3.95 (m, 5H, H31, H14, H19), 3.94 (s, 3H, H10), 2.43 (t, J = 7.3 Hz, 2H, H18), 2.13 (h, J = 7.1, 5.7 Hz, 2H, H20), 1.64 (d, J = 6.4 Hz, 3H, H8), 1.45 (s, 9H, H25–H27).

<sup>13</sup>C-NMR (63 MHz, CDCl<sub>3</sub>, 25 °C) δ/ppm: 172.21, 169.03, 156.30, 154.18, 147.44, 143.72, 143.69, 141.31, 141.27, 139.64, 132.41, 127.77, 127.09, 125.04, 120.03, 108.94, 108.01, 80.61, 69.79, 68.41, 67.27, 56.42, 47.03, 42.95, 31.79, 28.13, 24.39, 21.98.

LC-MS: (ESI+) m/z calc. for C<sub>34</sub>H<sub>38</sub>N<sub>2</sub>O<sub>10</sub> [M+Na]<sup>+</sup>, 657.24 g/mol; found 657.25 g/mol.

*(8) 4-(4-(1-(((9H-fluoren-9-ylmethoxy)carbonyl)glycyl)oxy)ethyl)-2-methoxy-5-nitrophenoxy)butanoic acid*

To a solution of tert-butyl 4-(4-(1-(2-(Fmoc-amino)acetoxy)ethyl)-2-methoxy-5-nitrophenoxy)butanoate (7) (500 mg, 0.787 mmol) in CH<sub>2</sub>Cl<sub>2</sub> (5 mL) was added TFA



(0.75 mL). The light yellow suspension becomes a deep yellow clear solution. After stirring for 5 h at room temperature, the solvent was evaporated under reduced pressure. The residue was taken up with CH<sub>2</sub>Cl<sub>2</sub> and was washed twice with 0.5 N HCl (40 mL). The organic layer was dried over Na<sub>2</sub>SO<sub>4</sub>. The solvent was removed under reduced pressure to afford a yellow powder that was further purified via column chromatography, eluting with 4% MeOH in CH<sub>2</sub>Cl<sub>2</sub>, yielding a light yellow solid (224 mg, 0.387 mmol, 49%).

Chemical formula C<sub>30</sub>H<sub>30</sub>N<sub>2</sub>O<sub>10</sub>. M = 578.57 g/mol.

R<sub>F</sub> (CH<sub>2</sub>Cl<sub>2</sub> with 4% MeOH) = 0.33.

<sup>1</sup>H-NMR (250 MHz, CDCl<sub>3</sub>, 25 °C) δ/ppm: 7.75 (d, J = 7.5 Hz, 2H, H33, H34), 7.55 (d, J = 6.7 Hz, 2H, H30, H37), 7.42 – 7.26 (m, 4H, H31, H32, H35, H36), 6.98 (s, 1H, H1), 6.53 (q, J = 6.4 Hz, 1H, H4), 5.30 (t, J = 5.8 Hz, 1H, H9), 4.39 – 4.23 (m, 2H, H38), 4.17 – 4.00 (m, 5H, H28, H20, H14), 3.94 (s, 3H, H8), 2.60 (t, J = 7.3 Hz, 2H, H19), 2.17 (h, J = 7.1, 5.7 Hz, 2H, H21), 1.64 (d, J = 6.3 Hz, 2H, H10).

<sup>13</sup>C-NMR (63 MHz, CDCl<sub>3</sub>, 25 °C) δ/ppm: 178.02, 169.08, 156.36, 154.20, 147.30, 143.68, 141.27, 139.63, 132.55, 127.77, 127.09, 125.03, 120.01, 109.03, 108.09, 69.79, 68.03, 67.30, 56.39, 47.03, 42.96, 30.16, 23.94, 21.96.

LC-MS: (ESI+) m/z calc. for C<sub>30</sub>H<sub>30</sub>N<sub>2</sub>O<sub>10</sub> [M+Na]<sup>+</sup>, 601.17 g/mol; found 601.20 g/mol.

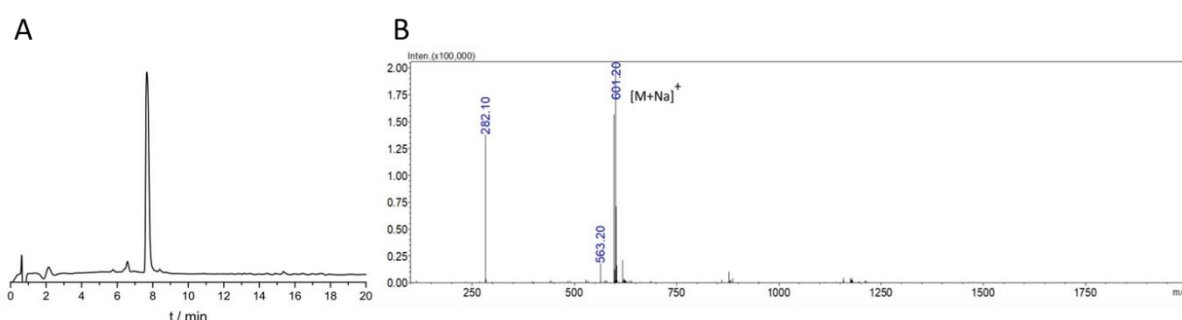
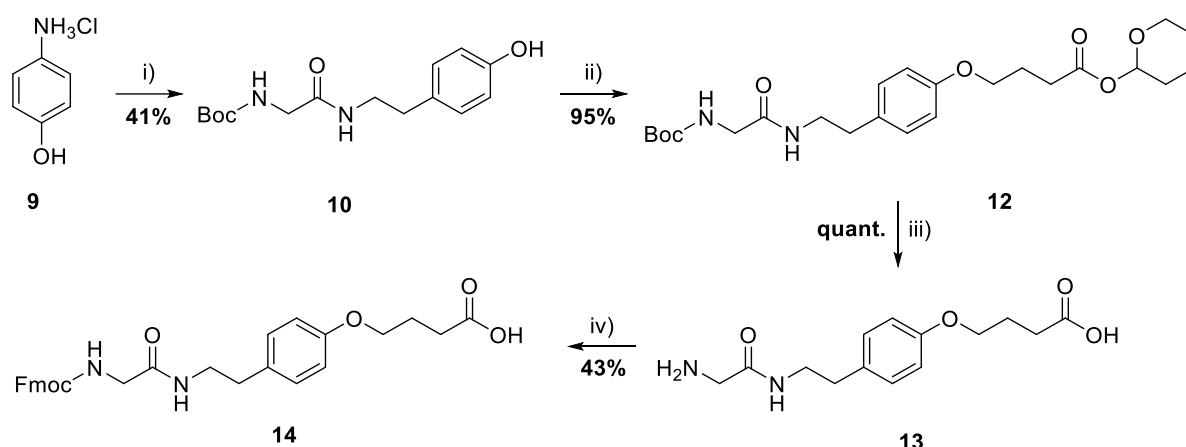


Figure S1: A) LC-MS chromatogram (detector: 214 nm) of compound (8). B) MS (ESI+) m/z, calc. for C<sub>30</sub>H<sub>30</sub>N<sub>2</sub>O<sub>10</sub> [M+Na]<sup>+</sup>, 601.17 g/mol; found 601.20 m/z.

## Synthesis of non-photo cleavable linker NCL (14), according to Sur et al.<sup>[1]</sup>



Scheme S2: Synthesis of 14. i) (tert-butoxycarbonyl)glycine, EDC, DMAP, NEt<sub>3</sub>, THF, 6 h, reflux; ii) tetrahydro-2H-pyran-2-yl 4-bromobutanoate 11, K<sub>2</sub>CO<sub>3</sub>, KI, acetone, 3 d, reflux; iii) TFA, CH<sub>2</sub>Cl<sub>2</sub>, 2 h, rt; iv) 1-((9H-Fluoren-9-ylmethoxy)carbonyloxy)-2,5-pyrrolidinedione, NEt<sub>3</sub>, H<sub>2</sub>O/ACN (1:1 v/v), 4 h, rt. Synthesis of 11 according to literature.<sup>[2]</sup>

### (10) tert-Butyl (2-((4-hydroxyphenethyl)amino)-2-oxoethyl)carbamate

4-Hydroxyphenethylamine hydrochloride (2.00 g, 11.5 mmol) was added to dry THF (20 mL) and NEt<sub>3</sub> (5 mL). To this suspension (tert-butoxycarbonyl)glycine (2.26 g, 12.9 mmol) was added, followed by EDC (2.47 g, 12.7 mmol) and DMAP (140 mg, 1.15 mmol). The white suspension was heated at reflux for 6 h, and then the solvent was removed under reduced pressure. The yellow residue was dissolved in CH<sub>2</sub>Cl<sub>2</sub> (40 mL), washed three times with water (40 mL) and dried over Na<sub>2</sub>SO<sub>4</sub>. The solvent was removed to yield a viscous yellow oil that was purified via column chromatography, eluting with 20% MeOH in CH<sub>2</sub>Cl<sub>2</sub>. The combined organic fractions were evaporated to yield a colorless solid with small impurities. The solid was recrystallized from chloroform and small amount of MeOH. The white crystals were washed with n-hexane. A colorless solid was obtained (1.39 g, 4.74 mmol, 41%).

Chemical formula C<sub>16</sub>H<sub>23</sub>NO<sub>4</sub>. M = 293.16 g/mol.

R<sub>F</sub> (CH<sub>2</sub>Cl<sub>2</sub> with 20% MeOH) = 0.72.

<sup>1</sup>H NMR (250 MHz, Chloroform-d with 10% CD<sub>3</sub>OD) δ 6.95 (d, J = 8.1 Hz, 2H, H1, H3), 6.68 (d, J = 8.2 Hz, 2H, H4, H6), 3.60 (s, 2H, H12), 3.38 – 3.24 (m, 2H, H9), 2.64 (t, J = 7.2 Hz, 2H, H8), 1.36 (s, 9H, H17–H19).

$^{13}\text{C}$  NMR (63 MHz,  $\text{CDCl}_3$  with 10%  $\text{CD}_3\text{OD}$ )  $\delta$  170.11, 156.47, 155.34, 129.67, 115.40, 77.67, 77.16, 76.65, 43.76, 40.97, 34.55, 28.19.

LC-MS: (ESI+)  $m/z$  calc. for  $\text{C}_{16}\text{H}_{23}\text{NO}_4$   $[\text{M}+\text{Na}]^+$ , 317.14 g/mol; found 317.15 g/mol.

(11) *Tetrahydro-2H-pyran-2-yl 4-bromobutanoate*

4-Bromobutanoic acid (2.50 g, 15.00 mmol) and 3,4-dihydro-2H-pyran (1.5 mL, 15.12 mmol) were dissolved in  $\text{CH}_2\text{Cl}_2$  and cooled down to 0 °C. To this solution was added pyridinium p-toluenesulfonate (0.376 g, 1.50 mmol) and stirred at 0 °C for 30 min and at ambient temperature for 4 h. The solution was washed three times with 4% aq.  $\text{Na}_2\text{CO}_3$  (100 mL) and three times with water (100 mL). The organic layer was then dried over  $\text{Na}_2\text{SO}_4$ . The solvent was removed to yield a viscous colorless oil (3.42 g, 13.68 mmol, 91%).

Chemical formula  $\text{C}_9\text{H}_{15}\text{BrO}_3$ .  $M = 251.12$  g/mol.

$^1\text{H}$ -NMR (250 MHz,  $\text{CDCl}_3$ , 25 °C)  $\delta$ /ppm: 5.99 (d,  $J = 3.3$  Hz, 1H, H8), 3.95 – 3.62 (m, 2H, H10), 3.48 (t,  $J = 6.4$  Hz, 2H, H2), 2.56 (t,  $J = 7.2$  Hz, 2H, H4), 2.19 (p,  $J = 6.8$  Hz, 2H, H3), 1.88 – 1.51 (m, 6H, H11 - H13).

$^{13}\text{C}$ -NMR (63 MHz,  $\text{CDCl}_3$ , 25 °C)  $\delta$ /ppm: 171.49, 92.86, 63.43, 32.87, 32.71, 29.26, 27.70, 25.01, 18.72.

(12) *Tetrahydro-2H-pyran-2-yl 4-(4-(2-(2-((tert-butoxycarbonyl)amino)acetamido)ethyl)phenoxy)butanoate*

tert-Butyl (2-((4-hydroxyphenethyl)amino)-2-oxoethyl)carbamate (10) (1.39 g, 4.72 mmol) and tetrahydro-2H-pyran-2-yl 4-bromobutanoate (11) (1.90, 7.08 mmol) were dissolved in acetone (15 mL) in a two necked flask with air condenser and a stirrer.  $\text{K}_2\text{CO}_3$  and KI were added to the solution and stirred at 80 °C for three days. The solution was dissolved in EtOAc (50 mL), washed three times with water (50 mL), once with brine (50 mL) and dried over  $\text{Na}_2\text{SO}_4$ . The solvent was removed to yield a viscous yellow oil that was purified via column chromatography, eluting with 4% MeOH in  $\text{CH}_2\text{Cl}_2$  to obtain a yellow oil (2.09 g, 4.51 mmol, 95%).

Chemical formula  $C_{24}H_{36}N_2O_7$ .  $M = 464.56$  g/mol.

$R_F$  ( $CH_2Cl_2$  with 4% MeOH) = 0.65.

$^1H$  NMR (250 MHz, Chloroform- $d$ )  $\delta$  7.08 (d,  $J = 8.2$  Hz, 2H, H13, H15), 6.81 (d,  $J = 8.3$  Hz, 2H, H16, H18), 6.14 (s, 1H, H26), 5.99 (d,  $J = 3.9$  Hz, 1H, H7), 5.13 (s, 1H, H22), 4.04 - 3.80 (m, 2H, H9), 3.73 (d,  $J = 5.9$  Hz, 2H, H20), 3.47 (q,  $J = 6.7$  Hz, 2H, H21), 2.73 (t,  $J = 7.0$  Hz, 2H, H1), 2.56 (t,  $J = 7.3$  Hz, 2H, H3), 2.12 (p,  $J = 6.7$  Hz, 2H, H2), 1.84 - 1.51 (m, 6H, H10 - H12), 1.43 (s, 9H, H29 - H31).

$^{13}C$  NMR (63 MHz,  $CDCl_3$ )  $\delta$  172.00, 169.30, 157.53, 130.70, 129.67, 114.64, 92.63, 66.64, 63.31, 40.76, 34.73, 30.99, 29.19, 28.30, 24.92, 24.53, 18.66.

LC-MS: (ESI+)  $m/z$  calc. for  $C_{24}H_{36}N_2O_7$   $[M+Na]^+$ , 487.24 g/mol; found 487.25 g/mol.

*(13) 4-(4-(2-(2-Aminoacetamido)ethyl)phenoxy)butanoic acid*

Tetrahydro-2H-pyran-2-yl 4-(4-(2-(2-((tert-butoxycarbonyl)amino)acetamido)ethyl)phenoxy)-butanoate (12) (2.09 g, 4.50 mmol) was dissolved in a mixture of TFA (7.87 mL) and  $CH_2Cl_2$  (31.00 mL) and stirred at ambient temperature for 120 min. The solvent was removed under reduced pressure. The residue was dissolved in  $Et_2O$  (100 mL) by sonicating for 10 min. A white precipitate was observed. The product was recovered by filtration. The solids were taken up in  $CH_2Cl_2$  with 20% MeOH and dried over  $Na_2SO_4$ . After removing the solvent under reduced pressure, a white powder was obtained (1.25 g, 4.45 mmol, quant.).

Chemical formula  $C_{14}H_{20}N_2O_4$ .  $M = 280.32$  g/mol.

$^1H$  NMR (250 MHz, DMSO- $d_6$ )  $\delta$  6.95 (d,  $J = 8.2$  Hz, 2H, H7, H9), 6.68 (d,  $J = 8.2$  Hz, 2H, H10, H12), 3.84 (t,  $J = 6.1$  Hz, 2H, H15), 3.42 (s, 2H, H18), 3.36 - 3.18 (m, 2H, H14), 2.60 (t,  $J = 7.4$  Hz, 2H, H1), 2.35 (t,  $J = 7.2$  Hz, 2H, H3), 1.93 (p,  $J = 6.7$  Hz, 2H, H2).

$^{13}C$  NMR (63 MHz, DMSO- $d_6$ )  $\delta$  175.83, 165.69, 157.40, 130.57, 129.47, 114.44, 66.68, 49.73, 41.07, 40.18, 34.30, 30.41, 24.46.

(14)

4-(4-(2-(2-((9H-fluoren-9-ylmethoxy)carbonyl]amino)acetamido)ethyl)phenoxy)butanoic acid

4-(4-(2-(2-Aminoacetamido)ethyl)phenoxy)butanoic acid (13) (1.53 g, 5.46 mmol) was dissolved in a mixture of H<sub>2</sub>O (12.4 mL) and NEt<sub>3</sub> (1.86 mL). 1-((9H-Fluoren-9-ylmethoxy)carbonyl]oxy)-2,5-pyrrolidinedione (2.26 g, 6.71 mmol) was dissolved by gentle heating in acetonitrile (12.4 mL) and added to the aqueous solution. After stirring the reaction mixture at ambient temperature for 4 h the reaction mixture was concentrated to 10 mL. To the remaining solution 5% aq. citric acid (60 mL) was added. The mixture was extracted 4 times with 10% MeOH in CH<sub>2</sub>Cl<sub>2</sub> (50 mL) and the combined organic layers were dried over Na<sub>2</sub>SO<sub>4</sub> and the solvent was removed under reduced pressure. The product was purified by recrystallization from EtOH (200 mL) to yield a white solid (1.08 g, 2.16 mmol, 40%).

Chemical formula C<sub>29</sub>H<sub>30</sub>N<sub>2</sub>O<sub>6</sub>. M = 502.557 g/mol.

<sup>1</sup>H NMR (250 MHz, DMSO-d<sub>6</sub>) δ 12.10 (s, 1H, H18) 7.87 (t, J = 8.2 Hz, 2H, H29, H30), 7.71 (d, J = 7.4 Hz, 2H, H26, H33), 7.54-7.26 (m, 4H, H27, H28, H31, H32), 7.09 (d, J = 8.1 Hz, 2H, H1, H3), 6.82 (d, J = 8.1 Hz, 2H, H4, H6), 4.29 (d, J = 6.8 Hz, 2H, H34), 4.20 (d, J = 7.5, 1H, H24), 3.91 (t, J = 6.5 Hz, 2H, H9) 3.56 (d, J = 6.0 Hz, 2H, H11), 3.23 (t, J = 6.9 Hz, 2H, H8), 2.63 (t, J = 7.4 Hz, 2H, H14), 2.36 (t, J = 7.4 Hz, 2H, H16), 1.90 (p, J = 6.9 Hz, 2H, H15).

<sup>13</sup>C NMR (63 MHz, DMSO-d<sub>6</sub>) δ 174.54, 169.31, 157.38, 156.90, 144.31, 141.18, 131.74, 130.01, 128.09, 127.52, 125.71, 120.56, 114.78, 66.93, 66.17, 47.12, 43.97, 40.92, 34.76, 30.59, 24.75.

LC-MS: (ESI+) m/z calc. for C<sub>29</sub>H<sub>30</sub>N<sub>2</sub>O<sub>6</sub> [M+Na]<sup>+</sup>, 525.20 g/mol; found 525.25 g/mol.

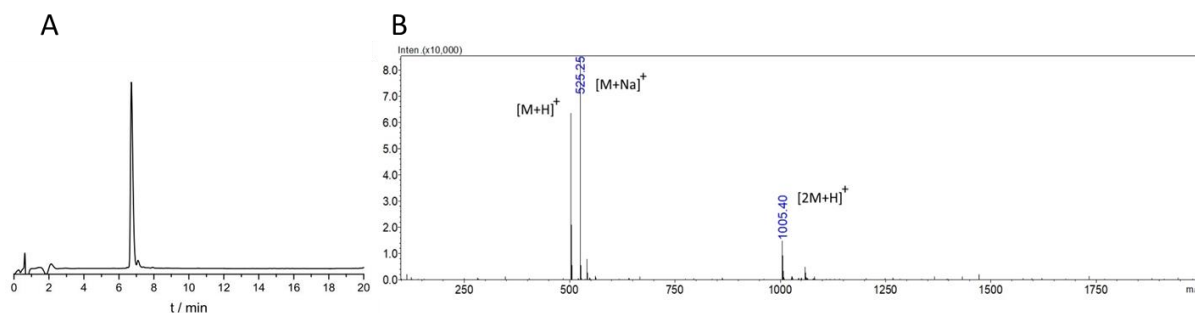


Figure S2: A) LC-MS chromatogram (detector: 214 nm) of compound (14). B) MS (ESI+)  $m/z$  calc. for  $C_{29}H_{30}N_2O_6$   $[M+Na]^+$ , 525.20 g/mol; found 525.25  $m/z$ .

### Standard Peptide Synthesis Strategy

SPPS-grade solvents were utilized together with Fmoc-L-Phe-Wang resin for Fmoc amino acid loading (0.65 mmol/g). The beads were swollen in DMF while shaking the reaction vessel for 1h. After draining the DMF a piperidine solution (20% in DMF) was added to the vessel, which was microwaved at 155 W, 75 °C for 15 s and at 30 W, 90 °C for 50 s. Afterwards the piperidine solution was sucked off and the beads were washed three times with DMF. After the addition of the Fmoc-protected amino-acid (5 eq relative to the resin loading capacity) in DMF, DIC (5 eq) in DMF and Oxyma Pure® (10 eq) in DMF were added to the reaction vessel. After microwaving at 170 W, 75 °C for 15 s and at 30 W, 90 °C for 110 s the solution was removed and the beads were washed with DMF. This procedure was repeated for each amino acid. In the final step, the Fmoc-cleavage was performed by microwaving at 155 W, 75 °C for 15 s and at 30 W, 90 °C for 50 s with piperidine solution (20% in DMF). The resin was washed manually with DCM after Fmoc-cleavage. The peptide was cleaved off the resin through treatment with 2 mL of trifluoroacetic acid (TFA) containing 2.5% water and 2.5% triisopropylsilane (TIPS) for 2 h. This solution was added to cold diethyl ether (40 mL) and afterwards centrifuged at 3000 rpm for 15 min to afford a white precipitate.

### Irradiation

Irradiation of samples were conducted with LED from Opulent Americas (Starboard Luminus SST-10-UV-A130) with a peak wavelength at 365 nm and a current of 1 A. The emission spectrum of the LED was measured *via* an Ulbricht sphere as shown in Fig. 3.

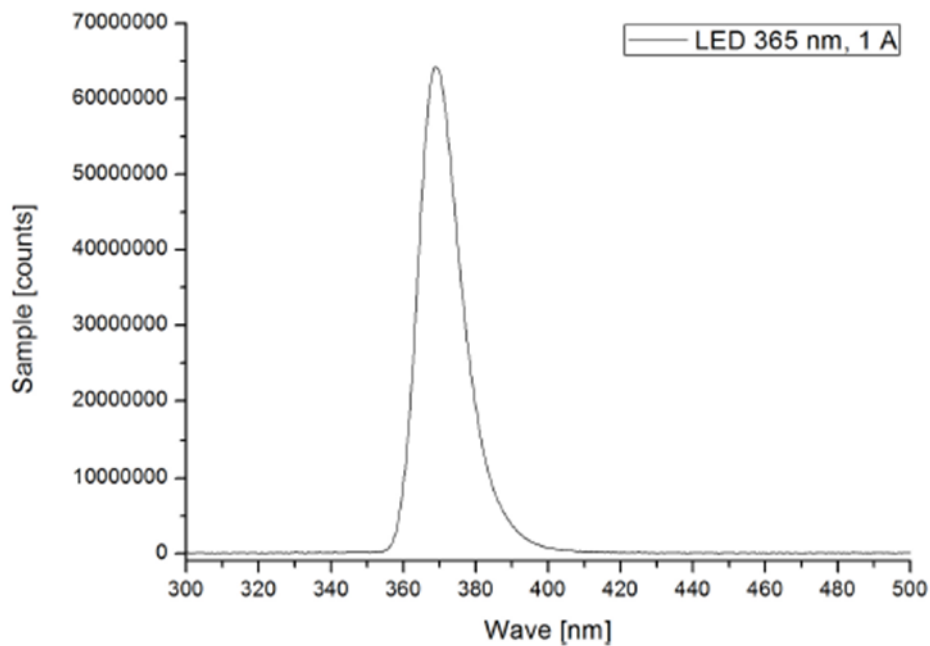


Figure S3: Emission spectrum of LED (Opulent Americas) at 365 nm, 1 A and a radiant flux of 875 mW.

#### 5.9.4. Additional Characterization RGD-NCL-CKFKQF (16)

##### LC-MS

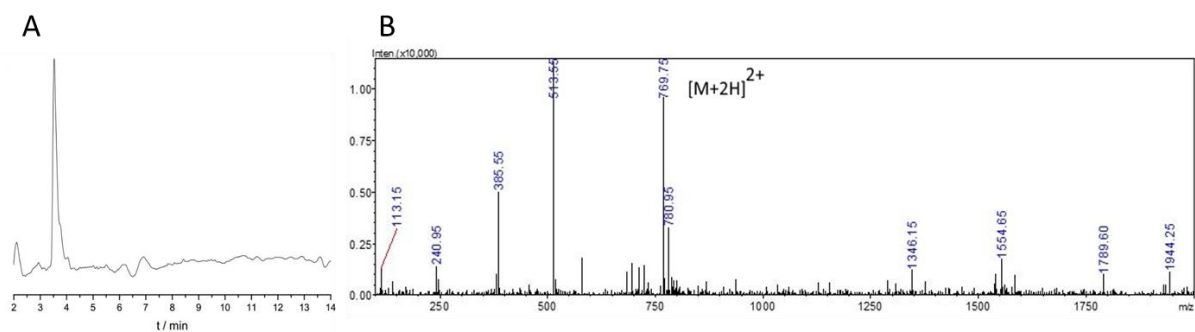
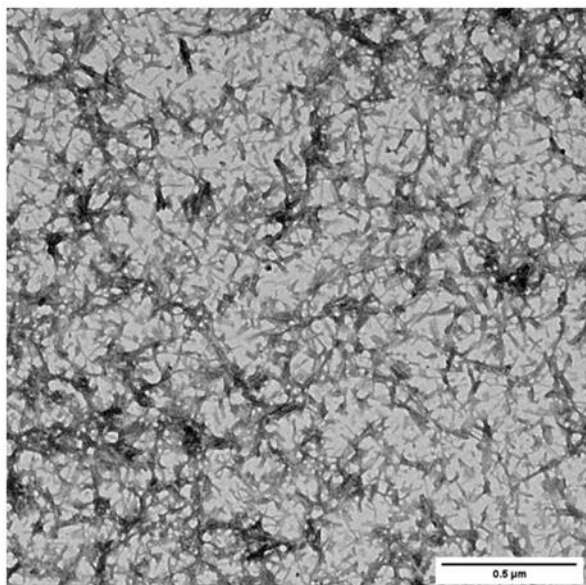


Figure S4: A) LC-MS chromatogram (detector: 214 nm) of RGD-NCL-CKFKQF (16). B) MS (ESI+)  $m/z$  calc. for  $C_{73}H_{104}N_{18}O_{18}S$   $[M+2H]^{2+}$ ,  $769.65 \text{ g mol}^{-1}$ ; found  $769.75 \text{ m/z}$

## TEM

A



B

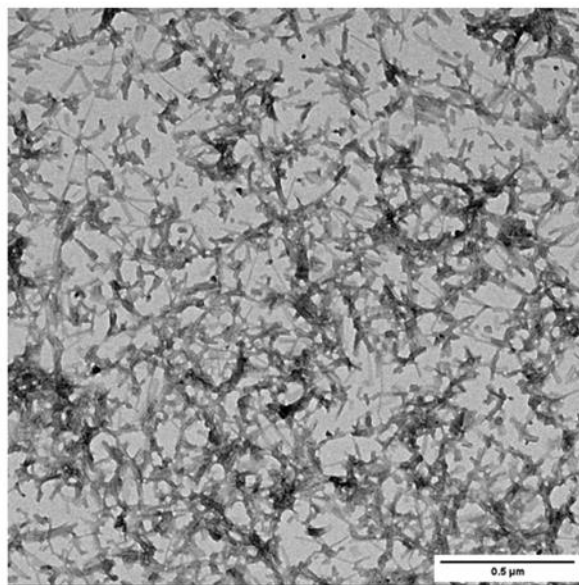


Figure S5: TEM images of RGD-NCL-CKFKFQF amyloid nanofibers formed in solution. A) Aqueous peptide solution without UV irradiation and incubation for 24h to form fibrils (**16**) and B) aqueous peptide solution after UV irradiation and subsequent incubation for 24h to form fibrils (**16-UV**).



## ThT-Assay

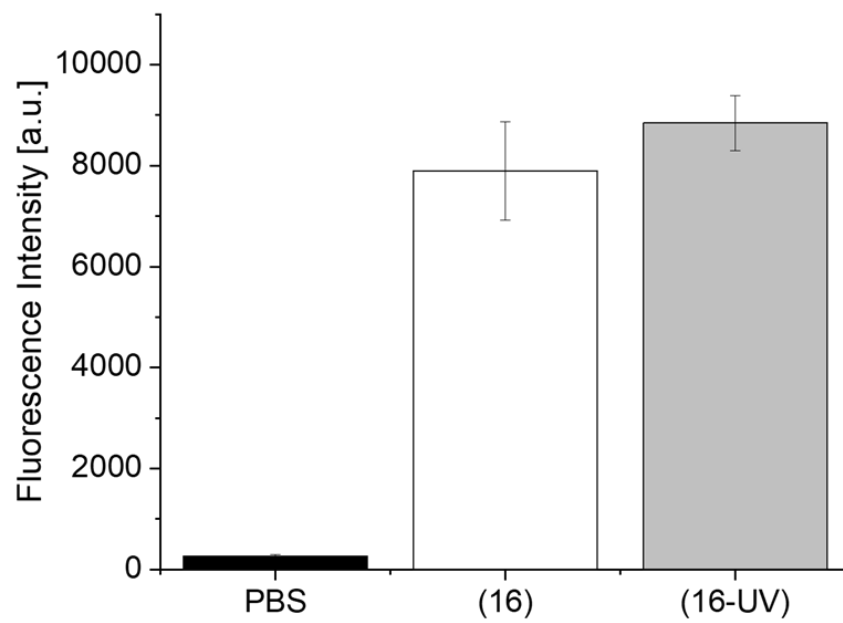


Figure S6: ThT assay shows high fluorescence for nanofibers before (16) and after UV irradiation (16-UV). As control PBS was used.

## Fourier-Transform Infrared Spectroscopy (FT-IR)

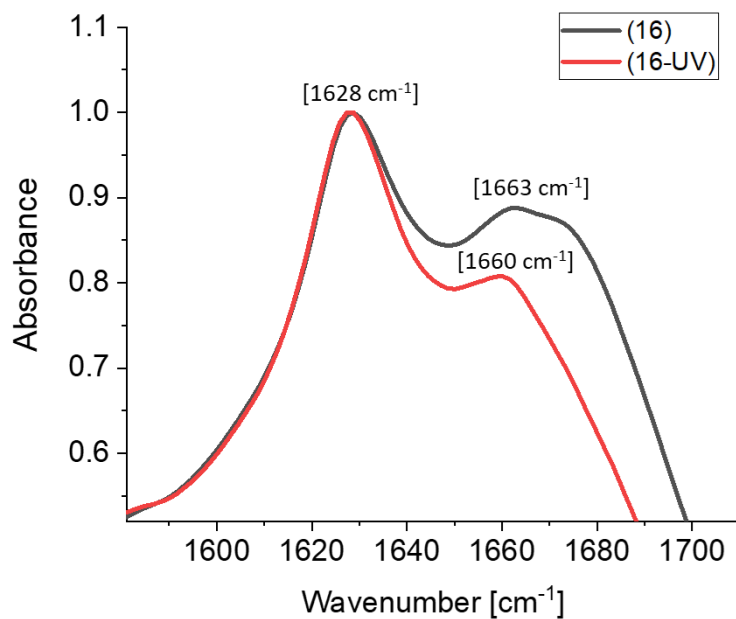


Figure S7: FT-IR spectra of peptide (**16**) structures show characteristic amyloid signals for both UV treated peptide (**16-UV**: red line) and non-treated (**16**: black line) samples.

## HPLC study

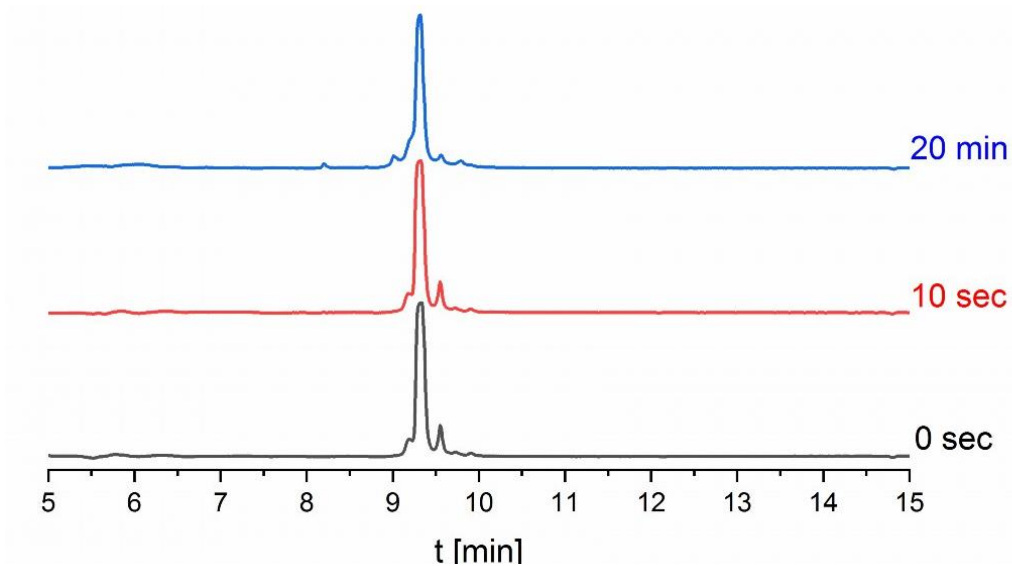


Figure S8: HPLC measurement (detector 190 nm) of RGD-NCL-CKFKFQF (**16**) without irradiation (0 sec) and after UV irradiation for 10 sec and 20 min.

## SEM

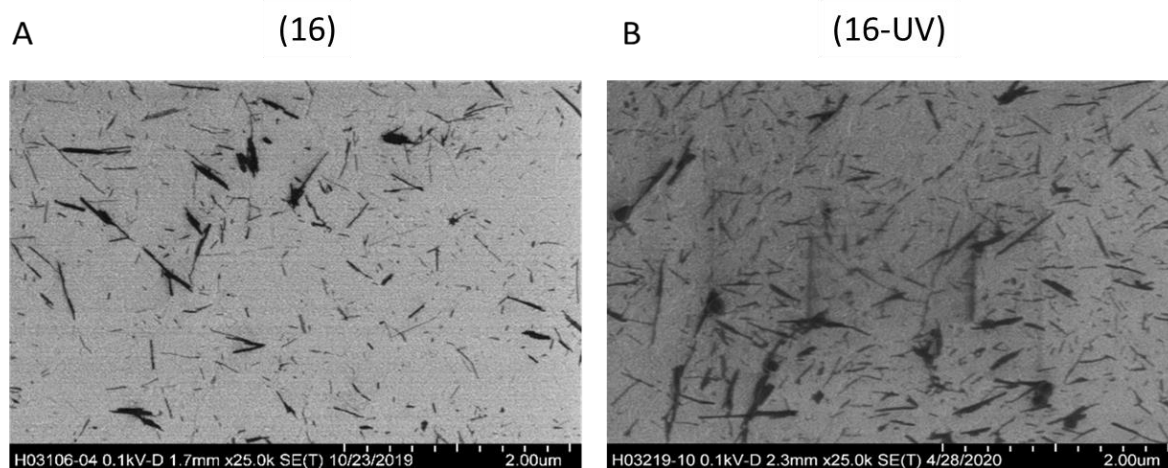


Figure S9: SEM images of RGD-NCL-CKFKFQF (**16**) amyloid nanofibers formed in solution. A) Sample (**16**) before irradiation and B) sample (**16-UV**) after irradiation.

## Proteostat-Assay on Surface

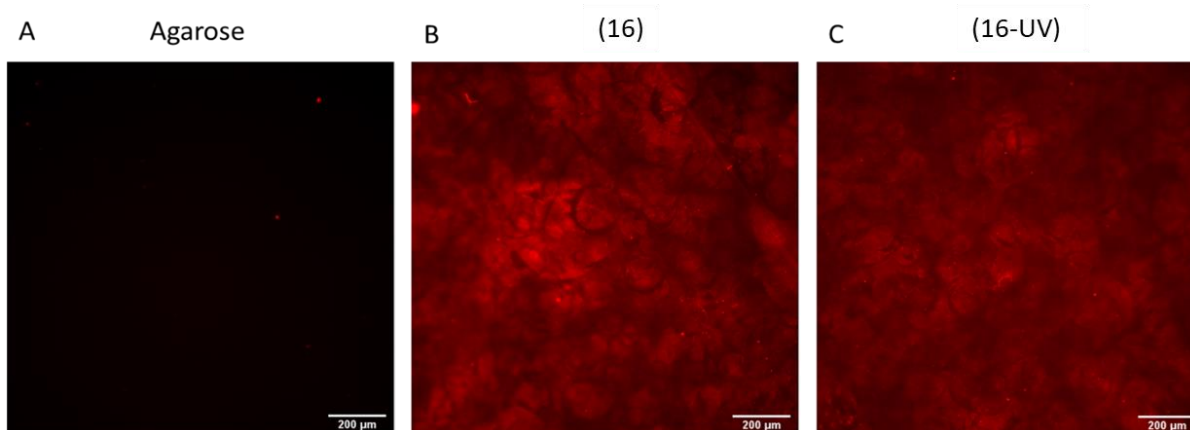


Figure S10: The Proteostat staining shows a homogeneous coating over a larger area for both, irradiated (**16-UV**, C) and non-irradiated samples (**16**, B). A) Control sample with only agarose coating.

## A549 Cell Adhesion Assay

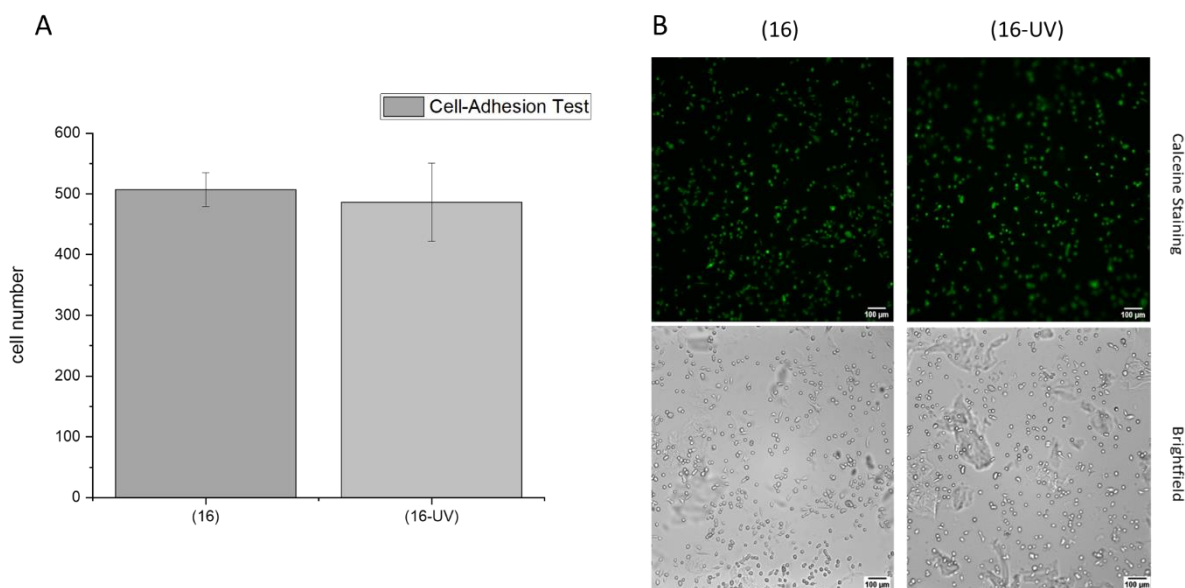


Figure S11: A549 cell adhesion assay with coated peptide fibers. A) Quantification of cells adhered to substrates coated with (16) which was either irradiated (16-UV) or left in the dark (16). B) Fluorescence images of cells confirming viability through calceine staining and corresponding bright field images. Scale bars represent 100  $\mu\text{m}$ .

## Cell-Viability Assay

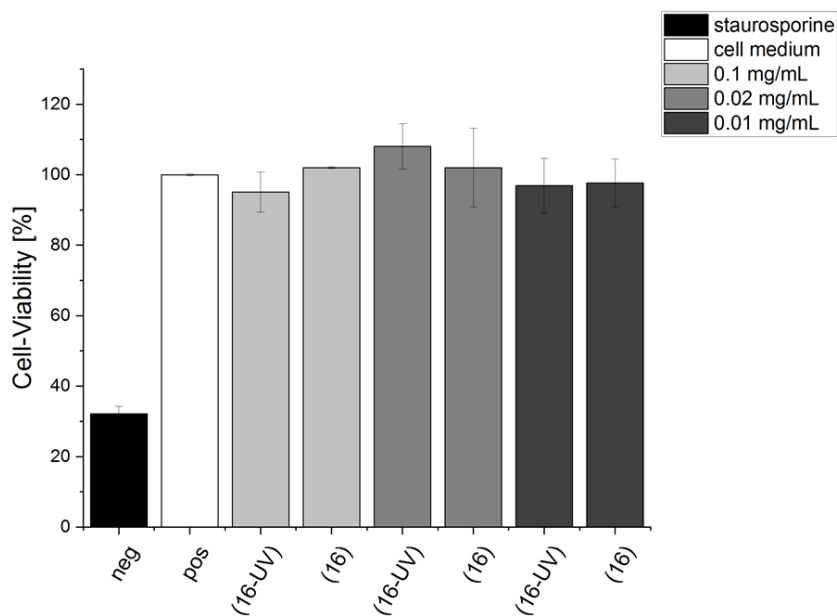


Figure S12: Cell-Titer-Glo Assay confirms the non-toxic character of the used fibers with (16-UV) and without (16) irradiation for 10 min. Negative control is a toxic stauroporine solution and positive control are cells without additive.

## 5.9.5. Additional Characterization RGD-PCL-CKFKQF (15)

### LC-MS

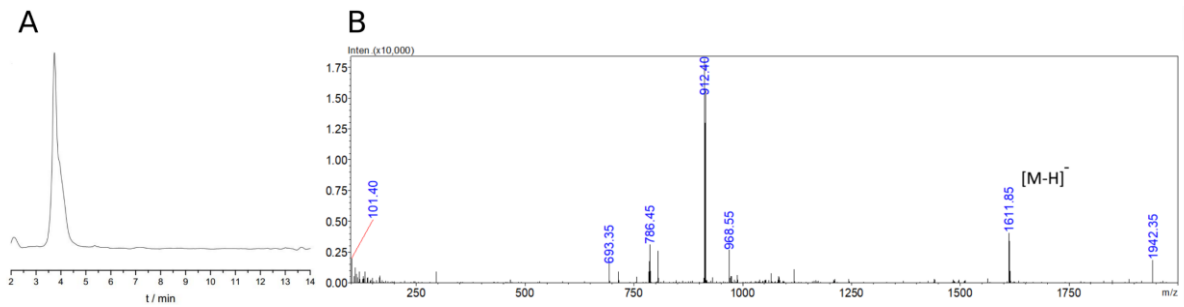


Figure S13: A) LC-MS chromatogram (detector: 214 nm) of RGD-PCL-CKFKQF (15). B) MS (ESI+) m/z calc. for C<sub>74</sub>H<sub>103</sub>N<sub>18</sub>O<sub>21</sub>S [M-H]<sup>-</sup>, 1611.73 g mol<sup>-1</sup>; found 1611.85 m/z

### A549 Cell Adhesion Assay without Gradient formation

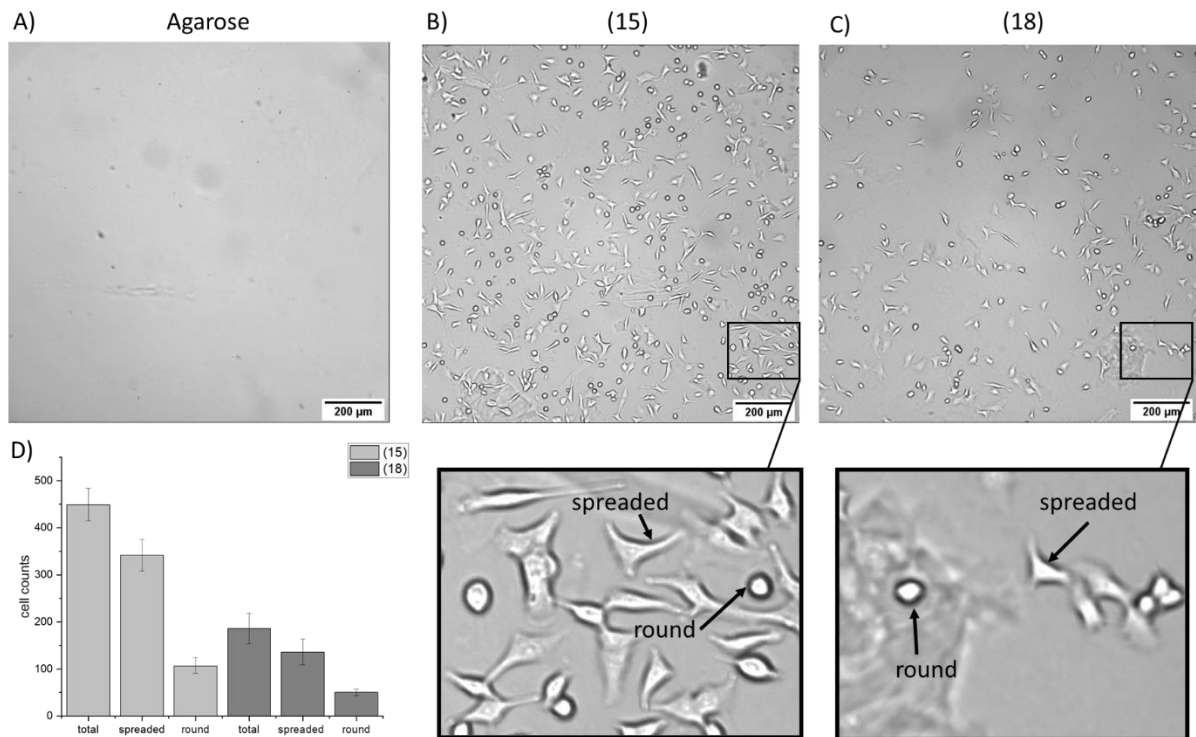


Figure S14: A549 cell adhesion assay. A) Agarose coating prevents adhesion of A549 cells. B) Agarose and peptide fibers (15) coated surfaces show adhesion with cell spreading (see arrow). C) After irradiation (18) less cells are visible on the surface. D) Quantification of cells adhered to substrates coated with (15) which was either irradiated (18) or left in the dark (15).

## LC-MS Measurements of Non-irradiated Molecule (15) and Irradiated Molecule (18)

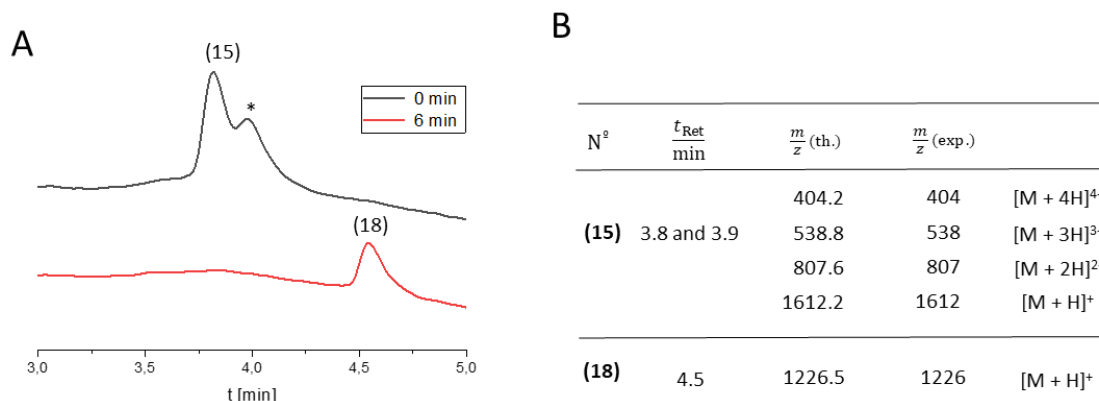


Figure S15: A) LC-MS chromatogram of HPLC fractions (0 sec irradiation for precursor **(15)**) and (6 min irradiation for fragment **(18)**) from the kinetic profiling in HPLC (see main text). Here, the second signal (\*) at 4 minutes has the same masses like the first signal **(15)**. The reason for this could be the formation of a disulfide bond between two precursor molecules that was enhanced because of the presence of DMSO in the peptide solution<sup>[3]</sup> B) Assignment of signals found in LC-MS measurements of samples before and after UV treatment.

## Comparison of cleavage kinetics of (15)

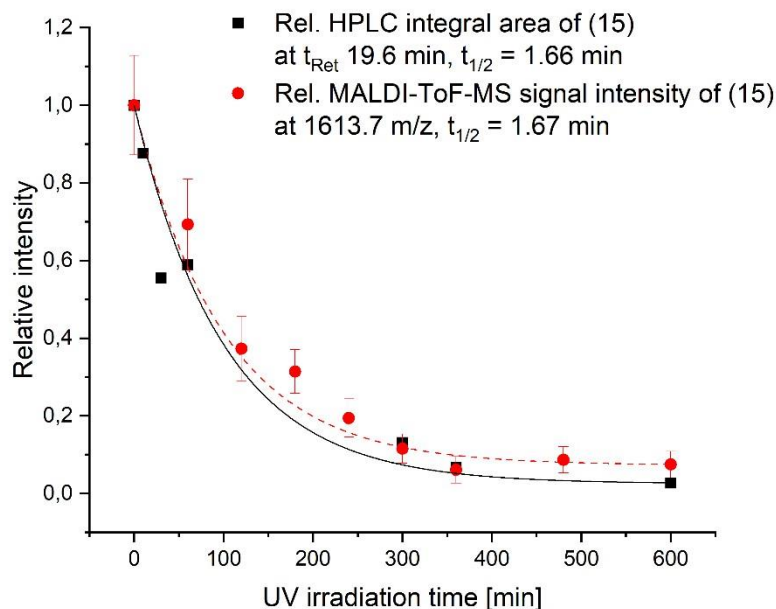


Figure S16. Relative HPLC integral area of **(15)** at  $t_{Ret}$  19.6 min (black square) and relative MALDI-ToF-MS signal intensities of **(15)** at 1613.7 m/z (red circle) after different UV-treatment times in aqueous solution and in dried state coated on ITO-glass substrate, respectively. Both data were set relative to non-irradiated **(15)** at time 0 and fitted to exponential decay first-order kinetics (solid black line HPLC integral area  $t_{1/2}$  = 1.66 min, dashed red line MALDI-ToF-MS  $t_{1/2}$  = 1.67 min).

## Scratch assay of ITO slides coated with (15) by atomic force microscopy

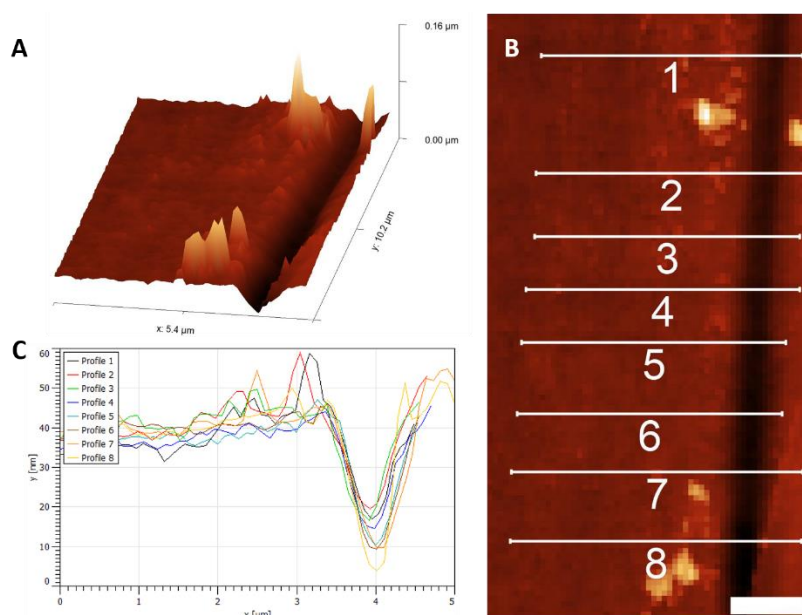


Figure S17: A) AFM measurement of ITO surface coated with (15). Prior to the measurement, the coating was scratched in order to measure profile thickness. B, C) Along the scratch, 8 profile lines were measured and height differences were calculated between lowest point and 3 μm left from lowest point. The average coating thickness was determined to be  $25 \pm 5$  nm. The scalebar represents 1 μm.

### 5.9.6. References

- [1] S. Sur, J. B. Matson, M. J. Webber, C. J. Newcomb, S. I. Stupp, *ACS Nano* **2012**, 6, 10776.
- [2] T. Kobayashi, T. Seki, *Langmuir* **2003**, 19, 9297.
- [3] Z. Papanyan, S. Markarian, *J. Appl. Spectrosc.* **2013**, 80, 775.

## 6. Summary and Outlook

This work intended to elucidate the importance of amyloid-like nanofibrils for medical applications, in which controlled cell-material interactions play a crucial role. This included the investigation of externally controllable amyloidogenic sequences by using rational peptide design to study the impact of amyloids' characteristics on cell-material interaction. Hence, a two-dimensional amyloid-like scaffold has been designed with the aim to precisely control cell adhesion. Here, we could show that through controlled chemical reactions, the amyloid-like scaffold was defunctionalized, destroyed or disassembled locally, which allowed the subsequent fabrication of macroscopic cell patterns and gradients on surfaces. The following Figure 17 depict an overview of achieved goals as well as possible application fields of the amyloidogenic platform.

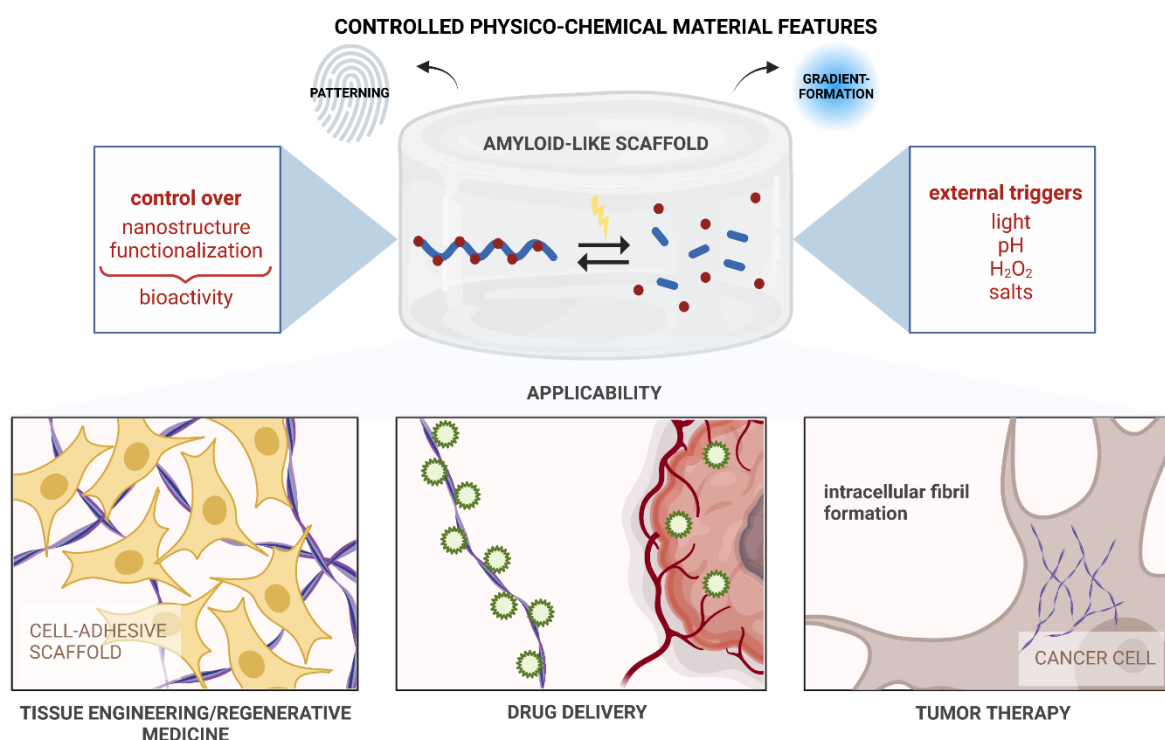


Figure 25. Overview of achieved goals within this thesis and future perspectives with possible applications of designed amyloidogenic platform.

In the first project, the ability of controlled (dis)assembly of amyloid-like fibrils in solution was studied. Through integration of orthogonal triggers in the peptides primary structure the kinked peptide  $\text{depsi(KIKI)pba(SQINM)}$  was designed. One of the chemical methods that shapes the designed molecule is the depsi-peptide, which



creates the kink in the molecule. The linearization of this molecule is achieved by an intramolecular nucleophilic attack of the amino group of the serine (*O,N*-acyl shift) towards the ester bond at pH higher than 2. Here, the linearization of the designed kinked peptide initiates the self-assembly process. As depsipeptides are only stable at pH values lower than 2, this approach reaches its limitations when using at cell-conditions. Therefore, within this work the depsipeptide was caged with a phenylboronic acid *via* a carbamate bond on the *N*-terminus of the serine to guarantee the stability of the depsipeptide at higher pH values than 2. The cleavage of this caging group is induced by hydrolysis of the carbamate. The implementation of a methionine within the amyloidogenic sequence the disassembly of the preformed fibrils by subsequent oxidation with hydrogen peroxide was controlled. Here, the balance between hydrophobic and hydrophilic residues within the sequence was changed by oxidation of the methionine to more polar methionine sulfoxide. Thus, we could demonstrate that even subtle changes in the amphiphilic pattern of amyloids have a considerable impact on their self-assembling features, which reflects the importance of the primary structure of self-assembling peptides. In summary, we could show that the design of controllable amyloid-like structures is feasible in solution by rational chemical design. The limitations of this project are referring to the chemical triggers as they may complicate the transition from solution to the surface. Consequently, in subsequent projects an *o*-nitrobenzyl linker was used as the chemical approach in order to design a two-dimensional platform to study cell-material interactions.

In the second project, I studied the effect of photo-triggered destruction of amyloid-like scaffolds on cell-material interactions. Hence, the photocleavable linkage group (PCL) was positioned at a critical position within the peptide sequence creating the sequence CKFK-PCL-FQF. After UV irradiation the sequence cleaves into a positively charged fragment CKFK and a lipophilic FQF fragment losing the ability to form amyloid-like fibrils. The cleavage results in loss of fibril morphology and  $\beta$ -sheet structure. TEM and ThT measurements indicated that the supramolecular structure was destabilized over an elongated time period, whereas the monomer packing within the nanofibrils changes already during the irradiation. Additionally, cell adhesion assays showed the loss of cell adhesiveness after irradiation on different cell lines like A549, Chinese Hamster Ovary (CHO) and Raw-Dual type cells as model cell-lines. By using photolithography patterning was achieved with resolutions of up to 10  $\mu\text{m}$ .

Summarized, the second project underpin the already known postulation about the correlation between the  $\beta$ -sheet amount and cell-adhesiveness.

In the last project, the effect on cell-material interaction caused by defunctionalisation of amyloid-like fibrils was studied. Additionally, a two dimensional gradient formation was aimed to reveal the sensitiveness of cell-attachment. The amyloid-forming peptide was functionalized by the integrin-binding sequence "RGD", resulting in the sequence RGD-PCL-CKFKFQF. The functionalization with the RGD enhances the number of attached cells 3-times. After spray-coating of the preformed fibrils on the surface the cleavage was performed by gradual irradiation with UV light through a photo mask. The gradient formation was evaluated by MALDI-MSI measurements indicating the molecular masses of intact peptide and corresponding fragments. This strategy was covering multiple length scales uncovering the UV-dose dependency.

Summarized we were able to underpin the literature known results of amyloid-like fibrils' intrinsic cell-adhesive and cell-supportive characteristics. Furthermore, we could show that the  $\beta$ -amount as well as the changes in morphology can tailor the intrinsic cell-adhesiveness. Consequently, through rational peptide design we were able to create amyloidogenic sequences with controllable bioactivities. As amyloids and amyloid-like fibrils provide several attractive features in comparison to other synthetic materials such as high biomimetic appeal caused by its complex architecture, within this work investigated platform has great potential in stem cell therapy. One of the issues of stem cell therapy is that stem cells after transplantation are becoming non-functional due to away migration from spot of application. By functionalizing our designed amyloid-fibrils with other bioactive signals as RGD and creating a gradient, migration behaviour of stem cells may be investigated. Furthermore, the in depth investigation of fundamental self-assembly processes and structure-function relationship may provide a higher scope for amyloid-like materials as the mechanical and biophysical properties of amyloid-like structures may be more predictable. For example computer-aided analytical techniques can be used to predict an amyloidogenic sequence with the ability to develop predefined 3D porous networks with specific characteristics.

## Amino Acid Code

<b>A</b>	Alanine
<b>R</b>	Arginine
<b>N</b>	Asparagine
<b>D</b>	Aspartic Acid
<b>C</b>	Cysteine
<b>E</b>	Glutamic Acid
<b>Q</b>	Glutamine
<b>G</b>	Glycine
<b>H</b>	Histidine
<b>I</b>	Isoleucine
<b>L</b>	Leucine
<b>K</b>	Lysin
<b>M</b>	Methionine
<b>F</b>	Phenylalanine
<b>P</b>	Proline
<b>S</b>	Serine
<b>T</b>	Threonine
<b>W</b>	Tryptophan
<b>Y</b>	Tyrosine
<b>V</b>	Valine

# Appendix

## List of Publications

### Orthogonally Stimulated Assembly/Disassembly of Depsipeptides by Rational Chemical Design

[REDACTED]

[REDACTED] ChemBioChem 2019, 20, 1376.

### Photoinduced Amyloid Fibril Degradation for Controlled Cell Patterning

[REDACTED]

[REDACTED]

[REDACTED]

[REDACTED] Macromol. Biosci. 2023, 23, 2200294.

# denotes equal contribution

### Cell-instructive surface gradients of photo-responsive amyloid-like fibrils

[REDACTED]

[REDACTED] ACS Biomater. Sci. Eng. 2021, 7,4798.

# denotes equal contribution

## List of Conferences and Summer Schools

GDCh-14<sup>th</sup> German Peptide Symposium, Cologne, 18.03. – 21.03.2019 (Poster Presentation)

ProMatLeben Polymere – 1<sup>st</sup> PhD and PostDoc Conference, Berlin, 03.09. – 04.09.2019 (Poster Presentation)

GDCh-100 Years Macromolecular Chemistry, Freiburg, 12.09.2021 – 14.09.2021 (Twitter Poster Presentation)

MPGC Retreat, Mainz, 08.06.2022 (Poster Presentation)

## Curriculum Vitae